# Final Project Report

# Embedded sensing system for continuous crack monitoring in concrete pavements

| Administration | |
|---|---|
| Lead researcher | Sajad Abolpour Moshizi |
| Contact details | Sajad.abolpourmoshizi@mq.edu.au |
| University | Macquarie University |
| Date of submission | 20/07/2026 |

# Table of Contents

**Acknowledgements and Project Team** ..... 5

**Executive Summary / Abstract** ..... 6

**1. Industry Problem, Needs and Relevance** ..... 8

**1.1 Specific Problems and Challenges the Research Addresses** ..... 8

**1.2 Why These Problems Remain Unsolved Today** ..... 8

**1.3 Who Faces These Challenges and What Costs Are Involved** ..... 9

**1.4 Impact of Adopting the Research Outcomes** ..... 9

**2. Project Objectives, Hypotheses and Impact Pathways** ..... 10

**2.1 Specific Industry Challenges Addressed by the Project** ..... 10

**2.2 Key Hypotheses and How Success Was Defined** ..... 10

**2.3 Intended Impacts of the Project** ..... 11

**2.4 Impact Pathways and Adoption by Industry** ..... 12

**3 Project Methodology and Key Activities** ..... 13

**3.1 Sensor Design and Development** ..... 13

**3.2 Laboratory Testing and Sensor Characterisation** ..... 14

**3.3 Numerical Modelling and Sensor Placement Analysis** ..... 15

**3.4 Data Acquisition and Wireless Communication** ..... 15

**3.5 Field Testing and System Validation** ..... 16

**3.6 Data Interpretation and Future Automation** ..... 16

**4 Analysis of Key Results, Deliverables, Description of Outputs and Project IP** 17

**4.1 Key Technical Results** ..... 17

4.1.1 Strain Sensor Performance (DEL-035, DEL-034, DEL-510) ..... 17

4.1.2 Temperature Sensing Results (DEL-034, DEL-510) ..... 21

4.1.3 Humidity Sensor (DEL-034, DEL-510) ..... 23

4.1.4 pH Sensor (DEL-034, DEL-510) ..... 26

4.1.5 Finite Element Analysis (FEA) of Concrete Pavements (DEL-725) ..... 27

4.1.6 Probabilistic Integration of Sensor Data with Pavement Performance Modelling (DEL-036) 29

4.1.7 Wireless Monitoring and Data Infrastructure (DEL-722, DEL-724) ..... 36

4.1.8 Field Experiments (DEL-723) ..... 39

4.1.9 Top Ryde Field Validation (DEL-723, DEL-342) ..... 43

4.1.10 Live Training Sensor Dashboard (DEL-511, DEL-724) ..... 46

**4.2 Project Deliverables and Outputs** ..... 50

**4.3 Intellectual Property and Commercial Potential** ..... 53

**4.4 Summary** ..... 54

**5 Next Steps – Commercialisation & Impact Plan** ..... 54

**5.1 Short-Term Next Steps** ..... 54

**5.2 Pathway to Commercialisation** ..... 55

**5.3 Impact Through Data Integration and Automation** ..... 55

5.4 Long-Term Industry Impact ..... 55
6 Education and Training ..... 55
7 Conclusions, Implications and Recommendations ..... 57
8 Publication List ..... 58
9 Acronyms and Abbreviations ..... Error! Bookmark not defined.
10 References ..... 59
11 Appendices and Attachments ..... 60

# Acknowledgements and Project Team

The author acknowledges the support and contribution of **Transport for NSW (TfNSW)** throughout the duration of this project. The guidance, technical input, and collaboration provided by the TfNSW team were instrumental in shaping the direction of the research and supporting field deployment activities. In particular, the contributions of **Hossein Asadi**, **Basil Ben**, and **Harish Srivastava** are gratefully acknowledged.

The author also acknowledges the academic support provided by **Macquarie University**, including valuable technical discussions, supervision, and research collaboration. Special thanks are extended to **Mohsen Asadnia**, **Golnaz Alipour Esgandani**, **Rouzbeh Abbassi**, and **Tracy Rushmer** for their contributions to the development, testing, and interpretation of the sensing system. The author also thanks **Kaveh Ghouchani** and **Yue Jiang**, PhD candidates at Macquarie University, for their assistance during the project.

Support from the **City of Ryde** is also gratefully acknowledged, particularly in facilitating aspects of field testing and engagement related to pavement infrastructure.

This project was conducted as part of the SmartCrete CRC program, and the support of all partners involved is sincerely appreciated.

# Executive Summary / Abstract

This project developed and validated an embedded sensing system for continuous, real-time monitoring of cracking and structural behaviour in concrete pavements, spanning both plain concrete pavements and continuously reinforced concrete pavements. The work was motivated by long-standing limitations in existing pavement monitoring technologies, including limited sensitivity, the inability to detect subsurface cracking, bulky sensor designs, and the high cost of commercial systems. In response to these challenges, the project delivered a low-cost, durable, and wireless-capable sensing platform designed for operation within the harsh environment of concrete pavements.

The research progressed from sensor development through laboratory testing and field validation. A high-performance piezoelectric strain sensor was developed using an optimised PLA encapsulation, enabling detection of microcrack-related strain changes before visible surface cracking occurred. In parallel, 3D-printed temperature sensors were designed and shown to track internal concrete temperature with good agreement to commercial devices across a temperature range relevant to pavement applications. The sensing system was supported by a functional IoT communication architecture that incorporated a high-resolution analogue-to-digital converter, MQTT-based data transmission, a web-based dashboard for real-time visualisation, and cloud-based data storage.

The system was validated through slab-scale field experiments and progressively deployed at larger in-pavement field sites, including a continuously reinforced concrete pavement on the M7 motorway corridor and an urban concrete slab at Cressy Road, Top Ryde. Across these trials, embedded sensors reliably detected pedestrian, scooter, motorcycle, and vehicle loading and demonstrated the ability to distinguish load location and magnitude with high spatial resolution, consistently resolving individual front and rear axle loads during vehicle passes. Finite element modelling corroborated the measured responses, and a quantitative analysis established a strong linear correlation between sensor voltage output and simulated principal stress ($R^2 = 0.978$), confirming that the sensor signal serves as a reliable proxy for the internal stress state. To support automated interpretation, a browser-based live training sensor dashboard incorporating a K-Nearest Neighbour (KNN) baseline classifier was developed, enabling real-time, on-the-fly classification of loading events into pedestrian, light vehicle, and heavy vehicle categories directly in the field. Collectively, these outcomes align closely with the objectives defined in the project proposal and demonstrate a viable pathway toward continuous in-pavement condition monitoring capable of supporting predictive maintenance strategies for Transport for NSW and other asset owners.

**Next Steps for Broad and Rapid Adoption**

The project is presently in the phase of in-field testing, where the embedded sensors are being evaluated for robustness, long-term durability, resistance to environmental and traffic-induced noise, and overall performance under real operational conditions. These trials are essential for demonstrating that the sensing system can function reliably once deployed in active pavement networks. The current KNN-based live classification dashboard provides a working baseline for real-time load classification, distinguishing pedestrian, light vehicle, and heavy vehicle events directly in the field. As the labelled dataset grows through continued field operation, development will progress toward an Artificial Neural Network classifier capable of distinguishing a broader range of load types and conditions, including:

- different load types (pedestrian, cycling, scooter, light vehicle, heavy vehicle)
- environmental effects (temperature and moisture variations)
- strain patterns associated with early crack initiation

This analytics platform will support broader industry adoption by enabling pavement operators to access actionable insights rather than raw sensor data, simplifying interpretation for asset managers across larger pavement networks.

**Further Research Required**

Further research is required to prepare the sensing system for wide-scale deployment across operational pavement networks. Key priorities are as follows.

Long-term sensor durability and signal stability under varying field conditions, including temperature fluctuations, moisture exposure, and repeated traffic loading, require systematic evaluation. Understanding potential signal drift and performance changes over time is essential for establishing confidence in extended monitoring applications.

Automated data interpretation tools require further development. The KNN baseline classifier will be progressively replaced by ANN-based methods capable of classifying a wider range of traffic loads and identifying strain patterns associated with crack initiation and progression, reducing reliance on manual interpretation and supporting scalable deployment.

Data management infrastructure requires scaling to support larger sensor networks. This includes optimisation of the cloud-based MQTT pipeline and continued development of the local SD module for offline data capture, ensuring reliable data handling, storage, and retrieval under continuous monitoring conditions across multiple field sites.

Finally, clear installation protocols and contractor-ready guidelines need to be developed to ensure consistent sensor placement, reliable installation during construction, and repeatable performance across different pavement project types. Collectively, these research activities define a clear pathway toward broad adoption of the SmartCrete sensing system across Australia's pavement networks.

# 1. Industry Problem, Needs and Relevance

## 1.1 Specific Problems and Challenges the Research Addresses

Concrete pavements form a critical component of the national road network and are expected to withstand heavy traffic loads and harsh environmental conditions throughout long service lives. Despite these expectations, one of the most significant deterioration mechanisms in plain concrete pavements (PCP) is internal tensile cracking. These cracks often begin below the pavement surface due to cyclic traffic loading, curling and warping from temperature and moisture gradients, inadequate support, or construction-related factors. Once cracks propagate to the surface, they accelerate structural deterioration and allow moisture ingress, ultimately compromising the pavement foundation and leading to costly rehabilitation.

The primary challenge is that current pavement monitoring methods cannot reliably detect subsurface cracking in real time. Most techniques, such as imaging, laser scanning, ground-penetrating radar (GPR), or manual inspections, identify only visible surface damage and are often insensitive to internal micro cracks. Even when internal evaluation is possible, these techniques are typically expensive, labour-intensive, slow to deploy across large networks, and impractical for continuous monitoring in live traffic environments.

Embedded sensor systems have been explored, but conventional sensing solutions suffer from high cost, low sensitivity, poor long-term survivability, bulky form factors, and persistent challenges related to data transmission when sensors are buried within concrete.

This project directly addresses these limitations by developing a low-cost, durable, high-sensitivity, and wireless-capable embedded sensing system that can detect internal cracking and strain redistribution before external damage appears.

## 1.2 Why These Problems Remain Unsolved Today

The detection of subsurface cracking in concrete pavements remains unresolved largely due to the high cost and limited durability of existing technologies. Commercial embedded sensors are typically priced at around $550 per unit, yet they often fail to deliver the sensitivity and long-term reliability required for in-pavement deployment at scale. The proposal identified this cost and performance gap as a primary barrier preventing widespread adoption of embedded monitoring solutions across road networks [1].

In addition to cost, many embedded sensing technologies exhibit poor survivability under concrete curing and service conditions. Industry evidence cited in the proposal indicates that up to 80 percent of MEMS-based pavement sensors fail within the first 10 months due to hydration reactions, alkaline environments, thermal cycling, construction damage, and repeated traffic loading [1]. As a result, asset owners continue to rely on surface-based inspection methods such as visual surveys, imaging, laser scanning [2], and ground penetrating radar [3], all of which are largely insensitive to internal micro cracking and provide only intermittent snapshots of pavement condition.

Technical challenges related to data transmission and system integration further limit progress. Wireless communication through concrete is difficult due to signal attenuation and noise, while traditional wired systems are costly and vulnerable to damage. The proposal also highlighted the lack of validated sensor placement strategies and the absence of internal environmental measurements, both of which restrict the ability to interpret strain behaviour and crack initiation accurately. Together, these limitations have prevented the development of continuous, real-time pavement monitoring systems capable of supporting predictive maintenance practices.

### 1.3 Who Faces These Challenges and What Costs Are Involved

Undetected subsurface cracking in concrete pavements primarily affects road asset owners and managers, including state road authorities such as Transport for NSW and local governments responsible for extensive networks of rigid pavements. Improved understanding of internal pavement condition enhances their ability to plan periodic maintenance efficiently and manage pavement life cycles effectively.

The economic impact is substantial. Australian governments including Commonwealth, state, territory and local spend roughly $30 billion dollars annually on maintenance, upgrade and expansion of the road network [4]. The government estimates that total state real expenditure on arterial road and bridge maintenance averaged 26,676 dollars per kilometre of arterial road over the ten-year period from 2014–15 to 2023–24, highlighting the ongoing financial costs associated with maintaining ageing pavement infrastructure [5].

Contractors and maintenance providers are also affected, as reliance on surface inspections and conservative assumptions reduces productivity and increases the risk of premature or delayed interventions. Beyond financial impacts, reactive maintenance increases material use, environmental costs, and limits evidence-based decision-making for long-term asset planning.

### 1.4 Impact of Adopting the Research Outcomes

The implementation of outcomes of this project could provide considerable economic, operational, environmental and social gains to the concrete and pavement industry. Thanks to the fact that the developed sensing system allows for early detection of internal cracking and dynamic monitoring of pavement behaviour, it will be possible to change from reactive maintenance procedures model towards a predictive model with a higher level of certainty. This enables asset owners to act sooner, extend the life of pavement and minimise the amount and size of large rehabilitation projects.

Operationally, the system enhances decision-making through monitoring of internal strain, load impacts and environmental conditions in real time. This diminishes the dependence on surface inspections and subjective judgement, so that maintenance activities can be planned with more confidence. Integration into wireless data transmission and cloud-based platforms further allows scalable deployment across an extensive pavement network.

There should be environmental and social advantages, too. Increasing pavement life reduces the materials needed and energy used for construction activities, while decreasing greenhouse gas emissions. Less major construction reduces traffic congestion, enhances road safety and protects both the road user and nearby communities. Enhanced knowledge of environmental effects on cracking also provides for sustainable pavement design and management.

# 2. Project Objectives, Hypotheses and Impact Pathways

## 2.1 Specific Industry Challenges Addressed by the Project

Concrete/rigid pavement deterioration is typically driven by processes that originate below the surface long before any visible signs appear. In both plain concrete pavements and continuously reinforced concrete pavements, tensile cracking initiates at the bottom of the slab under the combined effect of traffic loading, temperature and moisture gradients, slab restraint, and construction-related factors. By the time damage becomes detectable through conventional inspection, significant internal deterioration has often already occurred and intervention costs are substantially higher. The fundamental challenge this project was designed to address is therefore the absence of a reliable, practical means of observing pavement behaviour continuously from within — before deterioration reaches the surface.

Five specific technical barriers shaped the project objectives. First, no low-cost embedded sensing solution existed that could survive the alkaline, thermally variable, and mechanically demanding environment of a concrete pavement over its service life. Commercial options with demonstrated field durability were either prohibitively expensive or too bulky to embed without compromising the host structure. This directly motivated the development of the PLA-encapsulated PZT strain sensor and 3D-printed temperature sensor as the core sensing deliverables of the project.

Second, wireless transmission of data from within concrete had not been demonstrated reliably at the scale required for continuous pavement monitoring. Concrete attenuates wireless signals significantly, and wired alternatives introduce installation complexity and long-term maintenance risks incompatible with road infrastructure. Addressing this barrier drove the design and field validation of the MQTT-based IoT communication architecture, including the solar-powered standalone power supply and cellular data link demonstrated at the M7 Motorway installation.

Third, there was no validated evidence that embedded piezoelectric sensors could detect microcracking at an early enough stage to support proactive maintenance. Laboratory testing under cyclic and fatigue loading was therefore designed specifically to establish this capability, and the finding that the 12 mm PZT sensor detects microcrack initiation 7–8 cycles before visible failure directly addresses this gap.

Fourth, sensor placement in prior studies had been largely arbitrary, without mechanistic evidence linking sensor location to zones of critical stress. Finite element modelling and analytical electromechanical modelling were used in this project to establish the relationship between sensor position, stress distribution, and voltage output, providing a quantitative basis for placement strategies in future deployments.

Fifth, interpretation of embedded sensor data had previously required specialist knowledge, limiting the practical usefulness of monitoring data for routine asset management. This project addressed that barrier by developing a browser-based live training sensor dashboard with a K-Nearest Neighbour classifier capable of distinguishing pedestrian, light vehicle, and heavy vehicle loading in real time directly in the field, establishing an initial automated-interpretation capability that can be extended as the labelled dataset grows.

## 2.2 Key Hypotheses and How Success Was Defined

This project was guided by four practical hypotheses, each directly linked to the industry challenges identified in Section 2.1 and each defined with a measurable success criterion against which outcomes could be evaluated.

Hypothesis 1: Early crack detection. Internal microcracking in concrete pavements produces measurable changes in the strain field that an embedded piezoelectric sensor can detect before cracks become visible at the surface. Success was defined as consistent, repeatable signal changes preceding visible failure in laboratory fatigue tests across multiple replicate specimens. This hypothesis was confirmed: the 12 mm PZT sensor detected microcrack initiation 7–8 cycles before visible failure in fatigue loading tests, with signal changes including a systematic deepening of voltage troughs in successive cycles that provided unambiguous early warning. The finding that the sensor response increased in magnitude and changed character in the cycles immediately preceding failure — with one cycle before main failure showing troughs more than three times deeper than the preceding cycle — establishes a clear and actionable detection signature.

Hypothesis 2: Sensor survivability and signal quality. A low-cost PZT ceramic sensor with Polydimethylsiloxane (PDMS) encapsulation can survive embedment in concrete and produce stable, low-noise signals under repeated mechanical loading without amplification. Success was defined as maintained sensor function, stable peak-to-peak voltage output across replicate specimens, and a signal-to-noise ratio sufficient to distinguish loading events from baseline noise without post-hoc filtration. This hypothesis was confirmed for the 12 mm sensor configuration: SNR values of 8.22 ± 0.47, 13.56 ± 0.82, and 10.22 ± 0.49 dB (at 0.5, 1, and 2 kN/s respectively, n = 3) were achieved without filtration, the sensor had no measurable effect on the flexural strength of the host concrete (5.6 ± 0.4 MPa, preserved), and output was reproducible across all three replicate beams. The 30 mm sensor, while producing higher absolute voltage, failed this criterion due to low SNR and a 9% reduction in host concrete strength, and was therefore not carried forward to field deployment.

Hypothesis 3: Wireless data transmission. Reliable, real-time wireless data transmission from sensors embedded within a concrete pavement is achievable using a low-cost IoT architecture without wired extraction. Success was defined as continuous data streaming to a cloud-based dashboard at a sufficient sampling rate during active field loading, with no loss of signal integrity attributable to the concrete medium. This hypothesis was confirmed through progressive field deployments: initial slab-scale trials established wireless transmission via MQTT broker, and the M7 Motorway corridor deployment demonstrated continuous real-time data streaming from sixteen sensors embedded in a continuously reinforced concrete pavement under live highway conditions, supported by a solar-powered standalone energy system with cellular connectivity.

Hypothesis 4: Environmental context. Temperature and moisture measurements from within the pavement provide meaningful context for interpreting embedded strain sensor output, and a 3D-printed temperature sensor can track internal concrete temperature with accuracy comparable to commercial devices. Success was defined as good agreement between the 3D-printed sensor output and a commercial reference device across the temperature range relevant to pavement service conditions. This hypothesis was confirmed: the 3D-printed temperature sensor tracked internal concrete temperature with good agreement to a commercial reference across the tested range. Integration of temperature and humidity sensors alongside strain sensors was demonstrated in both the M7 Motorway and Top Ryde field deployments, with environmental readings streamed to the same real-time dashboard as strain data.

### 2.3 Intended Impacts of the Project

The primary intended impact of this project is to enable a structural shift in how concrete pavement assets are managed, from reactive maintenance triggered by visible surface deterioration to predictive maintenance informed by continuous, real-time data from within the pavement structure. By providing early warning of internal cracking and stress accumulation before damage reaches the surface, the sensing system gives asset owners a fundamentally different basis for intervention: one

grounded in measured pavement behaviour rather than periodic visual inspection or subjective condition ratings.

The economic case for this shift is substantial. Unplanned pavement rehabilitation is significantly more expensive than targeted preventive intervention, and large road authorities managing extensive rigid pavement networks, including Transport for NSW, carry considerable exposure to this cost differential. Earlier and more precise identification of deteriorating sections allows maintenance budgets to be directed where they are most needed, extends the serviceable life of existing assets, and reduces the frequency and scale of full-depth reconstruction events. The project does not claim a specific savings figure, but the order of magnitude of potential benefit grows with network scale, making the technology particularly relevant to authorities with large rigid pavements sections such as urban motorway corridors and highways.

Operationally, the system reduces dependence on surface inspections and subjective assessments that can miss subsurface damage entirely. Continuous internal data improves confidence in maintenance planning, supports more transparent and auditable asset management decisions, and provides a factual basis for prioritising works across competing sections of a network.

From an environmental perspective, extending pavements service life through earlier intervention reduces the frequency of rehabilitation, decreasing demand for new materials, construction traffic, and the associated carbon emissions. Socially, fewer and shorter roadworks episodes reduce disruptions to road users, improves safety, and contribute to more reliable transport networks, outcomes that align with the broader service obligations of road authorities.

Finally, the project outputs align with current government priorities in infrastructure resilience, digital transformation of asset management, and more efficient use of public investment. The combination of a low-cost sensing platform, a wireless Internet of Things (IoT) architecture, and an on-site real-time dashboard positions the SmartCrete system as a practical and near-term contributor to the digital infrastructure agenda, rather than a long-horizon research aspiration.

### 2.4 Impact Pathways and Adoption by Industry

The pathway from research output to industry adoption follows three overlapping phases, each building on the credibility and maturity established in the phase before it.

**Short term:** field validation and partner engagement. The immediate priority is consolidating the evidence base from the deployments completed during this project. Continued in-field testing at the Cressy Road, Top Ryde site and ongoing monitoring of the M7 Motorway corridor installation provides the performance data needed to demonstrate sensor durability and signal consistency under real pavement conditions and variable traffic loading. These activities are being conducted in direct collaboration with Transport for NSW and other industry participants, ensuring that the validation program is shaped by the questions asset managers actually need answered before they can commit to broader adoption. Outputs from this phase include field-validated performance benchmarks, refined installation procedures for both cast-in and drill-and-embed sensor configurations, and an expanded labelled dataset for classifier training.

**Medium term:** pilot deployment and operational integration. Once field validation has established sufficient confidence in sensor performance and system reliability, the technology is suited for pilot deployment on selected pavement sections within a managed network. At this stage, the deliverables shift from research outputs to operational tools: installation guidelines and quality assurance procedures suitable for use by contractors, a data dashboard configured for asset-manager users rather than researchers, and structured training for the staff responsible for interpreting monitoring outputs and acting on them. Industry participants play a central role in this phase, not only as recipients of the technology but as active partners in refining it for operational contexts, identifying

integration points with existing pavement management systems, and building the internal capability needed for sustained adoption.

**Long term:** network-scale deployment and automated decision support. Broad adoption of the sensing system across a road network depends on two developments beyond the current project scope: a reduction in per-unit deployment cost through manufacturing scale, and the maturation of the automated data interpretation capability to a level where it can support network-level decision-making with minimal specialist input.

The foundation for the second of these has been laid in this project. A browser-based live training sensor dashboard incorporating a K-Nearest Neighbour (KNN) baseline classifier was developed and field-validated, enabling real-time, on-the-fly classification of loading events into pedestrian, light vehicle, and heavy vehicle categories directly in the field without post-processing. The operator labels events through a dedicated Training Mode using single-key shortcuts, and the dashboard automatically extracts a 16-feature vector covering per-channel peak amplitude and signal energy, the number of simultaneously active sensors, spatial centroid coordinates, and timing-based wave propagation features, that characterises each loading event across the sensor array. Once sufficient labelled examples have been collected, the KNN model (K = 5) is trained within the dashboard and the system transitions to live classification, assigning a class label and confidence score to each subsequent event and logging results in a timestamped record exportable for offline analysis. The classifier was validated during SUV drive-over tests at the Ryde field site, where it reliably distinguished vehicle from pedestrian loading and the spatial activation map correctly reflected the lateral wheel path across the slab.

This implementation represents a first working baseline rather than a final solution. Expanding the labelled training dataset across a wider range of vehicle categories, loading speeds, and pavement configurations, and progressively replacing the KNN baseline with more capable models as the dataset grows, will be the primary machine-learning development tasks in subsequent project phases. Integration of the classification output with pavement management frameworks, where load history, cumulative damage estimates, and condition forecasts can inform network-level maintenance scheduling, represents the longer-term target for automated decision support.

# 3 Project Methodology and Key Activities

The project followed a structured and progressively staged methodology in which findings from each phase directly informed the next. Laboratory studies established the sensing principles and encapsulation strategies that guided modelling decisions; modelling results shaped field implementation choices; and field deployments provided the real-world validation data needed to assess system performance against the project hypotheses. This sequencing ensured that the system evolved in a technically rigorous and practically relevant manner rather than as a series of disconnected experiments.

### 3.1 Sensor Design and Development

The initial phase focused on identifying an embedded sensing solution capable of surviving and functioning reliably inside concrete pavements under repeated mechanical and environmental loading. Strain sensing was the primary focus, since changes in the internal strain field are directly linked to microcrack initiation and progression. A range of sensor types, sizes, and encapsulation strategies were evaluated systematically across laboratory specimens, with assessments covering

sensitivity to dynamic loading, signal clarity, structural impact on the base concrete, and practical suitability for casting-in during construction.

Table 1 summarises the candidate configurations evaluated and their assessed suitability for field deployment. Piezoresistive sensors were excluded at an early stage due to their large size relative to the concrete aggregate and their susceptibility to noise under dynamic loading. However, that same larger size proved capable of capturing microcracks, so a follow-up test was carried out to characterise this behaviour. Four piezoresistive sensors were embedded in a concrete beam, two above the neutral axis and two below it. Under a constant deflection rate in the UTM machine, microcracks were induced in the sample, and the sensors captured these microcracks throughout, as shown in Video 0 – Piezoresistive sensor response. The video plots sensor response against load on the same axes, showing the load drop and corresponding sensor output at each microcrack event. The sensors positioned below the neutral axis showed a higher response than those above it.

Among piezoelectric configurations, the 30 mm sensor encapsulated in PDMS produced higher absolute voltage output but introduced stress concentrations that reduced the flexural strength of the host concrete by approximately 9% and generated noisier signals requiring filtration. The 12 mm sensor in PDMS partially addressed these issues but was subsequently superseded by the 3D-printed Polylactic acid (PLA) housing, which provided a more rigid and geometrically controlled encapsulation that further improved signal clarity and reduced sensitivity to electromagnetic interference. The Thermoplastic polyurethane (TPU) encapsulation was also trialled but was found to produce noisier outputs under sustained cyclic loading due to its softer mechanical response.

Table 1. Candidate sensor configurations evaluated during the design phase, showing sensing element size, overall packaged sensor size, and suitability for field deployment based on signal quality, structural impact, and practical installation requirements.

| Material | Encapsulation | Sensing element size (mm) | Packaged sensor size (mm) | Suitable for deployment |
|---|---|---|---|---|
| Piezoresistive | None | 26 | 26 | No |
| Piezoelectric (PZT) | PDMS | 12 | 15 | Yes (superseded) |
| Piezoelectric (PZT) | PDMS | 30 | 33 | No |
| Piezoelectric (PZT) | 3D-printed PLA | 12 | 20 | Yes (selected) |
| Piezoelectric (PZT) | 3D-printed TPU | 12 | 20 | No |

The PLA-encapsulated 12 mm PZT sensor was selected as the primary sensing element for all subsequent laboratory, modelling, and field work. In parallel, temperature and humidity sensing was addressed through 3D-printed conductive TPU temperature sensors validated against commercial reference devices, providing the environmental context needed to interpret strain behaviour under varying pavement conditions.

### 3.2 Laboratory Testing and Sensor Characterisation

A comprehensive laboratory testing program was undertaken using concrete beam specimens prepared to TfNSW R83 specification (80% OPC, 20% fly ash; flexural strength 5.6 ± 0.4 MPa). Sensors

were embedded at multiple locations within specimens to investigate how placement relative to the neutral axis and to anticipated crack initiation zones affected signal quality and detection capability.

Four-point bending tests were used to characterise the relationship between applied load, stress distribution, and sensor output voltage, with tests conducted across a range of loading rates (0.5 to 2 kN/s) to establish the dynamic sensitivity of the sensor under conditions representative of traffic loading. Cyclic and fatigue loading tests were then used to evaluate early crack detection capability under repeated loading. These tests confirmed that sensors placed in regions of higher tensile stress, specifically in the midsection and lower third of the beam cross-section, provided consistently earlier and more reliable detection of microcrack initiation than sensors placed closer to the supports or neutral axis.

Key quantitative outcomes from this phase included a signal-to-noise ratio of 13.56 ± 0.82 dB for the 12 mm PLA-encapsulated sensor at 1 kN/s (n = 3), a noise floor of approximately 0.1 mV, and the detection of microcrack initiation 7 to 8 cycles before visible failure in fatigue tests, with signal character changes in the final cycle before failure exceeding three times the amplitude of preceding cycles. These results established a clear, repeatable, and quantitatively characterised early-warning signature that provided the evidential basis for the field deployment program.

### 3.3 Numerical Modelling and Sensor Placement Analysis

Finite element modelling was developed in parallel with laboratory testing to provide a mechanistic understanding of stress distributions within instrumented concrete specimens and to guide sensor placement decisions at slab and pavement scale. Models were calibrated against the four-point bending experimental results and subsequently extended to simulate slab-scale and pavement-scale geometries under static and moving load conditions.

The calibrated models reproduced the experimental voltage-output trends with good accuracy, confirming that normal stress predominantly governs sensor response and that the analytical electromechanical model developed for the project accurately captures the underlying physics. A strong linear correlation between simulated principal stress and measured sensor voltage output ($R^2$ = 0.978, RMSE = 2.69 kPa) was established, confirming that the sensor signal serves as a reliable quantitative proxy for the internal stress state at the sensor location.

Dynamic simulations representing moving vehicle loads across a pavement slab were also conducted to assess how sensor responses evolve spatially and temporally as an axle traverses the instrumented section. These simulations provided direct guidance for the sensor array layout used in the Cressy Road field deployment, including the lateral spacing between sensor rows and the positioning of sensors relative to anticipated wheel paths.

### 3.4 Data Acquisition and Wireless Communication

Developing a reliable data acquisition and communication system was a central and technically demanding component of the methodology, given the signal attenuation challenges associated with wireless transmission through concrete and the need for sufficient sampling frequency to capture dynamic loading events from vehicle passes.

Several hardware and software configurations were evaluated iteratively during the project. The final system incorporated a high-resolution analogue-to-digital converter connected to a microcontroller, with data transmitted wirelessly using an MQTT publish-subscribe protocol to a cloud broker (HiveMQ) and visualised through a custom browser-based real-time dashboard. Cloud storage provided continuous data archiving for post-processing and longitudinal analysis. The system operated at 100 Hz (10 ms sample interval), sufficient to resolve individual axle load events and the front-to-rear axle timing sequence of passing vehicles.

To address the power supply requirements of remote field installations, a standalone solar-powered energy system was designed and deployed, comprising a 40 W solar panel, an MPPT charge controller, a 12 V deep-cycle battery, and a DC-DC converter providing regulated 5 V to the microcontroller. Cellular connectivity via an IoT SIM module was used at the motorway (M7 corridor) site to provide cloud data transmission independent of local Wi-Fi infrastructure. This architecture enabled stable real-time monitoring during field deployments at both the driveway (Cressy Road, Top Ryde) and motorway (M7 corridor) sites without reliance on mains power or fixed network connections.

### 3.5 Field Testing and System Validation

Field validation followed a staged progression from small, controlled specimens to in-pavement deployment at operational road sites, with each stage building directly on the lessons and system configurations established in the preceding one.

The first stage used small concrete slabs (400 x 400 x 100 mm) with a single embedded sensor to confirm that the wireless transmission architecture and real-time dashboard functioned correctly outside the laboratory. These trials were followed by larger slab-scale experiments (1.0 x 1.0 x 0.24 m) with four embedded strain sensors and one temperature and moisture sensor, subjected to pedestrian, scooter, and motorcycle loading. Sensors consistently captured these events, with signal magnitude across the array reflecting both load position and intensity, demonstrating spatial resolution of loading at the slab scale.

Building on these results, the project deployed the sensing system at two operational road sites. At Cressy Road, Top Ryde, eight PLA-encapsulated strain sensors were installed in a newly constructed concrete slab using a drill-and-embed method, with sensors connected through two buried junction boxes to the wireless acquisition system. SUV drive-over tests recorded at this site confirmed reliable detection of individual front and rear axle passes, with the live training dashboard used to collect labelled loading events in real time. At the M7 Motorway corridor, sixteen strain sensors and two temperature and humidity sensors were installed in a continuously reinforced concrete pavement during construction, with data transmitted via cellular connection to the cloud dashboard under live highway traffic conditions.

Installation procedures were refined progressively across these deployments, resulting in documented cast-in and drill-and-embed protocols suitable for use in future pilot deployments.

### 3.6 Data Interpretation and Future Automation

Sensor data collected across laboratory and field programs were analysed to identify patterns associated with specific loading types, spatial load position, and early damage development. This interpretation work progressed from manual signal inspection in the early laboratory phase to a structured, automated approach in the field phase.

A browser-based live training sensor dashboard incorporating a K-Nearest Neighbour (KNN) baseline classifier was developed to enable on-the-fly load classification directly in the field. The dashboard extracts a 16-feature vector from each detected loading event, covering per-channel peak amplitude and signal energy, the number of simultaneously active sensors, spatial centroid coordinates derived from sensor positions weighted by signal amplitude, and timing-based wave propagation features. Operators label events in real time using a dedicated Training Mode, and once sufficient labelled examples have been collected, the KNN model (K = 5) is trained within the dashboard and the system transitions to live classification, assigning each subsequent event to one of three categories: pedestrian, light vehicle, or heavy vehicle. Field validation at the Ryde site confirmed that the classifier reliably distinguished vehicle from pedestrian loading events and that the spatial activation map correctly reflected the lateral wheel path across the slab.

This capability represents the first stage of what is intended to become a progressively more capable automated interpretation system. The labelled dataset accumulated during field operations provides the training foundation for more advanced classifiers to be introduced in subsequent project phases. The longer-term objective is integration of the classification and damage-assessment outputs with pavement management frameworks, where continuously updated load history and structural condition data can support network-level maintenance scheduling and asset life prediction.

# 4 Analysis of Key Results, Deliverables, Description of Outputs and Project IP

This section summarises the key technical results achieved during the project and evaluates how these outcomes address the original project objectives. The results demonstrate that the developed sensing system is technically sound, practically deployable, and well positioned for further development and industry adoption.

### 4.1 Key Technical Results

4.1.1 Strain Sensor Performance (DEL-035, DEL-034, DEL-510)

One of the key technical outcomes of this project was the development and systematic evaluation of embedded piezoelectric strain sensors suitable for long-term use in concrete pavements. A structured laboratory testing program was conducted to characterise sensor response, repeatability, signal quality, and early crack detection capability under cyclic and fatigue loading conditions representative of pavement behaviour. Two sensor sizes were evaluated across three concrete beam replicates each (n = 3), allowing statistically meaningful comparisons of performance metrics.

Initial testing focused on piezoelectric sensors encapsulated using PDMS, a flexible elastomeric polymer that distributes stress across the sensor surface and provides electrical insulation. These sensors produced stable and repeatable voltage responses during cyclic loading, confirming that the sensing principle functioned reliably when the sensor was embedded within concrete. The sensor configuration, component layout, and experimental setup are illustrated in Figure 1.

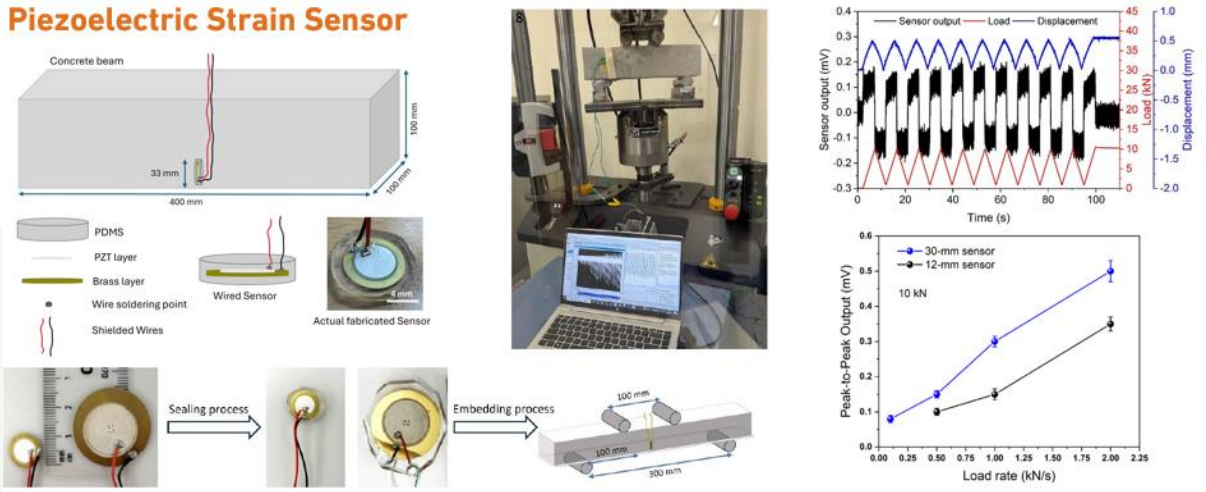


Figure 1. Piezoelectric strain sensor with PDMS encapsulation, including exploded view of the sensor components, experimental setup, and overall sensor dimensions used in laboratory testing.

Testing was then extended to evaluate the effect of sensor size on performance. Two commercially available PZT diaphragms (Murata Manufacturing Co., Ltd.) were compared: a 12 mm sensor (Part No. 7BB-12-9, 9 mm PZT element on a 12 mm brass plate) and a 30 mm sensor (Part No. 7BB-27-4, 20 mm PZT element on a 27 mm brass plate). Both were sealed with PDMS and embedded in concrete beams prepared to TfNSW R83 specification (80% OPC, 20% fly ash; mean flexural strength 5.6 ± 0.4 MPa). Signals were recorded directly into a National Instruments NI-9239 data acquisition device at 5 kHz, without an external charge amplifier. A baseline correction was applied to remove DC offset, and where required, a causal moving average filter with a 10-sample window (2 ms at 5 kHz) was applied prior to peak-to-peak voltage extraction.

Under cyclic loading with a maximum load of 10 kN, the 12 mm sensor produced peak-to-peak voltages of 0.1 mV at 0.5 kN/s, 0.15 mV at 1 kN/s, and 0.3 mV at 2 kN/s, while the 30 mm sensor produced higher absolute voltages at each rate. However, the more important finding was in signal quality: the 12 mm sensor achieved mean signal-to-noise ratio (SNR) values of 8.22 ± 0.47, 13.56 ± 0.82, and 10.22 ± 0.49 dB at 0.5, 1, and 2 kN/s respectively, compared with substantially lower values of 1.06 ± 0.07, 2.26 ± 0.11, and 7.75 ± 0.47 dB for the 30 mm sensor under the same conditions. A one-way repeated-measures ANOVA confirmed that this difference was statistically significant ($F = 288.03$, $p < 0.0001$), with post-hoc Tukey comparisons confirming that the 12 mm sensor produced significantly higher SNR at all corresponding load rates ($p < 0.0001$). The noise floor of the 12 mm sensor was approximately 0.1 mV under unloaded conditions, compared with approximately 0.4 mV for the 30 mm sensor.

The lower noise of the 12 mm sensor is attributable to its smaller size relative to the maximum concrete aggregate (20 mm), which means the sensor acts as a smart aggregate rather than a stress concentrator. In contrast, the 30 mm sensor exceeded the aggregate size, inducing localised stress concentrations that both reduced the flexural strength of the host concrete by approximately 9% (from 5.6 ± 0.4 MPa to 5.1 ± 0.3 MPa) and introduced microcracking around the sensor that elevated baseline electrical noise. The 12 mm sensor had no measurable effect on host concrete strength.

An indicative dynamic sensitivity of approximately 3 to 10 µV/µε was derived for the 12 mm sensor from beam theory (four-point bending, sensor at $z = 17$ mm below the neutral axis, $E = 33$ GPa from ACI 318 for $f'c = 49.5$ MPa), yielding a host-concrete strain of approximately 31 µε under 10 kN load. This range reflects the load-rate dependence inherent to piezoelectric transducers: the same applied strain produces different voltage outputs depending on the rate at which it is applied, because the piezoelectric response is governed by the rate of polarisation change rather than the static strain magnitude. The value at 1 kN/s, approximately 5 µV/µε, is the most representative for vehicular loading conditions given the typical pulse duration of an axle pass. For context, optimised surface-bonded PVDF film sensors reported in the literature achieve sensitivities of 400 to 970 µV/µε, but these figures apply to sensors measured with charge amplifiers and in direct contact with the host surface. The lower µV/µε value for the SmartCrete sensor reflects deliberate design trade-offs: no charge amplifier (reducing cost and complexity), a PDMS coupling layer that partially decouples the ceramic from host-concrete strain (providing protection at the expense of strain transfer efficiency), and embedding rather than surface bonding (necessary for subsurface crack detection but introducing additional shear-lag loss). Critically, the achieved sensitivity is sufficient for the application: field-measured traffic-induced strains in concrete pavements range from approximately 1 to 40 µε per axle pass, placing the expected signal well above the 0.1 mV noise floor even for passenger car loading.

The performance comparison between the 12 mm and 30 mm sensors is summarised in Table 2, along with the key specification and characterisation parameters for each configuration. The 12 mm PLA-encapsulated PZT sensor was selected as the recommended configuration for field deployment on the basis of its superior signal-to-noise ratio, absence of structural impact on the host concrete, and production of signals that required no filtration.

Table 2. Performance comparison of the 12 mm and 30 mm PZT piezoelectric strain sensor configurations evaluated under four-point bending cyclic loading in TfNSW R83 concrete beams (n = 3 per configuration; values reported as mean ± SE unless otherwise stated).

| Parameter | 12 mm sensor (recommended) | 30 mm sensor |
|---|---|---|
| Sensing element | PZT diaphragm, Murata 7BB-12-9 (9 mm PZT on 12 mm brass plate), PDMS-sealed | PZT diaphragm, Murata 7BB-27-4 (20 mm PZT on 27 mm brass plate), PDMS-sealed |
| Resonant frequency / capacitance | 9.0 ± 1.0 kHz / 8.0 nF | 4.0 ± 0.5 kHz / 20.0 nF |
| Peak-to-peak output (10 kN max load) | 0.1 mV at 0.5 kN/s; 0.15 mV at 1 kN/s; 0.3 mV at 2 kN/s | Higher amplitude than 12 mm at each rate |
| Signal-to-noise ratio (dB) | 8.22 ± 0.47 / 13.56 ± 0.82 / 10.22 ± 0.49 (at 0.5 / 1 / 2 kN/s) | 1.06 ± 0.07 / 2.26 ± 0.11 / 7.75 ± 0.47 (ANOVA: $F = 288.03$, $p < 0.0001$) |
| Noise floor (unloaded Vpp) | ~0.1 mV | ~0.4 mV |
| Crack-detection lead time | 7 to 8 cycles before visible failure | Same sensor family; not independently tested in fatigue |
| Structural impact on host concrete | No strength reduction; 5.6 ± 0.4 MPa preserved | 9% reduction; 5.1 ± 0.3 MPa (stress concentrations from sensor exceeding aggregate size) |
| Filtration required | No; clear signal without post-processing | Yes; moving average required |
| Piezoelectric voltage coefficients | g11 = 0.0452, g31 = 0.0447 V·m/kN | Not modelled |
| Unit cost | Low-cost commercial diaphragm | Low-cost commercial diaphragm |

Fatigue testing was conducted to assess the sensor's ability to detect microcracking early on under repeated loading cycles. The results demonstrated that the sensor reliably detected microcrack initiation 7 to 8 cycles before visible failure, as shown in Figure 2. The detection signature was consistent and unambiguous: in the cycles preceding failure, the peak-to-peak voltage output increased, and the voltage troughs deepened progressively, with the trough in the cycle immediately before main failure exceeding three times the depth of the preceding cycle. This pattern provides a clear, actionable early-warning signal that does not require specialist interpretation.

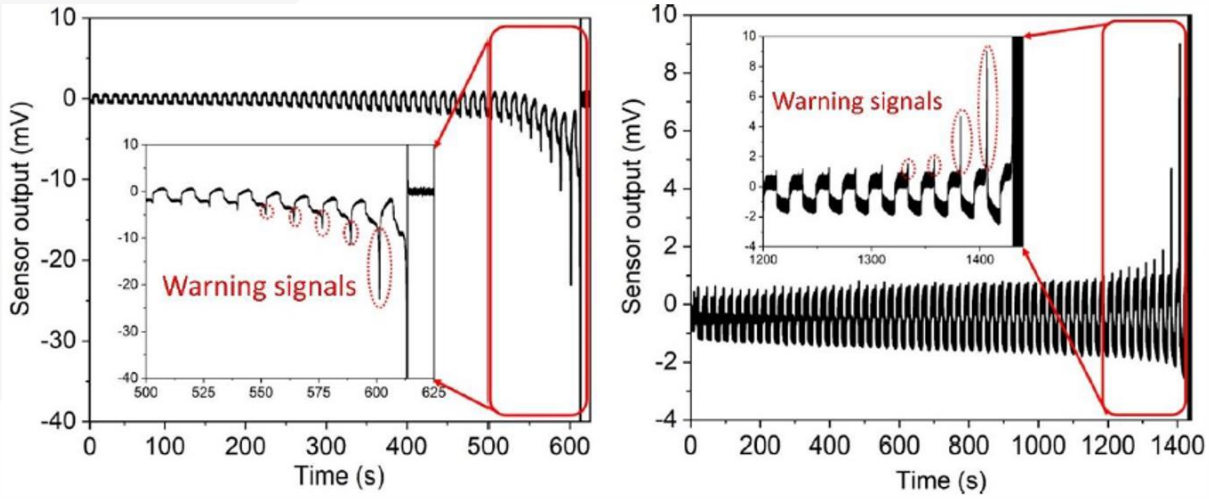


Figure 2. Example strain sensor output during fatigue loading, showing the change in signal character associated with microcrack initiation and progression in the cycles preceding visible failure.

The effect of sensor encapsulation material on signal quality was investigated by comparing PDMS, TPU, and PLA housings. As illustrated in Figures 3 and 4, sensors encapsulated in rigid PLA housings produced consistently cleaner and more stable signals than those using softer materials. PDMS and TPU encapsulations, while effective at protecting the sensing element, allowed greater mechanical decoupling from the surrounding concrete under dynamic loading, resulting in noisier outputs and reduced repeatability. The rigid PLA housing constrains the sensor within a well-defined geometry, promotes more consistent stress transfer from the concrete to the PZT element, and provides better electromagnetic shielding than flexible alternatives. All subsequent laboratory characterisation and field deployments used the PLA-encapsulated 12 mm PZT sensor on the basis of these results.

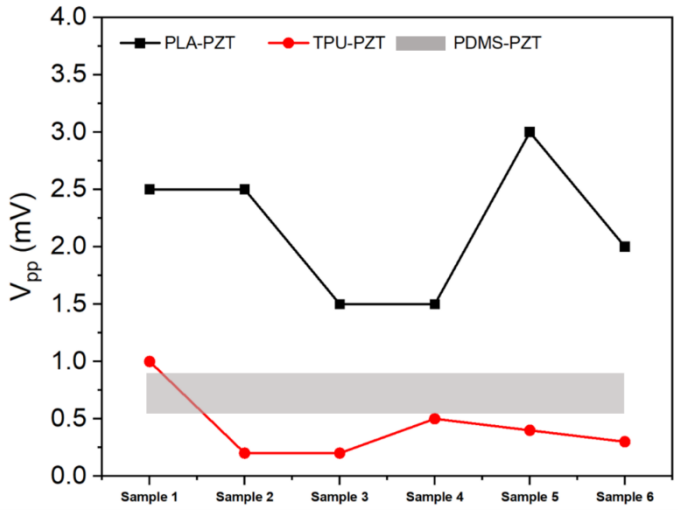


Figure 3. Voltage response of a piezoelectric strain sensor encapsulated using a soft material TPU and PDMS and rigid one, PLA.

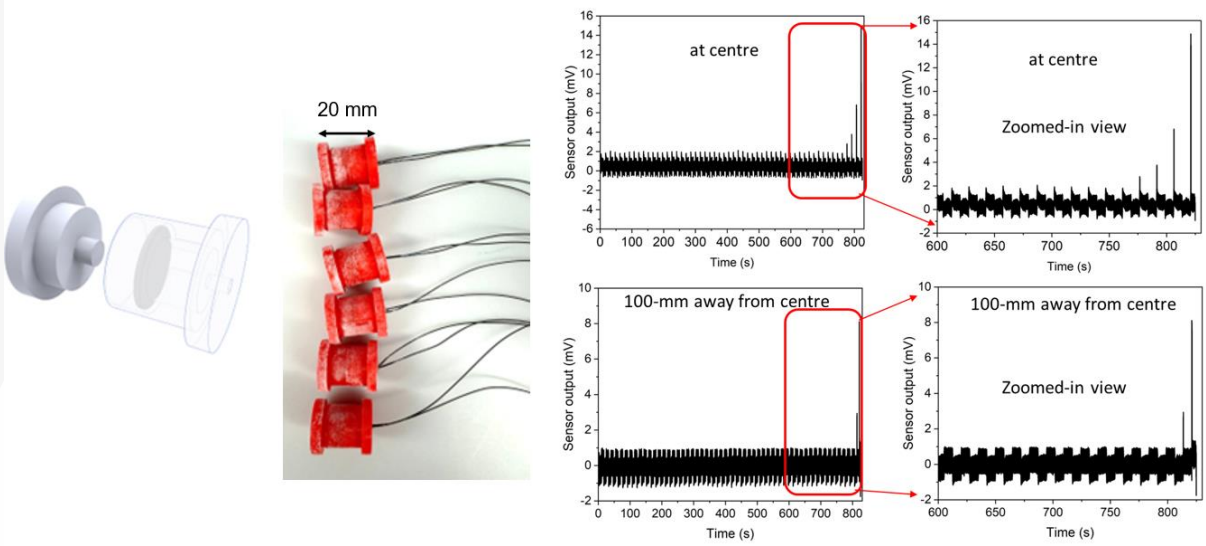


Figure 4. Voltage response of a piezoelectric strain sensor encapsulated in a rigid PLA housing, demonstrating clearer signal patterns and improved stability under repeated loading.

Sensor placement experiments confirmed that position within the beam cross-section and along the beam length significantly affects signal magnitude and timing. Sensors placed in the midsection and lower third of the beam, in zones of maximum tensile stress, produced the earliest and most reliable detection of damage. Output voltage decreased consistently as the sensor was moved toward the supports, consistent with the reduction in bending moment and tensile stress at those locations. These findings directly informed the sensor placement strategy used in the Cressy Road and motorway (M7 corridor) field deployments, where sensors were positioned to intercept the anticipated tensile stress field beneath the wheel path.

Taken together, these results establish the 12 mm PLA-encapsulated PZT sensor as a technically sound and practically viable embedded sensing element for concrete pavement health monitoring. The sensor detects microcracking before visible damage, produces clean signals without amplification or filtration, does not compromise host concrete strength, and generates outputs that are interpretable in terms of the internal stress state through the validated electromechanical model presented in Section 4.1.5.

### 4.1.2 Temperature Sensing Results (DEL-034, DEL-510)

Environmental sensing was incorporated to support interpretation of strain sensor data and to distinguish between mechanically driven responses and environmentally induced effects. A 3D-printed temperature sensor was developed using conductive TPU as the sensing element, encapsulated within a PLA housing designed for concrete embedment. The use of Fused deposition modeling (FDM) 3D printing allowed rapid prototyping of multiple geometric configurations without tooling cost, and the conductive TPU material provides a piezoresistive response to temperature change expressed as a relative resistance variation, characterised by its Temperature Resistance Coefficient (TRC, %/°C). A total of 12 sensors were fabricated across four design configurations, with three sensors produced per configuration to allow assessment of inter-specimen variability. The design variations investigated the influence of sensing element geometry and encapsulation on sensitivity, repeatability, and durability under concrete embedment conditions. The fabrication process, sensing element structure, and the four design configurations are illustrated in Figure 5.

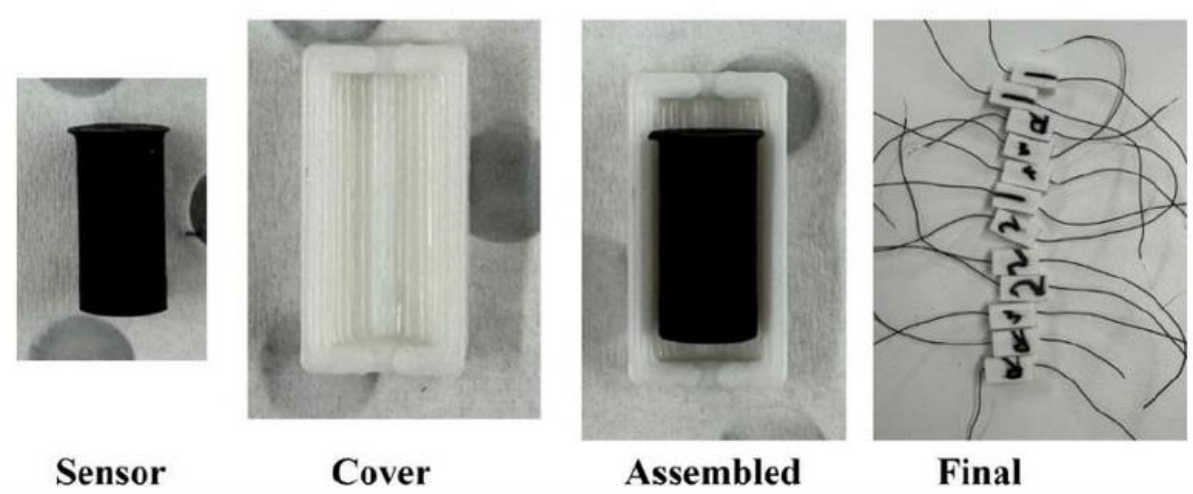


Figure 5. Fabrication and assembly of the 3D-printed temperature sensors, including the conductive TPU sensing element, PLA encapsulation, and the four sensor design configurations. A total of 12 sensors were fabricated, with three sensors produced for each design.

Table 3 presents a quantitative comparison of the TRC and operating temperature range of the developed sensor against flexible temperature sensors reported in the literature. The developed sensor achieved a TRC of 2.10 %/°C over the 10–50°C range and 7.20 %/°C over the 50–70°C range. Both values exceed those of all six comparator sensors in the literature, which range from 0.205 to 1.23 %/°C. The two-zone behaviour reflects a non-linear increase in sensitivity at elevated temperatures, which is a characteristic of conductive polymer composites where thermal expansion progressively modifies the conductive network within the TPU matrix. The 10–50°C range is directly relevant to Australian pavement service conditions, where internal concrete temperatures typically span this range under seasonal and diurnal variation. The higher sensitivity at 50–70°C provides additional resolving power during summer extremes and early hydration, when temperature gradients within the slab are largest and most consequential for cracking risk.

Table 3. Comparison of Temperature Resistance Coefficient (TRC) and operating temperature range of the developed FDM 3D-printed conductive TPU sensor with flexible temperature sensors reported in the literature.

| Materials and method | TRC (%°C⁻¹) | Range (°C) |
|---|---|---|
| Pt NFs networks/silk Fibroin (Doping) [6] | 0.205 | – |
| WNCNT, PDMS (Extrusion) [7] | 0.55 | 0–100 |
| PEDOT: PSS-SWCNTs/PU (Dip-coating) [8] | 0.93 | – |
| Carbon fibre (Carbonization) [9] | 0.81 | 0–80 |
| CNT- ionic liquid/silk/PET (Coating) [10] | 1.23 | – |
| SWCNT/PI/ PET (Electropolymerization) [11] | 1.0 | 15–45 |
| This work (FDM 3D printing) | 2.10<br>7.20 | 10–50<br>50–70 |

It should be noted that the comparator sensors in Table 3 are primarily drawn from the flexible electronics and wearable sensor literature, where the substrate materials (silk, PDMS, PU, PET) and fabrication methods differ substantially from an embedded concrete monitoring context. The comparison nonetheless demonstrates that the conductive TPU sensor achieves a competitive and in

fact superior TRC relative to established flexible sensing technologies, while offering the additional advantage of being directly 3D-printable into geometries suited for embedment in concrete.

Validation testing was conducted by embedding both the developed sensor and a commercial reference sensor within concrete specimens placed inside a controlled environmental chamber. Temperature was cycled systematically through heating and cooling sequences across the range relevant to pavement service conditions. As shown in Figure 6, the developed sensor closely tracked the temperature trends recorded by the commercial reference during both heating and cooling phases, responding consistently to incremental temperature changes and reproducing the same temporal patterns as the reference device. This agreement confirms that the conductive TPU sensing element produces a reliable and repeatable resistance response to internal concrete temperature change and is suitable for use in continuous pavement monitoring applications.

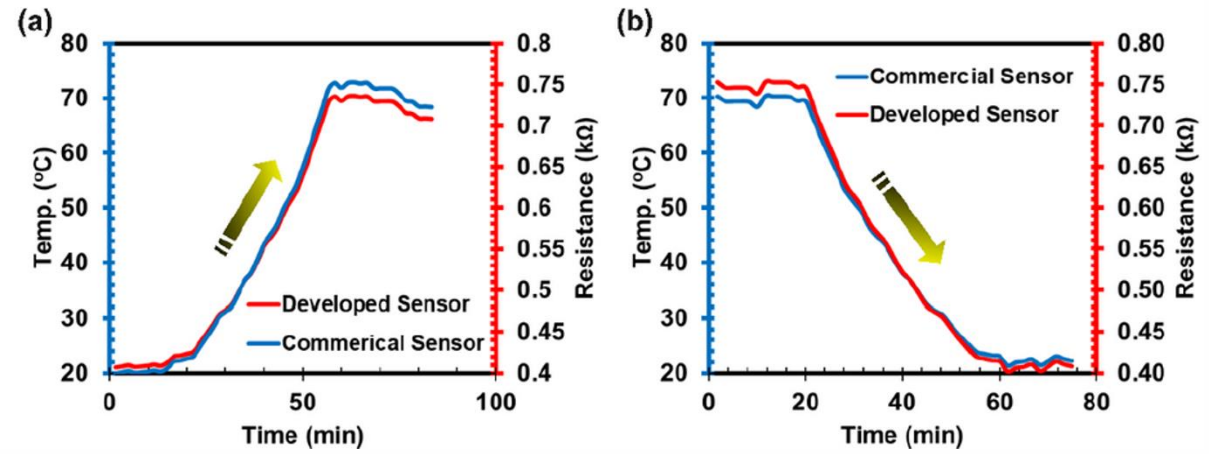


Figure 6. Comparison of the developed temperature sensor response, expressed as relative resistance change, with a commercial temperature sensor during controlled heating and cooling cycles in an environmental chamber.

4.1.3 Humidity Sensor (DEL-034, DEL-510)

Humidity monitoring and humidity compensation were addressed through a 3D-printed tesseract-structured piezoresistive sensor designed for direct embedment in cementitious materials. The sensor was fabricated from carbon-black-filled conductive thermoplastic polyurethane (TPU) using a single-step fused deposition modelling process. Its tesseract-inspired geometry was selected because the internal spacing between conductive domains changes under compression, creating additional conductive contacts and amplifying the resistance response without requiring expensive nanomaterials, complex electrodes, or post-processing. This design is consistent with the broader SmartCrete objective of developing low-cost embedded sensors that can be manufactured at scale and integrated into concrete infrastructure.

The fabrication and testing workflow is shown in Figure 7. The sensor has an overall size of approximately 10 x 10 x 10 mm, making it suitable for embedment within mortar or concrete without creating a large mechanical discontinuity. The conductive TPU filament was printed into a controlled three-dimensional geometry, electrodes were attached to the printed sensor body, and the sensor was embedded centrally within cementitious specimens for electromechanical characterisation. The small form factor, soft polymeric material, and single-step FDM fabrication route make the sensor

suitable for future integration with the SmartCrete wireless acquisition system and field-deployable sensor packages.

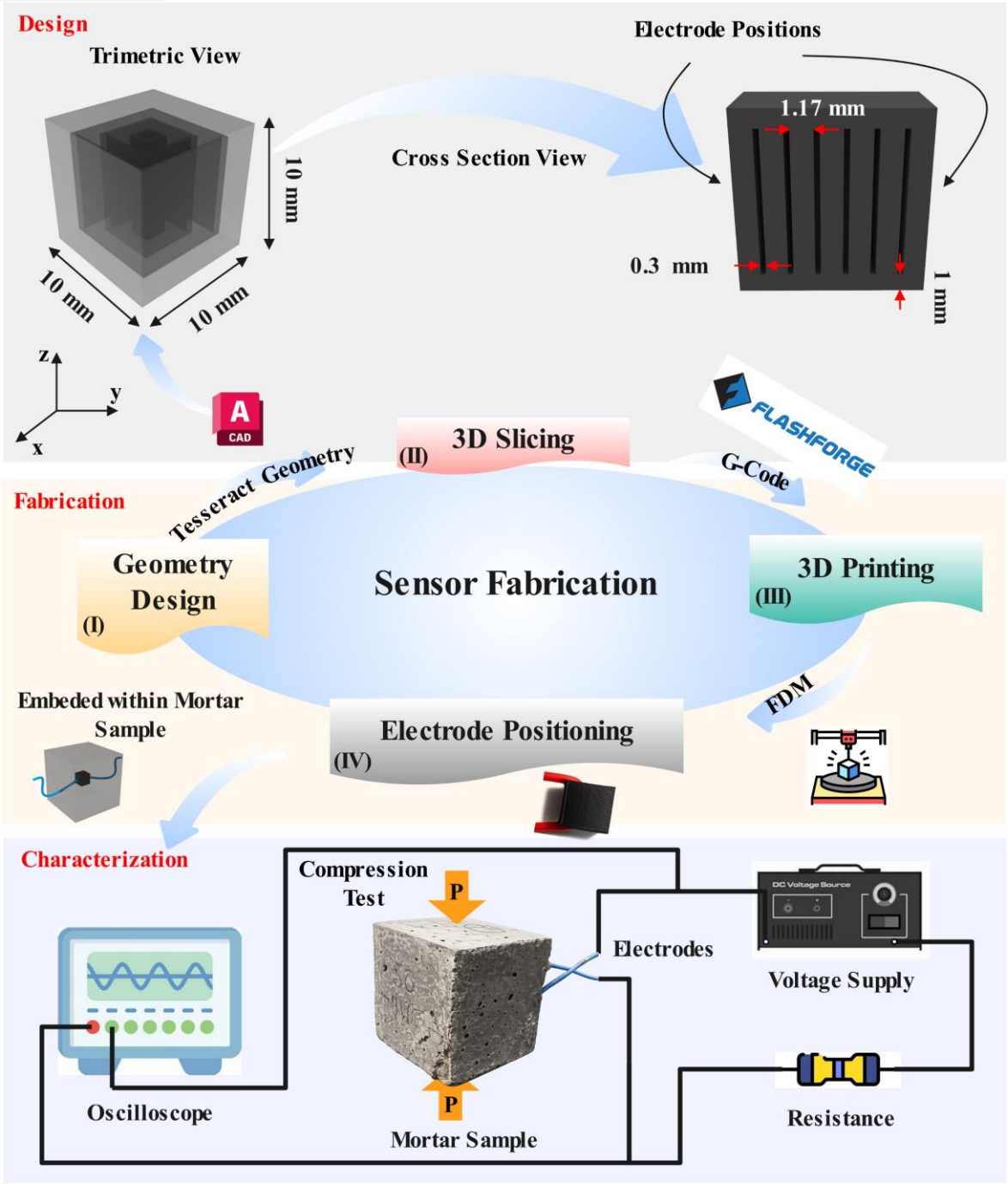


Figure 7. Design, fabrication, and characterisation workflow of the 3D-printed tesseract piezoresistive sensor for embedded monitoring of cementitious materials.

After embedment, the sensor was evaluated under compressive loading and compared with a commercial strain gauge under identical environmental conditions. The mechanical response of mortar specimens with and without the embedded sensor remained comparable, indicating that the compliant TPU sensor did not significantly compromise the load-bearing behaviour of the host matrix. The embedded sensor also followed the strain evolution measured by the commercial strain gauge

during loading, confirming that the resistance signal can be used as a reliable indicator of internal deformation in cementitious materials.

The key humidity-related result is summarised in Figure 8. For all tested relative humidity levels, the relative resistance change increased consistently with strain, confirming that the embedded sensor retained strain-dependent electromechanical functionality after exposure to different moisture conditions. However, the magnitude of the response was strongly influenced by humidity. The highest sensitivity was obtained under dry conditions, with a gauge factor of approximately 0.011 at 10% RH. Sensitivity decreased to approximately 0.007 at 65% RH and further to approximately 0.003 at 100% RH. This reduction indicates that absorbed moisture within the surrounding cementitious matrix and at the sensor-matrix interface partially suppresses the resistance modulation produced by compression. In practical terms, the result shows that humidity must be measured or compensated when interpreting piezoresistive sensor output in field pavement applications.

Temperature produced a similar environmental effect. At a constant relative humidity of 65%, the embedded sensor showed the greatest response at 10 °C, a moderate response at 25 °C, and the lowest response at 45 °C, with the corresponding gauge factor decreasing from approximately 0.011 to 0.007 and then to 0.003. This behaviour is attributed to temperature-dependent changes in the conductive TPU network and thermal softening of the polymer, which reduce resistance modulation under the same mechanical strain. These findings are particularly relevant for concrete pavements, where internal humidity and temperature vary over daily and seasonal cycles and can otherwise be misinterpreted as mechanical damage or traffic-induced strain.

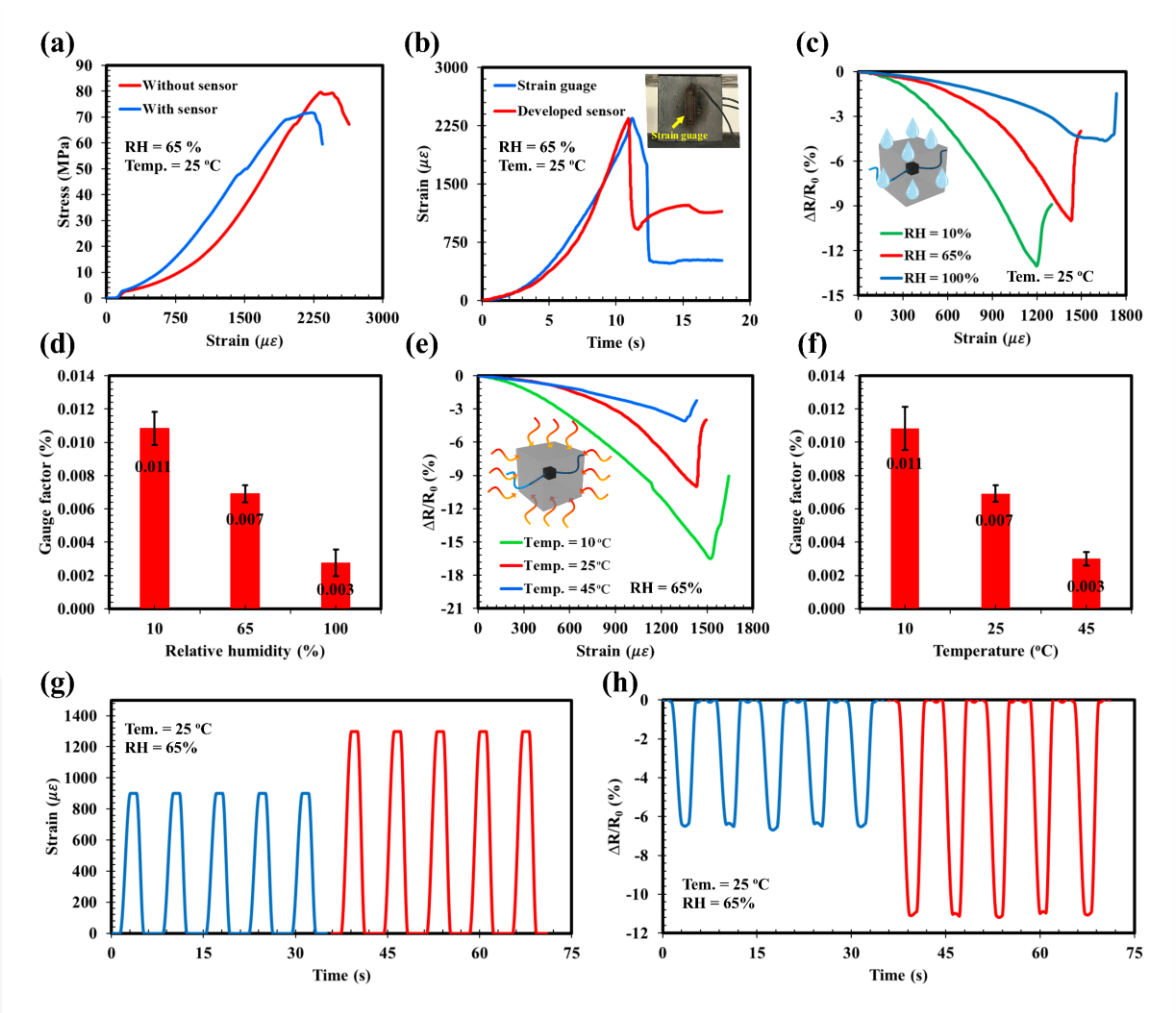






OFFICIAL

Figure 8. Mechanical and electromechanical performance of the embedded tesseract piezoresistive sensor, including comparison with mortar without the sensor, strain tracking against a commercial strain gauge, humidity and temperature sensitivity, and cyclic response under repeated loading.

Cyclic tests further demonstrated stable and repeatable sensor behaviour under repeated strain loading. The resistance response followed the imposed cyclic strain profile, with lower-amplitude cycles producing smaller resistance changes and higher-amplitude cycles producing proportionally larger responses. No pronounced drift or irregular fluctuation was observed during repeated loading, demonstrating that the tesseract geometry provides reversible conductive-pathway modulation after embedment.

Overall, the humidity-sensing work establishes that the 3D-printed conductive TPU sensor can provide two important functions for the SmartCrete platform. First, it offers a low-cost embedded piezoresistive element for monitoring internal strain and deformation in cementitious materials. Second, its quantified response under different humidity and temperature conditions provides the calibration basis needed to separate environmental effects from mechanical loading effects in future pavement deployments. This is important for long-term monitoring because changes in sensor output must be interpreted together with moisture and temperature state to avoid false identification of structural damage.

### 4.1.4 pH Sensor (DEL-034, DEL-510)

pH sensing was reviewed as part of the environmental monitoring scope for DEL-034 and DEL-510. The literature shows that embedded pH sensors are valuable in reinforced concrete when the main durability question is carbonation, chloride ingress, loss of pore-solution alkalinity, and the onset of steel reinforcement corrosion. Iridium-oxide and related electrochemical sensors can measure internal pH changes in mortar or concrete in real time, and recent studies have demonstrated their use for acid attack, carbonation, and rebar-interface monitoring [12-14].

For this project, however, the primary failure mechanism was not reinforcement depassivation or corrosion. The project target was crack initiation and strain redistribution in plain concrete pavement and in concrete pavement slabs under traffic loading. In this context, pH is not a primary crack-generation parameter. Crack initiation is governed mainly by tensile strain, traffic-induced stress, thermal movement, shrinkage, moisture gradients, support condition, and load position rather than by pore-solution pH. This scope decision is summarised in Figure 9.

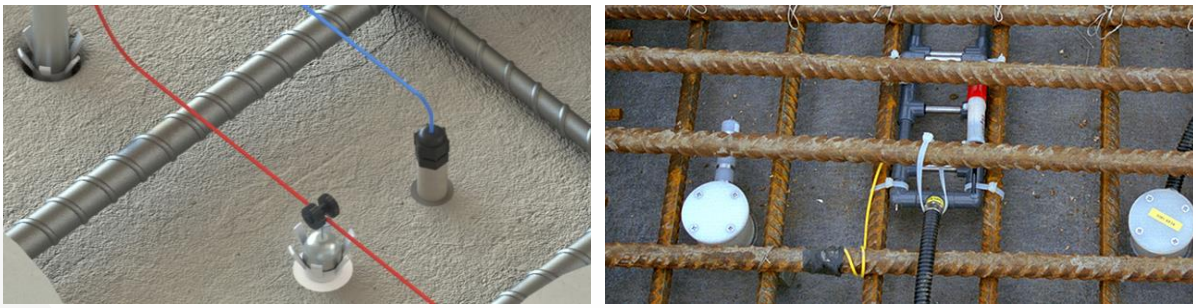

Figure 9. Example applications of embedded pH sensing in reinforced concrete, showing pH electrodes installed within the concrete cover and reinforcement cage for monitoring alkalinity loss, carbonation, chloride ingress, and steel depassivation/corrosion risk.

The review therefore led to a deliberate project choice: no dedicated pH sensor was developed during this phase. Research effort was instead concentrated on the PZT strain sensor, temperature and humidity context measurements, wireless telemetry, field deployment, and live data interpretation, because these outputs directly capture the load-induced strain and crack activity required for the

pavement-monitoring objective. This prioritisation also reduced system complexity and avoided adding a sensor stream that would have limited diagnostic value for the main plain-pavement crack-generation problem.

pH sensing remains a relevant future option if the SmartCrete platform is extended toward reinforced concrete durability monitoring, continuously reinforced concrete pavement corrosion risk, chemically aggressive exposure, sewer or industrial environments, or structures where carbonation and chloride ingress are the dominant deterioration mechanisms. In such cases, a pH sensor would be most useful as part of a multi-parameter corrosion-monitoring package, combined with chloride, humidity, temperature, and electrochemical corrosion measurements rather than as a standalone crack-detection sensor.

4.1.5 Finite Element Analysis (FEA) of Concrete Pavements (DEL-725)

Finite element analysis was carried out to support interpretation of the experimental results and to provide a mechanics-based framework for sensor placement within concrete pavements. The modelling work was closely integrated with the laboratory and field testing program and focused on understanding stress and strain distributions under representative loading conditions.

Initially, finite element models were developed to replicate the concrete beam and slab configurations used in laboratory testing. Figure 10 shows the model geometry, material properties, boundary conditions, and applied loading used to simulate the experimental setup. These models were used to identify regions of maximum tensile stress and strain, which are critical locations for crack initiation and therefore optimal positions for embedded strain sensors.

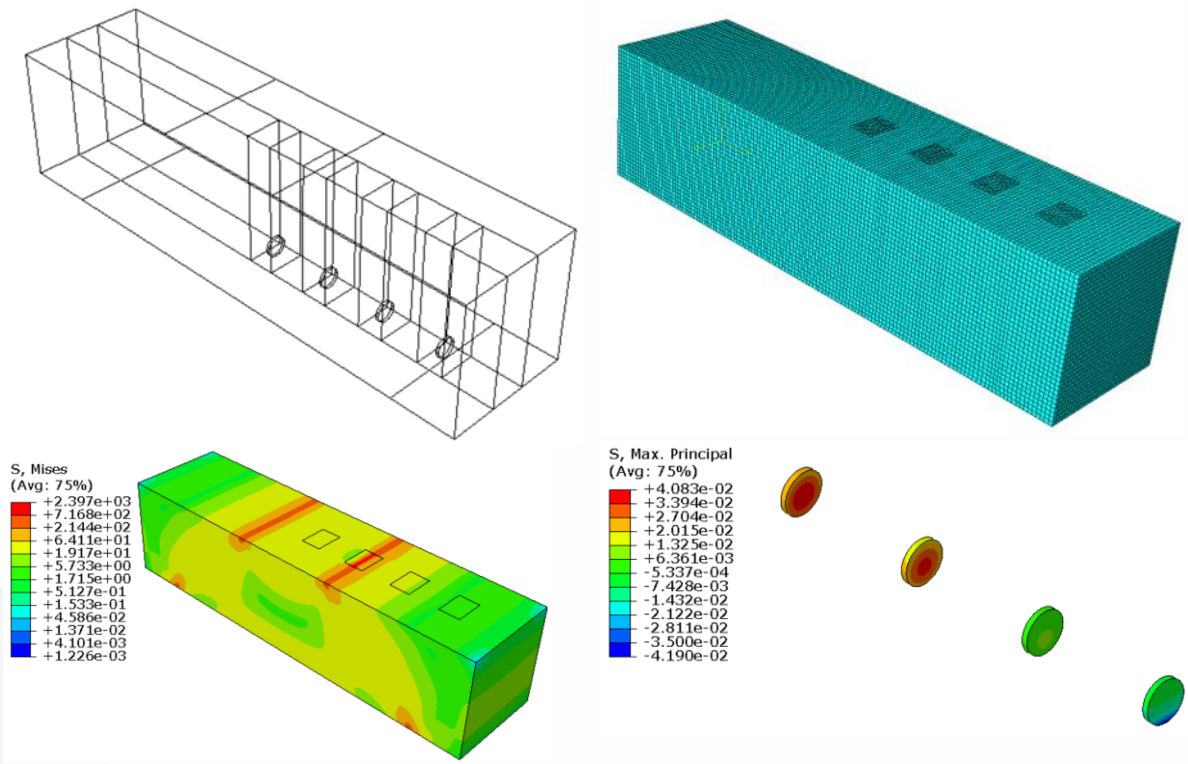


Figure 10. Finite element model geometry and boundary conditions used to simulate the concrete beam and applied loading.

The model predictions were then compared directly with experimental sensor outputs. As shown in Figure 11, a clear correspondence was observed between the simulated principal stress on the sensor

surface and the measured peak-to-peak voltage response from the embedded piezoelectric sensors. This agreement confirms that the sensor signals reflect the underlying mechanical behaviour of the concrete rather than noise or installation artefacts. The comparison also provides confidence in the use of sensor voltage response as a proxy for changes in internal stress and strain.

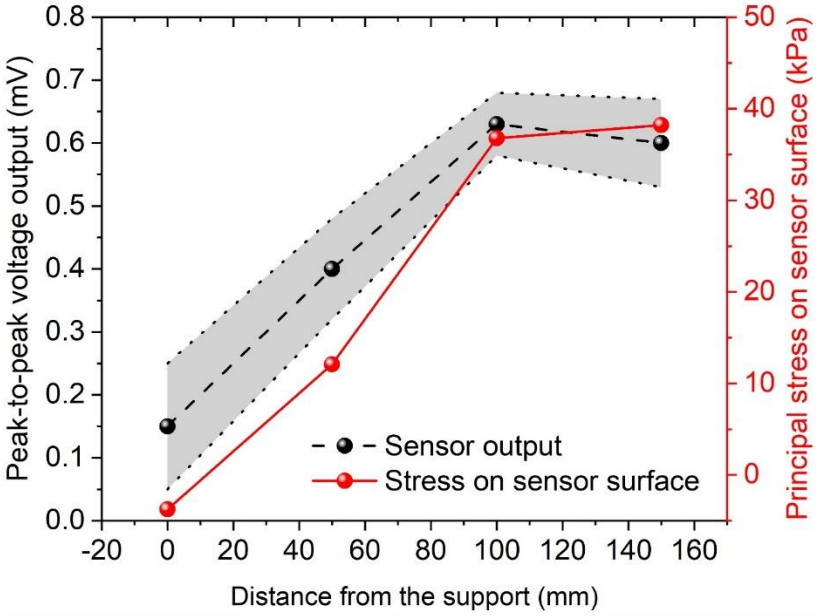


Figure 11. Comparison of trends between experimental sensor output (peak-to-peak voltage) and simulated principal stress on the sensor surface

**Quantitative Correlation Between Sensor Output and Principal Stress**

To further validate the agreement observed in Figure 11, a quantitative statistical analysis was performed to establish the relationship between the measured peak-to-peak voltage output (mV) and the simulated principal stress on the sensor surface (kPa). Data points were extracted at four sensor locations corresponding to distances of 0, 50, 100, and 150 mm from the support, yielding voltage values of 0.15, 0.40, 0.62, and 0.60 mV and corresponding stress values of −6, 12, 36, and 38 kPa, respectively. The negative stress value at the support location reflects local compression in that region, consistent with the expected stress distribution in a loaded beam.

Linear regression analysis produced the following predictive model:

$$\text{Stress (kPa)} = 94.80 \times \text{Voltage (mV)} - 21.95$$

This relationship indicates that for every 1 mV increase in sensor output, the principal stress on the sensor surface increases by approximately 94.8 kPa, confirming strong sensitivity of the piezoelectric sensor to changes in the local stress state across the full compressive-to-tensile stress range observed in the specimen.

The Pearson correlation coefficient was $r = 0.989$, indicating a very strong positive linear relationship between the two variables. The coefficient of determination $R^2 = 0.978$ demonstrates that approximately 97.8% of the variance in simulated principal stress is explained by the measured sensor voltage output, confirming the high predictive capability of the sensor signal.

The root mean square error (RMSE) was calculated as 2.69 kPa. Given the total stress range of 44 kPa observed across measurement positions (from −6 to +38 kPa), this represents approximately 6.1% of the full range, indicating good absolute accuracy. The mean absolute percentage error (MAPE), evaluated across the three positive-stress data points, was 14.5%. MAPE was not computed for the

support location where the actual stress value is negative, as the metric is mathematically unreliable under such conditions.

Statistical significance testing was conducted using a t-test on the Pearson correlation coefficient. The calculated t-statistic was 9.46 with 2 degrees of freedom (n − 2), which exceeds the critical value of 4.303 at the 95% confidence level (α = 0.05, two-tailed), confirming that the correlation is statistically significant and unlikely to be attributable to chance. The 95% confidence interval for the regression slope was [51.7, 137.9] kPa/mV, which excludes zero and further supports the statistical validity of the linear model.

Collectively, these results provide quantitative evidence that the embedded piezoelectric sensor voltage output is a reliable and statistically significant proxy for the principal stress state at the sensor surface, across both compressive and tensile stress regimes. This strengthens confidence in using sensor signals for real-time structural interpretation and supports the broader application of the developed sensing system for condition monitoring in concrete pavements.

To extend the analysis beyond static loading conditions, the modelling was further developed to simulate moving loads across the concrete slab. Figure 12 illustrates the evolution of the strain field as a load travels across the pavement surface. These simulations demonstrate how the magnitude and distribution of strain change with load position and explain the variations observed in signals recorded by multiple embedded sensors during field testing, as shown in Video 1- FEA simulation.

The moving load analysis also supports future development of load localisation and classification approaches based on relative sensor responses. By linking multi-sensor signal patterns to predicted strain distributions, the modelling establishes a foundation for automated interpretation of loading conditions and early damage detection in later project stages.

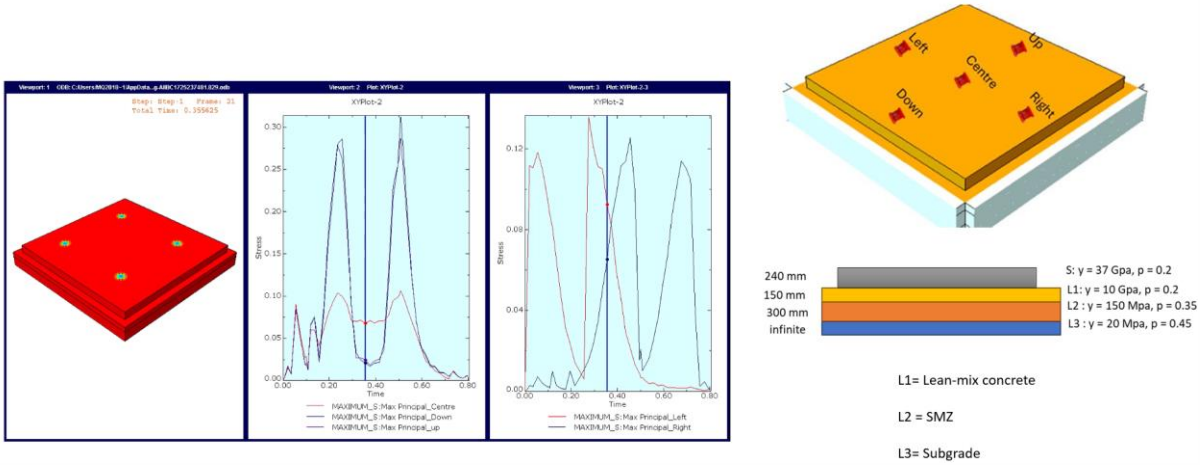


Figure 12. Finite element simulation of a moving load across the concrete slab, showing evolution of strain distribution relevant to multi-sensor response patterns.

Overall, the finite element analysis strengthened the project by linking experimental observations with fundamental structural mechanics. It provided a clear technical basis for sensor placement, supported interpretation of measured strain responses, and established a modelling framework that can be expanded in future work to include crack propagation modelling and large-scale pavement deployment planning.

### 4.1.6 Probabilistic Integration of Sensor Data with Pavement Performance Modelling (DEL-036)

The validated linear relationship between sensor voltage output and simulated principal stress (Stress = 94.80 x Voltage - 21.95 kPa; $R^2$ = 0.978, r = 0.989) established in Section 4.1.5 means that the

SmartCrete sensor output can be interpreted not merely as a raw electrical signal but as a calibrated proxy for the internal stress state of the pavement at each sensor location. This capability is significant because it elevates the SmartCrete system from a detection tool to a quantitative structural monitoring instrument whose outputs are directly compatible with probabilistic pavement condition frameworks. To exploit this compatibility, a Bayesian Network (BN) framework was developed in parallel with the sensor work to provide exactly that type of model.

A Bayesian Network was adopted in preference to a deterministic mapping because pavement condition assessment is inherently probabilistic: sensor evidence is not continuously available at every location, and the relationship between internal stress state and long-term serviceability outcomes is mediated by multiple, only partially observed distress mechanisms. The BN framework accommodates this directly, propagating whatever evidence is available to update condition estimates and remaining operational even when individual sensors are offline or noisy, while expressing the driver-distress-outcome relationships through conditional probability tables that can be interrogated through sensitivity and mutual information analysis rather than functioning as an opaque model.

The BN's outcome node, IRI, was selected because it is not a distress measure specific to a single pavement type. It is a profile-derived roughness index recorded consistently across the LTPP program's rigid pavement sections, including the jointed plain concrete (JPCC) sections used to build this model, as well as its flexible pavement sections. IRI was retained as the outcome node because it is the one serviceability measure available consistently across the analysed dataset, and because it is the metric road agencies, including Transport for NSW, already use for network-level condition reporting, meaning the BN output is directly compatible with existing pavement management workflows.

**Data source and dataset**

The BN was developed using data from the Long-Term Pavement Performance (LTPP) database, available through the FHWA InfoPave platform [15]. The LTPP program monitors pavement performance across the United States under varied materials, traffic loads, and climatic conditions, providing one of the most comprehensive longitudinal pavement datasets available for probabilistic modelling. The dataset was filtered to retain California pavement sections only, reducing regional variability and producing a more consistent pavement population for probabilistic analysis. The final BN dataset contained 463 section-year observations from 63 unique pavement sections covering the period 1991 to 2020. Each observation represented one pavement section in one survey year, with traffic, structural, environmental, distress, and roughness data aligned within a single modelling unit.

**BN structure and variable hierarchy**

The BN was structured as a three-layer driver-distress-performance hierarchy, as illustrated in Figure 13. The explanatory layer included AnnualKESAL (annual equivalent single axle load), Age in Years, Modulus, MeanTemp, RH, and FreezeIndex. These variables represent the main deterioration drivers: traffic loading, pavement age, structural stiffness, and environmental exposure. The intermediate layer included four distress indicators: Cracking_total (the sum of transverse and longitudinal cracking length), Rutting (maximum mean rut depth from transverse profile measurements), Deflection (peak deflection from Falling Weight Deflectometer loading), and EdgeFault (differential vertical movement at joints or slab edges). The presence of a Rutting node in the distress layer reflects the composite structure of the LTPP sections used in this model. Rut depth values are recorded against the JPCC sections used in this analysis, consistent with these sections carrying an asphalt concrete (AC) surface layer over the underlying concrete slab rather than an exposed rigid surface, and Rutting is an expected distress mode on that surface layer. The same composite structure explains the Deflection node: with an AC layer present over the JPCC slab, pavement response under Falling Weight

Deflectometer loading is not governed purely by rigid-slab behaviour, so the general deflection measure used in the model reflects the structural makeup of these sections. EdgeFault continues to represent the joint-faulting behaviour of the underlying concrete slab directly. The final outcome node was IRI (International Roughness Index), represented as the mean IRI from both wheel paths to give a representative section-level roughness value. This layered structure preserves a clear distinction between external deterioration conditions, observable damage mechanisms, and the final functional serviceability response, which is consistent with the engineering understanding that ride quality is the cumulative outcome of multiple interacting deterioration processes rather than a detached index.

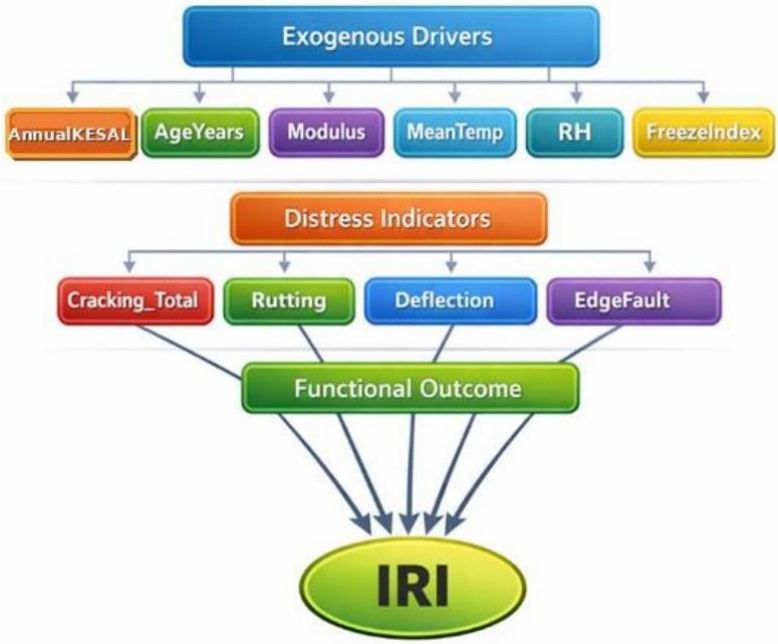


Figure 13. Bayesian Network variable hierarchy showing the three-layer structure: Exogenous Drivers (AnnualKESAL, AgeYears, Modulus, MeanTemp, RH, FreezeIndex), intermediate Distress Indicators (Cracking_total, Rutting, Deflection, EdgeFault), and the final Functional Outcome (IRI).

All continuous variables were discretised into ordered condition states (Low, Medium, High) before model construction. This discretisation step was necessary because the BN uses conditional probability tables (CPTs) to represent dependencies, and it also allowed each variable to be interpreted as an engineering condition regime rather than a raw measurement. Each distress node was intentionally restricted to two direct parents. This restriction reduced CPT dimensionality, improved parameter stability, and preserved interpretability while still capturing the dominant mechanistic controls for each distress type. The parent assignments were informed by both the learned BN structure and the pavement engineering literature: Cracking_total was assigned AnnualKESAL and MeanTemp, reflecting load-driven fatigue and temperature-related stress redistribution; Rutting was assigned AnnualKESAL and RH, reflecting load-driven permanent deformation under moisture-sensitive conditions; Deflection was assigned Modulus and MeanTemp, reflecting stiffness-dependent structural response and temperature-driven slab curling; and EdgeFault was assigned AgeYears and Modulus, reflecting the long-term development of support-related faulting. The learned BN structure is shown in Figure 14.

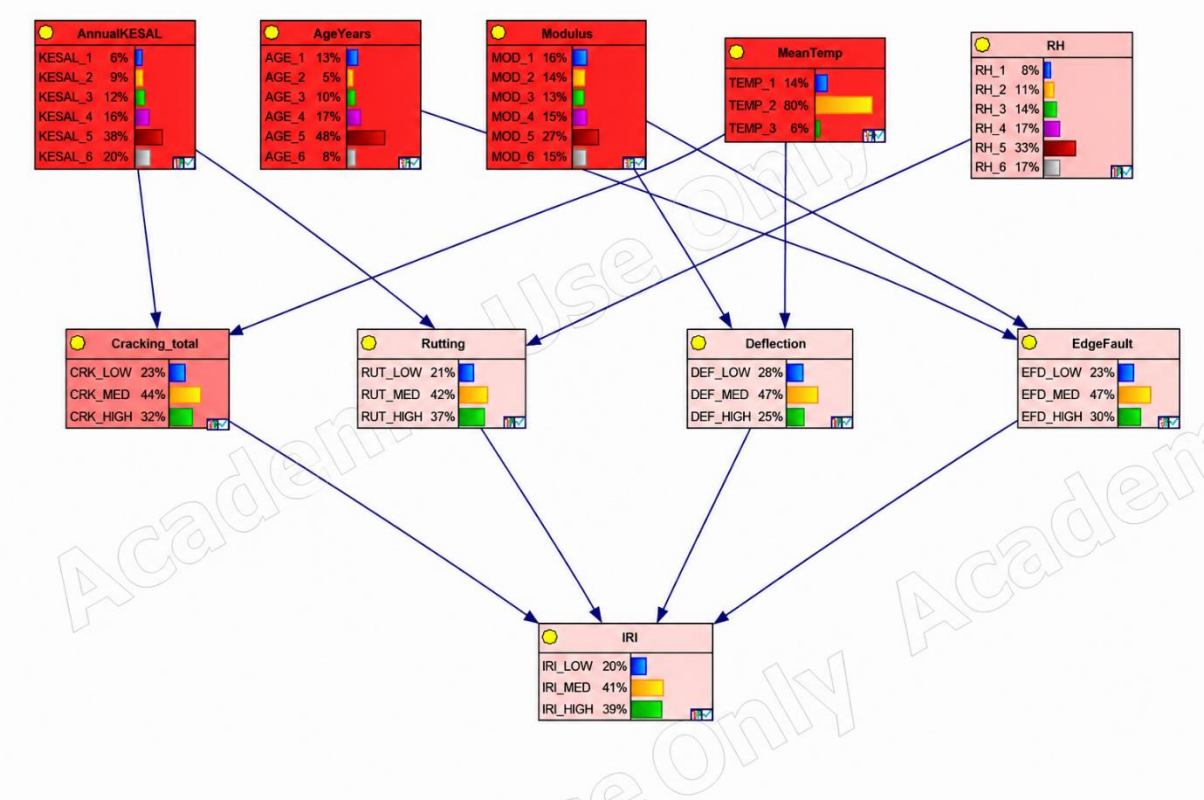


Figure 14. Learned static Bayesian Network structure showing the two-parent configuration of each distress node and the direct conditional influence pathways from explanatory drivers through distress indicators to IRI.

**Model outputs and marginal distributions**

The marginal probability distributions from the BN summary, shown in Figure 15, revealed that the analysed pavement population was dominated by moderate deterioration conditions. The distress layer was likewise dominated by intermediate states: Cracking_total peaked in the medium state (44.5%), followed by the high state (32.2%); Rutting showed medium at 41.7% and high at 37.3%; Deflection was most concentrated in the medium class (47.4%); and EdgeFault was dominated by its medium state (46.7%). The IRI node followed the same pattern, with the most probable state being IRI_MED at 40.9%, followed by IRI_HIGH at 39.0% and IRI_LOW at 20.1%. This distribution means the analysed network was not centred on a clearly good ride quality condition. Instead it was concentrated in a transitional to deteriorated serviceability regime, with a large fraction already shifted toward poor roughness, confirming that medium IRI in this dataset should be interpreted as an active transition state rather than a satisfactory condition.

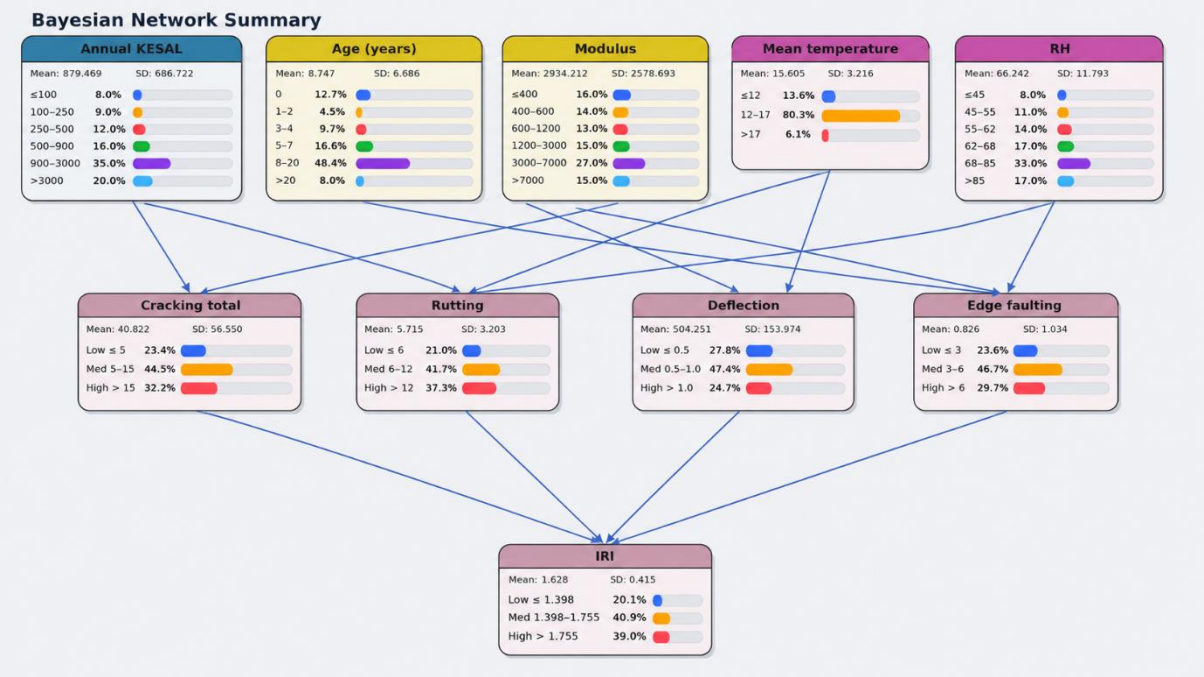


Figure 15. Bayesian Network summary showing marginal probability distributions for all model nodes. The IRI node is distributed as 20.1% Low, 40.9% Medium, and 39.0% High, confirming that the analysed pavement population is concentrated in transitional to deteriorated serviceability conditions.

**Sensitivity analysis**

Sensitivity analysis using tornado diagrams revealed different patterns across the three IRI states. The medium IRI state was controlled primarily by combined distress configurations, particularly mixed states of Cracking_total, Rutting, Deflection, and EdgeFault acting together, rather than by any single distress mechanism in isolation. This means that transitional ride quality is a multi-mechanism phenomenon in which several distress processes have already progressed enough to affect functional performance, but none has shifted fully into its highest severity class. In contrast, the high and low IRI states were both dominated by upstream explanatory parameters, particularly AnnualKESAL, AgeYears, and Modulus. This means that poor ride quality is not only a result of the visible distress condition at one point in time; it is also connected to the broader deterioration environment, including annual traffic loading intensity, pavement age, and structural stiffness.

**Mutual Information analysis**

Information-theoretic relationship diagnostics were applied to the final BN by computing Mutual Information (MI) values for the main variable pairs, as shown in Figure 16 and Table 4. While the BN graph shows which connections exist, MI quantifies the strength of each relationship numerically. The full MI results are summarised in Table 4.

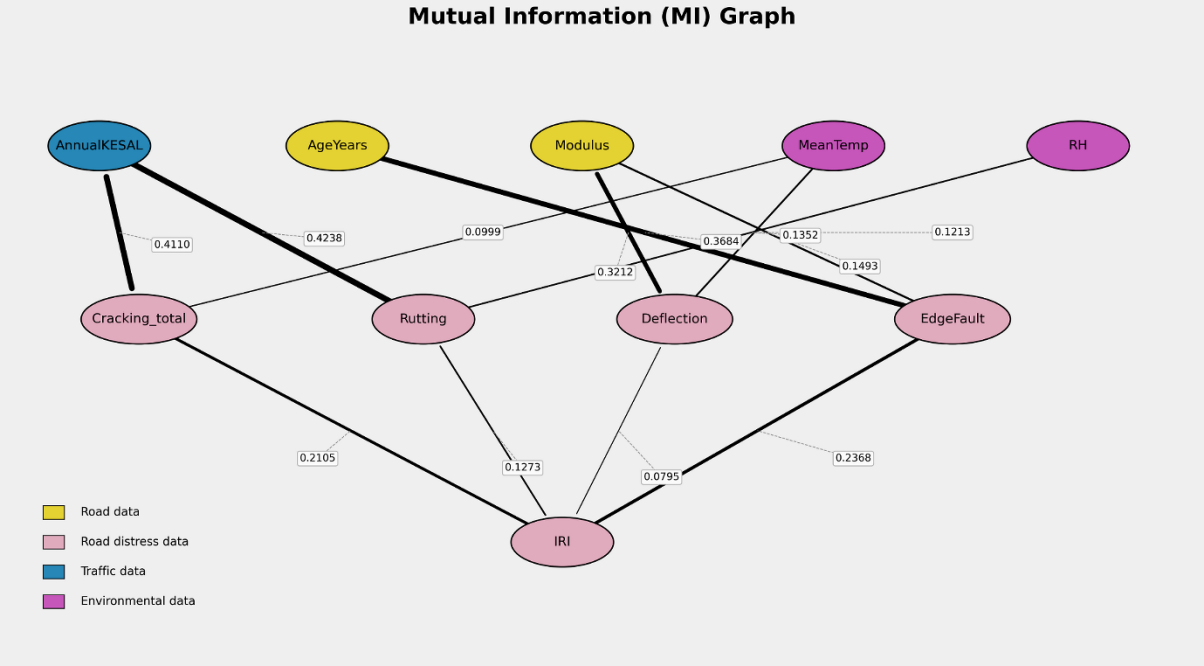


Figure 16. Mutual Information (MI) graph for the final Bayesian Network, showing the strength of dependencies between parent variables and distress nodes, and between distress nodes and IRI. EdgeFault and Cracking_total carry the strongest direct information about ride quality.

Table 4. Mutual Information values for the main relationships in the final Bayesian Network, ranked by strength.

| Rank | Source node | Target node | Relationship type | MI value |
|---|---|---|---|---|
| 1 | AnnualKESAL | Rutting | Parent to Distress | 0.4238 |
| 2 | AnnualKESAL | Cracking_total | Parent to Distress | 0.4110 |
| 3 | AgeYears | EdgeFault | Parent to Distress | 0.3684 |
| 4 | Modulus | Deflection | Parent to Distress | 0.3212 |
| 5 | EdgeFault | IRI | Distress to IRI | 0.2368 |
| 6 | Cracking_total | IRI | Distress to IRI | 0.2105 |
| 7 | Modulus | EdgeFault | Parent to Distress | 0.1493 |
| 8 | RH | Rutting | Parent to Distress | 0.1352 |
| 9 | Rutting | IRI | Distress to IRI | 0.1273 |
| 10 | MeanTemp | Deflection | Parent to Distress | 0.1213 |
| 11 | MeanTemp | Cracking_total | Parent to Distress | 0.0999 |
| 12 | Deflection | IRI | Distress to IRI | 0.0795 |

The strongest parent-to-distress relationships were AnnualKESAL to Rutting (MI = 0.4238) and AnnualKESAL to Cracking_total (MI = 0.4110), confirming that annual traffic loading carried the strongest information contribution to both load-driven distress mechanisms. AgeYears to EdgeFault (MI = 0.3684) and Modulus to Deflection (MI = 0.3212) confirmed that pavement age and structural stiffness are the dominant controls for faulting and structural response respectively. For the final outcome node, EdgeFault carried the highest direct information about IRI (MI = 0.2368), followed by

Cracking_total (MI = 0.2105), Rutting (MI = 0.1273), and Deflection (MI = 0.0795), showing that surface unevenness and cracking are the distress mechanisms most directly informative about ride quality in this dataset, while deflection, though structurally significant, carries the weakest direct information link to IRI among the four distress nodes.

**Integration with SmartCrete sensor outputs**

The BN framework connects directly to the SmartCrete sensing system at three nodes. For the Deflection node, the sensor calibration result ($R^2$ = 0.978) confirms that the voltage signal reliably encodes the principal stress at the sensor surface. Stress values derived from the sensor can therefore be used to classify the Deflection node into its Low, Medium, or High state, providing real-time continuously updated structural evidence without relying on periodic Falling Weight Deflectometer campaigns. For the Cracking_total node, the laboratory finding that sensors detected microcrack initiation 7 to 8 cycles before visible failure provides a real-time observable that can update this node continuously, directly improving the quality of IRI condition estimates given the node's high MI value of 0.2105. For the MeanTemp node, the 3D-printed temperature sensors embedded alongside the strain sensors, validated against commercial reference devices as described in Section 4.1.2, provide continuous real-time internal concrete temperature measurements that replace static or climatological estimates.

The traffic loading variable AnnualKESAL, identified as the parameter with the strongest information contribution to both cracking (MI = 0.411) and rutting (MI = 0.4238), can also be progressively enriched by the SmartCrete system. The field validation results demonstrated that embedded sensors consistently produced two distinct signal peaks per vehicle pass corresponding to front and rear axle loads, and the KNN-based live classification dashboard described in Section 4.1.8 already distinguishes pedestrian, light vehicle, and heavy vehicle loading events in real time. As the labelled training dataset is expanded to include heavier vehicle categories, this could support derivation of effective annual KESAL estimates for individual pavement sections without reliance on remote weigh-in-motion stations.

Taken together, these connections define a coherent data pathway from embedded sensor output to probabilistic pavement condition assessment. At the base level, the SmartCrete piezoelectric strain sensors and temperature sensors provide continuous in-situ measurements of internal stress state, microcrack activity, and thermal exposure. These measurements are translated into calibrated physical quantities using the validated regression and temperature response relationships established in this project. The resulting variables, specifically the stress-derived deflection state, cracking activity indicator, and internal temperature, are entered as observed evidence nodes into the Bayesian Network, updating the posterior probability distributions of the distress nodes and indirectly influencing the IRI outcome node through the network's conditional probability structure.

This integration is practically significant for three reasons. First, it converts continuous sensor streams into actionable pavement condition probabilities without requiring expert manual interpretation of individual sensor traces. Second, the BN's capacity for inference under incomplete evidence means the framework remains operational even when some sensors are temporarily offline or produce noisy data, as occurred during the motorway (M7 corridor) deployment: the BN simply updates its posteriors using whatever evidence is available. Third, by providing continuous updates to both the Deflection and Cracking_total nodes, the SmartCrete system directly addresses the distress-layer evidence that governs transitional ride quality, the regime that represents the largest proportion of the analysed pavement population (40.9% medium IRI) and the most critical window for preventive intervention.

Looking ahead, the MI ranking provides a principled guide for future sensor development priorities. EdgeFault carried the highest direct information about IRI (MI = 0.2368) yet is not currently detectable by the SmartCrete system in its present form. Future sensor configurations designed to detect

differential vertical movement at slab edges would directly address this gap and, given the MI ranking, would deliver the largest incremental improvement in the BN's IRI condition estimation capability. The BN framework therefore acts not only as a consumer of sensor data but also as a design guide for the evolution of the SmartCrete sensing platform toward full network-scale pavement condition monitoring.

The BN presented here was developed at the pavement-section level, using 463 section-year observations across 63 California JPCC sections, and is intended to demonstrate the sensor-to-BN integration pathway rather than to deliver network-level, sub-section condition prediction. Extending this framework to predict IRI at finer spatial resolution, for example at 100 m intervals using machine learning techniques, would require condition data resolved at that spatial scale, which is beyond what the current LTPP extract provides. This is identified as a direction for future work, either by discretising LTPP's continuous profile records where available, or by training against a network-scale dataset generated by the SmartCrete sensor deployment itself as field coverage expands.

### 4.1.7 Wireless Monitoring and Data Infrastructure (DEL-722, DEL-724)

Developing a reliable data acquisition and wireless communication system was one of the central engineering challenges of the SmartCrete project. Concrete attenuates wireless signals and provides a chemically and mechanically harsh environment for electronics. Wired alternatives introduce installation complexity and long-term maintenance risks that are incompatible with road infrastructure. The system described in this section was developed iteratively, with each component evaluated against the requirements of continuous real-time monitoring, field deployability without mains power or fixed network connections, and low cost and maintenance burden suitable for extended unattended operation.

**Data acquisition hardware**

The acquisition system is built around a high-resolution analogue-to-digital converter connected to a microcontroller. The system was developed in two configurations corresponding to the two field deployments in this project. For the Ryde slab deployment, two independent microcontroller systems (System A and System B) were deployed in parallel, each managing a subset of the eight embedded strain sensors, with data from both systems received simultaneously by the dashboard through the HiveMQ MQTT broker. For the M7 motorway deployment, the system was scaled to support a larger sensor network comprising 16 piezoelectric strain sensors, two temperature sensors, and two humidity sensors, for a total of 20 monitored channels. A dedicated web-based monitoring dashboard (https://smoshizi.github.io/sensor-dashboard/) was developed specifically for the motorway configuration, providing real-time visualisation of all 20 sensor channels in a layout that reflects the physical sensor placement across the pavement section. Signals from the piezoelectric strain sensors are digitised at 100 Hz (10 ms sample interval) across both configurations, a rate sufficient to resolve individual axle load events and to capture the front-to-rear axle timing sequence of passing vehicles. The analogue input stage accepts the direct voltage output of the PZT sensors without requiring an external charge amplifier, consistent with the low-cost design philosophy of the overall system.

**Wireless communication architecture**

Data are transmitted wirelessly using an MQTT (Message Queuing Telemetry Transport) publish-subscribe protocol, which is well suited to sensor network applications because of its low overhead, tolerance for intermittent connectivity, and native support for multi-subscriber architectures. Each microcontroller publishes sensor data to the HiveMQ cloud broker, which acts as the central message routing hub. Subscribing clients, including the real-time dashboard and the cloud storage pipeline, receive data independently from the broker without requiring a direct connection to the embedded

hardware. This decoupled architecture means that additional analytical clients can be added to the data stream without modifying the field hardware or firmware.

In laboratory and small-scale field settings, data transmission was achieved over local Wi-Fi. For the M7 motorway corridor deployment, where local network access was not available, a solar-powered Wi-Fi system with an integrated 4G communication module and an IoT SIM card was used to provide cellular data access. This configuration allows the sensing system to operate entirely independently of local infrastructure, making it suitable for deployment on remote or actively trafficked road sections where network access cannot be guaranteed.

**Power supply system**

A standalone solar-powered energy system was designed and deployed to support continuous 24/7 field operation without mains power, as shown in Figure 17. The system comprises a 40 W solar panel, an MPPT (Maximum Power Point Tracking) charge controller that optimises solar energy harvesting under varying sunlight conditions, a 12 V deep-cycle battery selected for its tolerance of repeated charge-discharge cycling, and a DC-DC converter that steps the battery voltage down from 12 V to 5 V to supply stable regulated power to the microcontroller and associated electronics. All components are housed in heavy-duty protective enclosures that provide mechanical protection against environmental exposure, construction activity, and compaction loads. The power system operated continuously throughout the motorway (M7 corridor) deployment, maintaining cellular connectivity and data transmission under live highway traffic conditions without manual intervention.

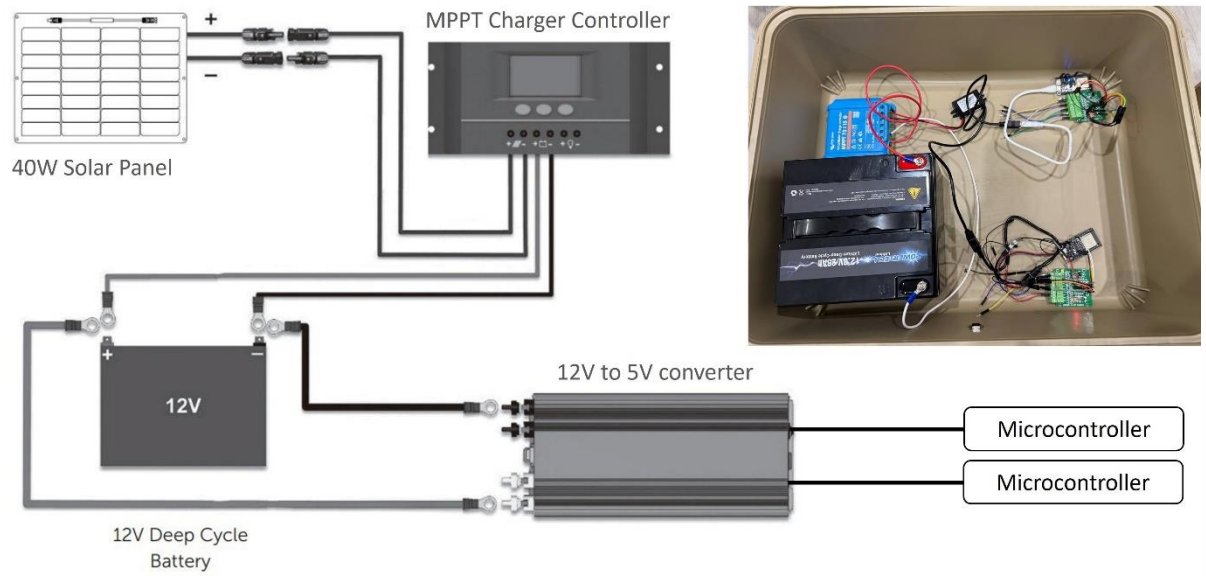


Figure 17. Standalone solar-powered energy system for in-field deployment, showing the 40 W solar panel, MPPT charge controller, 12 V deep-cycle battery, and DC–DC converter supplying regulated 5 V power to the microcontroller, with all components housed in protective enclosures for continuous 24/7 operation.

**Real-time dashboard and cloud storage**

Data from both microcontroller systems are visualised through a custom browser-based dashboard that connects directly to the HiveMQ MQTT broker and simultaneously receives data from all active sensor channels. The dashboard is implemented as a standalone HTML file using Chart.js and MQTT.js loaded from CDN, hosted on GitHub Pages, and accessible from any device with a browser during field operations without installation or network configuration. This deployment approach was a deliberate design choice to minimise the technical barriers to field use by non-specialist operators.

The dashboard displays eight independent waveform plots, one per sensor channel, rendered on a 20-second rolling time window at 100 Hz. Alongside the live waveforms, a spatial activation map of the instrumented slab displays sensor nodes that glow and decay in proportion to their instantaneous signal amplitude, providing field operators with an immediate visual indication of load position and spatial extent across the slab. Cloud storage implemented through the MQTT broker pipeline provides continuous data archiving, enabling post-processing, longitudinal analysis, and retrieval of historical records without requiring local data logging hardware at the field site. The overall system architecture is illustrated in Figure 18.

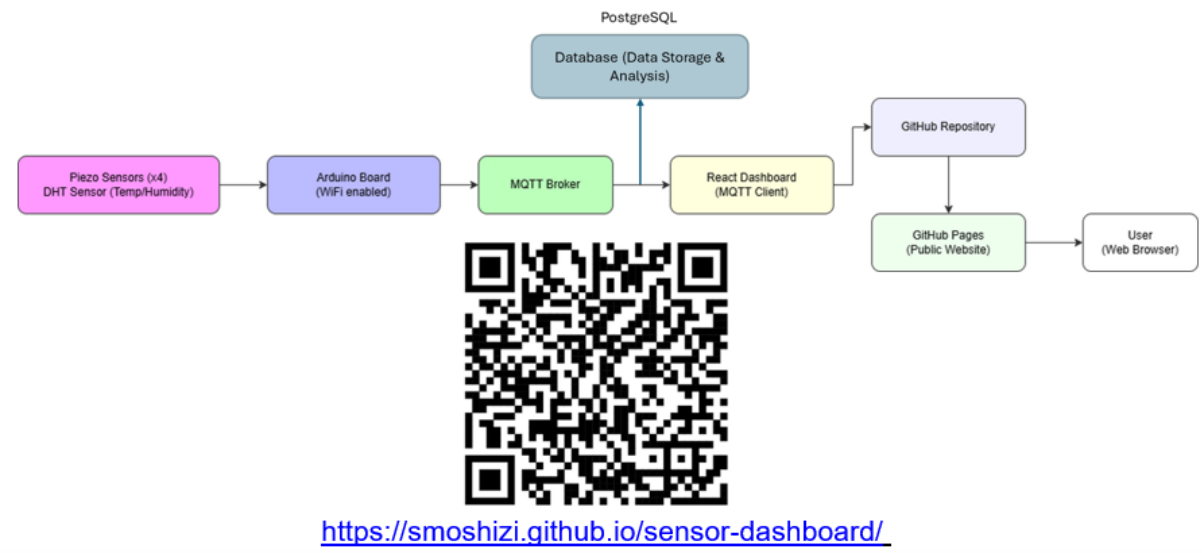


Figure 18. Wireless data acquisition and transmission architecture, showing the two-microcontroller acquisition system, MQTT-based data transmission to the HiveMQ cloud broker, and the browser-based real-time visualisation dashboard with spatial activation map and cloud storage pipeline.

**System performance and validation**

The wireless communication system was validated progressively across three deployment contexts. In the laboratory, continuous data streaming was demonstrated during four-point bending and fatigue tests, confirming that the system could capture signal events at the required 100 Hz rate without data loss under controlled conditions. In small-scale field trials using 400 x 400 x 100 mm and 1 x 1 x 0.24 m concrete slabs, real-time transmission was confirmed during pedestrian, scooter, and motorcycle loading, with the dashboard correctly displaying the spatial pattern of sensor responses across the array. At the M7 motorway corridor, the complete end-to-end system, including sixteen embedded strain sensors, two temperature and humidity sensors, two microcontroller acquisition units, the solar power supply, the cellular data link, and the cloud dashboard, was operated continuously under live highway traffic. The successful operation of the wireless link, power system, and real-time visualisation under these conditions directly confirms Hypothesis 3 from Section 2.2: reliable, real-time wireless data transmission from within a concrete pavement is achievable using a low-cost IoT architecture without wired extraction.

The system also demonstrated operational resilience under partial connectivity. Because the MQTT broker architecture decouples data producers from consumers, temporary interruptions in dashboard connectivity do not result in data loss: the broker retains messages for reconnecting subscribers, and the cloud storage pipeline continues to log data independently of the visualisation client. This characteristic is important for long-term unattended deployments where intermittent network interruptions are inevitable.

**Integration with the broader SmartCrete architecture**

The data infrastructure described in this section underpins every other technical result in the project. The fatigue and cyclic loading results in Section 4.1.1 were recorded through this acquisition system. The temperature and moisture data described in Section 4.1.2 were streamed through the same MQTT pipeline. The FEA correlation in Section 4.1.5 used voltage records collected at 100 Hz through this hardware. The live training dashboard and KNN classifier described in Section 4.1.8 run directly on the MQTT data stream from this system in real time. The system therefore represents not merely a communication layer but the foundational data infrastructure on which the project's sensing, modelling, and interpretation capabilities all depend.

4.1.8 Field Experiments (DEL-723)

Small-scale field testing was carried out to evaluate the performance of the sensing system under realistic loading conditions and to assess the reliability of wireless data transmission outside the laboratory environment. The testing was conducted in stages, with increasing slab size and sensor density to progressively reflect more realistic pavement scenarios.

The first field trial involved three replicate concrete slabs, each with dimensions of 400 × 400 × 100 mm, as shown in Figure 19. A single strain sensor was embedded in each slab during casting and connected to the wireless communication system. Each slab was subjected to controlled loading scenarios including walking, running, and direct impact on the concrete surface. Testing across three independent specimens confirmed the repeatability of the sensor response and the reliability of wireless data transmission under dynamic loading. Video 2 – Small concrete slab documents the sensor output and real-time dashboard behaviour during these tests.

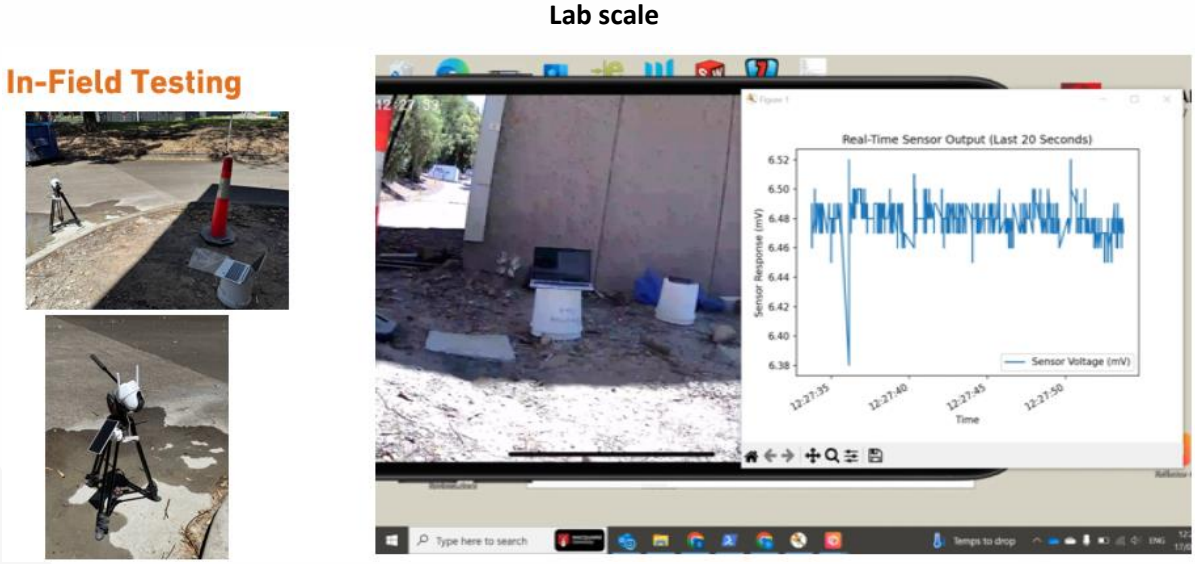


Figure 19. First small-scale field testing using a 400 × 400 × 100 mm concrete slab with a single embedded strain sensor subjected to pedestrian loading and impact tests with wireless data transmission.

Following the initial trial, a larger concrete slab measuring 1 × 1 × 0.24 m was constructed to evaluate system performance under a wider range of loading conditions. Four strain sensors and one combined temperature and moisture sensor were embedded at predefined locations, as illustrated in Figure 20. The four-sensor arrangement was selected to characterise spatial sensing behaviour across the slab: with a maximum diagonal separation of 1 m between sensors, the layout allowed investigation of how

sensors distant from a load source respond relative to the sensor nearest the load, providing evidence of the spatial sensitivity and cross-sensor coupling of the array. All four embedded sensors remained fully functional throughout casting, curing, and the complete loading program, with no signal degradation or failures observed. The slab was subjected to pedestrian loading as well as scooter and motorcycle passes. Results demonstrated consistent and repeatable sensor responses across all loading types. Differences in signal amplitude across the array reflected both load magnitude and sensor proximity to the load, confirming that the system can resolve not only the presence of a loading event but also its spatial position within the slab.

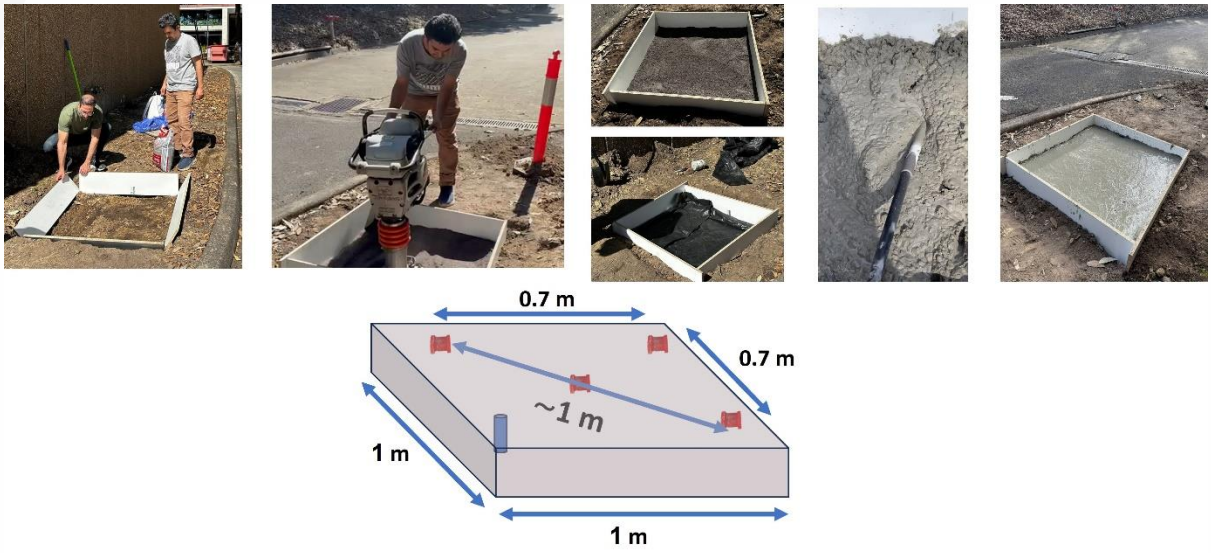


Figure 20. Larger-scale concrete slab (1 × 1 × 0.24 m) with four embedded strain sensors and one temperature and moisture sensor used to evaluate sensor response under pedestrian, scooter, and motorcycle loading.

To ensure stable and continuous network connectivity during in-field testing, a self-powered solar Wi-Fi system was selected to support the SmartCrete wireless communication setup. The system consists of a solar panel, an integrated 4G communication module, and four rechargeable high-capacity lithium batteries. An IoT SIM card provides cellular data access, enabling the system to operate independently of local Wi-Fi infrastructure. This configuration allows the SmartCrete sensors and microcontroller to transmit data reliably to the cloud without interruption, significantly improving the feasibility and resilience of in-field testing under real operating conditions.

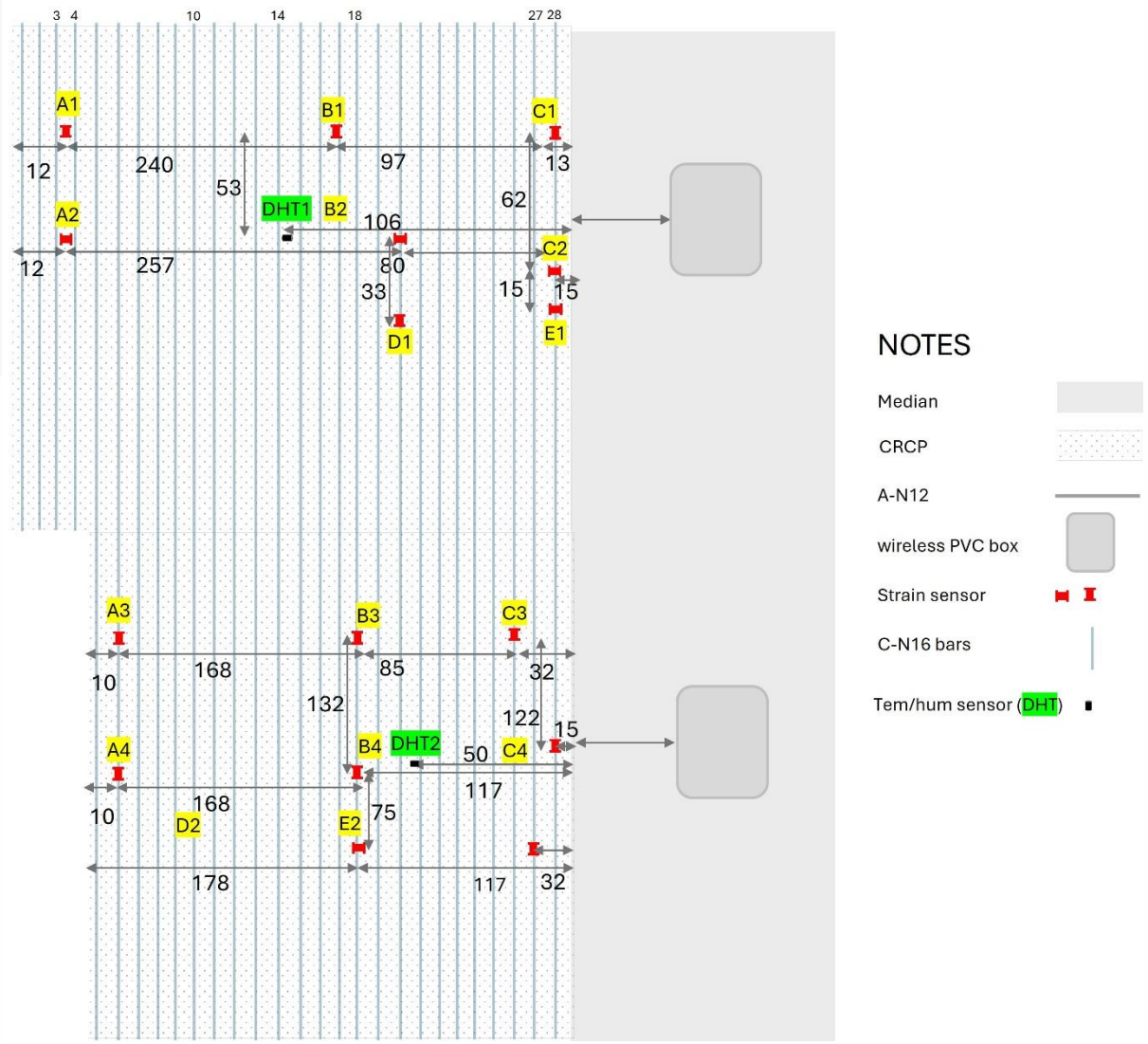


Figure 21. Sensor placement map for the second in-field experiment, illustrating the locations of piezoelectric strain sensors, temperature and humidity sensors, reinforcing bars, and wireless PVC boxes across the two concrete slabs.

Figure 21 presents the corresponding sensor placement map used for the M7 deployment, alongside the SmartCrete sensor dashboard. The dashboard is designed to visualise data from a total of 16 piezoelectric sensors together with two temperature and two humidity sensors. Each horizontal row of plots in the dashboard corresponds directly to one row of sensors in the physical layout shown in the placement map. In the configuration shown, nine piezoelectric sensors were connected and active, representing three sensor rows associated with PVC 1, PVC 2, and PVC 4. The row corresponding to PVC 3 was not connected during this initial test and therefore shows no active sensor signals. The environmental sensors (temperature and humidity) were connected through PVC 2 and PVC 4, with their real-time readings displayed at the bottom of the dashboard. This setup demonstrates the functionality and scalability of the monitoring system, confirming its ability to handle partial sensor connections while maintaining a clear spatial relationship between sensor data and physical layout. The in-situ installation of the sensors within the M7 pavement is shown in Figure 22. Following installation of the sensors and wireless communication equipment, Video 3 – Motorway (M7) dashboard documents the operational dashboard during live vehicle loading at the M7 site.

Critically, this video confirms that wireless transmission through the concrete pavement, one of the principal technical barriers identified at the start of the project, was achieved reliably under field conditions. The solar-powered Wi-Fi and standalone energy system maintained continuous cellular connectivity via the IoT SIM module, while the high-resolution analogue-to-digital converter and microcontroller streamed sensor data to the HiveMQ broker and onward to the cloud dashboard without manual intervention. The successful operation of the wireless link, the power system, and the real-time visualisation together demonstrate that the SmartCrete system can be deployed and operated remotely within a live highway pavement, providing continuous, real-time access to embedded sensor data and validating the readiness of the full monitoring chain for extended in-field evaluation.



Figure 22. In situ sensor installation at the M7 corridor extension project site.



Figure 23. Routing of sensor wiring through protective conduits and storage within heavy-duty waterproof containers.

4.1.9 Driveway Field Validation (DEL-723, DEL-342)

A new test site was identified at Cressy Road, Top Ryde, with support from the City of Ryde. The selected location is a concrete slab at the vehicle exit of a parking area adjacent to a soccer field. This site provides realistic vehicle loading conditions while remaining accessible for installation, inspection, and follow-up testing, making it well suited for continued in-field evaluation of the SmartCrete sensing system in an urban environment.




Figure 24. Proposed test slab at the exit of the parking area near the soccer field on Cressy Road, Top Ryde, showing the site access point and concrete surface.

Since the slab was already constructed, sensors could not be embedded during casting. Instead, a drill-and-embed method was adopted. Holes slightly larger than the sensor dimensions were drilled to approximately 60 mm depth, with sensors seated at around 40 mm depth to balance embedment protection with sensitivity to vehicle-induced loading. Shallow surface grooves (approximately 8 mm deep) were cut to route wiring from each sensor cavity to roadside connection boxes. This approach was validated in a prior controlled trial at the researcher's own property before being applied at the field site.

Eight sensors were installed across the slab in two groups: sensors A1–A4 connected to a right-side junction box and B1–B4 to a left-side box. Each sensor was encapsulated in a revised PLA housing incorporating internal support poles and reduced wall thickness to improve mechanical coupling and

sensitivity. Sensing elements were enlarged to 20 mm, selected in relation to the concrete aggregate size to improve interaction with the surrounding matrix. After placement, all cavities and grooves were sealed with concrete patch material to protect the installation and restore the surface. The connection boxes were buried flush with the ground surface, with lids exposed for access to the wireless communication components.



Figure 25. Fabricated SmartCrete sensors with revised package design, showing modified housing, internal support poles, reduced wall thickness, enlarged sensing element, and extended wiring prepared for field installation.

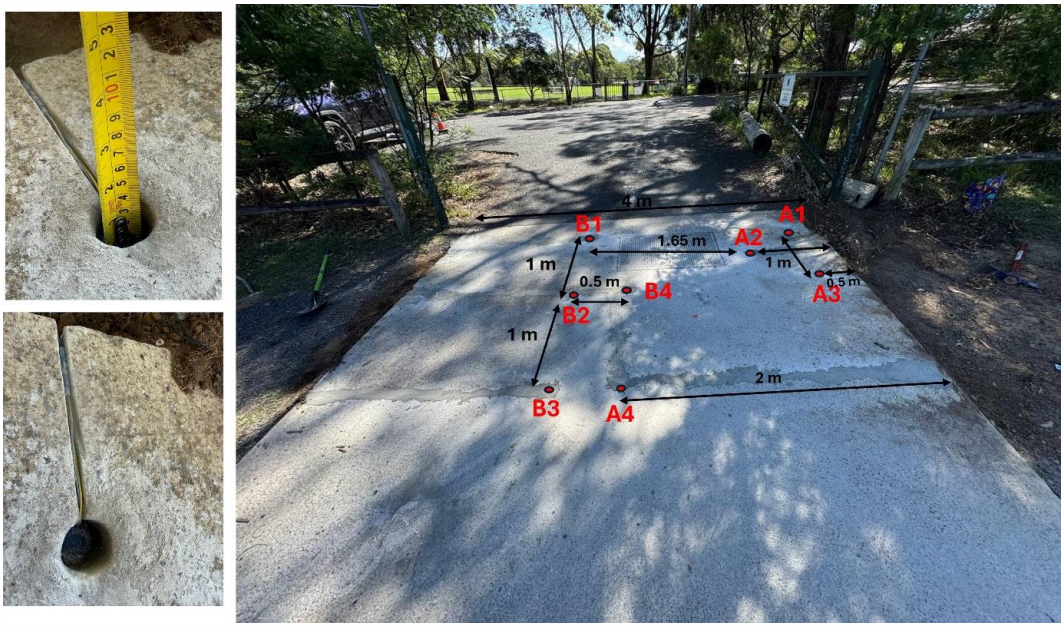


Figure 26. Planned sensor layout for the Cressy Road slab, showing sensor positions A1–A4 (right-side box) and B1–B4 (left-side box), with buried connection boxes and exposed lids for wireless system access.



Figure 27. Installed connection boxes at the Cressy Road test site, buried adjacent to the slab with lids exposed above ground to provide access to the wireless communication components.

In-field performance was assessed by driving an SUV over the instrumented slab and observing sensor outputs on the real-time dashboard. Four videos (Videos 2 to 5) were recorded during the testing program at the Cressy Road site to capture different loading conditions and to compare sensor responses under vehicle and pedestrian loading, complementing the M7 wireless communication demonstration presented earlier in Video 3. Overall, most sensors detected traffic-induced loading clearly, with response magnitude depending on wheel proximity to each sensor location. It should be noted that the y-axis values in the sensor output plots are not yet calibrated; the plots are used primarily to compare relative signal behaviour, peak-to-peak trends, and response timing. Calibration work is ongoing and outputs will be revised accordingly.

**Video 4 – First SUV Pass**

The vehicle passed over the slab with a wheel path not precisely aligned with the sensor layout. Despite this misalignment, the dashboard showed clear responses from sensors A2, A4, B1, B2, and B3, with B4 producing a smaller output. The strongest peak-to-peak signals came from B1, B2, and B3, consistent with the right wheels passing very close to those locations. A2 and A4 showed lower but noticeable responses where the left wheels were nearby, while A1 and A3 received little direct wheel load. During the vehicle's reverse movement, a second set of peaks was recorded on the same responsive sensors. This test established the expected relationship between wheel proximity and response amplitude.

**Video 5 – Repeated SUV Pass**

A repeat pass produced more clearly observable sensor responses. Output amplitudes again reflected the distance between each sensor and the vehicle wheels. Most sensors recorded large responses, while A1 and A3 remained unresponsive. The lower outputs from A4 and B4 are consistent with their positions closer to the middle of the vehicle path, where the direct wheel load effect was less concentrated. This test further confirmed stable and repeatable sensor behaviour, and that the amplitude variation across the slab was physically consistent with the loading path.

**Video 6 – Two Successive Vehicles**

Two vehicles passed sequentially over the instrumented slab. The sensors responded clearly to both, demonstrating the system's ability to detect repeated traffic events. The second vehicle produced a larger peak-to-peak output, likely due to its higher travelling speed and the resulting increase in dynamic excitation. As in earlier tests, A1 and A3 showed no measurable response, while all remaining sensors behaved as expected. Notably, across all vehicle-loading videos, each vehicle pass consistently produced two distinct signal peaks corresponding to the front and rear axle loads, providing strong evidence that the signals are directly linked to wheel loading rather than background noise.

**Video 7 – Pedestrian Loading**

This video examined sensor response under pedestrian loading. The first part shows a crowd walking across the slab on the way to the adjacent soccer field, with several sensors producing detectable responses. A stronger, deliberate footstep was then applied to compare responses against normal walking. The results show a clear difference between the two cases, with the deliberate impact producing a more pronounced signal. This highlights the system's sensitivity across different loading intensities and suggests the sensors can distinguish between vehicle loads, normal foot traffic, and stronger localised impacts. All sensors appeared functional except A1 and A3, which remained unresponsive throughout.

Collectively, these results confirm the feasibility of the drill-and-embed installation approach and establish the Cressy Road site as a functional platform for continued monitoring. Sensors A1 and A3 — unresponsive throughout all tests — will be replaced in the next stage. Calibration work is ongoing to bring all sensor outputs to a corrected baseline for quantitative comparison across sites and loading conditions.

#### 4.1.10 Live Training Sensor Dashboard (DEL-511, DEL-724)

A browser-based live training dashboard was developed to support real-time data collection, event labelling, and on-the-fly classification during field testing (https://smoshizi.github.io/Live-training-sensor-dashboard/). The dashboard connects directly to the HiveMQ MQTT broker and simultaneously receives data from both microcontroller systems (System A and System B), covering all eight piezoelectric sensors embedded in the concrete slab and the temperature/humidity sensor. This architecture provides a complete, synchronised view of slab behaviour during each loading event without requiring any additional post-processing or data export steps.

The dashboard displays eight independent waveform plots, one per sensor channel, each rendered on a 20-second rolling time window at a 10 ms sample interval (100 Hz). Alongside the live waveforms, a spatial activation map of the 4.0 m × 3.0 m slab is rendered using the true sensor coordinates: B1–B3 at x = 1.5 m, B4 at (2.0, 1.5), A1–A3 at x = 3.0 m, and A4 at (2.0, 2.5). Each sensor node on the map glows and decays in proportion to its instantaneous signal amplitude, giving field operators an immediate visual indication of load position and spatial extent across the slab. The overall dashboard layout is shown in Figure 28.

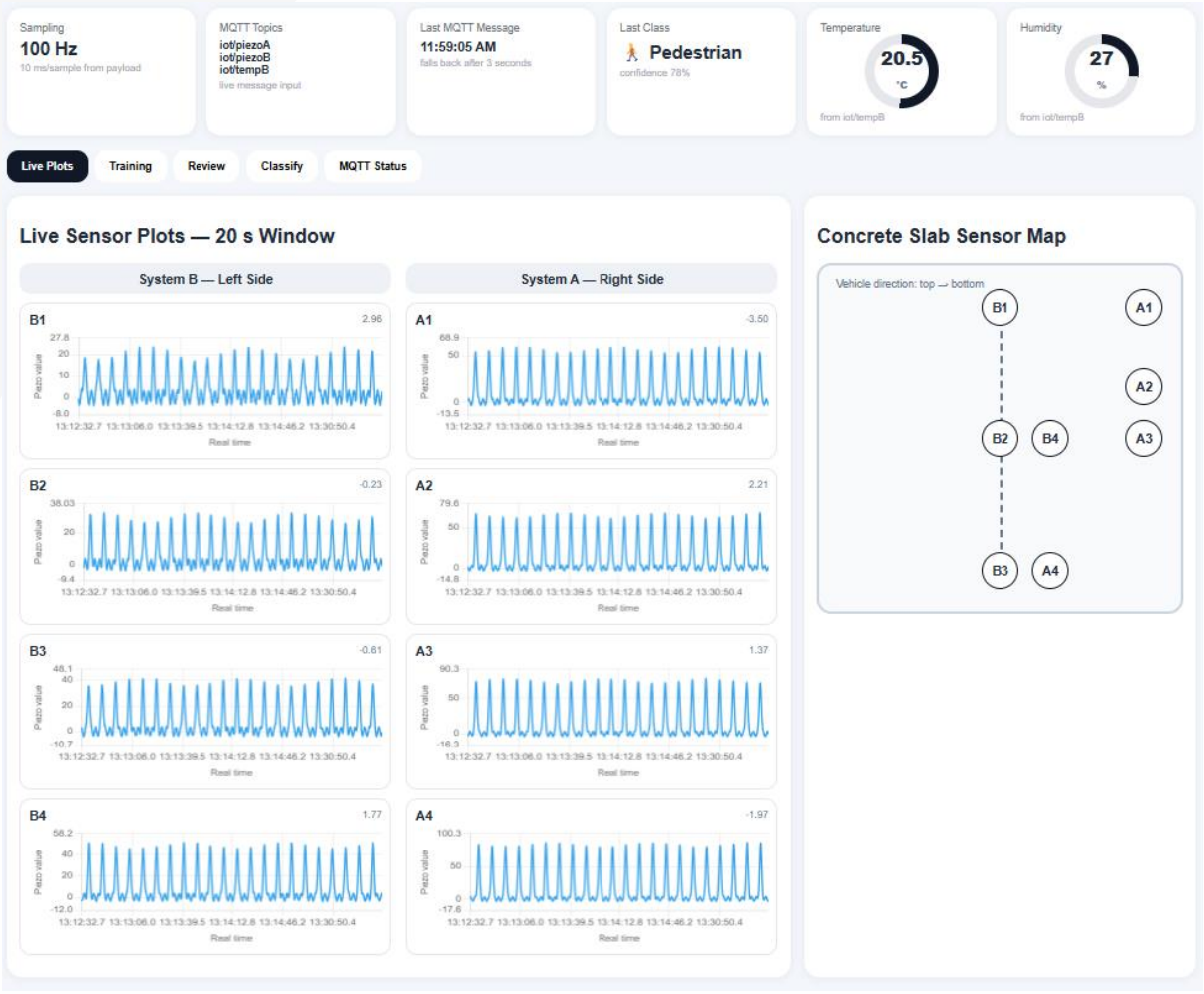


Figure 28. Browser-based live training sensor dashboard showing the eight real-time waveform plots (one per sensor channel on a 20-second rolling window at 100 Hz) and the spatial activation map of the 4.0 m × 3.0 m slab, with sensor nodes glowing in proportion to instantaneous signal amplitude to indicate load position during field testing.

A dedicated Training Mode was integrated into the dashboard to allow supervised data collection directly in the field. While in Training Mode, the operator uses single-key shortcuts (N for no load, P for pedestrian, L for light vehicle, H for heavy vehicle) to label loading events as they occur. For each labelled event, the dashboard automatically extracts a 16-feature vector that characterises the signal across all sensor channels. The feature set includes peak amplitude and root-mean-square energy per channel, the count of simultaneously active sensors (which serves as the primary discriminator between pedestrian and vehicular loading, since a human footstep cannot physically activate three or more sensors at the same time), spatial centroid coordinates derived from weighted sensor positions, and timing-based features that capture the propagation pattern of the stress wave across the slab. Sub-peak detection within a 6-second event window is used to handle multi-step pedestrian events correctly, preventing their segmentation into false vehicle detections. The Training Mode interface is illustrated in Figure 29.

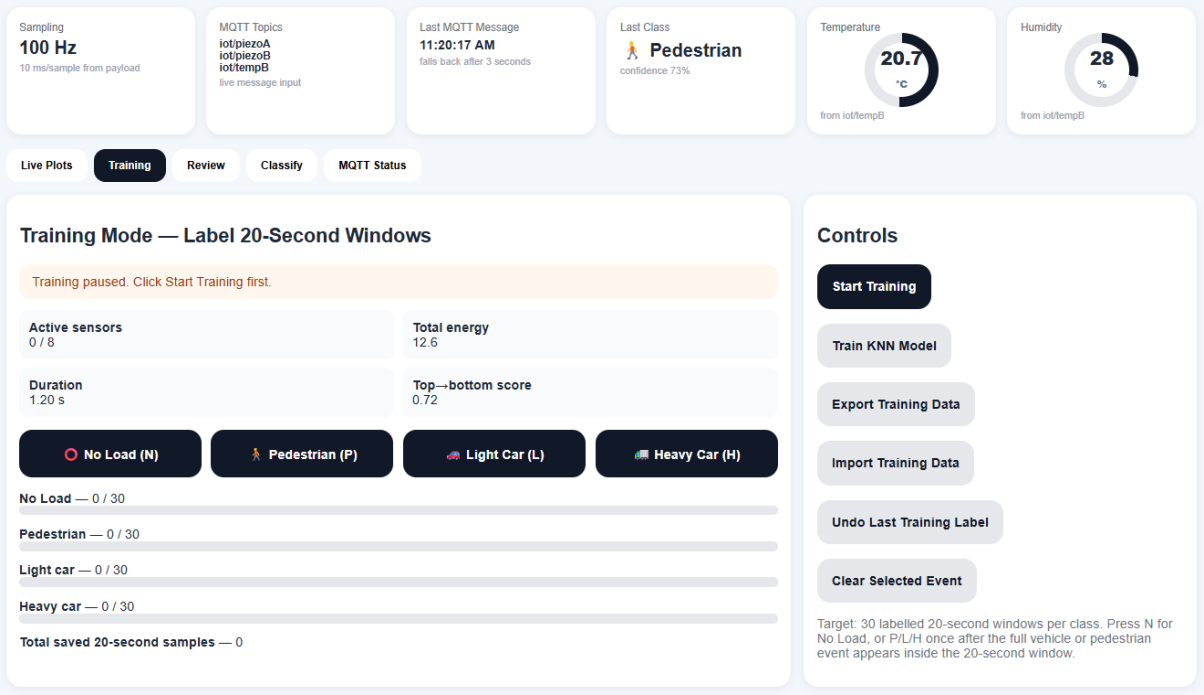


Figure 29. Training Mode panel showing the single-key event labelling interface (N – No Load, P – pedestrian, L – light vehicle, H – heavy vehicle) and the real-time extraction of the 16-feature vector for each labelled loading event, including peak amplitude, RMS energy, simultaneous active sensor count, spatial centroid coordinates, and timing-based wave propagation features.

Once a sufficient number of labelled examples has been collected, the operator initiates classifier training from within the dashboard. A K-Nearest Neighbour (KNN) model with K = 5 is fitted to the accumulated labelled feature vectors. After training, the Training tab transforms into a Model Info panel that reports the number of examples per class and the feature importance summary, and the dashboard automatically transitions to Live Classification mode. In this mode, each subsequent loading event is classified in real time and a colour-coded classification banner is displayed at the top of the screen, together with a timestamped event log that records the class label, confidence score, and the feature values associated with each event. The Model Info panel after training is shown in Figure 30, and the Live Classification mode is illustrated in Figure 31.

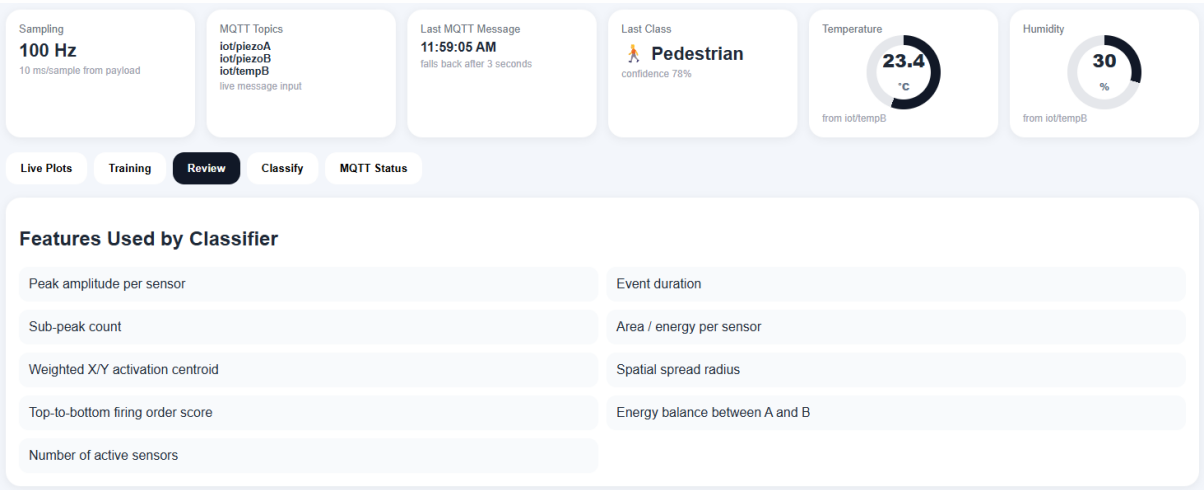


Figure 30. Model Info panel displayed after K-Nearest Neighbour (KNN, K = 5) classifier training, showing the number of labelled examples per class and the feature importance summary used to guide further data collection in the field.

All labelled training data and classification results can be exported as a CSV file directly from the dashboard, enabling offline re-training, extended analysis, and longitudinal comparison of model performance across field sessions. The dashboard is implemented as a standalone HTML file with no server-side build process, using Chart.js and MQTT.js loaded from CDN, and is hosted on GitHub Pages. This deployment approach ensures that the tool can be accessed from any device with a browser during field testing without installation or network configuration overhead.

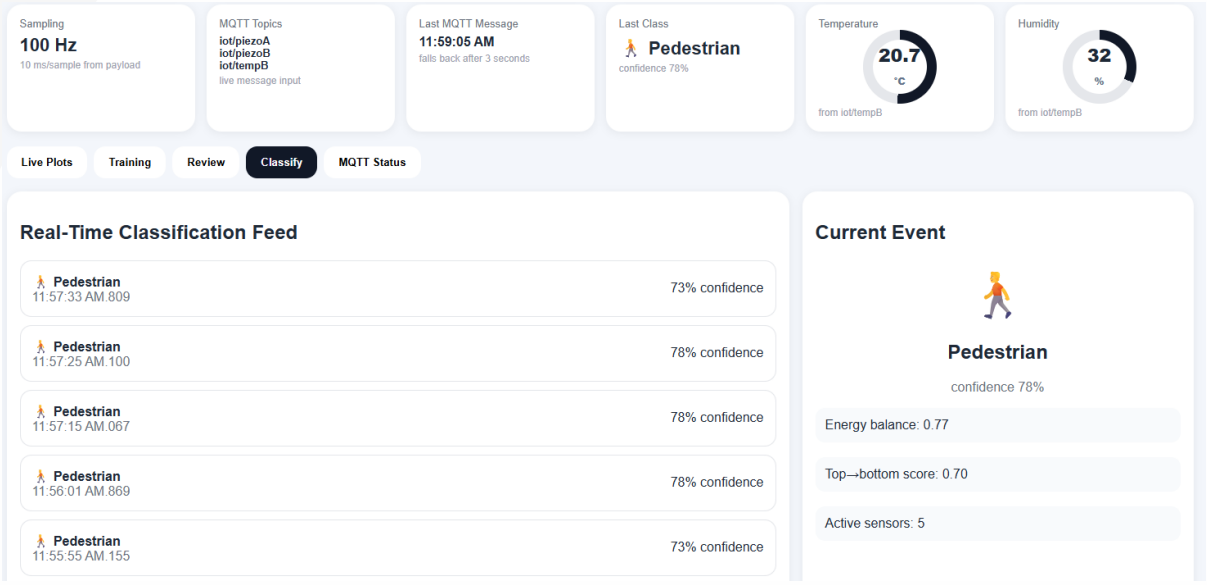


Figure 31. Live Classification mode showing the colour-coded classification banner at the top of the screen and the timestamped event log recording class label, confidence score, and feature values for each detected loading event, with CSV export available for offline re-training and longitudinal analysis.

Field validation of the dashboard was conducted during SUV drive-over tests on the instrumented slab at the Ryde site. The system reliably captured front and rear axle loading sequences on the relevant sensor channels, and the spatial activation map correctly reflected the lateral wheel path offset relative to the sensor layout. These results confirm that the live training dashboard provides an effective and practical interface for generating labelled datasets and deploying real-time classification models directly in the field, supporting the broader goal of automated traffic load characterisation from embedded pavement sensors. A representative output from this field validation is shown in Figure 32.

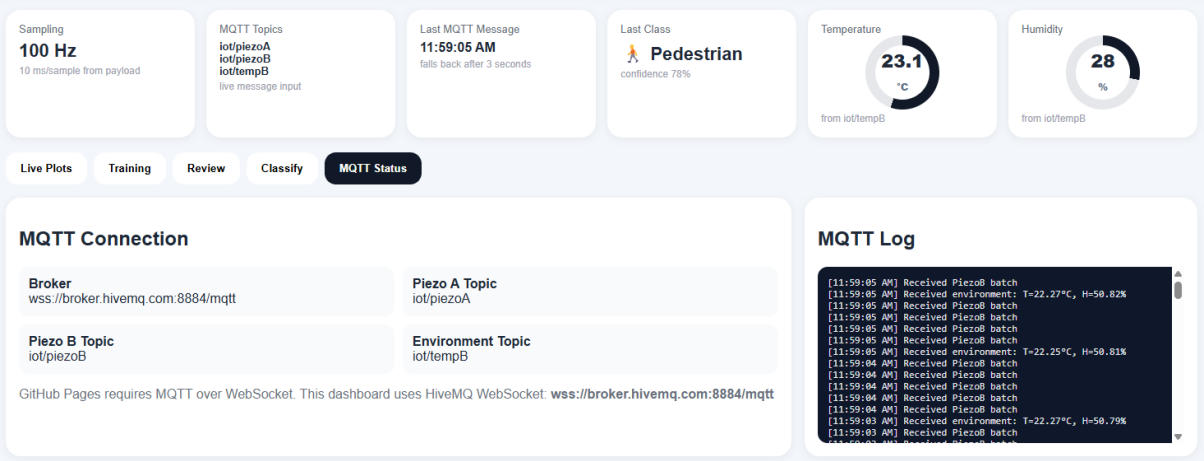


Figure 32. Field validation result from the live training dashboard during SUV drive-over tests at the Ryde site, showing the spatial activation map correctly reflecting the lateral wheel path offset across the slab and the sensor channels capturing the sequential front and rear axle loading peaks for each vehicle pass.

**Video 8 – Live training sensor dashboard**

Before testing the dashboard, the microcontrollers were configured with a peak-preserving filtering design to keep the idle piezo sensor baseline close to zero while avoiding attenuation of real impact events. Each raw ADC reading is first converted to millivolts and then passed through a one-pole high-pass DC-blocker filter, which removes DC offset and slow baseline drift without applying smoothing or low-pass averaging. This prevents the signal baseline from wandering during idle periods while allowing sharp transient peaks caused by footsteps, impacts, or vibrations to pass through with their amplitude largely preserved. Since the noise gate threshold was set to `0.0 mV`, no additional threshold-based suppression was applied, allowing even very small sensor responses to remain visible while the high-pass filter maintains the resting baseline near zero.

After implementing the filtering, the dashboard system was tested using a full wireless sensing setup, including the microcontrollers, MQTT communication, and the dashboard client. An SUV was driven over the concrete slab to evaluate the sensor response under a real loading condition and to verify the effectiveness of the filtering method. The recorded response showed clear peak signals as the vehicle passed over the instrumented area, followed by a return of the sensor output to the zero baseline after the load was removed. This confirms that the dashboard can capture transient vehicle-induced responses while maintaining a stable baseline during idle conditions.

### 4.2 Project Deliverables and Outputs

This project delivered a set of tangible technical outputs that align closely with the original project objectives and address the industry challenges identified at the outset.

A core deliverable was the development of a low-cost embedded piezoelectric strain sensor suitable for deployment within concrete pavements. At current production volumes the unit cost is below $1, with further reduction expected at bulk manufacturing scale. The sensor design was refined through systematic laboratory testing across three replicate beam specimens per configuration, arriving at the 12 mm PLA-encapsulated PZT sensor as the recommended configuration. In laboratory fatigue tests, this sensor detected microcrack initiation 7 to 8 cycles before visible failure, with the signal trough in the cycle immediately before main failure exceeding three times the depth of preceding cycles. This detection capability was established under controlled laboratory conditions and provides the

evidential basis for the field deployment program. In parallel, a 3D-printed conductive TPU temperature sensor was developed and validated against commercial reference devices, providing internal environmental data required for accurate interpretation of strain measurements under varying pavement conditions.

Validated sensor placement strategies were developed by combining experimental testing with finite element modelling. The FEA model, calibrated against four-point bending results, established a strong linear correlation between simulated principal stress and measured sensor voltage output ($R^2 = 0.978$), confirming that the sensor signal serves as a reliable proxy for the internal stress state. These placement strategies provide practical, mechanistically grounded guidance on sensor location to maximise sensitivity to crack initiation and strain redistribution, replacing trial-and-error installation with a quantitative basis for deployment decisions.

A complete data acquisition and wireless communication system was developed and field-validated. The system operates at 100 Hz across all sensor channels, sufficient to resolve individual axle load events and front-to-rear axle timing sequences. Data are transmitted wirelessly via an MQTT publish-subscribe protocol to the HiveMQ cloud broker and visualised through a custom browser-based real-time dashboard, with continuous cloud archiving supporting post-processing and longitudinal analysis. For remote deployments without mains power or fixed network access, a standalone solar-powered energy system was designed and demonstrated, comprising a 40 W solar panel, MPPT charge controller, 12 V deep-cycle battery, and DC-DC converter. The complete system was operated continuously under live highway traffic at the M7 motorway corridor, directly confirming the wireless transmission hypothesis.

A browser-based live training sensor dashboard incorporating a K-Nearest Neighbour (KNN) classifier was developed and field-validated as an automated load interpretation tool. The dashboard extracts a 16-feature vector from each detected loading event and supports on-the-fly operator labelling through a dedicated Training Mode. Once sufficient labelled examples are collected, the KNN model ($K = 5$) is trained within the dashboard and transitions to live classification, assigning each subsequent event to one of three categories: pedestrian, light vehicle, or heavy vehicle, with a confidence score logged in a timestamped exportable record. Field validation at the Cressy Road site confirmed reliable discrimination between vehicle and pedestrian loading events.

Documented installation protocols for both cast-in and drill-and-embed sensor configurations were produced through iterative refinement across the M7 and Cressy Road deployments. These protocols provide contractor-ready guidance covering sensor placement, wiring routing, junction box installation, and wireless hardware deployment, supporting repeatable installation in future pilot deployments.

The project also generated a substantial body of experimental and field data across laboratory beam tests, slab-scale trials, and two operational field sites. These datasets are stored through the cloud-based MQTT pipeline and are additionally archivable to a local SD module for offline access, providing the training foundation for more advanced classifiers and supporting future model validation and longitudinal performance analysis.

Table 5. SmartCrete Project Deliverables: Proposed Scope vs. Achieved Progress

| Deliverable ID | Deliverable Name | Progress in Project |
|---|---|---|
| **DEL-035** | Understanding of failure mechanisms and failure locations in concrete pavements | Achieved. Failure mechanisms characterised through laboratory four-point bending and fatigue testing, identifying microcrack initiation 7-8 cycles before visible |

| Deliverable ID | Deliverable Name | Progress in Project |
|---|---|---|
| | | failure and establishing midsection/lower-third placement as optimal for early detection (Section 4.1.1). |
| **DEL-342** | Feasibility assessment for implementation technology and pathway to market | Achieved. Low-cost sensor design (sub-$1 unit cost), field deployment at two operational sites, and a defined commercialisation pathway through pilot installations established (Sections 4.1.9, 4.2, 4.3, 5.2). |
| **DEL-034** | New sensory system for early detection of cracks in plain concrete pavements (strain, temperature, humidity, and pH sensing) | Partially achieved. A 12 mm PLA-encapsulated PZT strain sensor and a 3D-printed conductive TPU temperature sensor were developed and field-validated (Sections 4.1.1, 4.1.2). The humidity and pH sensing components were scoped and reported as future calibration/development items, with commercial temperature-humidity sensing used in parallel to maintain reliable environmental monitoring during field trials (Sections 4.1.3, 4.1.4). |
| **DEL-036** | Model correlating traffic loading, environmental factors, and crack propagation with remaining pavement life | Substantially progressed. Bayesian Network model developed using LTPP data, linking traffic loading (AnnualKESAL), environmental drivers, and distress indicators to IRI; SmartCrete sensor outputs identified as real-time inputs to three BN nodes (Section 4.1.6). Full integration of live sensor data into the BN remains a future development item. |
| **DEL-724** | Post-processing and data analysis | Achieved. Cloud-based MQTT data pipeline supports continuous archiving and post-processing; 16-feature event extraction implemented in the live training dashboard (Sections 4.1.7, 4.1.10). |
| **DEL-722** | Integration of telemetry system | Achieved. MQTT publish-subscribe architecture integrated with HiveMQ cloud broker, validated across laboratory, slab-scale, and field deployments at M7 and Cressy Road (Section 4.1.7). |
| **DEL-723** | Concrete pavement configuration | Achieved. Sensor arrays deployed in two pavement configurations: an urban plain concrete slab at Cressy Road using drill-and-embed installation and a continuously reinforced concrete pavement on the M7 using cast-in installation (Sections 4.1.8, 4.1.9). |
| **DEL-510** | Sensor development | Achieved. Strain sensor design progressed from PDMS encapsulation through to the optimised 12 mm PLA housing; 3D-printed conductive TPU temperature sensor also developed and validated, with humidity and pH sensing documented as follow-on |

| Deliverable ID | Deliverable Name | Progress in Project |
|---|---|---|
| | | calibration/development items (Sections 4.1.1, 4.1.2, 4.1.3, 4.1.4). |
| **DEL-509** | Submission of PhD theses | In progress. Reflects ongoing candidature and thesis submission activities; related education and training outcomes are summarised in Section 6. |
| **DEL-511** | Analytics | Achieved. Browser-based live training dashboard with KNN baseline classifier (K = 5) developed and field-validated, performing real-time classification of pedestrian, light vehicle, and heavy vehicle loading events (Section 4.1.10). |
| **DEL-725** | Finite Element Analysis (FEA) and validation | Achieved. FEA model calibrated against four-point bending results, achieving strong linear correlation with measured sensor voltage ($R^2$ = 0.978); extended to moving-load slab simulations (Section 4.1.5). |
| **DEL-726** | Reports on expected outcomes and deliverables | Achieved. This wrap-up report, including technical results, deliverables summary, and commercialisation pathway (Sections 4, 5). |

Table 5 shows that the project delivered the core sensing, telemetry, modelling, field validation, and analytics outcomes required for the SmartCrete monitoring system. The main achievements are concentrated in the strain sensing platform, temperature sensing, FEA validation, wireless data infrastructure, field deployment, and live event-classification dashboard, which together demonstrate a complete pathway from embedded measurement through to real-time interpretation. The partially achieved items relate mainly to humidity and pH sensing, where preliminary capability and technical scoping were completed but further calibration, durability testing, and low-maintenance field validation are required before they can be treated as mature standalone SmartCrete sensors. Overall, the deliverables confirm that the project has moved beyond laboratory proof-of-concept toward operational field deployment, while also identifying clear follow-on development priorities for broader commercial and network-scale adoption.

### 4.3 Intellectual Property and Commercial Potential

Formal intellectual property protection was not the primary focus during this phase of the project. Instead, the emphasis was placed on developing a technically sound, practical, and scalable sensing solution that could be evaluated under realistic conditions.

Despite this focus, several outcomes from the project have clear potential for future intellectual property consideration. These include the design and encapsulation of the embedded strain sensor, the integration of sensing hardware with a robust wireless data pipeline, and the system-level architecture that enables real-time monitoring and cloud-based data management.

Importantly, the project deliberately prioritised low-cost materials, simple fabrication methods, and practical installation approaches. This design philosophy improves the feasibility of large-scale manufacturing and deployment and strengthens the commercial potential of the technology. The

outcomes provide a solid foundation for future patent assessment, licensing discussions, or collaboration with industry partners should the project progress to a commercialisation phase.

### 4.4 Summary

Overall, the project met its technical objectives across laboratory, modelling, and field phases, delivering a validated embedded sensing system for continuous structural health monitoring of concrete pavements.

Sensor performance was characterised through a structured laboratory program conducted on three replicate concrete beam specimens per sensor configuration (n = 3), with all values reported as mean ± SE. Cyclic four-point bending tests were performed at a maximum load of 10 kN across five load rates (0.01, 0.1, 0.5, 1, and 2 kN/s), and at reduced maximum loads of 1 kN and 0.5 kN at selected rates, to characterise the load-rate dependence of the piezoelectric response. The 12 mm PLA-encapsulated PZT sensor achieved mean SNR values of 8.22 ± 0.47, 13.56 ± 0.82, and 10.22 ± 0.49 dB at 0.5, 1, and 2 kN/s respectively (n = 3), significantly outperforming the 30 mm sensor at all corresponding rates (one-way repeated-measures ANOVA: $F = 288.03$, $df = 5$, $p < 0.0001$; post-hoc Tukey comparisons: all $p < 0.0001$). The 12 mm sensor produced no measurable reduction in host concrete flexural strength (5.6 ± 0.4 MPa preserved), while the 30 mm sensor reduced strength by approximately 9% (5.1 ± 0.3 MPa), attributed to stress concentrations from its size exceeding the 20 mm maximum aggregate.

Fatigue tests using a zigzag cyclic loading pattern on the same four-point bending configuration demonstrated that the 12 mm sensor reliably detected microcrack initiation 7 to 8 cycles before visible failure in two representative specimens, with the voltage trough in the cycle immediately preceding main failure exceeding three times the depth of the preceding cycle. This detection signature was consistent and unambiguous across both tested cases.

Sensor placement characterisation, conducted across three replicate beams per position (n = 3, mean ± SE), confirmed that voltage output decreased consistently as the sensor moved away from the crack initiation zone toward the supports, with sensors at the centre and 50 mm from centre producing comparable responses prior to failure due to the combined effect of normal and shear stress at those locations.

Wireless data transmission, cloud-based storage, and real-time visualisation were demonstrated reliably across laboratory, slab-scale, and operational field deployments at the M7 motorway corridor and Cressy Road, Top Ryde. A KNN-based live classification dashboard was developed and field-validated, enabling real-time discrimination of pedestrian, light vehicle, and heavy vehicle loading events without post-processing. These results collectively provide a strong and quantitatively grounded basis for larger-scale trials and future adoption by Transport for NSW and other road asset owners.

# 5 Next Steps – Commercialisation & Impact Plan

The project has demonstrated that the sensing system performs reliably across laboratory testing, slab-scale trials, and operational field deployments. The next phase focuses on building the evidence base and infrastructure required for practical industry adoption.

### 5.1 Short-Term Next Steps

The immediate priority is continued in-field testing at the current deployment sites. Ongoing monitoring under live traffic conditions will confirm long-term sensor durability, signal stability, and

system resilience under varying environmental and loading conditions. These results will provide the longitudinal performance data that industry partners need before committing to broader deployment.

Installation procedures for both cast-in and drill-and-embed configurations will be further refined based on field experience, with the aim of producing contractor-ready guidelines suitable for use across different pavement project types.

### 5.2 Pathway to Commercialisation

The sensing system was designed from the outset for low-cost manufacture, with a current unit sensor cost below $1 and further reduction expected at production scale. This positions the technology well for large-scale deployment once field validation is complete.

The next stage involves pilot installations on selected road sections in collaboration with industry partners. These trials will allow partners to evaluate sensor installation practicality, long-term data reliability, and the usefulness of monitoring outputs for routine asset management decisions. Findings from pilot deployments will be used to refine sensor packaging, system configuration, and deployment procedures ahead of broader rollout.

Intellectual property outcomes from this project provide a foundation for future patent assessment and licensing discussions as the technology progresses toward commercial readiness.

### 5.3 Impact Through Data Integration and Automation

The KNN-based live classification dashboard delivered in this project provides a working baseline for automated load interpretation, capable of distinguishing pedestrian, light vehicle, and heavy vehicle events in real time. Future development will replace this baseline with an Artificial Neural Network classifier, trained on the expanding labelled dataset accumulated during field operations. This will improve classification accuracy across a wider range of vehicle types, loading speeds, and pavement configurations, and reduce reliance on expert input for routine data interpretation.

Integration of classification outputs with existing pavement management frameworks will allow continuously updated load history and structural condition data to inform network-level maintenance scheduling, supporting broader adoption across large road networks.

### 5.4 Long-Term Industry Impact

In the longer term, the sensing system supports a fundamental shift from reactive to condition-based pavement management. Early detection of internal strain changes and microcracking allows maintenance to be planned before surface damage appears, reducing the scale and cost of interventions and extending pavement service life.

At network scale, fewer and earlier interventions reduce material consumption, construction traffic, and associated carbon emissions. Reduced roadworks frequency also lowers disruption to road users and improves network reliability, outcomes that align directly with the asset management and sustainability obligations of road authorities managing large concrete pavement portfolios.

# 6 Education and Training

This project contributed to education and training through practical work on embedded sensing and digital monitoring systems. For the first time in this research, piezoresistive and piezoelectric sensors were used in a systematic way to detect strain inside concrete. This created a strong learning platform for future research in smart infrastructure sensing.

Researchers gained hands-on experience in sensor packaging and protection for use inside concrete. They learned how different packaging approaches affect sensor performance and reliability. The

process of embedding sensors during casting and ensuring they survived testing provided valuable practical training.

The project also developed a complete wireless communication and data storage workflow. This included data collection, wireless transmission, cloud storage, and real-time visualisation. Working with this full system helped researchers understand how sensing data can be transferred and managed in real applications.

Basic data analysis and early machine learning tools were explored to classify loading events. This work supported training in data handling and interpretation.

Overall, the project provided practical training in sensor-based monitoring, wireless systems, and data workflows. The methods developed in this project can be used for training and research in future sensing projects.

# 7 Conclusions, Implications and Recommendations

This project showed that embedded sensing can be used to monitor internal behaviour in concrete pavements. The sensing system detected changes in strain inside concrete before surface damage appeared. Laboratory testing and small-scale field trials confirmed that the system can work reliably under realistic conditions.

**Challenges Overcome and Challenges Remaining**

Several challenges were addressed during the project. Developing sensors that could survive inside concrete was a major challenge. This was overcome through improved sensor packaging and careful installation methods. Reliable wireless data transmission from inside concrete was also challenging. This was addressed through system refinement and the use of high-resolution data acquisition and cloud-based platforms.

Some challenges remain. Long-term durability under extended field exposure still needs to be confirmed. Sensor calibration is ongoing to improve quantitative interpretation of strain data. Automated detection of cracking using machine learning methods also requires further development.

Simplifying the data input and analysis workflow for non-specialist field use also remains an open challenge. While the current dashboard (Section 4.1.10) demonstrates real-time sensor visualisation and an operator-driven training workflow, further work is needed to consolidate this into a streamlined, user-friendly interface suited to routine field adoption by asset-management personnel rather than research use. Formal training modules for field engineers, covering system deployment, data interpretation, and event classification, are also identified as a remaining requirement to support wider rollout of the technology.

**Project Highlights and Key Achievements**

The project achieved several important outcomes. For the first time in this research, piezoresistive and piezoelectric sensors were systematically used to detect strain inside concrete. The project delivered a complete sensing system, including sensor packaging, wireless communication, real-time visualisation, and cloud data storage.

Successful laboratory testing and in-field trials demonstrated the ability to detect different loading events such as pedestrian and light vehicle loads. These results provide strong evidence that the system can operate under real conditions and produce meaningful data.

**Key Learnings for Future Research and Commercial Activities**

The project generated several important learnings. Sensor packaging and installation are critical to performance and reliability. Low-cost materials can be used successfully if the design is carefully optimised. Wireless communication inside concrete is achievable but must be considered early in system design.

The project also showed the importance of collecting environmental data alongside strain measurements. For future work, early planning for data interpretation and automation will be essential, particularly for large-scale deployment. These learnings provide clear guidance for future research and support the pathway toward commercial application.

# 8 Publication List

M. Razbin, **S. A. Moshizi**, H. Asadi, B. Ben, H. Srivastava, G. Alipour Esgandani, R. Abbassi, M. Asadnia "Piezoresistive polymer nanocomposite sensors for structural health monitoring of concrete beams," Smart Materials and Structures, 2025, (DOI: 10.1088/1361-665X/ae2a83)

**S. A. Moshizi**, Milad Razbin, Chunyu Zhang, Golnaz Alipour Esgandari, Rouzbeh Abbassi and Mohsen Asadnia "Thermoplastic Nanocomposite 3D-Printed Temperature Sensor," Concrete 2025 Conference, Adelaide, 7 September 2025

**S. A. Moshizi**, M. Razbin, H. Asadi, B. Ben, H. Srivastava, G. Alipour Esgandani, R. Abbassi, M. Asadnia "Investigating Piezoelectric Sensor Performance for Crack Detection in Concrete Pavements," Innovative Infrastructure Solutions, **Accepted**, Under publication, 2026

M. Razbin, S. Sathorn, **S. A. Moshizi**, S. Wu, M. Asadnia, V. Vimonsatit, "Tesseract-Structured Piezoresistive Sensors for Embedded Monitoring of Cementitious Materials," Measurement, Under review, 2026

# 9 References


[1] H. Ceylan, Liang Dong, Shuo Yang, Yueyi Jiao, Sunghwan Kim, Kasthurirangan Gopalakrishnan, and Peter Taylor, "Field Demonstration of Embedded Sensors for Monitoring Concrete Pavements," Iowa State University Institute for Transportation, 2016, vol. Final Report, Volume I. [Online]. Available: https://prosper.intrans.iastate.edu/wp-content/uploads/2018/03/wireless_MEMS_volume_I_field_demo_w_cvr.pdf

[2] S. Guo, Z. Xu, X. Li, and P. Zhu, "Detection and characterization of cracks in highway pavement with the amplitude variation of GPR diffracted waves: Insights from forward modeling and field data," *Remote Sensing,* vol. 14, no. 4, p. 976, 2022.

[3] R. Hussein, B. Etete, H. Mahdi, and H. Al-Shukri, "Detection and delineation of cracks and voids in concrete structures using the ground penetrating radar technique," *Journal of Applied Geophysics,* vol. 226, p. 105379, 2024/07/01/ 2024, doi: https://doi.org/10.1016/j.jappgeo.2024.105379.

[4] B. O. I. A. T. R. ECONOMICS, "The Economics of Road Maintenance," RESEARCH REPORT 156, 2023.

[5] V. P. B. Office, "Victorian road asset management: comparison with other states' expenditure," 2025.

[6] J. Huang *et al.*, "Stretchable and heat-resistant protein-based electronic skin for human thermoregulation," *Advanced Functional Materials,* vol. 30, no. 13, p. 1910547, 2020, doi: https://doi.org/10.1002/adfm.201910547.

[7] Y. Li *et al.*, "Smart glove integrated with tunable MWNTs/PDMS fibers made of a one-step extrusion method for finger dexterity, gesture, and temperature recognition," *ACS Applied Materials & Interfaces,* vol. 12, no. 21, pp. 23764-23773, 2020, doi: https://doi.org/10.1021/acsami.0c08114.

[8] J. Lee *et al.*, "Intrinsically strain-insensitive, hyperelastic temperature-sensing fiber with compressed micro-wrinkles for integrated textronics," *Advanced Materials Technologies,* vol. 5, no. 5, p. 2000073, 2020, doi: https://doi.org/10.1002/admt.202000073.

[9] C. Wang, K. Xia, M. Zhang, M. Jian, and Y. Zhang, "An all-silk-derived dual-mode e-skin for simultaneous temperature–pressure detection," *ACS applied materials & interfaces,* vol. 9, no. 45, pp. 39484-39492, 2017, doi: https://doi.org/10.1021/acsami.7b13356.

[10] R. Wu *et al.*, "Silk composite electronic textile sensor for high space precision 2D combo temperature–pressure sensing," *Small,* vol. 15, no. 31, p. 1901558, 2019, doi: https://doi.org/10.1002/smll.201901558.

[11] S. Y. Hong *et al.*, "Stretchable active matrix temperature sensor array of polyaniline nanofibers for electronic skin," *Advanced materials,* vol. 28, no. 5, pp. 930-935, 2016, doi: https://doi.org/10.1002/adma.201504659.

[12] R. Sampaio, A. Bastos, and M. Ferreira, "New Sensors for Monitoring pH and Corrosion of Embedded Steel in Mortars during Sulfuric Acid Attack," *Sensors,* vol. 22, no. 14, p. 5356, 2022. [Online]. Available: https://www.mdpi.com/1424-8220/22/14/5356.

[13] A. Martínez-Ibernón, I. Gasch, J. Lliso-Ferrando, and M. Valcuende, "Development of a new Ni voltammetric sensor for hardened concrete conditions estimate," *Sensors and Actuators Reports,* vol. 5, p. 100155, 2023/06/01/ 2023, doi: https://doi.org/10.1016/j.snr.2023.100155.

[14] Y. Wang *et al.*, "In-situ monitoring of pH and Cl− concentration and rebar corrosion at the rebar/mortar interface," *Construction and Building Materials,* vol. 400, p. 132712, 2023/10/12/ 2023, doi: https://doi.org/10.1016/j.conbuildmat.2023.132712.

[15] F. H. A. U.S. Department of Transportation. *Long Term Pavement Performance InfoPave, Data Selection and Download, SDR 39*. [Online]. Available: https://infopave.fhwa.dot.gov/Data/DataSelection

# 10 Appendices and Attachments

Smart Materials and Structures

PURPOSE-LED PUBLISHING™

**PAPER** • **OPEN ACCESS**

# Piezoresistive polymer nanocomposite sensors for structural health monitoring of concrete beams

To cite this article: Milad Razbin *et al* 2026 *Smart Mater. Struct.* **35** 015006

View the article online for updates and enhancements.

You may also like

- A review of woven textile circuit boards: fundamentals, development strategies, and joining techniques
Faisal Ahmed, James Reynolds, Amanda C Mills et al.
- The effect analysis of MRE's component to the damper's character based on the system dynamic model
Zhiyang Niu, Bing Chen, Yu Sun et al.
- Fully-passive implementation of multi-branch piezoelectric shunts for multimodal vibration damping
Pierre Flament, Boris Lossouarn, Jean-François Deü et al.




This content was downloaded from IP address 122.150.154.250 on 28/12/2025 at 00:43

Smart Materials and Structures

Check for updates

PAPER

OPEN ACCESS

RECEIVED
29 April 2025

REVISED
15 November 2025

ACCEPTED FOR PUBLICATION
9 December 2025

PUBLISHED
22 December 2025

Original content from this work may be used under the terms of the Creative Commons Attribution 4.0 licence.

Any further distribution of this work must maintain attribution to the author(s) and the title of the work, journal citation and DOI.

# Piezoresistive polymer nanocomposite sensors for structural health monitoring of concrete beams

**Milad Razbin[1], Sajad Abolpour Moshizi[2], Hossein Asadi[3], Basil Ben[3], Harish Srivastava[3], Golnaz Alipour Esgandani[2], Rouzbeh Abbassi[2] and Mohsen Asadnia[2,*]**

[1] School of Aerospace, Mechanical and Mechatronic Engineering, The University of Sydney, Sydney, NSW 2006, Australia
[2] School of Engineering, Macquarie University, Sydney, NSW 2109, Australia
[3] Transport for NSW (TfNSW), Sydney, NSW, Australia
[*] Author to whom any correspondence should be addressed.

**E-mail:** mohsen.asadnia@mq.edu.au

**keywords:** concrete beam, four-point bending test, 3D printing, piezoresistive sensors, health monitoring

## Abstract

Various methods such as fiber optic sensors, acoustic emission techniques, digital image correlation, embedded sensors, and strain gauges are utilized to monitor stress/strain in concrete. The embedded sensors offer advantages of real-time monitoring, high accuracy and sensitivity, and long-term performance data. These sensors can be embedded in concrete to monitor the condition of a section of the concrete at critical points throughout its life cycle. This work presents an innovative approach using a 3D-printed piezoresistive sensor composed of a conductive thermoplastic polyurethane filament to monitor strain within a concrete sample under four-point loading conditions. The performance of the sensor at different locations, temperature and humidity within the concrete was studied. The findings demonstrate that the 3D-printed sensor effectively captures strain within concrete samples under cyclic loading. The sensor's signal output varies between 20% and 120% based on its distance from the crack location, enabling accurate crack position monitoring. Additionally, the sensor's response depends on temperature and humidity, and prior to failure it closely follows a mathematical model based on beam theory, achieving an $R^2$ value greater than 0.94. Furthermore, artificial intelligence-based clustering achieves 98.9% accuracy in identifying crack locations from sensor data, highlighting its potential as a practical tool for structural health monitoring. The results suggest that when the sensor is positioned close to a theoretical crack formation location, a high-confidence signal is obtained.

## 1. Introduction

The integrity and longevity of concrete are critical to modern transportation systems, making structural health monitoring (SHM) an essential aspect of civil engineering. In road asset management, SHM plays a pivotal role in improving safety, reducing maintenance costs, and extending the lifespan of concrete. The monitoring of concrete involves the detection of potential failures before they become critical and require costly repairs. Techniques for real-time data acquisition and continuous condition assessment enable the development of proactive maintenance planning strategies, which are far more cost-effective than traditional reactive approaches [1, 2]. Moreover, by preserving the structural health of concrete, SHM contributes significantly to the sustainability of transportation infrastructure like concrete pavements, reducing the need for frequent and unplanned slab replacement and minimizing the environmental impacts of higher greenhouse gas emissions. Thus, the implementation of SHM systems not only enhances durability and safety of roads but also promotes a more sustainable approach to concrete maintenance [3].

Multiple techniques have been developed to monitor the health of concrete, each employing different principles and technologies [4]. Traditional methods, such as visual inspections and core sampling, though straightforward, are labor-intensive and often lack the precision required for early detection of

© 2025 The Author(s). Published by IOP Publishing Ltd

internal defects. In contrast, non-destructive testing methods have gained prominence due to their ability to assess structural integrity without compromising the concrete's condition [5]. Techniques such as ultrasonic pulse velocity [6], ground-penetrating radar [7], and acoustic emission [8] are notable for their efficacy in detecting cracks, voids, and other anomalies. Additionally, high-resolution digital imaging and infrared thermography are used for detailed surface monitoring, enabling the detection of minute deformations and thermal anomalies indicative of underlying structural issues [9]. The diversity of these methods allows engineers to select the most suitable approach based on the specific requirements and conditions of the section of the concrete being monitored. Beyond traditional methods, innovative materials and techniques have been explored to enhance the self-healing capabilities of concrete. For instance, conductive asphalt-based systems leveraging microwave-heating techniques have been developed to promote self-repair at the aggregate-asphalt interface. Recent advancements show that coating aggregate surfaces with carbon nanotube–polymer nanocomposites enables efficient microwave heating, improving crack healing rates while maintaining the mechanical integrity of the concrete [10]. Similarly, incorporating basic oxygen furnace slag (BOFS) as a reinforcing material in asphalt mixtures has demonstrated improvements in mechanical strength and interfacial bonding, reducing the risk of premature failure. Studies indicate that BOFS-enhanced asphalt mixtures exhibit improved tensile strength, fracture resistance, and adhesion properties due to their rough surface texture and high chemical reactivity [11].

Embedded sensors represent a revolutionary advancement in the field of SHM, offering real-time data acquisition and effective internal defect identification of concrete [12]. Embedded sensors used for stress monitoring in concrete include piezoelectric sensors [13, 14], piezoresistive sensors [15, 16], and fiber optic sensors [17, 18]. Piezoelectric sensors generate an alternating current when subjected to mechanical stress, due to changes in their resistance. In contrast, fiber optic sensors measure mechanical stress by analyzing wavelength interrogation and intensity modulation [19]. Piezoelectric and piezoresistive sensors are more cost-effective options as compared to fiber optic sensors, as fiber optic sensors have significantly higher costs. Piezoresistive sensors offer several advantages over piezoelectric sensors when used as embedded sensors for SHM. They are capable of measuring static or low-frequency strain, making them suitable for long-term continuous monitoring, whereas piezoelectric sensors are more sensitive to dynamic or high-frequency signals and cannot measure static strain [20]. The advent of 3D printing technology has further enhanced the capabilities of these sensors. 3D-printed sensors, designed with custom geometries and materials tailored to specific monitoring needs, can be produced rapidly and cost-effectively [21–24].

Despite the advancements in concrete SHM techniques, significant gaps remain, particularly in the areas of early detection capabilities and long-term sensor durability under harsh environmental conditions. Current methods often struggle to identify subtle changes in structural integrity before they evolve into serious problems, limiting the potential for preventive interventions. Additionally, many sensors still suffer from issues related to long-term stability and reliability, which can compromise data accuracy over time. In our previous work [25], we optimized 3D printing parameters using an artificial neural network (ANN) coupled with a genetic algorithm. This work aims to address these challenges by developing an advanced SHM system that integrates newly designed 3D-printed piezoresistive sensors with enhanced sensitivity and durability. Additionally, it provides an analytical study of stress within concrete, mapping the stress distribution on the sensor at different positions. These sensors are engineered to detect minute structural changes at an early stage, and their robust construction is tailored to withstand the rigorous conditions typical of concrete infrastructure. The aim of this research is to validate the effectiveness of these sensors through extensive testing under various stress conditions and to demonstrate their potential in improving the predictive maintenance capabilities of SHM systems.

## 2. Experimental study

### 2.1. Fabrication of a 3D-printed piezoresistive sensor

A piezoresistive sensor was developed through 3D printing using conductive thermoplastic polyurethane (PE-ETPU 95–250). The printing parameters were set, as summarized in table 1. These parameters were determined through a systematic previous study [25] to achieve the highest sensitivity for the piezoresistive sensor. The CAD design of the sensor is depicted in figure 1. The sensor's geometry was

**Table 1.** 3D printing parameters of the piezoresistive sensor.

| Parameter | Unit | Value |
|---|---|---|
| First layer height | mm | 0.40 |
| Layer height | mm | 0.40 |
| Printing speed | mm $s^{-1}$ | 40 |
| Printing temperature | °C | 220 |
| Platform temperature | °C | 100 |
| Shell count | — | 5 |
| Infill angle | degree | 90 |
| Fill density | % | 100 |
| Overlap perimeter | % | 15 |

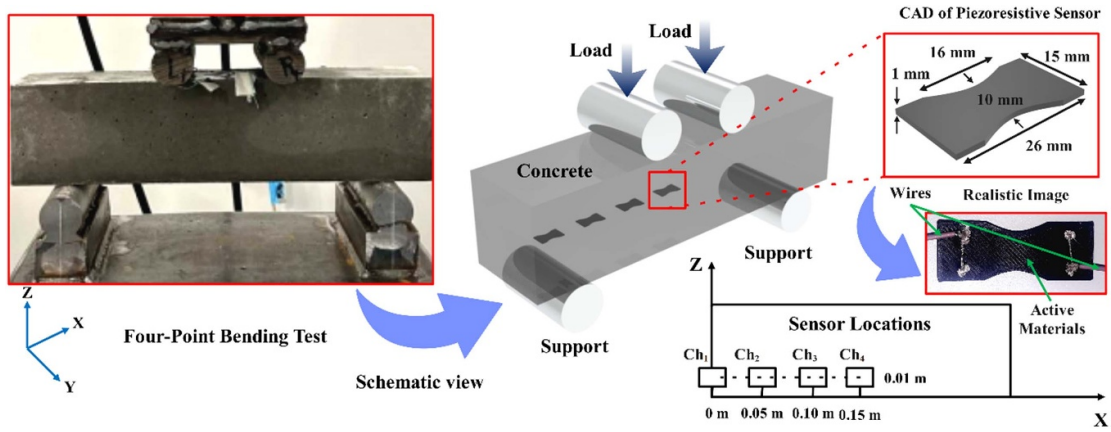


**Figure 1.** Four-point bending fixture (left side of the figure), and the schematic illustration of sensor locations within concrete sample and CAD design of 3D printed piezoresistive sensor (right side of the figure).

designed such that slippage was prevented. Electrodes were attached to the sensor by punching through the sensor, connecting the wires, and then using silver paste to ensure a reliable electrical connection.

### 2.2. Preparation of concrete samples and sensor embedment

The reliability of a concrete mix is crucial in measuring its mechanical properties. The composition and ratios of the materials in the concrete mix directly influence how the material perform under flexural stresses. For this study, an 80% ordinary Portland cement and 20% fly ash concrete mix, listed in the Transport for NSW (TfNSW) approved concrete mix register [26] and meeting the TfNSW R83 specification requirements, was used to prepare sample beams for embedding sensors. After preparing the piezoresistive sensors and the concrete mix, four different locations were selected to place the sensors during the casting of the concrete mix into molds. Channel 1 corresponds to the sensor positioned at the left support (reference point) at a height of 0.01 m from the bottom of the span. Channels 2, 3, and 4 were then positioned 0.05 m, 0.10 m, and 0.15 m away from the reference point, respectively, all at the same height from the bottom of the span (0.01 m). The concrete beams were cast using steel molds measuring 400 mm in length, 100 mm in depth, and 100 mm in width. All samples were cured by submerging them in water for a period of 28 d. Figure 1 schematically demonstrates the locations of the sensors within concrete samples.

To justify the sensor locations, it is important to note that the sensors are strain sensors, and analytically, the strain experienced by the sensor increases with distance from the neutral plane in the height direction of the beam. To ensure the sensor remains securely embedded in the concrete beam, it was placed 0.01 m from the bottom surface, which experiences tensile stress. The chosen distances in the length direction (0, 0.05, 0.10, and 0.15 m) will be validated using the theoretical model proposed in this study, which predicts maximum stress accumulation at the load application points in the four-point

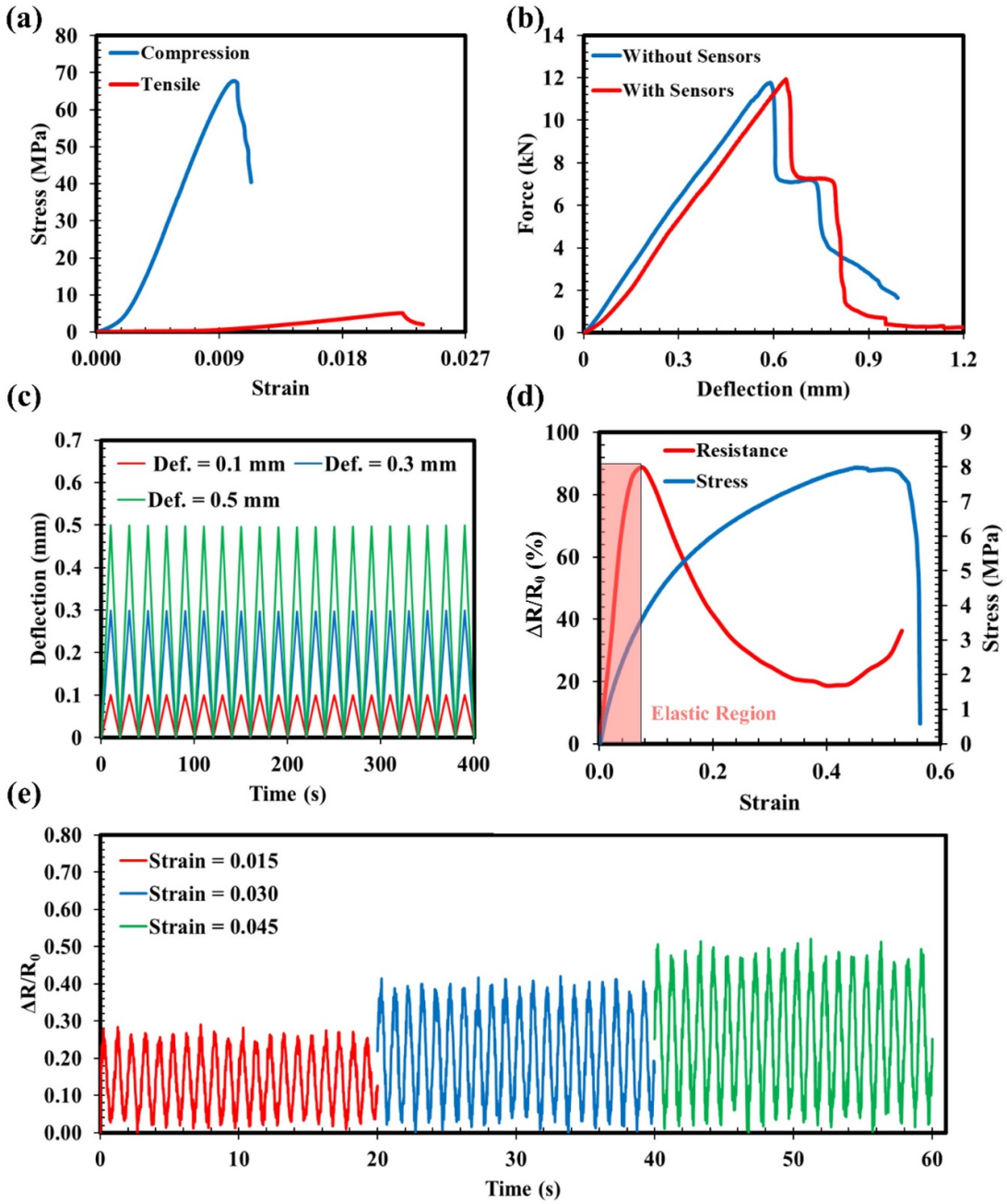


**Figure 2.** (a) Compression and tensile behavior of concrete samples without a sensor, (b) bending behavior of concrete sample with and without sensors under four-point bending test, (c) displacement controlled cyclic loading with deflections ranging between 0.1 mm and 0.5 mm with a frequency of 0.05 Hz (d) electromechanical behavior of 3D-printed piezoresistive sensor under quasi–static tensile loading condition, and (e) stability test for 3D printed piezoresistive sensor under different strains.

bending test. These various sensor positions will also help identify crack locations at different points along the concrete beam.

### 2.3. Four-point bending characterization of the concrete beam

The concrete trial mix and experimentation strictly followed the guidelines of Australian Standards (AS), including the preparation of the concrete mix (AS 1012.2), compressive strength test (AS 1012.9), indirect tensile strength test (AS 1012.10), and flexural modulus test (AS 1012.11). The concrete behavior under a quasi–static four-point bending test, detailed in figures 2(a) and (b), conforms to TfNSW R83 specification. Additionally, a cyclic four-point bending test with deflections ranging between 0.1 mm and 0.5 mm at a frequency of 0.05 Hz for 400 s was performed as shown in figure 2(c).

### 2.4. Electromechanical characterization of piezoresistive sensor

A quasi–static tensile test was employed to evaluate the electromechanical properties of the 3D printed piezoresistive sensor. The sensor was strained at a crosshead speed of 1 mm $s^{-1}$ under environmental conditions of 25 °C and 60% relative humidity (RH). To measure resistance changes, a digital multimeter (Keysight E4980 AL) was used. A crucial parameter in piezoresistive sensors is the gauge factor (GF), which measures sensitivity to deformation by indicating the ratio of the change in electrical resistance to the applied mechanical strain. The GF of the sensor before embedding within the sample was determined using equation (1) [27], as detailed below:

$$\mathrm{GF}_{\mathrm{Free}} = \frac{\Delta R/R_0}{\Delta L/L_0} \tag{1}$$

where $R$ and $L$ are the resistance and length of the piezoresistive sensor, respectively. The characterization indicated that the 3D-printed sensor had a tensile modulus of 46 MPa and a GF of 12.5 as shown in figure 2(d). The cyclic tensile loading conditions of the 3D-printed sensor demonstrated a stable signal across various strains in the elastic region as shown in figure 2(e).

### 2.5. Health monitoring of concrete beam

To monitor the structural health of the concrete beam, a Wheatstone bridge was employed for each sensor to measure the output voltage using an analog-to-digital converter (National Instruments NI 9239 cDAQ). The input voltage for all Wheatstone bridges was set to 12 V, with three resistors, each having a value of 5 kΩ.

## 3. Theoretical study of strains acting on the sensor within concrete

When a sensor is embedded within concrete, it is subjected to complex loading conditions that are different from the uniaxial tensile mode typically employed to characterize the sensor. Such characterization may not be representative of stress monitoring in practical applications where sensors are subjected to multi-directional stresses. To resolve this issue, we have incorporated the fundamental principles of bending to more accurately simulate these conditions. Under four-point bending conditions, it is realistic to assume that both normal and shear stresses influence the sensor as the concrete deflects [28]:

$$\frac{\Delta R(x,z)}{R} = \mathrm{GF}\left(\varepsilon_{11}(x,z) + \gamma_{21}(x,z)\right). \tag{2}$$

The magnitude of both normal ($\varepsilon_{11}$) and shear ($\gamma_{21}$) strains experienced by the sensors depends on the sensor's location within the concrete sample. It should be noted that $x$ represents the length direction, while $z$ denotes the height direction, as shown in figure 1. It is assumed that the normal and shear strains are independent of the sensor's location in the width direction ($y$) within the concrete sample. The strains applied to the sensor are equal to the strains occurring in the concrete sample to avoid any disruptions at the interfaces. Assuming a linear and elastic behavior for the concrete [29], we have:

$$\varepsilon_{11}(x,z) = \frac{\sigma_{11}(x,z)}{E} \tag{3}$$

where $\sigma_{11}$ represents the normal stress and $E$ denotes Young's modulus, respectively. The normal stress can be expressed as a function of the applied bending moment ($M$), the distance from the neutral plane ($z_n$), and the second moment of area ($I$) [29]:

$$\sigma_{11}(x,z) = -\frac{M(x)(z-z_n)}{I} \tag{4}$$

in which

$$M(x) = \sum_{i=1}^{2} M_i(x) = M_1(x) + M_2(x) \tag{5}$$

$$M_1(x) = \begin{cases} \frac{P}{2}x & 0 \leqslant x \leqslant L/3 \\ \frac{P}{4}(L-x) & L/3 \leqslant x \leqslant L \end{cases} \tag{6}$$

$$M_2(x) = \begin{cases} \frac{P}{4}x & 0 \leqslant x \leqslant 2L/3 \\ \frac{P}{2}(L-x) & 2L/3 \leqslant x \leqslant L \end{cases} \tag{7}$$

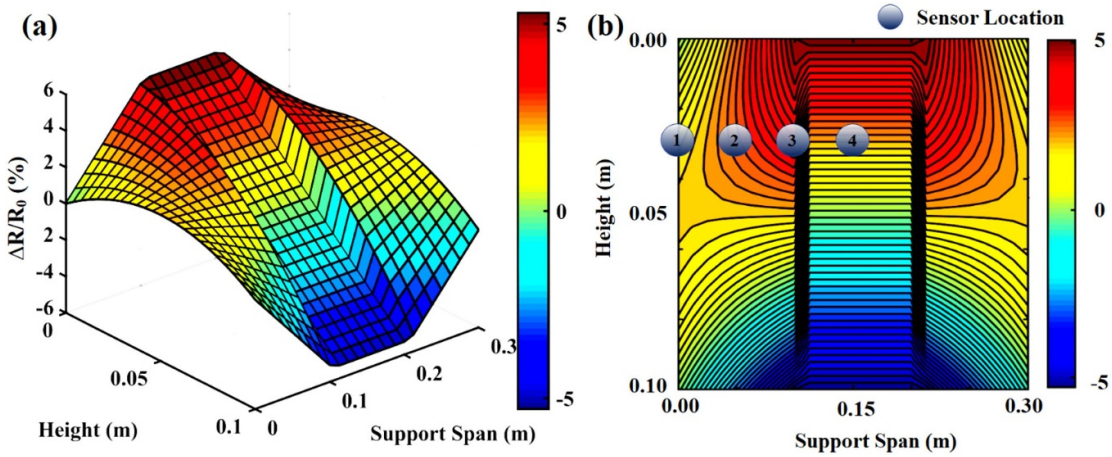


**Figure 3.** Theoretical computations for (a) 3D plot showing the relative resistance change of a 3D-printed sensor as a function of height and length coordinates within concrete, and (b) 2D projection of the relative resistance change for four sensors positioned within concrete, using 3D printing technology.

$$I = \frac{1}{12} w h^3 \tag{8}$$

where $M_1$ and $M_2$ are moments due to the forces applied at different points under the four-point bending. The parameter $P$ represents the force, and $L$ is the total length of the concrete sample, which is 300 mm. The width and depth of the concrete sample are 100 mm each, denoted by $w$ and $h$ respectively. Similarly, the shear stress can be expressed based on elastic theory [29] as follows:

$$\gamma_{21}(x,z) = \frac{\tau_{21}(x,z)}{G} \tag{9}$$

where $\tau_{21}$ represents the shear stress and $G$ denotes shear modulus, respectively. To determine the shear stress as a function of the shear force ($S$) [29], we have,

$$\tau_{21}(x,z) = \frac{S(x)}{2I}\left(\frac{h^2}{4} - (z - z_n)^2\right). \tag{10}$$

In which

$$S(x) = \begin{cases} \frac{P}{2} & 0 \leqslant x \leqslant L/3 \\ 0 & L/3 \leqslant x \leqslant 2L/3 \\ -\frac{P}{2} & 2L/3 \leqslant x \leqslant L \end{cases} \tag{11}$$

$$G = \frac{E}{2(1+\nu)} \tag{12}$$

where $\nu$ is Poisson's ratio of the concrete. Using MATLAB software, equation (2) can be computed and plotted as shown in figure 3(a). As is evident, the relative resistance changes of the sensor increase when it is positioned closer to the points where forces are applied (0.10 and 0.20 m from the left support). Conversely, as the distance from the left support decreases, the relative resistance change of the sensor also decreases. In figure 3(b), a 2D projection of the relative resistance changes for four sensors embedded within concrete is depicted.

It can be observed that the sensor at location 3 experiences the highest relative resistance change, while the lowest change is observed at location 1. The relative resistance changes at locations 2 and 4 are nearly identical. This theoretical analysis offers a physical understanding of the strains experienced by sensors when concrete is subjected to a four-point bending test.

## 4. Results and discussions

### 4.1. Response of the sensors under four-point bending tests

Figure 4 illustrates the responses of sensors embedded at various distances from the left support under a quasi–static four-point bending test. Before the failure of concrete, without exception, the sensor positioned at 100 mm ($Ch_3$) exhibited the highest relative resistance change, while the sensor at 0 mm ($Ch_1$)

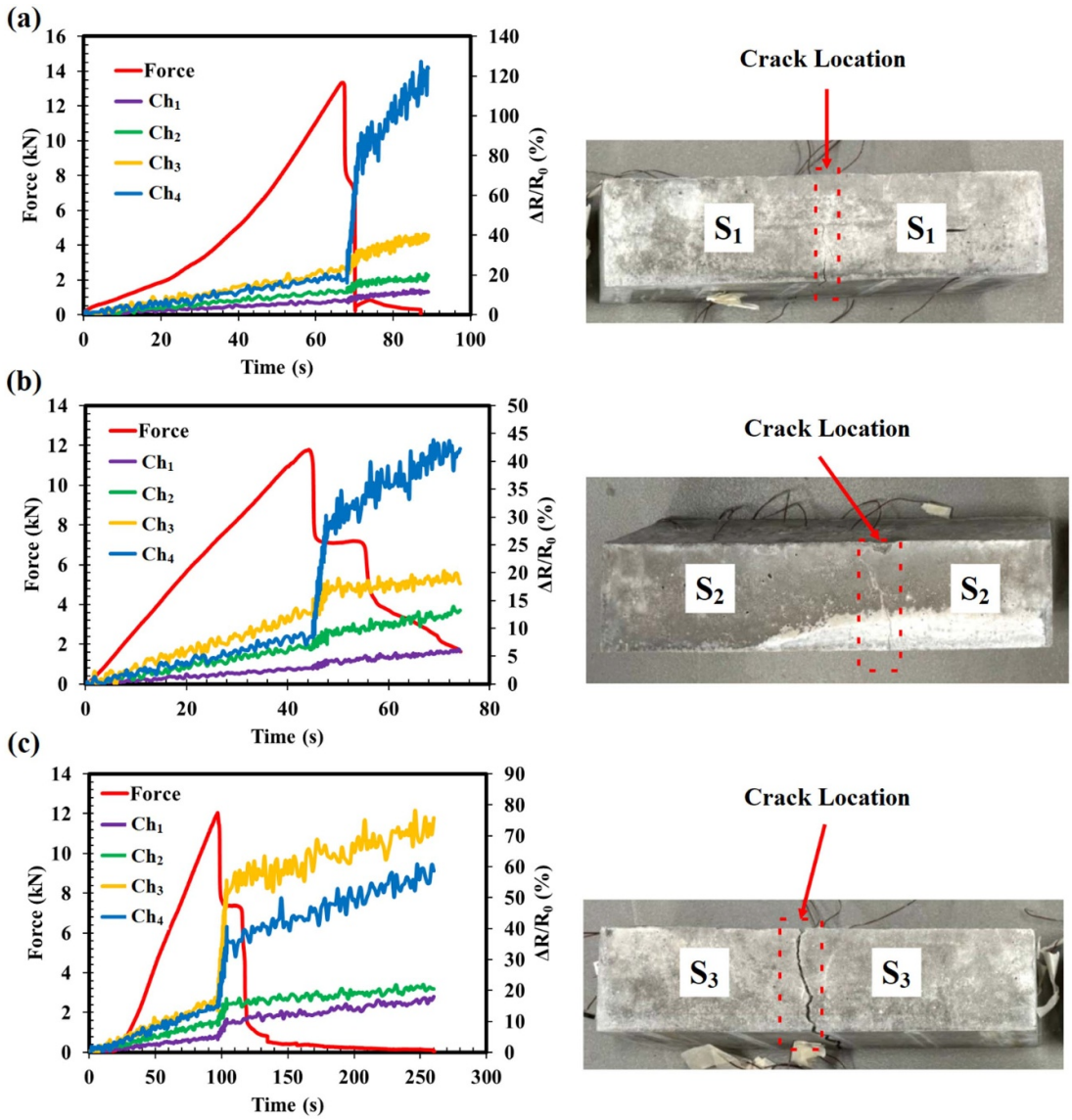


**Figure 4.** Sensor behavior in different locations before and after crack formation in various positions, (a) at middle position, (b) at right side position, and (c) at left side position (the left column displays the sensor behavior and force applied during the four-point bending test, and the right column displays the associated sample).

showed the lowest. These results are attributable to the strains acting on the embedded sensors within the concrete. According to the theoretical study, the sensor at 100 mm experienced the highest normal and shear strains. Consequently, this sensor underwent more deformation, resulting in a higher relative resistance change. In contrast, the sensor at 0 mm was predominantly subjected to shear strain, leading to the lowest relative resistance change. The sensor at 50 mm experienced the lowest normal strain compared to $Ch_3$, with nearly the same shear strain. Meanwhile, the sensor at 150 mm was under normal strain.

When failure occurred, three scenarios of crack formation were possible: at the middle (as shown in figure 4(a)), on the right side (as shown in figure 4(b)), and on the left side (as shown in figure 4(c)). The failure behavior led to different sensor responses due to their arrangement from the left to the middle direction. When the crack was in the middle, it was close to $Ch_4$. As the crack began to open, the sensor at 150 mm experienced the highest strain, causing $Ch_4$ to trigger a crack formation alarm. The same behavior was observed when the crack formed on the right side. However, if the crack occurred on the left side, the response of $Ch_3$ dominated over $Ch_4$. This dominance of $Ch_3$ was attributable to its proximity to the crack location and the highest normal and shear strains acting on it.

Figure 5 presents the responses of $Ch_3$ under a dynamic four-point bending test with varying deflections at a frequency of 0.05 Hz. The sensor effectively captured the strains within the concrete under cyclic loading conditions, with its response increasing from 14.8% to 23.9% as the deflection increased

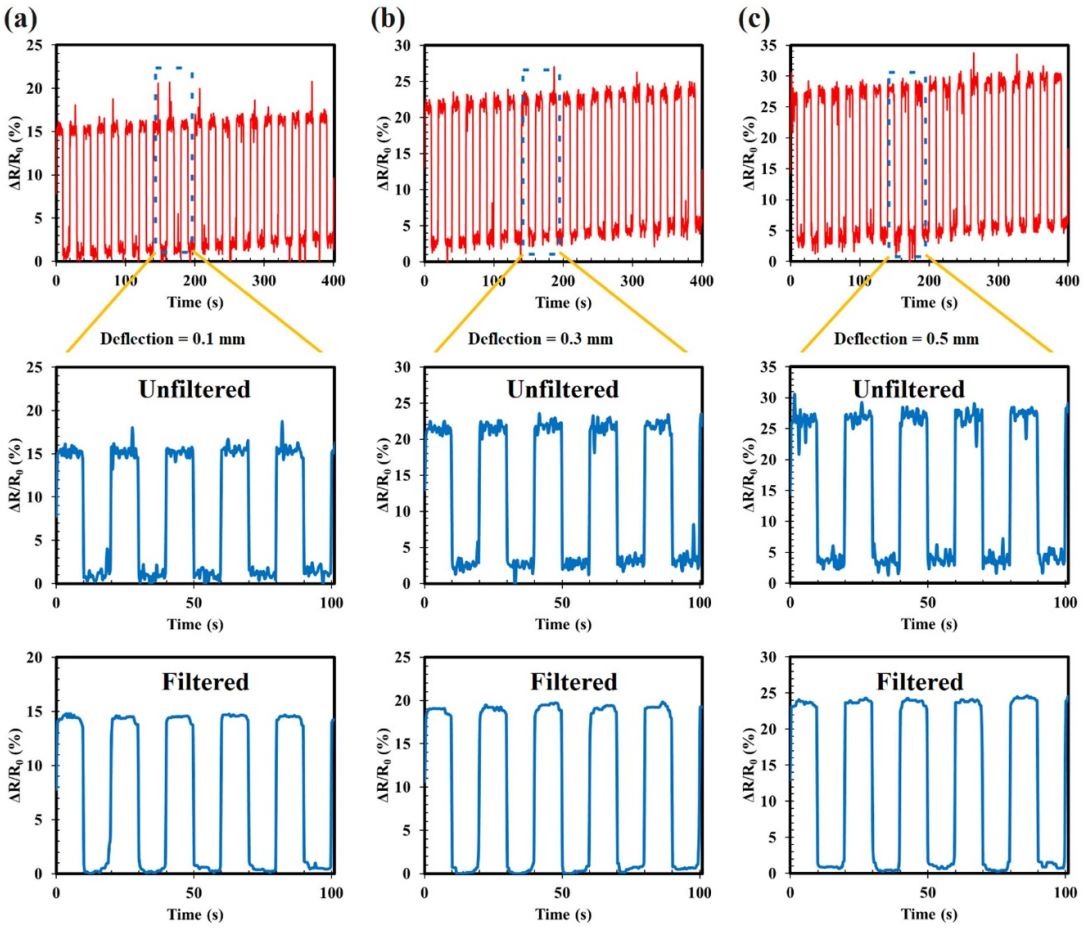


**Figure 5.** Relative resistance changes of the $Ch_3$ sensor with a concrete deflection ranging from 0.05 mm to (a) a maximum deflection of 0.1 mm, (b) a maximum deflection of 0.3 mm, and (c) a maximum deflection of 0.5 mm at a frequency of 0.05 Hz.

from 0.1 mm to 0.5 mm. However, the sensor exhibited hysteresis, suggesting that the conductive TPU exhibits viscoelastic properties, resulting in temporary hysteresis. This behavior indicates that the response of the material to strain is time-dependent, with internal molecular rearrangements causing a lag between the applied strain and the sensor's resistance change [30]. By applying appropriate filtering, the hysteresis effect and noise can be eliminated for stress monitoring purposes.

In practice, the resistance value of the developed sensor should be mapped to the deflection value. Thus, based on the results in figure 5, the GF for the embedded 3D-printed sensor can be defined as follows:

$$\mathrm{GF}_{\mathrm{embedded}} = \frac{\Delta R/R_0}{d} \times 100 \tag{13}$$

where $d$ is the maximum deflection. Figure 6(a) illustrates the relative resistance variations of the embedded 3D-printed sensor concerning maximum deflection and estimates GF as 0.6171 $\mathrm{mm}^{-1}$, based on the $Ch_3$ sensor output presented in figures 5(a)–(c). The error bars represent variations in GF among the three tested sensors, likely due to fabrication or embedding differences. Despite minor variability, the sensor demonstrates high sensitivity (slope = 61.71), making it effective for SHM.

To investigate the sensor response under different thermal conditions, concrete samples with an embedded sensor at the mid-span location ($channel_4$) were pre-conditioned in an environmental chamber prior to the quasi–static four-point bending test (figure 6(b)). At a constant RH of 10%, the resistance change ($\Delta R/R_0$) exhibited a strong dependence on temperature. At 25 °C, the response remained relatively stable with only moderate fluctuations, whereas at elevated temperatures of 45 °C and 65 °C, $\Delta R/R_0$ increased steeply over time. This pronounced rise can be attributed to two coupled mechanisms: (i) thermal expansion of the 3D-printed conductive matrix, which alters the percolation network of conductive fillers, and (ii) enhanced carrier mobility at higher temperatures, leading to greater modulation of electrical resistance [31]. Similar temperature-induced weakening mechanisms have been observed

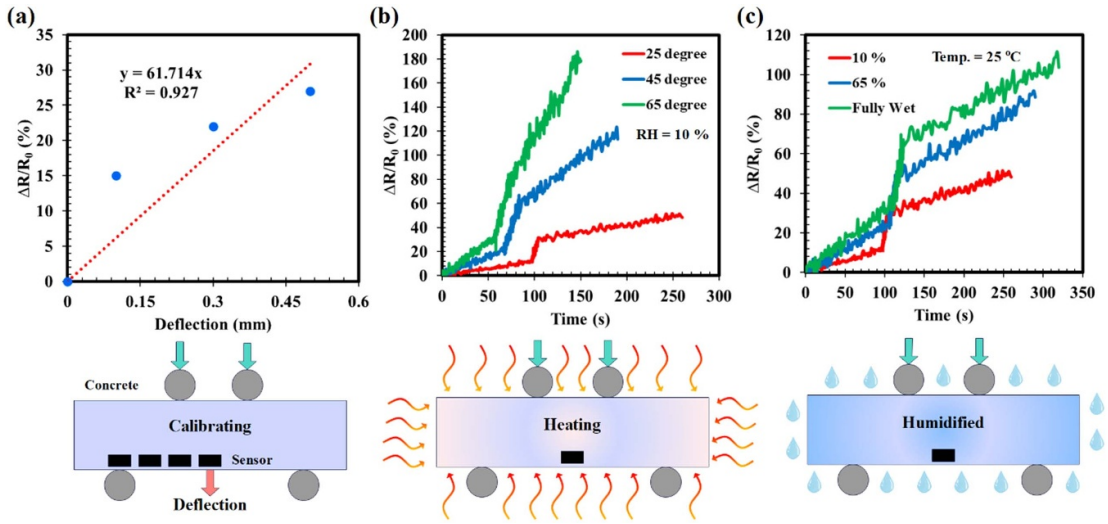


**Figure 6.** (a) Relative resistance change ($\Delta R/R_0$) of the embedded 3D-printed sensor as a function of maximum deflection. The linear fit (red dotted line) yields a gauge factor (GF) of 61.71%mm$^{-1}$, with an $R^2$ value of 0.927, (b) channel$_4$ response under different temperatures and (c) channel$_3$ response under different humidities.

in cementitious composites, where higher thermal loads accelerate hydration heterogeneity, coarsen pore structure, and promote microcracking [32, 33]. The combined effects highlight the sensor's strong thermal sensitivity, indicating its potential to serve as a self-reporting temperature probe when embedded in structural materials. Furthermore, increasing temperature not only amplified the sensor signal but also accelerated deterioration of the concrete matrix. At higher thermal loads, microcracking and early softening of the cementitious binder occurred due to differential thermal expansion of the composite phases [33].

A parallel evaluation was conducted under different humidity conditions to assess the environmental responsiveness of the embedded sensor (figure 6(c)). At a constant temperature of 25 °C, the sensor exhibited distinct resistance responses as a function of RH. At 10% RH, $\Delta R/R_0$ remained modest and stable, reflecting minimal water adsorption within the printed sensing matrix. In contrast, at 65% RH and under fully wet conditions, $\Delta R/R_0$ increased sharply with time. This enhanced sensitivity is attributed to moisture absorption by the polymer matrix, which induces volumetric swelling and disrupts conductive networks, thereby hindering charge transport and elevating resistance [34]. Analogous humidity effects have been reported in concrete systems, where increased RH softens the cementitious paste, retards crack propagation, and alters fracture mode from brittle to more ductile behavior [35]. At very high moisture levels, pore filling and swelling further accelerate mechanical property degradation by inducing microstructural rearrangements and microcracking [36]. Interestingly, the host concrete's mechanical performance was also influenced by humidity. At higher RH, failure was delayed compared to low-humidity conditions, consistent with prior studies that highlighted the lubricating effect of absorbed water in microcracks and its ability to redistribute stress more evenly within the matrix. At lower RH, incomplete hydration and pore desaturation reduced strength development and fracture toughness [35]. Together, these results indicate that the embedded sensor not only functions as a humidity monitor capable of detecting early-stage deterioration but also reflects broader environmental influences on the mechanical integrity of concrete structures [32, 36].

### 4.2. Validation of proposed theoretical model

To validate the proposed theoretical model, equation (2) has been modified with experimental constants, as follows:

$$\frac{\Delta R(x,z)}{R} = \mathrm{GF}\left(A\varepsilon_{11}(x,z) + B\gamma_{21}(x,z)\right). \tag{14}$$

In equation (14), the GF value of 12.51 for the 3D-printed piezoresistive sensor was previously determined through a uniaxial test.

Normal and shear strains are calculated theoretically. To obtain the values of $A$ and $B$, a comparison between experimental and theoretical relative resistance changes is made. The fitting results, as shown in figures 7(a)–(c) for three samples, suggested constant values of $A = 10.58$ and $B = 2.59$. Using these

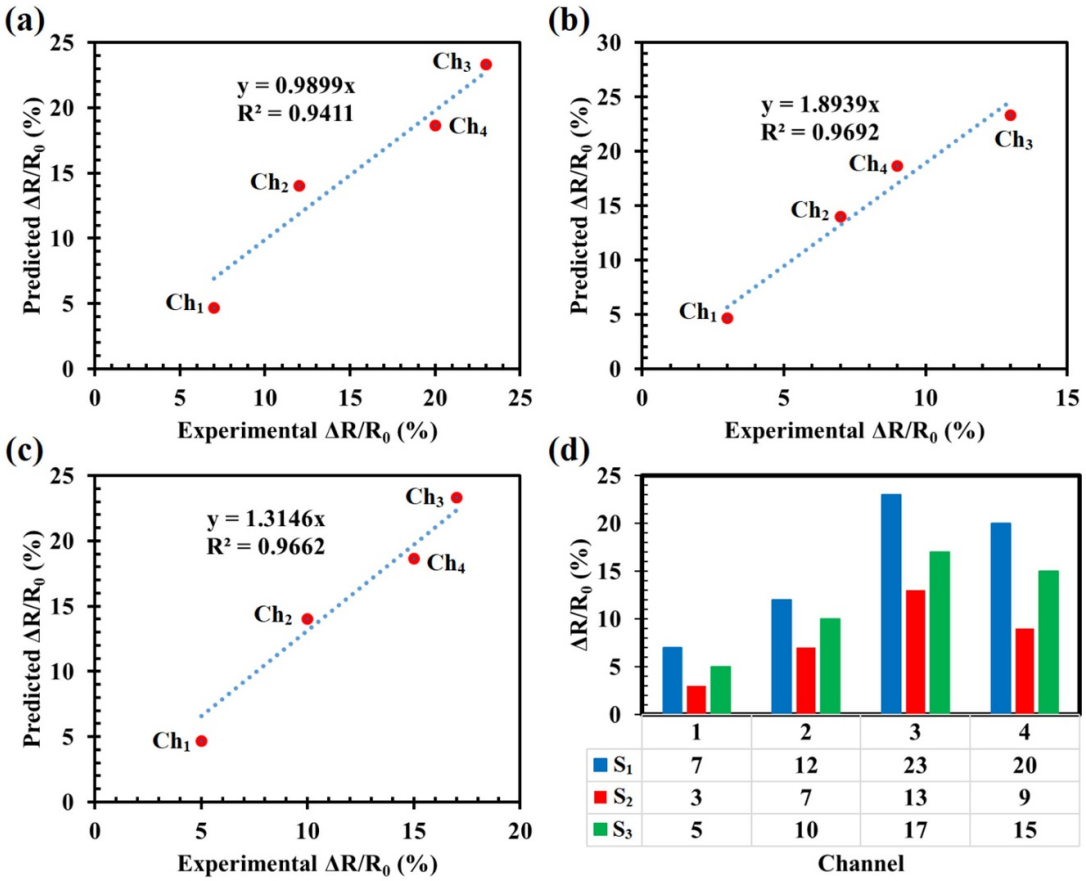


**Figure 7.** Comparison of experimental and predicted values of relative resistance change in various sensors (a) sample $S_1$, (b) sample $S_2$, and (c) sample $S_3$, and (d) experimental value of relative resistance change for different channels in various samples.

constants, the sensor's response, as given in figure 7(d), can be accurately predicted. Even though the constant values are not equal to 1, it effectively predicts sensor behavior at various locations and offers valuable physical insights into the strains within the concrete sample.

Calibrating the embedded piezoresistive sensor is particularly challenging due to the complex loading conditions within concrete, which differ significantly from conventional characterization methods. The theoretical model deployed here only offers mechanical insights. It has also been demonstrated that artificial intelligence (AI), especially ANNs, can be applied for calibration purposes [37, 38]. Recent studies [39, 40] have demonstrated the efficiency of ANNs for prediction tasks. Besides, signals obtained from four embedded sensors in a concrete beam vary depending on the location of cracks. The signal features can be clustered using AI to identify various crack locations. We used signals from four sensors ($Ch_1$–$Ch_4$) to determine crack locations. As shown in figure 8, the sensors monitored stress in four positions within the concrete, resulting in a dataset of 891 pairs. These data points were categorized into three crack locations including left, middle, and right positions. The dataset was processed through a fully connected feed-forward neural network in MATLAB, using a tangent sigmoid activation function for the hidden layers and a softmax activation function for the output layer. Optimization was carried out using the scaled conjugate gradient method. The network architecture consisted of three hidden layers with 30, 23, and 8 neurons, respectively.

The number of neurons and hidden layers was determined through a trial-and-error method. K-fold cross-validation was used, and the model's average accuracy based on the confusion matrix was found to be 99%. This result highlights the sensor reliability in practical applications, particularly for detecting cracks in SHM of the concrete beam. To demonstrate the novelty of this work in terms of the GF, the results of the current study and previous works are summarized in table 2. As shown, the current work outperforms previous studies in terms of GF (0.6171 $mm^{-1}$), which ensures a high signal-to-noise ratio during health monitoring.

Overall, the results indicate that the 3D-printed sensor made from conductive TPU, integrated with an AI model, is suitable for detecting stress and failures in buildings under bending loads. Like most

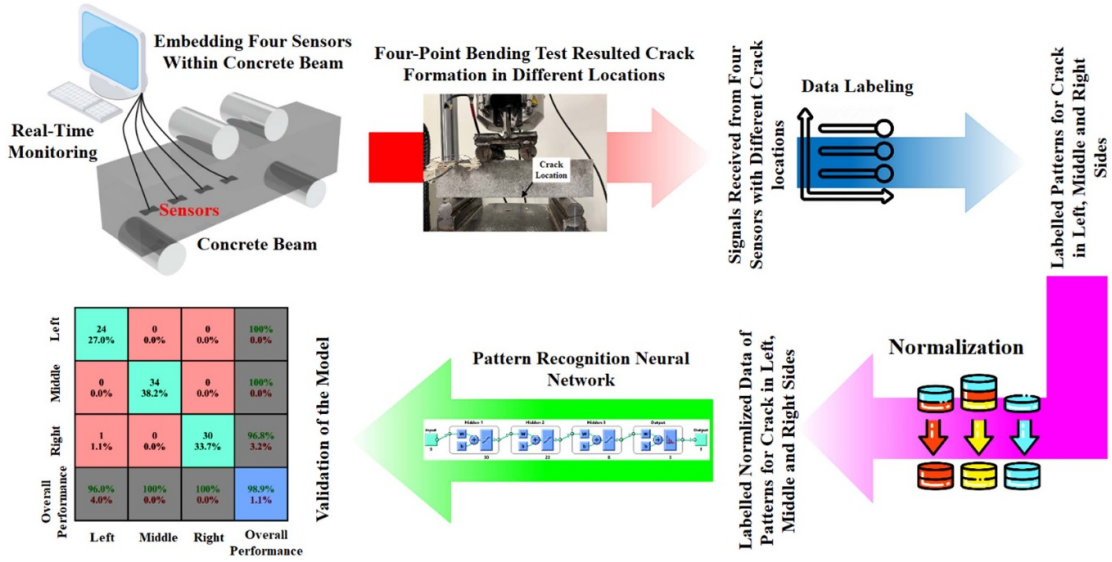


**Figure 8.** Utilizing sensor output data in conjunction with machine learning algorithms to identify the location of crack in the concrete beam.

**Table 2.** Comparison of the results of the current work and previous studies.

| Materials | Self-sensing | Deflection (mm) | Gauge factor ($mm^{-1}$) | References |
|---|---|---|---|---|
| Carbon fiber-reinforced epoxy | Yes | 5.25 | 0.0124 | [41] |
| Carbon fiber-reinforced Portland cement | Yes | 0.09 | 0.0356 | [42] |
| This work | No (embedded) | 0.50 | 0.6171 | — |

polymer nanocomposites, conductive TPU is also sensitive to temperature and humidity in addition to deformation. This property can be leveraged to develop an enhanced model with additional features, improving the accuracy and precision of SHM.

In real-world applications, buildings are exposed to varying temperature and humidity conditions. However, this study was conducted at room temperature (25 °C) with 50% humidity, which limits the applicability of the developed model. To generalize the AI model, additional data from four-point bending tests under different environmental conditions should be collected and incorporated into future updates.

In addition to the effects of temperature and humidity, the long-term durability of the conductive TPU-based sensor is a critical consideration for real-world SHM applications. TPU, widely used in fused filament fabrication due to its flexibility and resilience, is recognized in the literature as one of the primary smart materials suitable for additive manufacturing in construction environments. TPU-based components generally exhibit strong resistance to mechanical fatigue, enabling their use in dynamic and cyclic loading scenarios. However, their long-term behavior, especially that of conductive TPU under extreme environmental exposure such as freeze–thaw cycles, chemical ingress, and sustained moisture, remains less extensively documented compared to conventional cementitious sensors.

Recent reviews on adaptive smart materials highlight that smart polymers integrated into construction systems must be evaluated for environmental durability when exposed to temperature fluctuations, humidity variations, and chemical deterioration mechanisms typical of concrete infrastructure [43]. Although TPU demonstrates promising elasticity and toughness, further experimental work is required to assess potential degradation mechanisms such as hydrolytic softening or stiffness loss under repeated freeze–thaw cycling.

Given this context, the present study acknowledges that while the TPU-based piezoresistive sensor demonstrated stable electromechanical performance under the tested conditions, its long-term environmental resistance has not yet been experimentally validated. Future work should therefore include systematic durability testing, specifically freeze–thaw exposure, chemical soaking (e.g., chlorides, sulfates, carbonation environments), and long-term cyclic humidity and temperature conditioning, to more comprehensively assess sensor reliability over the full-service life of concrete structures. Incorporating these tests will not only strengthen the practical deployment prospects of the sensor but will also align with current trends in smart construction materials research, which emphasize multifunctionality coupled with robust durability under harsh environmental conditions.

## 5. Conclusion

This study presents a successful application of a health monitoring method for concrete beams using 3D-printed piezoresistive sensors based on conductive TPU. A series of four-point bending tests, including both quasi–static and dynamic loading, were conducted to demonstrate the sensor's capability for health monitoring at various locations and its effectiveness in monitoring cyclic loading conditions. Additionally, a theoretical model was developed and shown to be an effective tool for predicting the normal and shear strains experienced by the sensor. The integration of AI further enabled the identification of crack locations through reliable sensor signals. The key findings of this study are summarized as follows:

- Theoretical analysis indicates that the force application points in the four-point bending test experience higher stress than other locations due to maximized normal and shear stresses. Signals from 3D-printed piezoresistive sensors placed at different locations confirmed this finding before crack formation.
- When cracks form and propagate, the signal from a sensor closer to the crack site is significantly stronger, making it easier to pinpoint the crack location. These strong signals can be used to train an AI model, enabling accurate crack detection and enhancing safety monitoring and early detection.
- Unlike piezoelectric sensors, which can only detect dynamic loading, the 3D-printed piezoresistive sensors can detect both dynamic and quasi–static loading, offering an excellent signal-to-noise ratio, making it highly suitable for health monitoring applications.
- The sensitivity of the proposed 3D-printed piezoresistive sensors to temperature and humidity can serve as additional information when concrete is subjected to bending loading conditions, and further studies on long-term durability under freeze-thaw and chemical exposure are needed to ensure reliable field performance.

Future studies could explore the effects of temperature and humidity on sensor signals during four-point bending tests to better simulate real-world conditions. Additionally, applying various loading conditions to concrete structures could further investigate the sensors' performance in different environments.

## Data availability statement

The underlying data from this study cannot be made publicly available because they were generated in collaboration with Transport for NSW, and are subject to confidentiality agreements and data-sharing restrictions imposed by the partner. The data that support the findings are available from the corresponding authors upon reasonable request, subject to approval from Transport for NSW.

## Conflict of interest

The authors declare that there is no conflict of interest regarding the publication of this article.

## Credit author statement

**Milad Razbin:** Methodology, Conceptualization, Formal analysis, Visualization, Hard computation, Writing original draft. **Sajad A. Moshizi**: Methodology, Formal analysis, Writing original draft. **Hossein Asadi:** Conceptualization, Supervision, Writing–Reviewing and Editing. **Basil Ben:** Conceptualization,

Supervision, Writing–Reviewing and Editing. **Harish Srivastava:** Conceptualization, Methodology, Supervision, Writing–Reviewing and Editing. **Golnaz Alipour Esgandani:** Conceptualization, Methodology, Writing–Reviewing and Editing, **Rouzbeh Abbassi:** Conceptualization, Supervision, Methodology, Writing–Reviewing and Editing, **Mohsen Asadnia:** Conceptualization, Supervision, Methodology, Writing–Reviewing and Editing.

## ORCID iDs

Milad Razbin 0000-0002-5409-1476
Sajad Abolpour Moshizi 0000-0001-5445-8883
Golnaz Alipour Esgandani 0000-0001-8370-0667
Rouzbeh Abbassi 0000-0002-9230-6175
Mohsen Asadnia 0000-0003-3157-7796

## References

[1] Peraka N S P and Biligiri K P 2020 Pavement asset management systems and technologies: a review *Autom. Constr.* **119** 103336
[2] Jiang X *et al* 2024 Advancing carbon nanomaterials-engineered self-sensing cement composites for structural health monitoring: a state-of-the-art review *J. Build. Eng.* **87** 109129
[3] Elizondo-Martínez E-J, Andrés-Valeri V-C, Jato-Espino D and Rodriguez-Hernandez J 2020 Review of porous concrete as multi-functional and sustainable pavement *J. Build. Eng.* **27** 100967
[4] Reddy P N, Kavyateja B V and Jindal B B 2021 Structural health monitoring methods, dispersion of fibers, micro and macro structural properties, sensing, and mechanical properties of self-sensing concrete—A review *Struct. Concr.* **22** 793–805
[5] Kot P, Muradov M, Gkantou M, Kamaris G S, Hashim K and Yeboah D 2021 Recent advancements in non-destructive testing techniques for structural health monitoring *Appl. Sci.* **11** 2750
[6] Hong S, Yoon S, Kim J, Lee C, Kim S and Lee Y 2020 Evaluation of condition of concrete structures using ultrasonic pulse velocity method *Appl. Sci.* **10** 706
[7] Alsharqawi M, Dawood T, Abdelkhalek S, Abouhamad M and Zayed T 2022 Condition assessment of concrete-made structures using ground penetrating radar *Autom. Constr.* **144** 104627
[8] Ma G and Du Q 2020 Structural health evaluation of the prestressed concrete using advanced acoustic emission (AE) parameters *Constr. Build. Mater.* **250** 118860
[9] Sendrowicz A, Myhre A O, Wierdak S W and Vinogradov A 2021 Challenges and accomplishments in mechanical testing instrumented by *in situ* techniques: infrared thermography, digital image correlation, and acoustic emission *Appl. Sci.* **11** 6718
[10] Lu D, Jiang X, Leng Z, Zhang S, Huo Y and Zhong J 2025 Targeted and highly effective technique for healing the aggregate-asphalt interface *Colloids Surf. A Physicochem. Eng. Aspect.* **709** 136165
[11] Lei B, Yu L, Chen J, Meng Y, Lu D, Li N and Qu F 2025 Sustainable asphalt mixtures reinforced with basic oxygen furnace steel slag: multi-scale analysis of enhanced interfacial bonding *Case Stud. Constr. Mater.* **22** e04198
[12] Ferreira P M, Machado M A, Carvalho M S and Vidal C 2022 Embedded sensors for structural health monitoring: methodologies and applications review *Sensors* **22** 8320
[13] Gomasa R, Talakokula V, Kalyana Rama Jyosyula S and Bansal T 2023 A review on health monitoring of concrete structures using embedded piezoelectric sensor *Constr. Build. Mater.* **405** 133179
[14] Sha F, Xu D, Cheng X and Huang S 2021 Mechanical sensing properties of embedded smart piezoelectric sensor for structural health monitoring of concrete *Res. Nondestr. Eval.* **32** 88–112
[15] Seo J, Jang D, Yang B, Yoon H N, Jang J G, Park S and Lee H K 2022 Material characterization and piezoresistive sensing capability assessment of thin-walled CNT-embedded ultra-high performance concrete *Cem. Concr. Compos.* **134** 104808
[16] Zhang J, Heath A, Ball R J, Chen B, Tan L, Li G, Pan J, Su-Cadirci T B and Paine K 2024 Piezoresistivity and piezopermittivity of cement-based sensors under quasi-static stress and changing moisture *Constr. Build. Mater.* **425** 136052
[17] Alwis L S, Bremer K and Roth B 2021 Fiber optic sensors embedded in textile-reinforced concrete for smart structural health monitoring: a review *Sensors* **21** 4948
[18] Berrocal C G, Fernandez I and Rempling R 2021 Crack monitoring in reinforced concrete beams by distributed optical fiber sensors *Struct. Infrastruct. Eng.* **17** 124–39
[19] Kazanskiy N L, Khonina S N and Butt M A 2024 A review on flexible wearables-Recent developments in non-invasive continuous health monitoring *Sens. Actuators A* **366** 114993
[20] Tanusha D and Badhulika S 2024 Comparative analysis of micro patterned PDMS-based piezoresistive pressure sensors with multifunctional strain and health monitoring applications *Sens. Actuators A* **369** 115139
[21] Zhang X *et al* 2024 Distributed fiber optic sensors for tunnel monitoring: a state-of-the-art review *J. Rock Mech. Geotech. Eng.* **16** 3841–63
[22] Teng F, Luo J, Gao Y, Zhou X, Zhang J, Gao S and Sun S 2021 Piezoresistive/piezoelectric intrinsic sensing properties of carbon nanotube cement-based smart composite and its electromechanical sensing mechanisms: a review *Nanotechnol. Rev.* **10** 1873–94
[23] Vlachakis C, McAlorum J and Perry M 2022 3D printed cement-based repairs and strain sensors *Autom. Constr.* **137** 104202
[24] Vlachakis C, Perry M, Biondi L and McAlorum J 2020 3D printed temperature-sensing repairs for concrete structures *Addit. Manuf.* **34** 101238
[25] Razbin M *et al* 2025 Application of soft computing techniques in the optimization of 3D-printed piezoresistive sensors *Sens. Actuators A* **385** 116277
[26] Transport for NSW (TfNSW) 2024 *Roads and maritime services, register of concrete mixes* (available at: https://tfnswassets.transport.nsw.gov.au/file-share-rms/conform-conc-mix.pdf)
[27] Vahdani M, Razbin M, Abolpour Moshizi S, Payne D, Huang S, Asadnia M, Peng S and Wu S 2024 Transient piezoresistive strain sensors based on elastic biopolymer thin films *ACS Appl. Polym. Mater.* **6** 6530–9
[28] Doll J C and Pruitt B L 2013 *Piezoresistor Design and Applications* (Springer)
[29] Beer F P *et al* 1992 *Mechanics of Materials* vol 1 (mcgraw-Hill)

[30] Qi H J and Boyce M C 2005 Stress–strain behavior of thermoplastic polyurethanes *Mech. Mater.* **37** 817–39
[31] Verma P, Schiffer A and Kumar S 2021 Thermo-resistive and thermo-piezoresistive sensitivity of carbon nanostructure engineered thermoplastic composites processed via additive manufacturing *Polym. Test.* **93** 106961
[32] Niu X-J, Li Q-B, Liu W-J and Hu Y 2020 Effects of ambient temperature, relative humidity and wind speed on interlayer properties of dam concrete *Constr. Build. Mater.* **260** 119791
[33] Shoukry S N, William G W, Downie B and Riad M Y 2011 Effect of moisture and temperature on the mechanical properties of concrete *Constr. Build. Mater.* **25** 688–96
[34] Vafaiee M, Ejehi F and Mohammadpour R 2023 CNT-PDMS foams as self-powered humidity sensors based on triboelectric nanogenerators driven by finger tapping *Sci. Rep.* **13** 370
[35] Mi Z, Hu Y, Li Q and An Z 2018 Effect of curing humidity on the fracture properties of concrete *Constr. Build. Mater.* **169** 403–13
[36] Du X, Li Z, Han J and Tan C 2020 Effect of different humidity-controlling modes on microstructure and compressive behavior of ordinary concrete *J. Mater. Civil Eng.* **32** 04019337
[37] Mikalef P and Gupta M 2021 Artificial intelligence capability: conceptualization, measurement calibration, and empirical study on its impact on organizational creativity and firm performance *Int. J. Inf. Manage.* **58** 103434
[38] Turkson R F, Yan F, Ali M K A and Hu J 2016 Artificial neural network applications in the calibration of spark-ignition engines: an overview *Eng. Sci. Technol. Int. J.* **19** 1346–59
[39] Darzi A A R, Razbin M, Allahdadi A, Mousavi S M, Taylor R A and Li M 2025 Designing high-efficiency parabolic trough receiver tubes via AI-assisted simulation *Renew. Energy* **251** 123366
[40] Razbin M, Gharehaghaji A A, Salehian M, Zhu Y, Kish M H and Kouchehbaghi N H 2024 Artificial neural network-assisted theoretical model to predict the viscoelastic–plastic tensile behavior of polyamide-6 multi-ply yarns *Neural Comput. Appl.* **36** 18107–23
[41] Wang S and Chung D 2006 Self-sensing of flexural strain and damage in carbon fiber polymer-matrix composite by electrical resistance measurement *Carbon* **44** 2739–51
[42] Wen S and Chung D 2001 Carbon fiber-reinforced cement as a strain-sensing coating *Cem. Concr. Res.* **31** 665–7
[43] Kallayil A, Patadiya J, Kandasubramanian B, Adamtsevich A, Kchaou M and Aldawood F K 2025 Adaptive smart materials in architecture: enhancing durability and sustainability in modern construction *ACS Omega* **10** 22305–22

# Investigating Piezoelectric Sensor Performance for Crack Detection in Concrete Pavements

Sajad A. Moshizi[1] , Milad Razbin[1] , Hossein Asadi[2], Basil Ben[2], Harish Srivastava[2], Golnaz Alipour Esgandani[1], Payam Rahnamayiezekavat[3], Rouzbeh Abbassi[1] , Mohsen Asadnia[1,*]

[1]School of Engineering, Macquarie University, Sydney, NSW, Australia
[2]Transport for NSW (TfNSW), Sydney, NSW, Australia
[3]School of Engineering, Design and Built Environment, Western Sydney University, Sydney, NSW, Australia
*Corresponding author, E-mail address: mohsen.asadnia@mq.edu.au

## Abstract

Crack detection in concrete pavements is crucial for ensuring their structural integrity, safety, and longevity, as undetected cracks can lead to severe deterioration and costly repairs. This study investigates the effectiveness of piezoelectric sensors embedded in concrete beams for crack detection under cyclic and fatigue loading, with a focus on their application in pavement health assessment. Employing lead zirconate titanate (PZT) ceramic sensors sealed with Polydimethylsiloxane (PDMS), four-point bending and cyclic loading tests were conducted using 30-mm and 12-mm sensors. Embedding a 30-mm sensor reduced the flexural strength of the concrete by approximately 9%, whereas the 12-mm sensor had no adverse effect, preserving the original strength of 5.6 ± 0.4 MPa. Under cyclic loading, the 12-mm sensor produced a clear and reliable response with peak-to-peak voltages increasing from 0.1 mV at 0.5 kN/s to 0.35 mV at 2 kN/s, while the 30-mm sensor, despite higher output, exhibited noisier signals requiring filtration. Fatigue experiments demonstrated that the sensors could detect microcrack initiation 7–8 cycles before visible failure, providing an early warning of impending damage. Sensor placement tests confirmed that although voltage output decreased with distance from the crack, detection remained possible even near the supports. Analytical and finite-element modeling further indicated that normal stress predominantly governs sensor response, in close agreement with experimental findings. These quantitative results establish piezoelectric sensors as a practical, cost-effective technology for early crack detection and proactive pavement maintenance.

*Keywords:* Piezoelectric Sensors; Concrete Pavement; Cyclic Loading; Crack Detection; Electromechanical Modelling

## 1. Introduction

Pavements are critical components of transportation infrastructure and need to be maintained and monitored regularly to ensure their functionality and safety. Cracks are a common problem in pavements, and if left untreated, they can lead to more severe damage, reduce the lifespan of the pavement, and increase the risk of accidents [1, 2]. Therefore, timely detection and repair of cracks are essential to maintain the safety and durability of the pavement [3].

In recent years, in-pavement sensor technology has emerged as a promising approach for monitoring pavement health. These systems typically involve embedding strain sensors within the concrete to monitor real-time changes in the strain field. Such changes serve as early indicators of crack initiation and progression, enabling proactive maintenance strategies. Several embedded sensor types are used in concrete structures including voltammetric sensors [4], accelerometers [5], piezoresistive sensors [6, 7], piezoelectric sensors [8, 9], and optical fibre sensors [10]. Although many of these technologies demonstrate potential, they are often hindered by issues related to

durability, complex installation, reliance on external power, or high costs [11-13]. Among available sensor types, piezoelectric sensors are particularly notable for their ability to function simultaneously as both sensors and actuators, as well as their cost-effectiveness compared to other technologies [14, 15]. Based on the material types, piezoelectric sensor can be categorized into polymeric and ceramic based. In the case of polymeric materials, Du et al. embedded polyvinylidene fluoride (PVDF) within concrete-filled steel tubular (CFST) columns. It was shown that a developed sensor is capable of monitoring the internal stress under impact loading conditions [16]. In other work, Shen et al. used PVDF to detect bottom-up cracks of an asphalt concrete pavement subject to dynamic loads. They also carried out finite element analysis and an excellent agreement between simulated and experimental data was found [17].

PZT, or lead zirconate titanate, is a ceramic material commonly used in piezoelectric sensors. PZTs provide various configurations for monitoring concrete structures, including surface-bonded piezo sensors (SBPS) [18, 19], non-bonded piezo sensors (NBPS) [20], and embedded piezo sensors (EPS) [21, 22]. EPS offers several benefits such as protection from environmental factors, long-term stability, and early detection of structural issues over other configurations, i.e., NBPS and SBPS, when it comes to monitoring concrete structures [23]. PZT sensors can be embedded within concrete for structural health monitoring. To ensure durability and maintain signal fidelity, appropriate encapsulation is essential. One effective approach involves using Polydimethylsiloxane (PDMS) as a protective coating. For instance, a recent study demonstrated that PZT sensors encapsulated with PDMS retain accurate strength monitoring capabilities in cementitious materials, showing minimal sensitivity loss and strong correlation with compressive strength during early-age hydration [24]. PDMS has been adopted as a protective encapsulant based on its proven flexibility and durability in PZT composites. Babu and de With demonstrated that 0–3 PDMS–PZT composites retain effective piezoelectric behaviour while offering mechanical flexibility under demanding conditions [25]. Yang et al. extracted the structural mechanical impedance of concrete from the signal of PZT sensor to detect damage. It was shown that the longer the distance from the PZT sensor and the damage location, the lower the strength of signal that is generated [26]. Kocherla and Kolluru conducted an investigation on embedded PZT sensors within concrete under compression test. They found that crack formation can be detected before surface cracking. It was also demonstrated that PZT is more sensitive to internal cracks than surface cracks [27]. Kocherla et al. carried out a study to highlight the capability of embedded PZT sensors to monitor crack formation and crack opening in concrete structures [28]. PVDF and PZT can also be combined and used as sensors to detect stress within pavement [29]. More recent advances further broaden the scope of piezoelectric sensing in cementitious systems. Al-Qaralleh demonstrated that applying a direct current during the curing of fresh cement paste can significantly enhance its intrinsic piezoelectric response, offering a practical and low-cost strategy for self-sensing concrete [9]. While significant progress has been made in the field of in-pavement sensor technology, gaps remain in the early detection of cracks and the detection of microcracking at the initial stages. Addressing these gaps is essential for advancing the practical application of piezoelectric sensors in pavement maintenance and enhancing their reliability and effectiveness in monitoring pavement health.

This work studies the performance of a piezoelectric sensor embedded in a concrete beam, focusing on its efficacy in detecting crack initiation and propagation under cyclic loading conditions. The developed sensors are not only highly sensitive but also cost-effective, holding promise as an efficient solution for crack detection in pavements. We study the sensors response under cyclic loading to simulate real-world conditions and explore the effects of

various parameters on its performance. Apart from conducting the experiments, a mathematical model is developed to investigate the stress and strain distribution changes in more details. This research contributes to enhancing the safety and durability of pavements by proposing cost-effective and reliable in-pavement sensor technology for early crack detection.

## 2. Material preparation and Experimental setup

### A. Concrete Mix Design and Properties

The mix design of concrete holds significant importance in determining its mechanical properties, with particular emphasis on its flexural behaviour. The composition and proportions of the constituents in the concrete mixture have a direct impact on how the material will behave under bending or flexural stresses. An 80% Ordinary Portland Cement (OPC) and 20% fly ash concrete mix was used to prepare sample beams for embedding sensors. This mix design is approved by Transport for New South Wales (TfNSW) [30] and complies with TfNSW R83 specification requirements. The concrete properties, which are detailed in Table 1, clearly adhere to TfNSW standards.

**Table 1**. Fresh and hardened properties of the concrete mix.

| Concrete properties | Value |
|---|---|
| Slump test (mm) | 70 |
| Compressive strength (MPa) | 49.5 |
| Indirect Tensile Strength (MPa) | 4.2 |
| Flexural strength (MPa) | 5.6 |

### B. Sensor Preparation and Embedment in Concrete

Piezoelectric ceramics are a type of material that can convert mechanical energy into electrical energy and vice versa. These ceramics are made from materials such as lead zirconate titanate (PZT) and barium titanate, which have a crystalline structure that allows them to generate an electric charge when subjected to mechanical stress or vibrations. Piezoelectric ceramics are widely used in a variety of applications, including sensors, actuators, and transducers. They are also used in medical ultrasound equipment, inkjet printers, and industrial equipment such as vibration sensors and accelerometers. When an external force is applied to a piezoelectric ceramic, the material becomes deformed, which causes a shift in the positions of the electric charges within the crystal lattice. This shift generates an electric field that can be measured as a voltage across the material. This phenomenon is known as the direct piezoelectric effect.

In this study, piezoelectric ceramics were chosen for embedding in concrete beams due to their high sensitivity and rigid structure. We used commercially available PZT piezoelectric diaphragms (Murata Manufacturing Co., Ltd., supplied by Core Electronics, Australia). Two different sizes were selected for comparison:

- 12-mm sensor: Part No. 7BB-12-9, consisting of a 12-mm brass plate bonded to a 9 mm PZT ceramic element with an 8 mm electrode area. The plate thickness is 0.22 mm and the ceramic thickness is 0.10 mm. Manufacturer specifications include a resonant frequency of 9.0 ± 1.0 kHz, capacitance of 8.0 nF ± 30% at 1 kHz, and resonant impedance ≤ 1000 Ω.
- 30-mm sensor: Part No. 7BB-27-4, consisting of a nominal 27 mm brass plate (close to 30 mm when accounting for solder pads and lead wires) bonded to a 20 mm PZT ceramic element. Manufacturer specifications include a resonant frequency of 4.0 ± 0.5 kHz, capacitance of 20.0 nF ± 30% at 1 kHz, and resonant impedance ≤ 500 Ω.

In both cases, electrical connections were made by soldering insulated copper leads to the silver-coated electrodes on the ceramic surface. These sensors can be considered as aggregates within the concrete matrix, providing a high sensitivity to stress. To protect the sensing element and connections, the entire sensor is sealed with PDMS Sylgard 184 by Dow Corning, a mineral-organic polymer (the mixing weight ratio of PDMS prepolymer and curing agent was 10:1 (w:w)). After mixing, the material was degassed under vacuum and applied as a coating with an average thickness of approximately 2 mm around the PZT sensors. The coated sensors were cured at 60 °C for 2 hours before embedding in concrete. PDMS, being an elastomeric polymer, distributes stress across the entire sensor surface, thereby increasing sensitivity. Fig. 1a shows the piezoelectric sensor structure, where a PZT disc is bonded to a brass substrate and connected through shielded wires soldered at the electrodes. The entire sensor is sealed with PDMS to ensure insulation, protection, and stability when embedded in concrete. The sensors were placed in the midsection and lower third of the beam, close to the expected crack initiation zone, to increase the chance of recording early crack signals. Fig. 1b shows the two sensor sizes used in the study, 12 mm and 30 mm in diameter, both sealed with PDMS and embedded in the concrete specimens to allow comparison of their signal sensitivity and performance.

a)

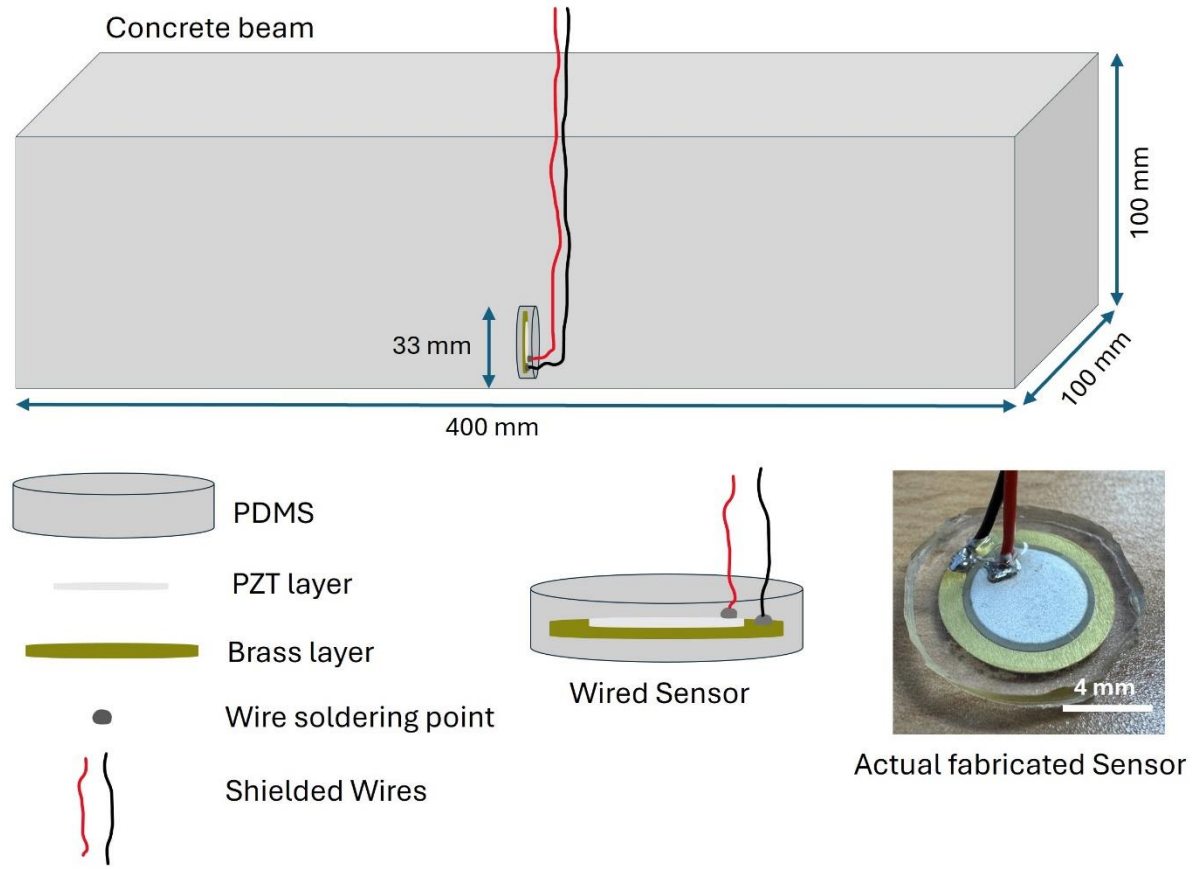


b)

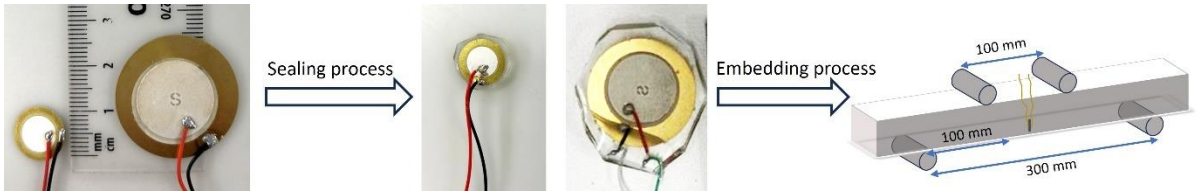


**Fig. 1.** a) Schematic of the sensor components, packaging, and actual fabricated sensor (12 mm diameter), including the placement, orientation, wiring, and PDMS encapsulation within the concrete beam. b) Piezoelectric sensors of two sizes (12 mm and 30 mm diameter). The PZT sensors were sealed with PDMS and embedded at the midsection and lower third of the concrete specimens.

### C. Experimental Setup

The concrete trial mix process and experimentation strictly conform to the guidelines delineated by Australian Standards (AS). The relevant test methods are AS 1012.2 (concrete mix preparation), AS 1012.3.1 (slump test), AS 1012.9 (compressive strength test), AS 1012.11 (flexural strength (modulus of rupture) test), and AS 1012.10 (indirect tensile strength test). A total of three concrete beams were prepared and tested for each sensor size (n = 3). All reported values (mean ± SD) are based on these three replicates unless otherwise noted.

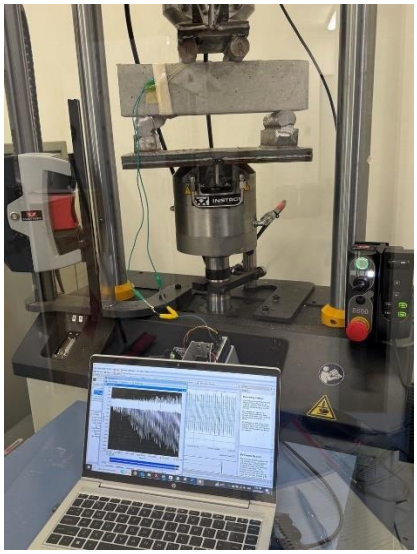

**Fig. 2**. Experimental setup on concrete beam with embedded sensor and recording sensor signal while cyclic loading test under four-point bending fixture

To understand the structural response to traffic loads, a four-point bending test using INSTRON-5985 and INSTRON-8801 universal testing machine was employed, aligning with AS 1012.11 specifications, as shown in Fig. 2. According to the standard, the support span is fixed at 300 mm, while the load span of centrally placed point loads measures 100 mm. This experiment yields crucial parameters, namely the maximum tolerated load, maximum deflection, and flexural stress. The flexural stress, $\sigma_f$ is calculated using the formula:

$$\sigma_f = \frac{FL}{bd^2} \tag{1}$$

Here, 'F' represents the total force applied to load rollers, 'L' denotes the support span, and 'b' and 'd' stand for the width and depth (or thickness) of the concrete sample, respectively.

The electrical signals from the embedded PZT sensors were recorded using a National Instruments (NI) NI-9239 Data Acquisition (DAQ) device. The sensors were connected directly to the DAQ without the use of an external amplifier or preamplifier. Data were collected at a sampling frequency of 5 kHz with an input range of ±10 V. To minimize electromagnetic interference, shielded coaxial cables and proper grounding were employed, and each DAQ channel was calibrated before testing to ensure accurate signal capture.

Prior to analysis, the recorded signals were processed to improve stability and reliability. A baseline correction was applied to remove DC offset and slow drift. In cases where the raw signals exhibited noise, a moving average filter with a window length of 10 samples (equivalent to 2 ms at the 5 kHz sampling frequency) was applied in a causal manner, using only the current and past samples. Following these steps, the peak-to-peak voltage ($V_{pp}$) was calculated over a window of five load cycles, providing a consistent measure of sensor response. While the system noise floor was not explicitly quantified, no significant random noise was observed in the majority of the signals.

## 3. Theoretical and Finite-Element Analysis

### A. Analytical Modelling of Piezoelectricity

A simple electromechanical model was formulated to help interpret the experimental results. The output voltage of piezoelectric materials in a specific direction is generally contingent upon the applied stress magnitude. Greater stress levels correspondingly yield higher voltage generation. Such stresses may be comprised of a combination of normal and shear stresses, as delineated in Fig. 3a.

In instances where a concrete beam was subjected to a four-point bending condition, as illustrated in Fig. 3b, internal forces manifest to establish equilibrium. These internal forces encompass both shear and normal forces. Shear forces are vertically oriented, while normal forces align with the beam axis. Normal forces inherently encompass tensile and compression forces contingent upon their distance from the neutral axis. The normal forces induce a moment, wherein the total moment is the amalgamation of both forces. Figs. 3c-d depict the shear force and bending moment values along the beam's length, respectively. It can be concluded that the bending moment attains its maximum within the middle region (between 0.1 m and 0.2 m), while the shear force reaches its zenith at the lateral regions (from 0 m to 0.1 m and from 0.2 m to 0.3 m). Upon scrutinizing the shear force and normal force distributions along the height, it can be observed from Figs. 3e-f that shear stress conforms to a parabolic profile, while normal stress adheres to a linear pattern with positive (tensile stress) and negative (compression stress) values, respectively. Additionally, the shear force is maximized at half of the height (0.05 m), while normal forces attain their maxima at the edges (0 m and 0.1 m) [31].

Consider the integration of an embedded piezoelectric sensor within a concrete beam at various distances from the support and below the neutral axis. It can be asserted that the piezoelectric sensor is subjected to both tensile and shear stresses. An increase in the distance from the support, ranging from 0 m to 0.1 m, results in an elevation of tensile stress, while shear stress remains constant. Progressing from 0.1 m to 0.2 m sustains constant tensile stress with zero shear stress. Advancing further, from 0.2 m to 0.3 m, tensile stress gradually diminishes to zero, whereas shear stress escalates and maintains a constant value. Any displacement of the sensor along the height, ranging from 0 m to 0.05 m, induces an escalation in shear stress and a reduction in tensile stress. Advancing from 0.05 m to 0.1 m alters the trend of shear stress from an increasing to a decreasing trajectory, while tensile stress undergoes a directional change with an increasing trend.

a)

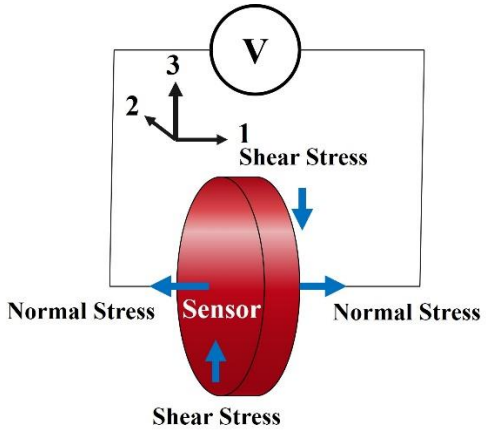


b)

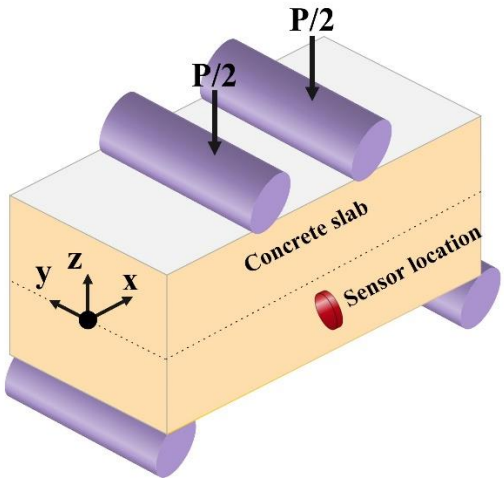


c)

d)

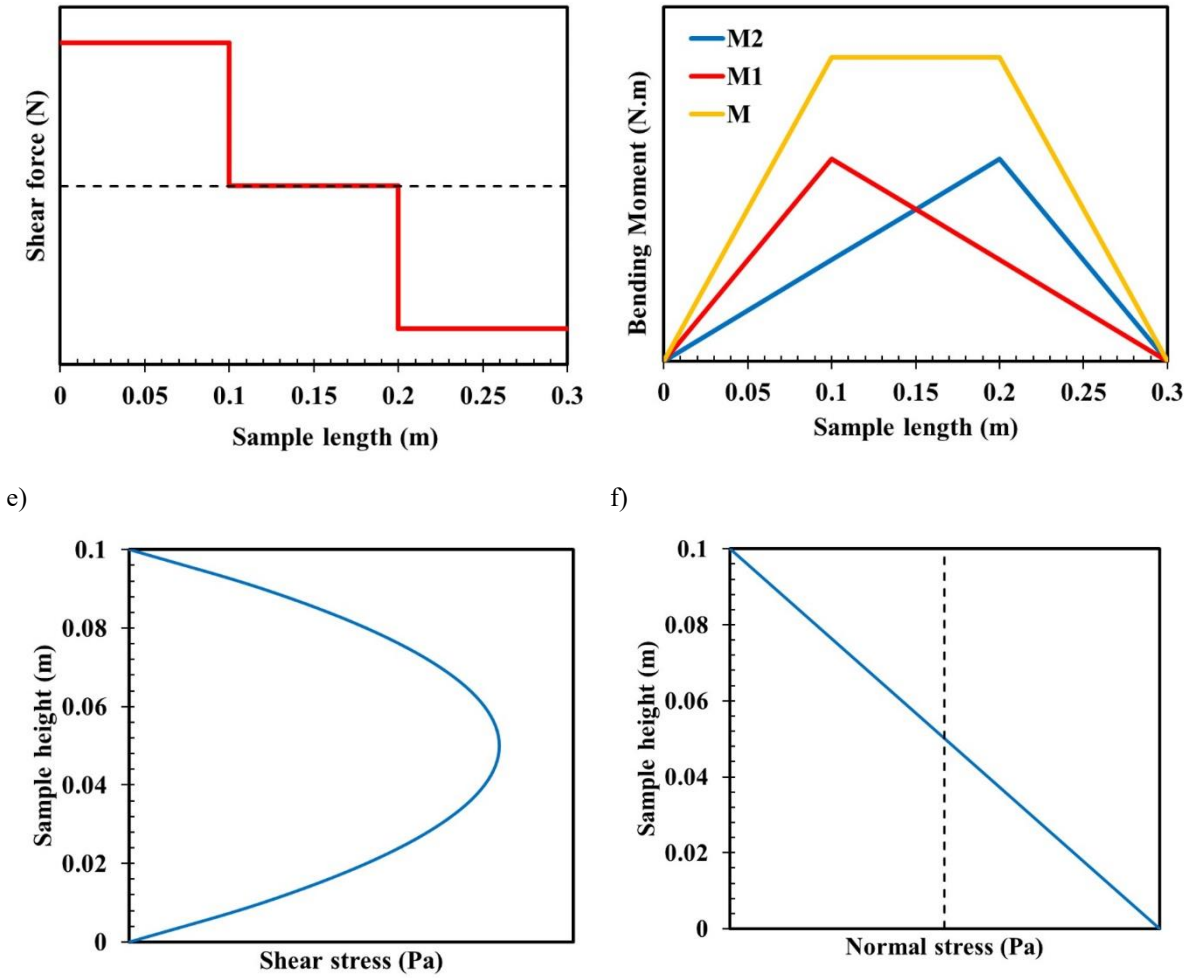


**Fig. 3**. a) Piezoelectric sensor under shear and normal stresses, b) schematic illustration of embedded sensor within concrete under four-point bending condition, c) shear force along beam length, d) bending moment along beam length, e) shear stress along beam cross section, f) normal stress along beam cross section [32].

As previously indicated, the output voltage of a piezoelectric sensor is regulated by two components, namely voltage ($V_{11}$) arising from the average normal stress ($\bar{\sigma}_{11}$) and voltage ($V_{31}$) arising from the average shear stress ($\bar{\tau}_{31}$). This relationship can be expressed mathematically as follows:

$$V(x,z) = V_{11}(x,z) + V_{31}(x,z) \tag{2}$$

Based on the correlation between stresses and the resulting voltage, it can be formulated as follows

$$V_{11}(x,z) = g_{11}t_1\bar{\sigma}_{11}(x,z) \tag{3}$$

$$V_{31}(x,z) = g_{31}t_1\bar{\tau}_{31}(x,z) \tag{4}$$

Where $g$ and $t$ represent the piezoelectric voltage coefficient, and thickness of the piezoelectric sensor, respectively. The indices 1 and 3 pertain to local coordinates [33]. Additionally, both stresses are functions of length and height. Consequently, voltages are contingent upon both length and height. In the scenario of normal stress, the bending moment can be articulated as follows:

$$M(x) = \sum_{1}^{3} M_i(x) = M_1(x) + M_2(x) \tag{5}$$

Two components of bending moment arise from two points of application of external forces. Assuming a linear relationship between the length of the sample and bending moments, it can be expressed as

$$M_1(x) = \begin{cases} \frac{P}{2}x & 0 \le x \le L/3 \\ \frac{P}{4}(L-x) & L/3 \le x \le L \end{cases} \tag{6}$$

$$M_2(x) = \begin{cases} \frac{P}{4}x & 0 \le x \le 2L/3 \\ \frac{P}{2}(L-x) & 2L/3 \le x \le L \end{cases} \tag{7}$$

Where $L$ is the length of the sample. To derive the normal stress in local coordinates as a function of the x-axis and z-axis, we can utilise the relationship between normal stress and bending moment.

$$\sigma_{11}(x,z) = -\frac{M(x)z}{I} \tag{8}$$

In which

$$I = \frac{1}{12}wh^3 \tag{9}$$

Where $w$ and $h$ represent the width and height of the concrete sample, respectively. To approximate the average normal stress on the piezoelectric sensor, the total stress can be computed and divided by the sensor's area, as follows:

$$\bar{\sigma}_{11}(x,z) = -\frac{4}{\pi R^2}\int_0^{\pi/2}\int_0^{R}\frac{M(x)(z_s + rsin\theta)}{I}rdrd\theta \tag{10}$$

Where $R$ and $z_s$ denote the radius of the piezoelectric sensor and the distance from the neutral axis to the central point of the sensor, respectively. To compute the shear stress, the distribution of shear force along the beam can be expressed as follows:

$$S(x) = \begin{cases} \frac{P}{2} & 0 \le x \le L/3 \\ 0 & L/3 \le x \le 2L/3 \\ -\frac{P}{2} & 2L/3 \le x \le L \end{cases} \tag{11}$$

Consequently, shear stress can be determined based on the shear force as follows:

$$\tau_{31}(x,z) = \frac{S(x)}{2I}\left(\frac{h^2}{4} - z^2\right) \tag{12}$$

Similarly, integrating the shear force and dividing it by the area of the sensor will yield the average shear force acting on the piezoelectric sensor.

$$\bar{\tau}_{31}(x,z) = -\frac{4}{\pi R^2}\int_0^{\pi/2}\int_0^R \frac{S(x)}{2I}\left(\frac{h^2}{4} - (z_s + r\sin\theta)^2\right) r\,dr\,d\theta \tag{13}$$

### B. Numerical Study of Stresses on Sensors

Fig. 4 illustrates the simulation setup used to evaluate the performance of embedded sensors in a concrete beam under four-point bending. In this model, sensors are positioned at 50 mm intervals from the centre of the beam toward the support, allowing us to study how stress distribution influences sensor output at various locations along the structure. This configuration is designed to replicate typical structural loading, with line loads applied to the top surface and two line supports at the bottom, mimicking the real-world stresses that concrete beams encounter.

To achieve reliable results, the concrete was meshed with fine linear hexahedral elements across the structure, with quadratic tetrahedral elements placed specifically around the sensors to capture detailed stress variations in these areas. This fine meshing reduces potential mesh dependency, ensuring that stress contours around the sensors are accurately represented. We applied tie constraints between the sensors and the concrete to prevent slippage, a crucial consideration given that this analysis focuses on the material's elastic region, prior to any cracking.

a) b)

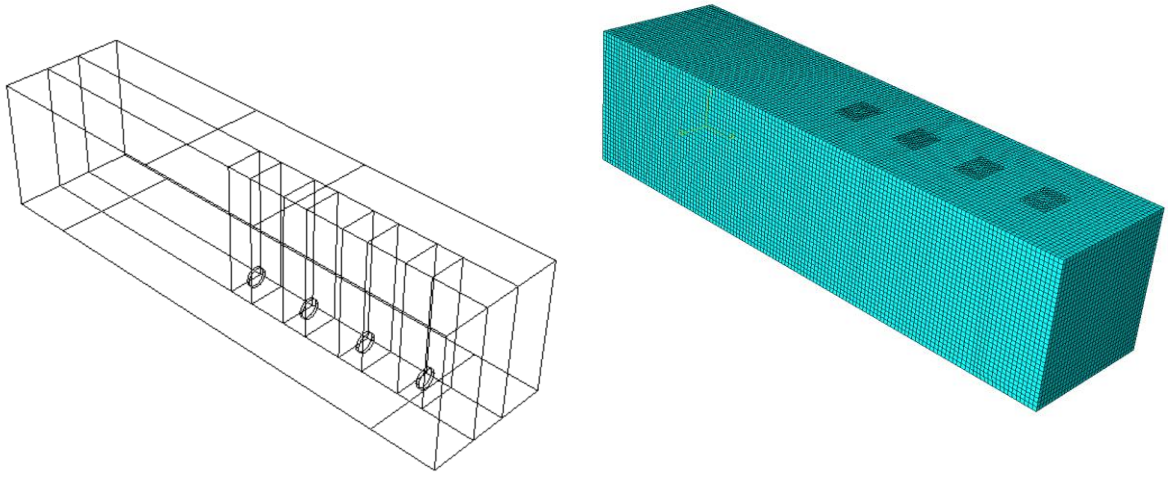

**Fig. 4**. a) Simulation setup illustrating the four-point bending test on a concrete beam with embedded sensors, b) Fine meshing and tie constraints around the sensors

## 4. Results and Discussion

### A. Mechanical Properties of Concrete Beam

Fig. 5 indicate flexural test of pure concrete (without sensor) with width and depth of 100 mm and 100 mm, and support span of 300 mm. The maximum load applied to the sample is 20.25 kN as per Fig. 5; therefore, according to Eq. 1, the flexural stress is calculated as 5.97 MPa. By repeating the flexural test on different concrete samples, the flexural stress was calculated as 5.6 ± 0.4 MPa.

To measure the failure load, piezoelectric sensors were placed between two load rollers within the concrete beams, which were then subjected to the four-point bending test, as shown in Fig. 1. As shown in Fig. 5, the concrete beam containing the embedded 30-mm sensor demonstrated the ability to withstand a maximum load of 17.84 kN. Using Eq. 1, the flexural strength was determined to be 5.1 ± 0.3 MPa, with corresponding values of 100 mm for b and 100 mm for d in Eq. 1. The standard error was calculated based on measurements of three concrete beams with 30-mm sensor. The presence of a 30-mm sensor decreases the flexural strength of the concrete by 9%. This reduction is attributed to the sensor being larger than the 20-mm size of the bigger concrete aggregates. Consequently, the sensor embedment causes stress concentrations around itself, which weakens the concrete. The stress concentration zone adjacent to the 30-mm sensor causes the formation and nucleation of microcracks in these areas before the concrete beam fails [34]. Conversely, tests with a 12-mm sensor (repeated for three concrete beams with 12-mm sensor) showed no change in strength, maintaining the same levels as concrete without any sensor embedded. The conclusion is that since the 12-mm sensor is smaller than the largest aggregates (20 mm), it functions effectively as a smart aggregate, detecting microcracks in its vicinity without causing stress concentration.

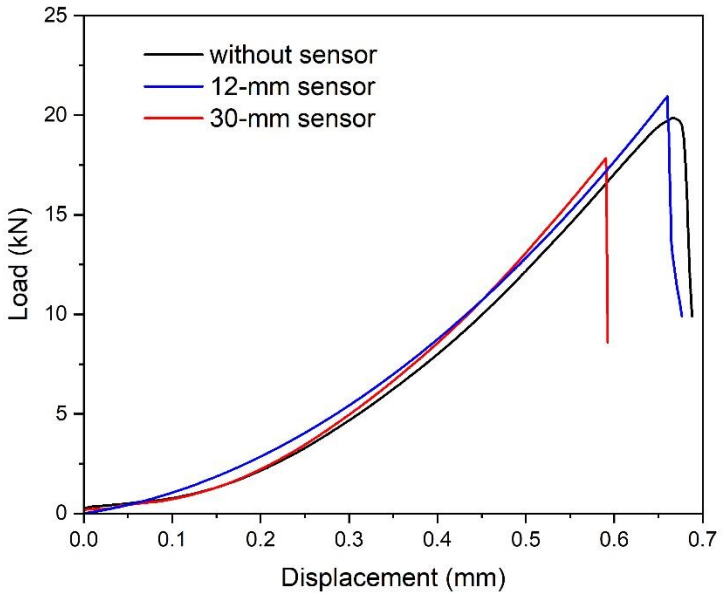


**Fig. 5**. Load-displacement curve for concrete beam with and without sensor with different sizes (three concrete beams for each test)

### B. Stress Monitoring of Cyclic Loading Test via 30-mm Piezoelectric Sensor

Various load types have been applied to study the stress behaviour of concrete pavements. These include static loads, dynamic loads, and cyclic loads. Static loads involve applying a constant load until failure, while dynamic loads involve loads that vary in magnitude and frequency. Cyclic loading, in particular, is widely selected for

fatigue testing of concrete pavements. This is due to its ability to closely mimic the repetitive nature of traffic loads that pavements are subjected to over their lifespan [35]. Cyclic loading through a four-point bending test proves to be a successful approach for simulating real-world traffic conditions on concrete pavement. A zig-zag loading pattern is a common method used to study the fatigue behaviour of structural composites, particularly concrete [27, 28]. The essential elements of this testing are maximum load (max load), minimum load (min load), and load rate. In the experiments, the minimum load was set to be close to zero, while the maximum load and load rate varied.

Figs. 6-8 illustrate the 30-mm sensor response during the cyclic loading test, depicting the load, displacement, and sensor output over time. The load (represented by the red line) and displacement (represented by the blue line) were simultaneously plotted with the sensor output. The sensor output's raw data appears in black, and to enhance the visibility of the signal pattern, a moving average filter was utilised on the original data. Initially, a maximum load of 10 kN was applied to the concrete specimen at a load rate of 0.01 kN/s. Applying the load at this slow rate took 33 minutes for a single cycle. When a load is applied slowly, the sensor has more time to adapt to the changing conditions, resulting in a relatively longer response time. This allows the material to gradually adjust to the applied load and modify its polarization accordingly. On the other hand, when a load is applied rapidly, the sensor has less time to respond, resulting in a shorter response time and a more rapid change in its electrical output. This distinction is evident in Figs. 6-8, where the maximum load remains constant at 10 kN, but the load rate increases from 0.01 kN/s to 2 kN/s. A step-like pattern becomes observable from a load rate of 0.1 kN/s onwards, with the slope of the steps and the peak-to-peak voltage output ($V_{PP}$) increasing. Piezoelectric ceramics exhibit a finite response time due to the time required for the polarization to adjust to the applied load. When a load is rapidly applied, the material may not be able to immediately reach its full polarization state. As a result, the sensor response shows a step-like pattern, where the electrical output increases in discrete steps or stages as the polarization aligns with the applied load. This step pattern represents the material's transient response.

a)

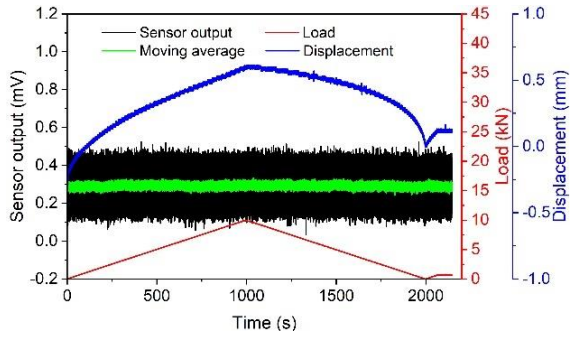


b)

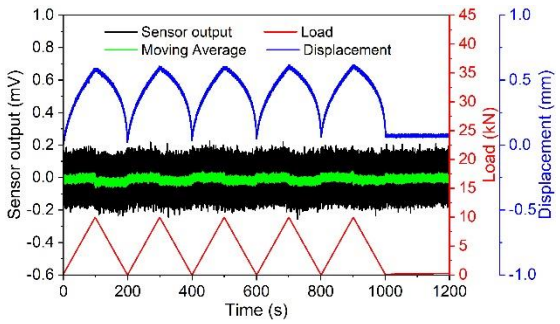


c)

d)

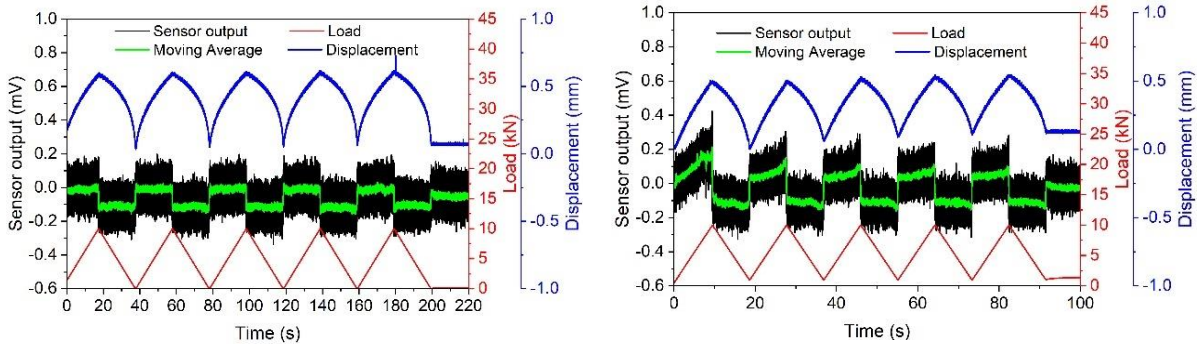


e)

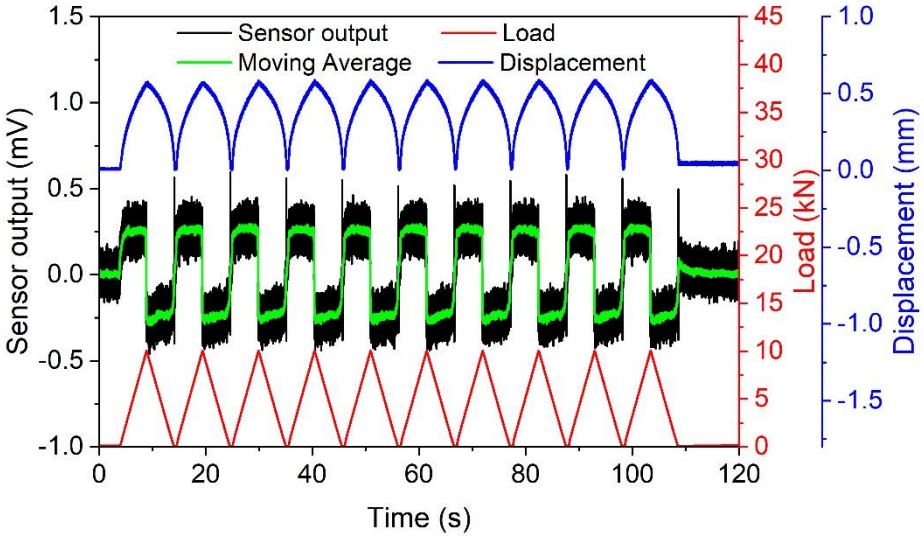


**Fig. 6**. Cyclic loading test with max load = 10 kN and load rates, a) 0.01kN/s, b) 0.1 kN/s, c) 0.5 kN/s, d) 1 kN/s, and e) 2kN/s

Even when the applied load decreases to 1 kN and 0.5 kN, the sensor exhibits a clear response as the load rate increases from 0.1 kN/s to 0.5 kN/s, as shown in Figs. 7 and 8. Based on the cyclic loading tests, it can be concluded that the embedded sensors in concrete specimens effectively respond to impact loads that simulate dynamic loads induced by vehicles. Passing vehicles generate dynamic forces and loads that can affect the structural integrity of roads and their supporting infrastructure. These dynamic loads induce transient stresses and strains in the layers of pavement. If these loads exceed the pavement structural capacity, it can lead to accelerated wear, fatigue, cracking, or other forms of damage. As can be seen from the test results, the proposed sensor exhibits a distinct peak in its output during cyclic loading, indicating its ability to reliably detect such impacts. These observations demonstrate the sensor's effectiveness in detecting load variations, proving it to be a valuable tool for monitoring the structural health of pavements. The clear response patterns seen in the cyclic loading tests indicate that the sensor can provide real-time data on stress and strain changes in concrete pavements.

a) b)

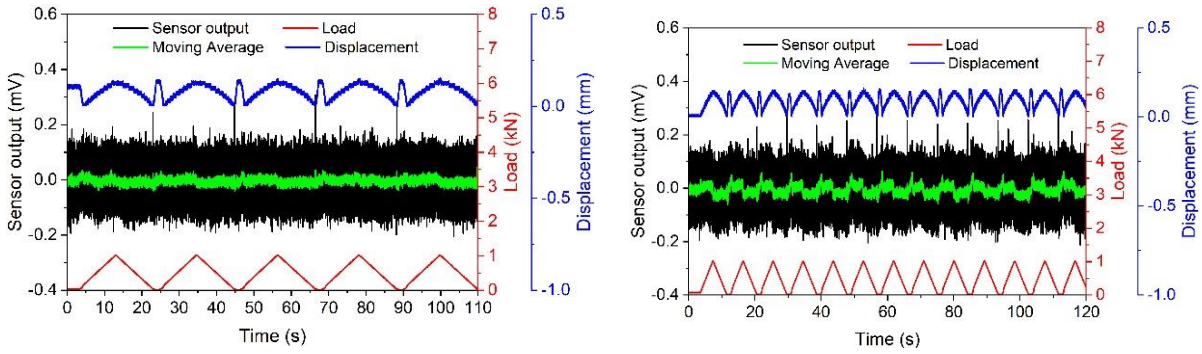


c)

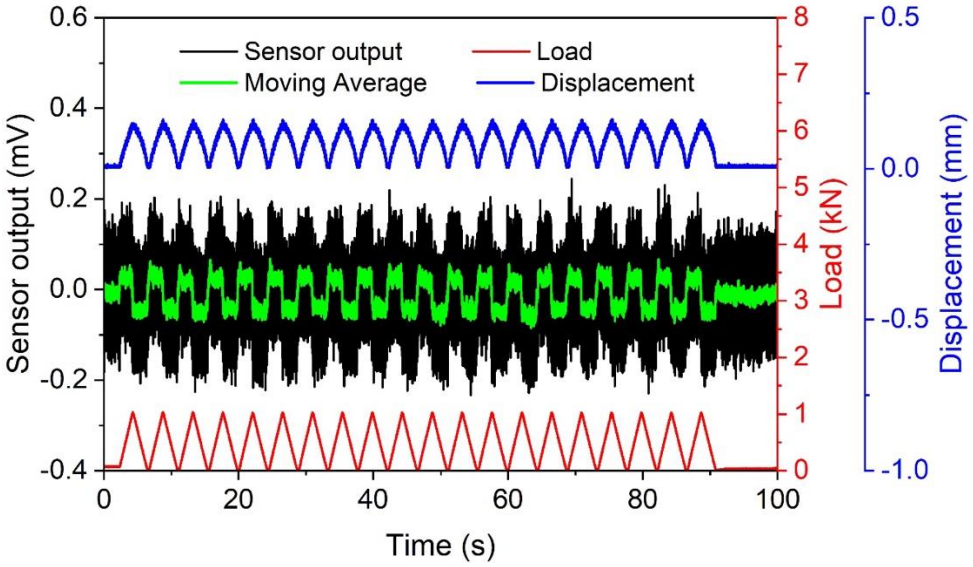


Fig. 7. Cyclic loading test with max load = 1 kN and load rates, a) 0.1 kN/s, b) 0.25 kN/s and c) 0.5 kN/s

a) b)

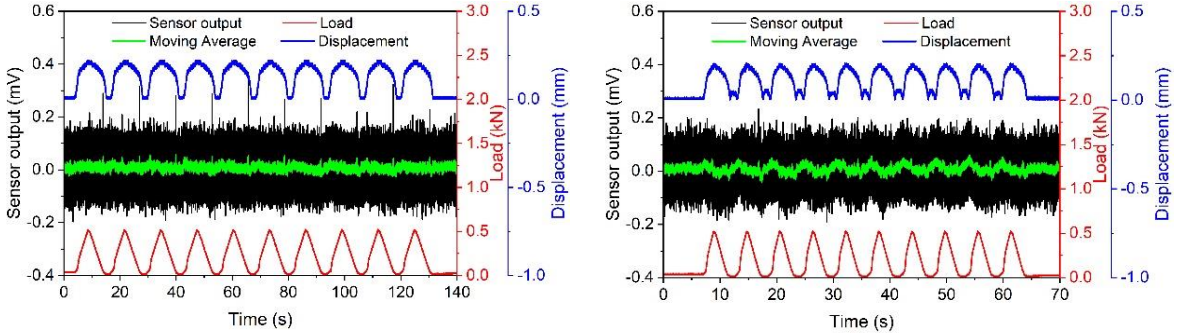


**Fig. 8**. Cyclic loading test with max load = 0.5 kN and load rates, a) 0.1 kN/s, and b) 0.25 kN/s

### C. Stress Monitoring of Cyclic Loading Test via 12-mm Piezoelectric Sensor

Cyclic loading tests were conducted with a maximum load of 10 kN using three different load rates: 0.5 kN/s, 1 kN/s, and 2 kN/s, as illustrated in Fig. 9. This figure illustrates the sensor output after undergoing the filtering

process. The results indicate that an increase in the load rate leads to a corresponding increase in the $V_{PP}$. For the case of 0.5 kN/s load rate, the PP voltage is approximately 0.1 mV, while for the cases of 1 kN/s and 2 kN/s, the PP voltages are 0.15 mV and 3 mV, respectively. It's noteworthy that, in all cases, the maximum displacement and load values remain the same, with only the speed of application differing.

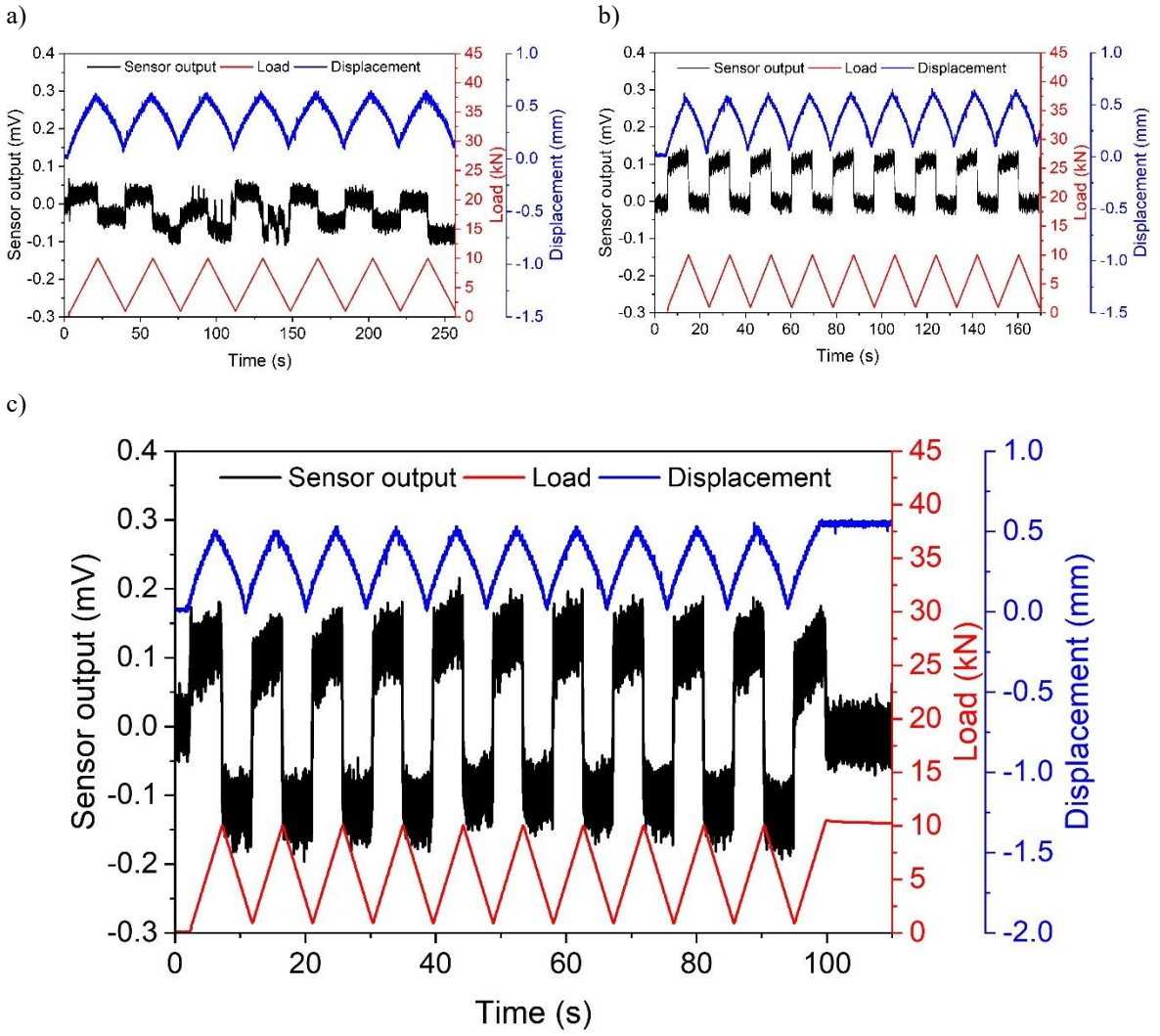


**Fig. 9**. Cyclic loading test with max load = 10 kN and load rate a) 0.5 kN/s, b) 1 kN/s and c) 2 kN/s

### D. Performance Comparison of 12-mm and 30-mm Embedded Sensors

Fig. 10a compares the $V_{PP}$ of two different sensors, one with a diameter of 30 mm and the other with a diameter of 12 mm, against varying load rates. These observations are consistent across three replicate beams for each sensor size, confirming the reproducibility of the results. The findings reveal that miniaturizing the sensor results in decreased sensor $V_{pp}$. The sensitivity of both sensors is the same because the slopes of the plots for both are approximately the same and upward. However, the 30-mm sensors have higher $V_{pp}$ values compared to the 12-

mm sensors. Conversely, the 30-mm sensors indicate a noisier sensor response, which requires filtration of the data, while the 12-mm sensors have a clear response and do not require any filtration. Although the 30-mm sensor produced a higher voltage output, it created significant stress concentrations within the concrete, leading to about a 9% reduction in flexural strength. In contrast, the 12-mm sensor had negligible impact on strength, thereby maintaining the structural integrity of the beam, as shown in Fig. 5. This comparison shows that although the smaller sensor produces lower voltage values, its advantages outweigh this limitation. In practical pavement applications, long-term reliability, minimal structural disturbance, and clear signals are more important than achieving the highest voltage output. For these reasons, the 12-mm sensor is considered the more effective option for real-world pavement health monitoring.

The signal-to-noise ratio (SNR) provides a quantitative measure of signal clarity and is defined as:

$$SNR(dB) = 20\log_{10}\left(\frac{A_{signal}}{A_{noise}}\right) \tag{14}$$

where $A_{signal}$ is the root-mean-square (RMS) amplitude of the useful signal during loading and $A_{noise}$ is the RMS amplitude of the baseline noise under unloaded conditions. A higher SNR indicates a cleaner and more reliable sensor output.

As shown in Fig. 10b, the 12-mm sensor consistently produced higher SNR values compared to the 30-mm sensor, with values reaching up to ~13.6 dB at a load rate of 1 kN/s. In contrast, the 30-mm sensor exhibited much lower SNRs, as low as ~1–2 dB under certain loading conditions. These results demonstrate that although the larger sensor generated higher absolute voltage outputs (Fig. 10a), its signal was accompanied by substantially more noise, requiring filtering and reducing its reliability. The reduced SNR of the 30-mm sensor is attributed to stress concentrations induced by its larger embedment size, which introduce microcracking and electrical instability. Conversely, the smaller 12-mm sensor minimizes stress interference, yielding more stable signals with less filtering required. Thus, despite producing lower voltage amplitudes, the 12-mm sensor is superior in terms of signal quality and long-term monitoring capability. In addition, we measured the $V_{pp}$ of the baseline noise as a worst-case representation of the noise floor (defined here as the RMS voltage of the baseline output under unloaded conditions), which was ~0.4 mV for the 30-mm sensor and only ~0.1 mV for the 12-mm sensor.

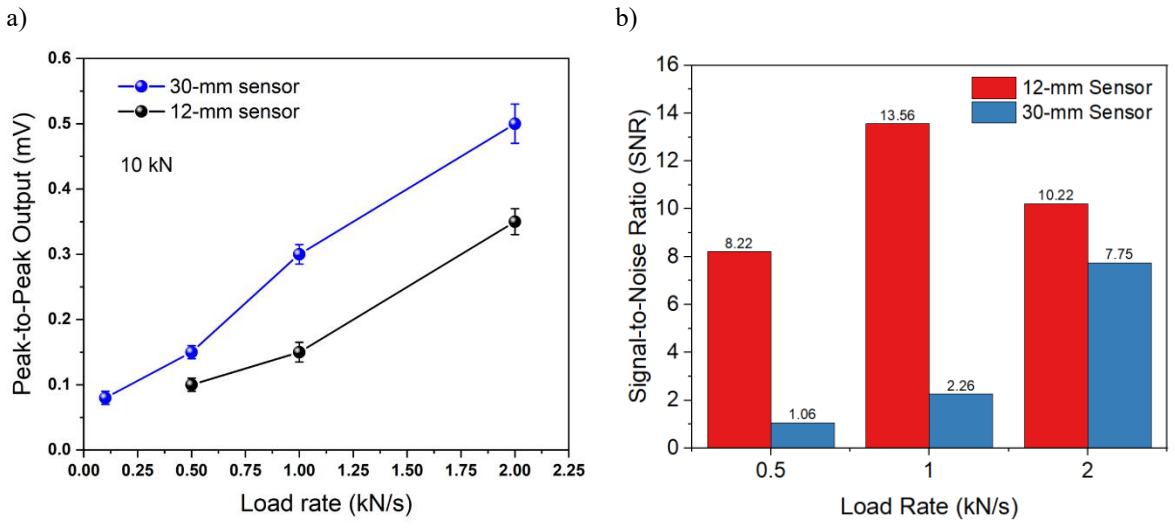

**Fig. 10**. a) Peak-to-peak voltage output ($V_{pp}$) of 30-mm and 12-mm sensors under different load rates (Values represent mean ± SD from three replicate beams (n = 3), b) Signal-to-noise ratio (SNR) of 30-mm and 12-mm sensors under the same load rate conditions and a constant maximum load of 10 kN.

### E. Effect of Sensor Position on Output Signal

Sensor location characterization inside a concrete structure is a critical aspect of structural monitoring and assessment. The precise placement and distribution of sensors within the slab can provide valuable information about the internal condition, behaviour, and performance of the concrete structure. In a series of experiments, we incorporated four sensors within concrete samples intended for fatigue loading tests using a four-point bending fixture. Although the sensors were not placed in the same samples, all of these samples were part of the same batch. The loading configuration and the precise sensor placement in the concrete samples are shown in Fig. 11a. Since we already knew that the initiation of cracks typically occurs around the centre of the sample, we positioned one sensor precisely at the centre, while the other sensors were placed at intervals of 50 mm away from the centre. We performed these experiments using an Instron 5985 Universal Machine, and the loading followed a zigzag pattern, with control parameters for minimum load, maximum load, and load rate, as depicted in Fig. 11a.

Fig. 11b-g illustrates how the sensor's output changes as the distance of the embedded sensor from the left support increases. The results reveal that the sensor is capable of detecting cracks even when positioned at a considerable distance from the crack location. Regardless of the sensor's location, a consistent response pattern was observed, signifying the sensor's ability to detect deflection within the lower third of the depth of the concrete sample.

In Fig. 11b, the maximum distance from the support is shown for a sensor positioned at the middle of the sample. Subsequently, Figs. 11c-e illustrate the sensor locations with respect to the left support at 50 mm intervals. The results indicate that the sensor response is similar when positioned in the centre and 50 mm away from the centre. This similarity can be due to the combination of normal stress and shear stress in these two locations, as elaborated in the "Electromechanical modelling" section. The plotted values in Fig. 11f–g represent mean ± SD calculated from three replicate beams. Fig. 11f illustrates the $V_{PP}$ for various sensors located at different positions within the concrete sample before any failure occurs. The reference coordinate is established at the left support, determining the sensor locations accordingly.

After analysing the $V_{PP}$ of the sensors after failure occurs, it was determined that as the sensor is positioned farther from the centre of the concrete sample, there is a consistent decrease in voltage output, as depicted in Fig. 11g. This observation is expected, as it's natural for the sensor's output to diminish as it moves away from the crack location. The reduction in voltage output is directly correlated with the diminishing applied strain on sensors positioned away from the centre. In simple terms, as we depart from the concrete sample's centre, we witness a concurrent decline in voltage output due to the decreasing strain on the sensor away from the crack location.

a)

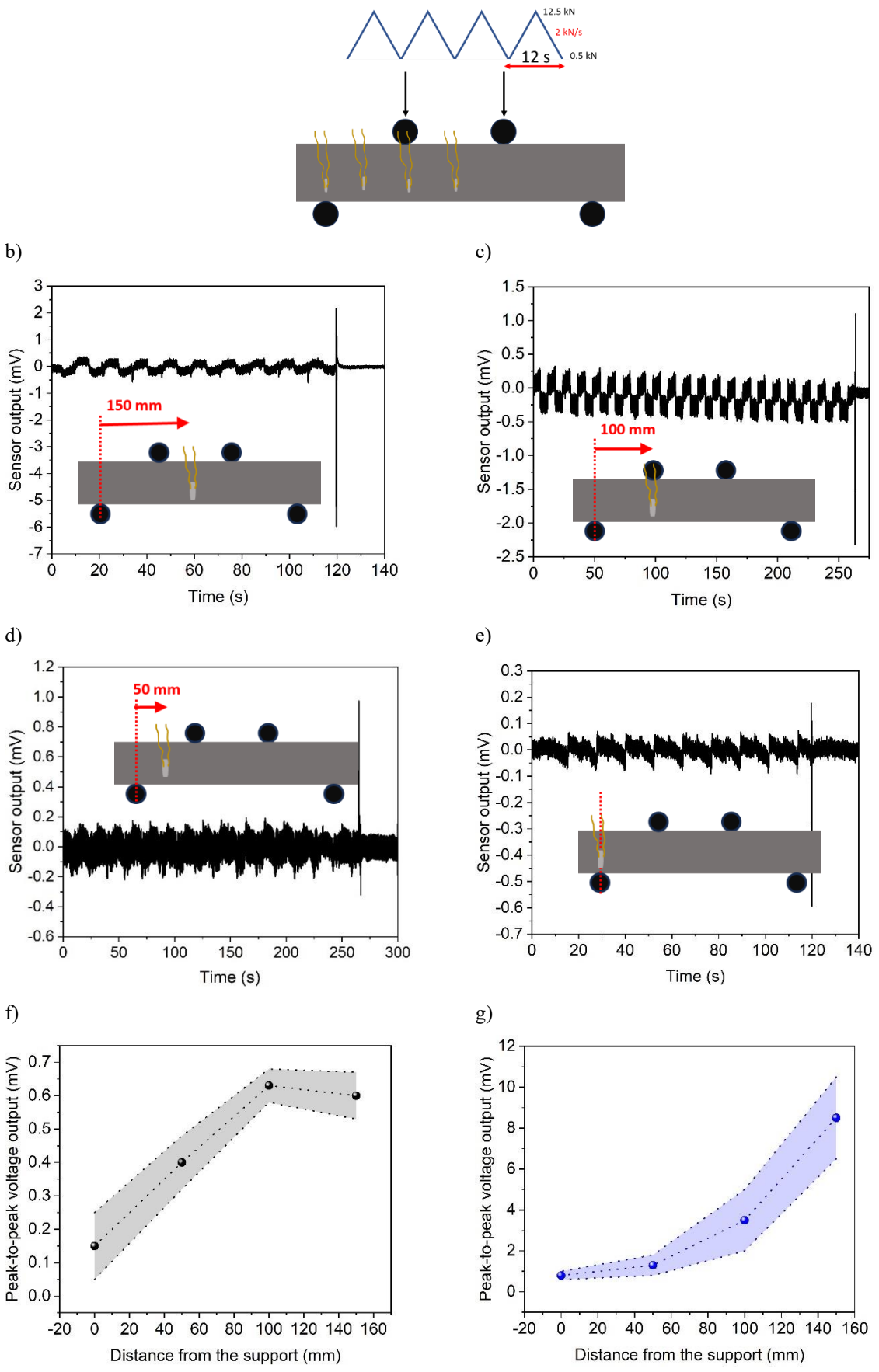


**Fig. 11**. a) A schematic diagram of the applied loading pattern including the maximum load, load rate and minimum load, and a sketch of the sensor locations in the concrete sample. Sensor response when placed at

varying distances from the support: b) positioned at the middle and 150 mm away from the support, c) 100 mm away from the support, d) 50 mm away from the support, and e) at the support f) $V_{PP}$ before the occurrence of the crack, g) $V_{PP}$ during the crack event in the sample. Data represent mean ± SD from three replicate beams.

### F. Fatigue Monitoring of Concrete Beam

The primary goal of conducting fatigue cyclic loading tests was to comprehensively evaluate the sensor's performance under conditions of repetitive loading. This investigative effort was specifically designed to ascertain the sensor's capacity to identify and capture the development of microcracks as the concrete undergoes the fatigue failure mechanism. Two illustrative instances, shown in Fig. 12, showcase the performance of the sensor in two distinct concrete samples, with the sensor positioned in the midsection and the lower third of each sample. The results demonstrate that, after a certain number of cycles, the sensor successfully detects microcracking and issues warning signals well in advance of the emergence of the visible crack. In Fig. 12a, the peak-to-peak voltage output of the sensor increases after a few cycles, but exactly within 7 cycles before the main failure, the sensor response shows significantly deeper troughs in each cycle. For instance, one cycle before the main failure, the trough in this cycle becomes more than three times deeper than that of the previous cycle, indicating that a large crack has occurred nearby. In contrast, in Fig. 12b, peak increments begin within 8 cycles before the main failure, indicative of microcracking initiation. This observation underscores the sensor's efficacy in monitoring the fatigue behaviour of concrete and providing valuable insights into the fatigue performance of the material under such conditions.

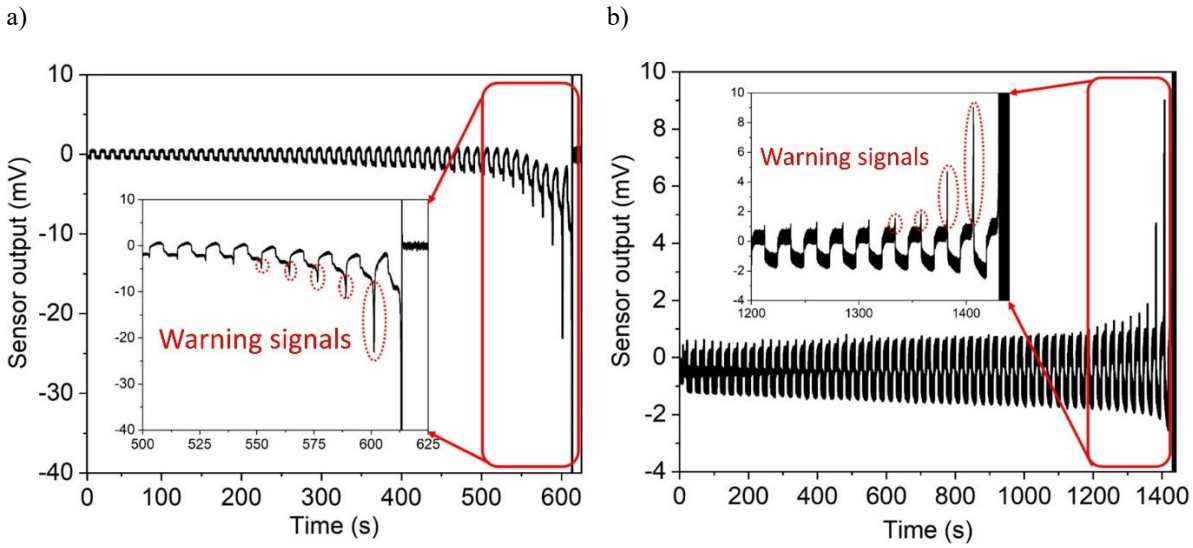


**Fig. 12**. Illustration of the sensor's effectiveness in monitoring concrete fatigue behaviour

### G. Theoretical and Finite-Element Analysis Results

Fig. 13a and 13b illustrates the distribution of voltage influenced by normal stress and shear stress as a function of the x and z axes, respectively. The combination of both voltages (Eqs. 3 and 4) results in the total voltage generated by the piezoelectric sensor, as depicted in Fig. 13c. This voltage is also dependent on the x and z axes. It is noteworthy that Figs. 13a-c are calculated based on the values given in Table 2. Consequently, the calculated

voltage appears to be higher than the actual values obtained in this study. This discrepancy can be due to inaccuracies in the source, heterogeneity and anisotropy properties of the concrete beam, changes in stress transition at interfaces due to the sealing of the piezoelectric sensor by PDMS to prevent corrosion, and displacement of the sensor from its designated position due to shaking.

**Table 2**. Specifications and piezoelectric properties of the PZT sensors.

| Property | Unit | Symbol | Value |
|---|---|---|---|
| Piezoelectric voltage coefficient | *Vm/kN* | $g_{11}$ | 0.0452 |
| | | $g_{31}$ | 0.0447 |
| Total force | *kN* | $P$ | 12.5 |
| Radius of sensor | *m* | $R$ | 0.012 |
| Thickness of sensor | *m* | $t$ | $3 \times 10^{-3}$ |
| Central z-axis of sensor | *m* | $z_s$ | -0.017 |
| Height of concrete beam | *m* | $h$ | 0.1 |
| Length of concrete beam | *m* | $L$ | 0.3 |
| Width of concrete beam | *m* | $w$ | 0.1 |

Furthermore, based on the voltage values, it can be concluded that normal stress predominates over shear stress. Fig. 13c confirms that when both voltages are combined, there is a slight increase where external forces are applied (at 0.1 m and 0.2 m of length). Correlating the theoretical values with experimental values, Fig. 13d was obtained. It is evident that as the distance of the sensor from the support increases, the voltage generated by the piezoelectric sensor also increases. In other words, when $L_1$=0 m, it can be stated that the voltage is a result of shear stress. In the case of $L_2$=0.05m, both shear and tensile stresses contribute to voltage generation. When $L_4$=0.1 m, normal force is maximized, and shear force is also maximized. Shifting the position of the sensor to 0.15 m, it can be concluded that only normal stress at its maximum level acts on the piezoelectric sensors. Fig. 13d shows that the mathematical model can accurately predict the trends and values observed in the experimental data from Fig. 10. This is because the embedded sensor is sensitive enough to detect even small strains in the concrete slab. The model's values fall within the acceptable range of the sensor's response. Ultimately, it can be concluded that the proposed mathematical model is capable of expressing the underlying physics of the problem.

a) b)

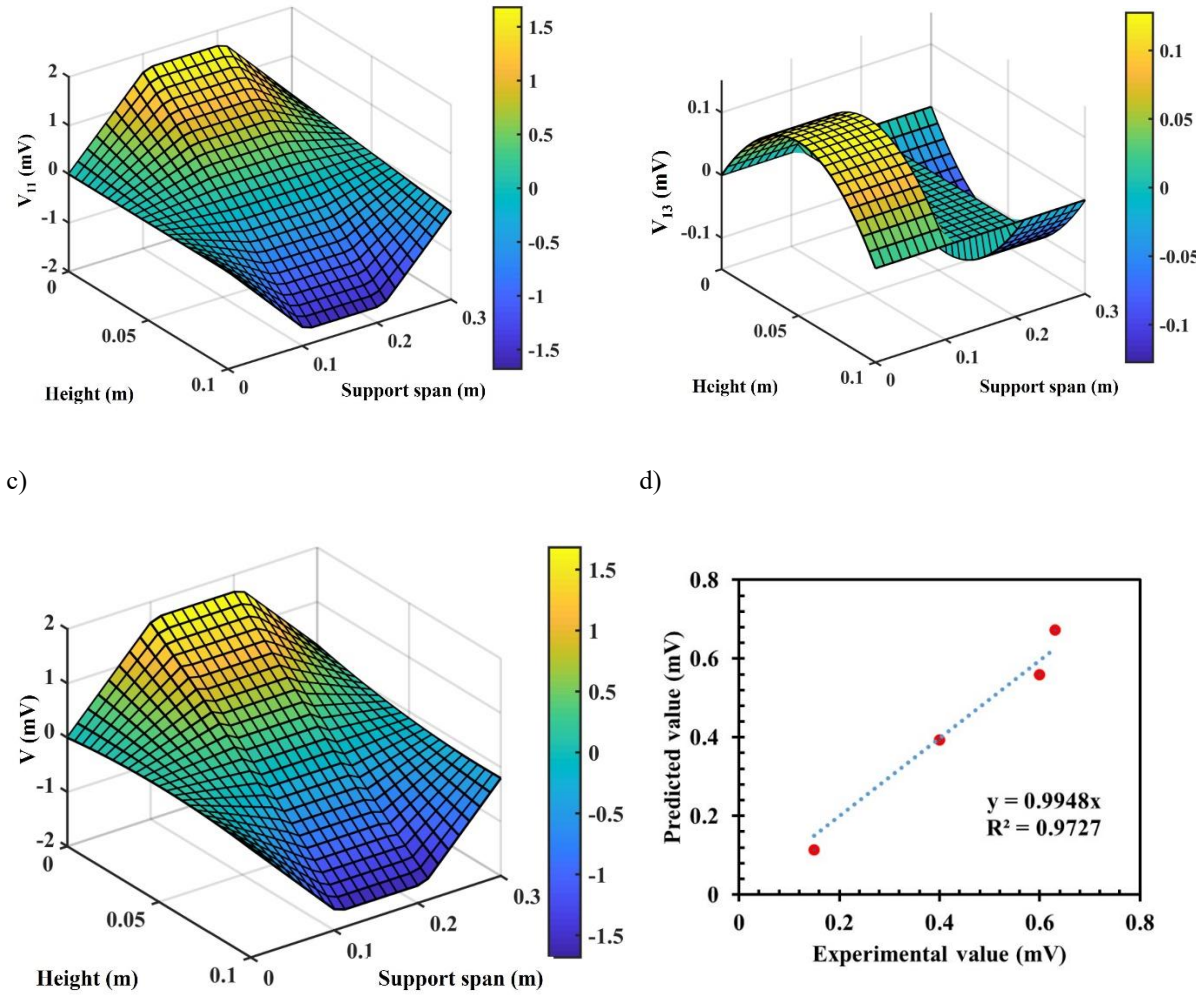


**Fig. 13**. Resultant voltage signal of piezoelectric sensor as a function of length and height due to different stresses, (a) normal stress, (b) shear stress, (c) total stress, and (d) correlation between predicted and experimental values.

Fig.s 14 and 15 illustrate stress distribution contours within a concrete sample embedded with piezoelectric sensors under static loading. These contours reveal critical insights into how stress is transferred across the concrete and concentrated around specific regions, particularly around the sensors and the load application points. In Fig. 14, the Mises stress contour highlights areas of elevated stress near the embedded sensors, showing that their presence causes localized stress concentrations. These high-stress areas are significant because they can lead to microcracking, which the piezoelectric sensors are designed to detect early on. The stress gradually diminishes as it moves from the points of load application toward the supports, displaying a typical dispersion pattern in concrete structures.

Fig. 15 builds on this by showing how stress changes at different distances from the support, specifically around the sensor locations. This figure reinforces the findings from the experimental data in Fig. 11f, where sensor output voltage drops as the distance from the crack origin increases. The stress contour in Fig. 15 supports this observation, showing that sensors closer to high-stress zones near the crack are more responsive, capturing

changes in stress effectively. This correspondence between stress contours and sensor response highlights the importance of sensor placement within high-stress zones for effective crack detection. By embedding the sensors in areas prone to higher stress, they are more likely to capture stress changes that indicate crack initiation. Therefore, these stress contours not only validate the experimental output but also underscore the strategic benefit of placing piezoelectric sensors in areas of concentrated stress for reliable, real-time structural health monitoring in concrete

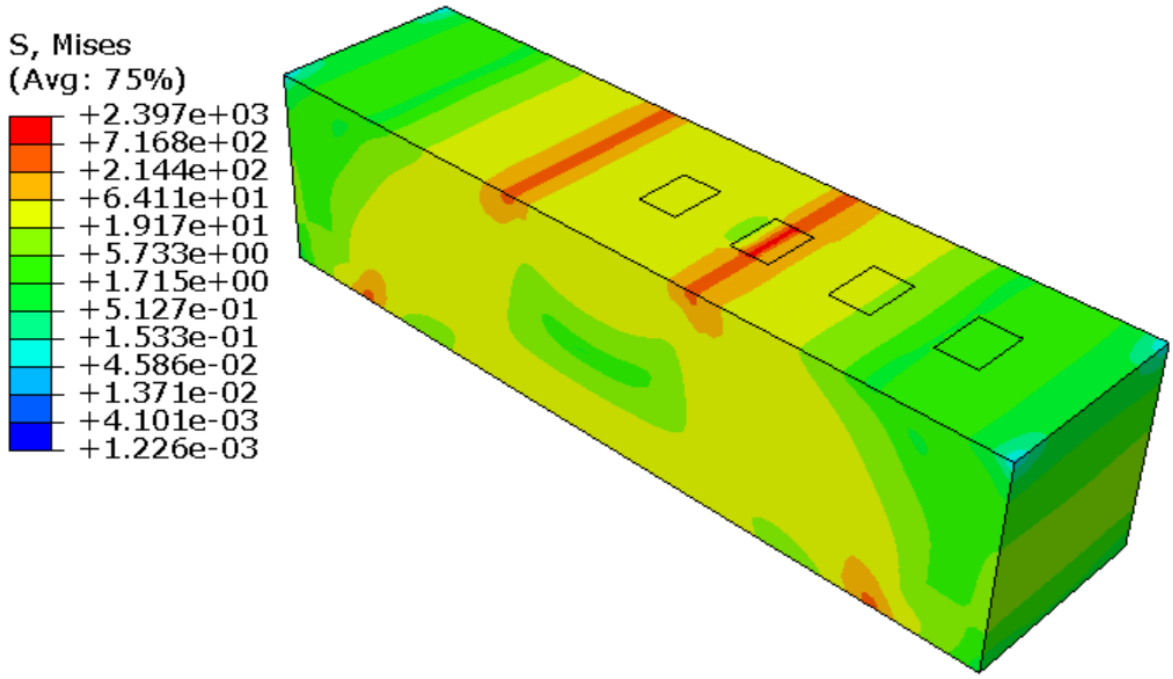


**Fig. 14**. Mises stress contour of a concrete sample with embedded piezoelectric sensors under static loading

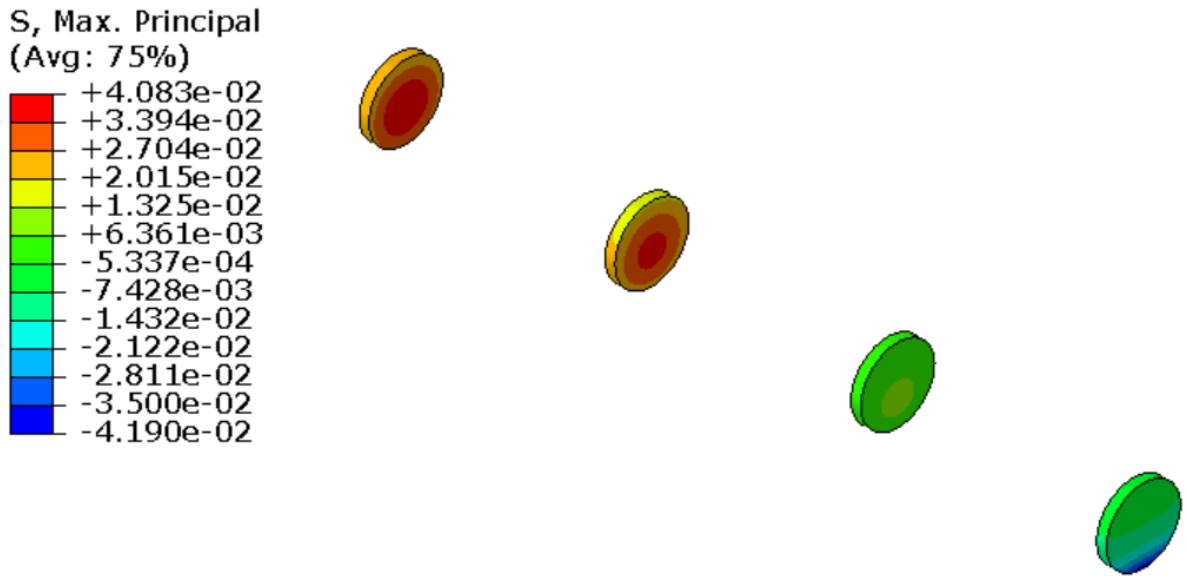


**Fig. 15**. Principal stress contour illustrating the variation in stress around embedded sensors at different distances from the support

Fig. 16 shows the experimental and simulated responses of a piezoelectric sensor embedded at varying distances along the length of a concrete beam, moving from the support toward the beam's midsection. In the experimental data, as the sensor position shifts closer to the middle of the beam, the peak-to-peak voltage output increases, reflecting the sensor's response to rising stress levels as it approaches the region of highest strain.

The simulation indicates a corresponding trend in principal stress on the sensor surface, which similarly increases as the sensor is positioned closer to the midspan, where bending stresses are typically at their peak in a concrete beam under load. This alignment between the experimental and simulated trends suggests that the voltage output from the piezoelectric sensor is directly linked to the principal stress experienced at its position within the beam.

The consistency between experimental voltage readings and simulated stress values supports the reliability of the model in predicting sensor response based on location within the concrete structure. By placing sensors strategically closer to regions of maximum stress, as indicated by both data sets, we can optimise their ability to detect early signs of cracking or stress changes. This figure underscores the piezoelectric sensor's effectiveness for structural health monitoring, as it reliably captures stress variations along the beam's length, providing valuable insights for proactive infrastructure maintenance.

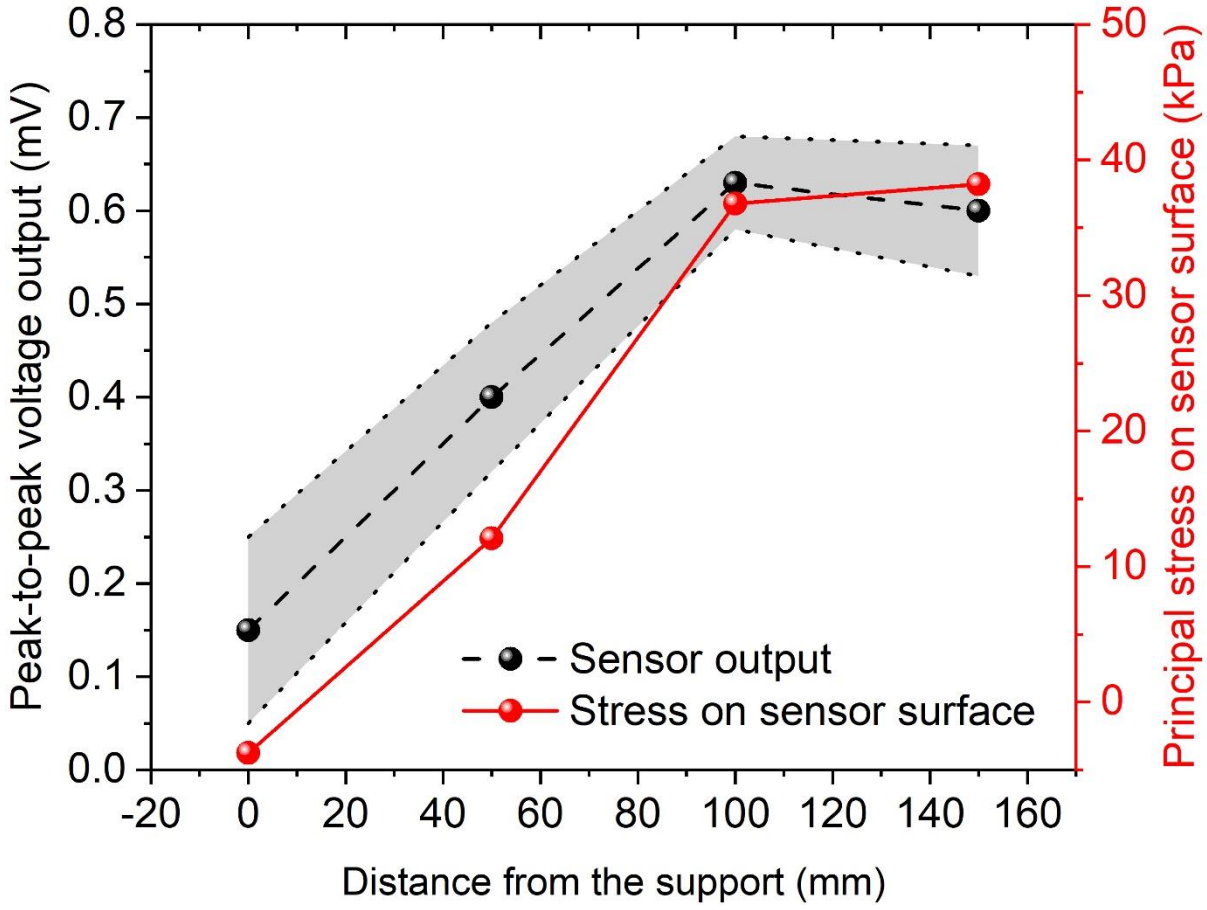


**Fig. 16**. Comparison of trends between experimental sensor output (peak-to-peak voltage) and simulated principal stress on the sensor surface

The analytical, numerical, and experimental analyses in this study together give a clear picture of how the piezoelectric sensor works to detect stress and cracks in concrete beams. The analytical analysis sets up basic relationships between stress and the sensor's voltage output, helping us understand how the sensor reacts to changes in stress. The simulation results match closely with the experimental data, which show the sensor's voltage increasing as it moves closer to the middle of the beam—where stress is naturally higher. This agreement across the theoretical, simulated, and real-world data confirms that the sensor is sensitive to stress changes and that the model is reliable. It also highlights that placing these sensors in high-stress areas is effective for monitoring the health of concrete structures.

## 5. Conclusion

The presented study aimed to evaluate the performance of piezoelectric sensors (PZTs) under cyclic loading and fatigue tests. Among various types of embedded sensors, piezoelectric sensors were selected for their high sensitivity to tiny load impacts, low hysteresis, and cost-effectiveness. This research examines the performance of piezoelectric sensors embedded in concrete beams, focusing on crack detection during cyclic loading. The sensing element of the piezoelectric sensors is lead zirconate titanate (PZT) ceramics, coated in a brass circular plate and sealed with Polydimethylsiloxane (PDMS) for protection. The sensors were embedded in concrete beams

to assess their response under various loading conditions. The experiments included cyclic loading tests with different load rates and maximum loads using 30-mm and 12-mm sensors, showcasing the sensors' ability to detect impacts and simulate real-world traffic conditions.

Although the 30-mm sensor shows a higher peak-to-peak voltage compared to the 12-mm sensors, the 30-mm sensor signals have a lower signal-to-noise ratio and require some filtration. In contrast, the 12-mm sensor signals have a clear response and high signal-to-noise ratio. The performance of both sensors under cyclic loading tests is significant, capturing the pattern of the applied load with clear results and no drift or drop. Therefore, the obtained results demonstrate promise for structural health monitoring. Fatigue cyclic loading tests have been conducted to ensure the sensor can detect internal microcracks before main failure. The research also investigated the performance of embedded sensors under fatigue cyclic loading tests, simulating real-world conditions. The sensors exhibited the ability to detect microcracking and send warning signals before the occurrence of main cracks, proving effective at monitoring the fatigue behaviour of concrete.

Our experimental, analytical, and finite-element analyses confirmed that normal stress predominantly affects sensor output, guiding effective sensor placement for optimised crack detection. The proposed electromechanical model accurately predicted sensor responses, aligning closely with experimental data and reinforcing the practical utility of these sensors in real-world applications. Consequently, piezoelectric sensors represent a promising, cost-effective solution for enhancing the durability and safety of concrete infrastructures by enabling early intervention in pavement maintenance. The findings contribute to ongoing efforts to enhance in-pavement sensor technology, addressing challenges and advancing the practical application of these sensors for pavement maintenance, durability, and safety.

Future research should focus on validating the long-term field performance of embedded sensors under real traffic and environmental conditions, as well as optimising sensor placement strategies for concrete pavements. In addition, integrating wireless data communication and cloud-based platforms for real-time data transfer and analysis could enable continuous remote monitoring and faster detection of pavement distress. Further work may also explore advanced encapsulation materials beyond PDMS to enhance sensor durability under harsh service environments. These directions will help advance the practical adoption of embedded piezoelectric sensors in large-scale pavement health monitoring.

**Acknowledgement**

The authors acknowledge the financial support of the SmartCrete Cooperative Research Centre, established and supported under the Australian Government’s Cooperative Research Centres Program.

**Declarations**

**Ethical approval** This manuscript has not been published in whole or in part elsewhere: The manuscript is not currently being considered for publication in another journal

**Disclosure of potential conflicts of interest** The authors declare that they have no competing interests.

**Informed consent** Not applicable.

**Research involving Human Participants and/or Animals** Not applicable.

**References**


[1] M. Tarabin, M. Leblouba, S. Barakat, and M. Zahri, "Experimental and probabilistic analysis of the crack propagation in fiber reinforced concrete," *Engineering Failure Analysis,* vol. 151, p. 107388, 2023/09/01/ 2023, doi: https://doi.org/10.1016/j.engfailanal.2023.107388.

[2] D. H. Chen and M. Won, "Field investigations of cracking on concrete pavements," *Journal of Performance of Constructed Facilities,* vol. 21, no. 6, pp. 450-458, 2007, doi: https://doi.org/10.1061/(ASCE)0887-3828(2007)21:6(450).

[3] X. Wang, S. Ding, Y.-Q. Ni, L. Zhang, S. Dong, and B. Han, "Intrinsic self-sensing concrete to energize infrastructure intelligence and resilience: A review," *Journal of Infrastructure Intelligence and Resilience,* vol. 3, no. 2, p. 100094, 2024/06/01/ 2024, doi: https://doi.org/10.1016/j.iintel.2024.100094.

[4] A. Martínez-Ibernón, I. Gasch, J. Lliso-Ferrando, and M. Valcuende, "Development of a new Ni voltammetric sensor for hardened concrete conditions estimate," *Sensors and Actuators Reports,* vol. 5, p. 100155, 2023/06/01/ 2023, doi: https://doi.org/10.1016/j.snr.2023.100155.

[5] S. Kavitha, R. Joseph Daniel, and K. Sumangala, "High performance MEMS accelerometers for concrete SHM applications and comparison with COTS accelerometers," *Mechanical Systems and Signal Processing,* vol. 66-67, pp. 410-424, 2016/01/01/ 2016, doi: https://doi.org/10.1016/j.ymssp.2015.06.005.

[6] F. Teng *et al.*, "Piezoresistive/piezoelectric intrinsic sensing properties of carbon nanotube cement-based smart composite and its electromechanical sensing mechanisms: A review," *Nanotechnology Reviews,* vol. 10, no. 1, pp. 1873-1894, 2021, doi: https://doi.org/10.1515/ntrev-2021-0112.

[7] M. K. Kim, M. A. Al-Qaralleh, and D. D. L. Chung, "Strong piezoresistivity and piezopermittivity of cement-based material without functional admixture and their correlation," *Cement and Concrete Composites,* vol. 151, p. 105587, 2024/08/01/ 2024, doi: https://doi.org/10.1016/j.cemconcomp.2024.105587.

[8] A. Kocherla, M. Duddi, and K. V. L. Subramaniam, "Smart embedded PZT sensor for in-situ elastic property and vibration measurements in concrete," *Measurement,* vol. 173, p. 108629, 2021/03/01/ 2021, doi: https://doi.org/10.1016/j.measurement.2020.108629.

[9] M. Al-Qaralleh, "Piezoelectric behavior of polarized fresh cement pastes under the effect of different direct current voltages," *Results in Engineering,* vol. 14, p. 100430, 2022/06/01/ 2022, doi: https://doi.org/10.1016/j.rineng.2022.100430.

[10] O. Fischer, S. Thoma, and S. Crepaz, "Distributed fiber optic sensing for crack detection in concrete structures," *Civil Engineering Design,* vol. 1, no. 3-4, pp. 97-105, 2019, doi: https://doi.org/10.1002/cend.201900008.

[11] N. Sabri, S. Aljunid, M. Salim, R. B. Ahmad, and R. Kamaruddin, "Toward optical sensors: Review and applications," in *Journal of Physics: Conference Series*, 2013, vol. 423, no. 1: IOP Publishing, p. 012064, doi: https://doi.org/10.1088/1742-6596/423/1/012064.

[12] M. F. Ferreira *et al.*, "Roadmap on optical sensors," *Journal of Optics,* vol. 19, no. 8, p. 083001, 2017, doi: https://doi.org/10.1088/2040-8986/aa7419.

[13] L. Tong, "Micro/nanofibre optical sensors: challenges and prospects," *Sensors,* vol. 18, no. 3, p. 903, 2018, doi: https://doi.org/10.3390/s18030903.

[14] R. Gomasa, V. Talakokula, S. K. R. Jyosyula, and T. Bansal, "A review on health monitoring of concrete structures using embedded piezoelectric sensor," *Construction and Building Materials,* vol. 405, p. 133179, 2023, doi: https://doi.org/10.1016/j.conbuildmat.2023.133179.

[15] T. Banerjee, S. Moharana, and L. Parida, "Early detection of thermal instability in railway tracks using piezo-coupled structural signatures," *Journal of Infrastructure Intelligence and Resilience,* vol. 2, no. 4, p. 100063, 2023/11/01/ 2023, doi: https://doi.org/10.1016/j.iintel.2023.100063.

[16] G. Du, Z. Li, and G. Song, "A PVDF-based sensor for internal stress monitoring of a concrete-filled steel tubular (CFST) column subject to impact loads," *Sensors,* vol. 18, no. 6, p. 1682, 2018, doi: https://doi.org/10.3390/s18061682.

[17] J. Shen, K. Bekiroglu, A. Tekeoglu, I. Boz, W. Chen, and M. Geng, "Numerical Study of a PVDF-Based Strain Sensor for Damage Detection of an Asphalt Concrete Pavement Subject to Dynamic Loads," *Engineering Proceedings,* vol. 27, no. 1, p. 31, 2022, doi: https://doi.org/10.3390/ecsa-9-13318.

[18] V. Talakokula and S. Bhalla, "Reinforcement corrosion assessment capability of surface bonded and embedded piezo sensors for reinforced concrete structures," *Journal of Intelligent Material Systems and Structures,* vol. 26, no. 17, pp. 2304-2313, 2015, doi: https://doi.org/10.1177/1045389X14554133.

[19] N. Kaur and S. Bhalla, "Numerical investigations on energy harvesting potential of thin PZT patches adhesively bonded on RC structures," *Sensors and Actuators A: Physical,* vol. 241, pp. 44-59, 2016/04/15/ 2016, doi: https://doi.org/10.1016/j.sna.2016.02.002.

[20] B. S. Divsholi and Y. Yang, "Application of reusable PZT sensors for monitoring initial hydration of concrete," in *Sensors and Smart Structures Technologies for Civil, Mechanical, and Aerospace Systems 2009*, 2009, vol. 7292: SPIE, pp. 698-706, doi: https://doi.org/10.1117/12.815877.

[21] P. M. Ferreira, M. A. Machado, M. S. Carvalho, and C. Vidal, "Embedded sensors for structural health monitoring: methodologies and applications review," *Sensors,* vol. 22, no. 21, p. 8320, 2022, doi: https://doi.org/10.3390/s22218320.

[22] M. Duddi, A. Kocherla, and K. V. L. Subramaniam, "Evaluation of boundary and material influences on the dynamic electromechanical impedance response of the embedded PZT sensor in concrete," *Sensors and Actuators A: Physical,* vol. 361, p. 114575, 2023/10/16/ 2023, doi: https://doi.org/10.1016/j.sna.2023.114575.

[23] Y. Chen, Y. Wen, and P. Li, "Characterization of PZT ceramic transducer embedded in concrete," *Sensors and Actuators A: Physical,* vol. 128, no. 1, pp. 116-124, 2006/03/31/ 2006, doi: https://doi.org/10.1016/j.sna.2006.01.001.

[24] Y.-F. Su, G. Han, Z. Kong, T. Nantung, and N. Lu, "Embeddable piezoelectric sensors for strength gain monitoring of cementitious materials: the influence of coating materials," *Engineered Science,* vol. 11, no. 26, pp. 66-75, 2020, doi: http://dx.doi.org/10.30919/es8d1114.

[25] I. Babu and G. de With, "Highly flexible piezoelectric 0–3 PZT–PDMS composites with high filler content," *Composites Science and Technology,* vol. 91, pp. 91-97, 2014/01/31/ 2014, doi: https://doi.org/10.1016/j.compscitech.2013.11.027.

[26] Y. Yang, Y. Hu, and Y. Lu, "Sensitivity of PZT impedance sensors for damage detection of concrete structures," *Sensors,* vol. 8, no. 1, pp. 327-346, 2008, doi: https://doi.org/10.3390/s8010327.

[27] A. Kocherla and K. V. Subramaniam, "Embedded smart PZT-based sensor for internal damage detection in concrete under applied compression," *Measurement,* vol. 163, p. 108018, 2020, doi: https://doi.org/10.1016/j.measurement.2020.108018.

[28] A. Kocherla, M. Duddi, and K. V. Subramaniam, "Embedded PZT sensors for monitoring formation and crack opening in concrete structures," *Measurement,* vol. 182, p. 109698, 2021, doi: https://doi.org/10.1016/j.measurement.2021.109698.

[29] P. Li, W. Jiang, R. Lu, D. Yuan, J. Shan, and J. Xiao, "Design and durability of PZT/PVDF composites based on pavement perception," *Construction and Building Materials,* vol. 323, p. 126621, 2022, doi: https://doi.org/10.1016/j.conbuildmat.2022.126621.

[30] R. a. M. Services. *Register of Concrete Mixes, https://tfnswassets.transport.nsw.gov.au/file-share-rms/conform-conc-mix.pdf*
[31] A. Bedford and K. M. Liechti, *Mechanics of materials*. Springer Nature, 2019.
[32] F. Beer, E. Johnston, and J. DeWolf, *Mechanics of materials, 5th SI Edition* (Stress, no. 10). 1999, pp. 1-12.
[33] D. J. Leo, *Engineering analysis of smart material systems*. John Wiley & Sons, 2007.
[34] H. Beushausen and T. Dittmer, "The influence of aggregate type on the strength and elastic modulus of high strength concrete," *Construction and Building Materials,* vol. 74, pp. 132-139, 2015, doi: https://doi.org/10.1016/j.conbuildmat.2014.08.055.
[35] N. Sudarsanan and Y. R. Kim, "A critical review of the fatigue life prediction of asphalt mixtures and pavements," *Journal of Traffic and Transportation Engineering (English Edition),* vol. 9, no. 5, pp. 808-835, 2022, doi: https://doi.org/10.1016/j.jtte.2022.05.003.

# Thermoplastic Nanocomposite 3D-Printed Temperature Sensor

Sajad Abolpour Moshizi[1,a], Milad Razbin[2, a], Chunyu Zhang[3], Golnaz Alipour Esgandari[4], Rouzbeh Abbassi[5] and Mohsen Asadnia[5]

[1]Postdoctoral Research Fellow, School of Engineering, Macquarie University
[2]PhD candidate, School of Aerospace, Mechanical and Mechatronic Engineering, The University of Sydney
[3]MRES candidate, School of Aerospace, Mechanical and Mechatronic Engineering, The University of Sydney
[4]Senior Lecturer, School of Engineering, Macquarie University
[5]Professor, School of Engineering, Macquarie University

[a]These authors contributed the same.

**Abstract**: Effective health monitoring of concrete structures is essential for ensuring the safety and durability of buildings and infrastructure. In this study, we present the design and fabrication of a novel temperature sensor using a fused deposition modeling (FDM) three-dimensional printed conductive nanocomposite polymer, thermoplastic polyurethane (TPU). The sensor features a customized geometry consisting of two coaxial cylinders with four different spacings including 0 mm, 0.025 mm, 0.05 mm, and 0.075 mm. These spacings are designed to leverage the high thermal expansion properties of TPU when embedded in concrete. The sensing element was encapsulated in an FDM three-dimensional printed polylactic acid (PLA) case, and the overall size of the sensor was 16 mm. For each design, three sensors were fabricated, resulting in a total of twelve sensors. Sensors were placed in an environmental chamber where temperature and humidity were controlled to evaluate their temperature response. Among the tested configurations at constant humidity, the sensor with a 0.025 mm spacing between the inner and outer cylinders demonstrated the highest sensitivity, with a response of 2.08 $\%C^{-1}$ in the temperature range from 10 $^{o}$C to 50 $^{o}$C and 7.06 $\%C^{-1}$ in the range from 50 $^{o}$C to 70 $^{o}$C. The proposed sensor shows higher sensitivity than most temperature sensors reported in the literature, highlighting its ability to detect even small temperature changes. This makes it a promising tool for continuous monitoring of thermal effects in concrete, and its integration into structural elements represents a significant advancement in proactive maintenance strategies that can enhance safety and extend the service life of buildings and infrastructure.

**Keywords**: Structural health monitoring, 3D printing technology, thermoresistive, embedded sensor.

## 1. INTRODUCTION

Structural health monitoring (SHM) of concrete infrastructure is essential for ensuring safety, durability, and long-term performance. Temperature variations can significantly impact the mechanical properties of concrete by influencing thermal expansion, shrinkage, and crack formation. These factors may eventually contribute to the structural integrity of the infrastructure (1, 2). Accurate and continuous monitoring of temperature fluctuations within concrete structures provides valuable insights into potential damage mechanisms and enables timely interventions to prevent structural failures. Effective thermal monitoring helps predict thermal stresses, which are especially critical in environments with significant temperature variations, such as bridges, tunnels, pavements, and high-rise buildings (3).

Traditional temperature sensors used for concrete monitoring, such as thermocouples and resistance temperature detectors, often face limitations including fragility, challenges in embedding, and relatively low sensitivity (4). Recent advancements in additive manufacturing and nanocomposite materials have enabled the development of novel sensing technologies with enhanced performance, effectively addressing many of the limitations associated with traditional sensors (5, 6). Among these emerging technologies, conductive polymer nanocomposites have attracted significant attention due to their flexibility, ease of fabrication, and tunable electrical and thermal properties (7). Conductive polymer-based sensors offer distinct advantages, such as mechanical resilience and adaptability to complex geometries, making them highly suitable for integration into concrete structures. Furthermore, the advancement of three-dimensional (3D) printing techniques, particularly fused deposition modeling (FDM), has opened new avenues for fabricating highly customizable and cost-effective sensors tailored to structural applications. FDM 3D printing has gained significant attention as a cost-effective and versatile method for fabricating polymer-based sensors (8). Thermoplastic polyurethane (TPU), a commonly used conductive nanocomposite polymer, exhibits excellent mechanical flexibility and a high coefficient of thermal expansion, making it a suitable material for

temperature sensing applications (9). TPU-based nanocomposite sensors offer enhanced sensitivity by leveraging the material's inherent thermal expansion properties, which induce measurable changes in electrical resistance in response to temperature variations (10). This characteristic makes TPU a promising alternative to traditional metal-based sensors, which are prone to material degradation over time (11). By harnessing the unique properties of TPU and the precision of FDM 3D printing, novel sensor designs can be developed to improve temperature measurement accuracy and sensitivity when embedded in concrete.

In this paper, we present the design and fabrication of a high-sensitivity temperature sensor based on an FDM 3D-printed conductive TPU nanocomposite. The sensor features a coaxial cylindrical geometry with varying spacings between the inner and outer cylinders, optimized to enhance its response to thermal expansion. Unlike conventional temperature sensors, this novel design maximizes interaction with the surrounding concrete matrix, thereby improving sensitivity to temperature variations. To assess its practical applicability, the sensor's performance was evaluated under controlled temperature and humidity conditions, demonstrating superior sensitivity compared to traditional sensors. This paper not only underscores the potential of FDM 3D-printed sensors for structural health monitoring (SHM) but also paves the way for large-scale implementation of smart sensing systems in modern infrastructure. The findings contribute to the advancement of SHM technologies by offering a robust solution for real-time thermal monitoring in concrete structures. Future work may explore the integration of these sensors with wireless monitoring platforms and advanced data analytics to support predictive maintenance strategies.

## 2. MATERIALS AND METHODS

### *2.1 Materials*

The development of a high-sensitivity temperature sensor required a strategic approach to material selection, fabrication techniques, and structural design. The objective was to create a sensor capable of detecting subtle temperature variations while ensuring durability and compatibility with concrete environments. To achieve these objectives, a conductive TPU filament (FILAFLEX, 92 A, 1.75 mm diameter), composed of thermoplastic polyurethane and carbon black with a volume resistivity of less than 800 Ω·m, was sourced from Recreus Industries, S.L., Spain, and used as the sensing material. A fused deposition modeling (FDM) using a FlashForge Creator Pro3 3D printer was employed to fabricate the sensor, enabling a precise and reproducible design.

### *2.2 Design and fabrication of sensors*

The temperature sensor was designed as a coaxial cylindrical structure with varying gaps between the inner and outer cylinders. This geometry was selected to leverage the high thermal expansion properties of conductive TPU (approximately 80–120 $\times 10^{-6}$/°C), which serves as the primary sensing element. As temperature changes occur, the thermal expansion of the conductive TPU alters the distance between the cylinders, resulting in measurable variations in electrical resistance. To evaluate the sensor's performance, four distinct designs were fabricated, each with a specific spacing of 0 mm, 0.025 mm, 0.05 mm, and 0.075 mm. These configurations were chosen to investigate the effect of inter-cylinder spacing on temperature sensitivity, with the objective of identifying the optimal design for accurate thermal monitoring. The dimensions of each sensor configuration are summarized in Table 1, which presents a detailed comparison of the outer diameter, second diameter, inner diameter, and spacing for each design.

**Table 1. Designs and dimensions of the temperature sensors.**

| Design | Outer Diameter (mm) | Second Diameter (mm) | Inner Diameter (mm) | Spacing (mm) | Length (mm) |
|---|---|---|---|---|---|
| #1 | 2.5 | 2.1 | 1.95 | 0.075 | 10 |
| #2 | 2.5 | 2.1 | 2.0 | 0.05 | 10 |
| #3 | 2.5 | 2.1 | 2.05 | 0.025 | 10 |
| Ref. | 2.5 | - | - | - | 10 |

During the printing process of the conductive TPU, the following parameters were applied: a layer thickness of 0.2 mm, printing speed of 20 mm/s, extrusion temperature of 215 °C, bed temperature of 60 °C, printing width of 0.4 mm, infill density of 100%, and an overlap of 15%. After fabrication, each sensor was carefully extracted and fitted with conductive silver paste at the connection points to ensure stable and reliable electrical conductivity. To provide mechanical stability and facilitate integration into concrete, each sensor was enclosed within a polylactic acid (PLA) casing, also fabricated using FDM 3D printing. The internal dimensions of the enclosure were intentionally designed to be slightly larger than the sensor to accommodate thermal expansion during temperature fluctuations. For optimal performance, only one end of each sensor was fixed within the enclosure, while the opposite end remained free to expand. This encapsulation not only protected the sensing element from environmental influences such as humidity and mechanical stress but also maintained the necessary flexibility for temperature-induced dimensional changes. The overall configuration of the temperature sensor is illustrated in Figure 1, which presents a schematic representation of its structural layout. Figure 2 further details the step-by-step assembly process, highlighting the individual components including the sensing element, protective cover, and the fully assembled sensor. The figure also illustrates the arrangement of multiple sensors, emphasizing the reproducibility and scalability of the fabrication approach. By combining the unique sensing properties of conductive TPU with the precision of 3D-printed geometries, this design offers an efficient and cost-effective solution for real-time temperature monitoring in structural health monitoring applications.




**Figure 1. Schematic illustration of the temperature sensor setup, showing two coaxial cylinders with adjustable gaps in Designs #1–3, along with a reference sample containing a single cylinder.**

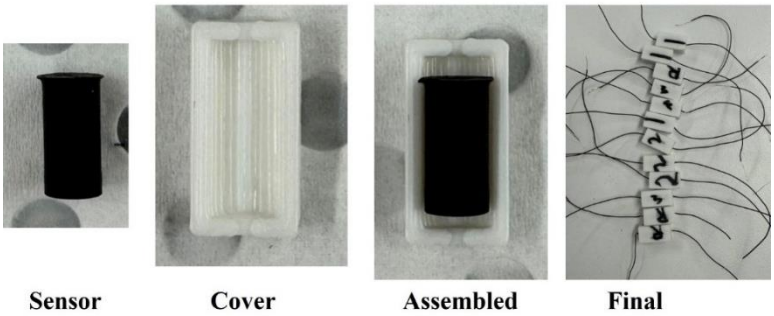


**Figure 2. Sequential assembly of the temperature sensor, from left to right: the sensing element, the cover, the assembled sensor with the cover, and the final configuration of twelve sensors.**

### *2.3 Preparation of concrete samples*

A consistent concrete mix is essential for accurate temperature measurements. In this study, a 400 × 400 × 100 mm concrete beam was prepared using a mix of 80% Ordinary Portland Cement (OPC) and 20% fly ash. This mix, approved by Transport for NSW (TfNSW) and compliant with R83 specifications, was chosen to embed temperature sensors (12).

### *2.4 Characterization methodologies*

Two series of experiments were conducted in an environmental chamber (Proeti H0135/1), where the temperature was varied from 10 °C to 70 °C while maintaining a fixed humidity level of 20%. The first series involved sensors not embedded in concrete, with the objective of identifying the best-performing design. The second series evaluated sensors embedded within concrete, alongside a commercial temperature sensor, to compare their performance under similar conditions. Finally, to assess the temperature selectivity of the developed sensor, the performance of the selected design was examined under varying humidity levels ranging from 20% to 90%. The temperature coefficient of resistance (TCR)of the sensors was calculated following Equation (1):

$$TCR(\%) = \frac{\Delta R}{R_0 T} \times 100 \quad (1)$$

## 3. RESULTS AND DISCUSSION

### *3.1 Selection of best design for thermoresistvie sensor*

The performance of the 3D-printed thermoplastic nanocomposite temperature sensor was assessed by analysing its sensitivity to temperature variations under controlled environmental conditions. The main aim was to investigate how the sensor's unique coaxial cylindrical geometry and various inter-cylinder spacings influenced its thermal response. This evaluation was essential to determine the most effective design for structural health monitoring applications. As shown in Figure 3a, relative resistance changes percentage ($\Delta R/R_0\%$) were recorded for sensors with different spacings (0 mm, 0.1 mm, 0.2 mm, and 0.3 mm) as temperature increased from 10 °C to 70 °C at a constant humidity level of 20%. All configurations exhibited a positive correlation between temperature and resistance, confirming the thermoresistive behavior of the conductive TPU material. Notably, the sensor with 0.1 mm spacing (red curve) demonstrated the highest percentage change in resistance across the tested temperature range, indicating superior sensitivity compared to other configurations. This trend is further quantified in Figure 3b, where the TCR is plotted for two temperature intervals: 10–50 °C and 50–70 °C. In both intervals, the 0.1 mm spacing sensor outperformed others. Specifically, in the high-temperature range (50–70 °C), it achieved a TCR of 7.2% °C$^{-1}$, the highest among all designs, demonstrating excellent sensitivity to small temperature changes. Even in the lower range (10–50 °C), its TCR of 2.1% °C$^{-1}$ remained the most responsive. These findings validate the hypothesis that optimizing the gap between the inner and outer cylinders enhances the thermal responsiveness of the sensor. The spacing of 0.1 mm strikes a critical balance between gap and thermal expansion sensitivity (minimizes the gap to amplify resistance changes while still allowing sufficient mechanical deformation of the TPU material during thermal expansion). Designs with either no gap or larger gaps exhibited lower sensitivity, likely due to either restricted expansion or less pronounced mechanical interaction between the two cylindrical surfaces. It was concluded that the sensor configuration with two coaxial cylinders at 0.1 mm spacing configuration is the optimal design, offering the highest temperature sensitivity and responsiveness, making it highly suitable for real-time thermal monitoring in concrete infrastructure.

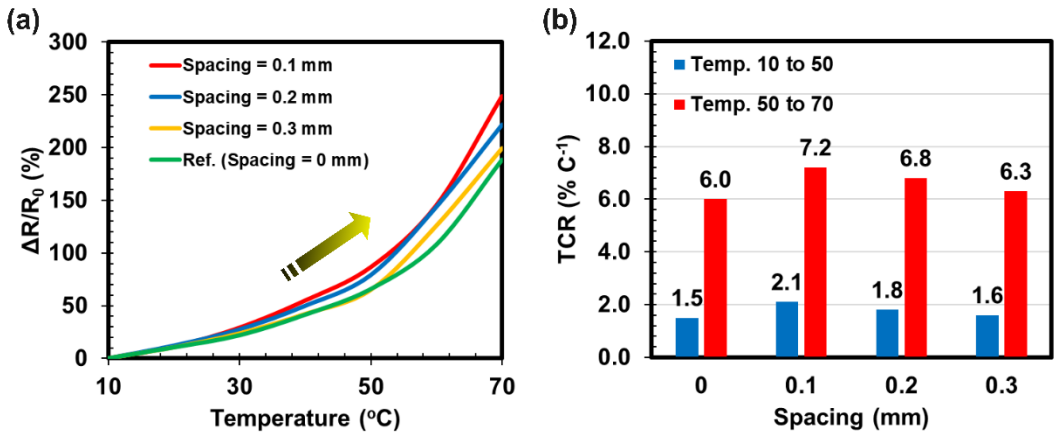

**Figure 3. Effect of spacing between cylinders in sensor design on TCR at different temperatures under fixed relative humidity of 20%, (a) relative resistance change profile, and (b) TCR at different temperature ranges.**

A comparative analysis of the developed sensor against previously reported temperature sensors is summarized in Table 2. The table presents key parameters, including sensing mechanisms, fabrication methods, and temperature sensitivity values across different ranges. The 3D-printed TPU-based sensor developed in this work demonstrated significantly higher sensitivity, achieving 2.10 % °C$^{-1}$ in the 10–50 °C range and 7.20 % °C$^{-1}$ in the 50–70 °C range. These values surpass those of conventional thermo-resistive and thermo-sensitive sensors reported in the literature, underscoring the advantages of using FDM 3D-printed conductive polymers for precise and reliable temperature sensing in structural health monitoring applications.

**Table 2. Comparative summary of temperature sensors reported in the literature, highlighting sensing mechanisms, fabrication methods, and thermal sensitivities.**

| Materials and method | TRC (%°C$^{-1}$) | Range (°C) |
|---|---|---|
| Pt NFs networks/silk Fibroin (Doping) (13) | 0.205 | – |
| WNCNT, PDMS (Extrusion) (14) | 0.55 | 0–100 |
| PEDOT: PSS-SWCNTs/PU (Dip-coating) (15) | 0.93 | – |
| Carbon fibre (Carbonization) (16) | 0.81 | 0–80 |
| CNT- ionic liquid/silk/PET (Coating) (17) | 1.23 | – |
| SWCNT/PI/ PET (Electropolymerization) (18) | 1.0 | 15–45 |
| This work (FDM 3D printing) | 2.10<br>7.20 | 10–50<br>50–70 |

### *3.2 Performance of best design compared to commercial sensor*

Figure 4 presents a comparative analysis of the thermal response of the developed 3D-printed thermoplastic nanocomposite sensor and a commercial temperature sensor under controlled environmental conditions. The tests were conducted within a temperature range of 20 °C to 70 °C at a constant relative humidity of 20%, with panel (a) representing the heating cycle and panel (b) the cooling cycle. The thermal response behavior of the developed 3D-printed sensor was benchmarked against a commercial temperature sensor under controlled conditions. As shown in Figure 4a, during the heating phase, both sensors exhibited an increase in resistance corresponding to the rise in ambient temperature, demonstrating the characteristic positive temperature coefficient behavior expected of thermoresistive materials. Notably, the developed sensor (plotted in red) showed a steeper slope in the resistance, temperature curve compared to the commercial sensor (plotted in blue). This behavior indicates a higher TCR, reflecting the superior sensitivity of the developed sensor to thermal variations. The enhanced sensitivity can be attributed to the thermal expansion of the conductive TPU nanocomposite, which leads to increased inter-particle distances within the sensing matrix, thereby significantly affecting the electron transport pathways. Figure 4b illustrates the cooling response from 70 °C to 20 °C. Both sensors demonstrated a reversible decrease in resistance with declining temperature. The response of the developed sensor closely followed that of the commercial sensor, confirming the repeatability and reliability of its thermal sensing performance. Importantly, the developed sensor maintained consistent tracking of temperature changes throughout the cooling cycle, with a slightly more pronounced resistance drop, further confirming its responsiveness. The close agreement between the two sensors across both thermal cycles, along with the higher sensitivity observed in the developed sensor, underscores its potential for accurate and real-time thermal monitoring in SHM applications. The results validate the effectiveness of the sensor's coaxial cylindrical design and the material's intrinsic thermal responsiveness, highlighting the advantages of using FDM 3D-printed conductive TPU nanocomposites for advanced temperature sensing solutions in concrete infrastructures.

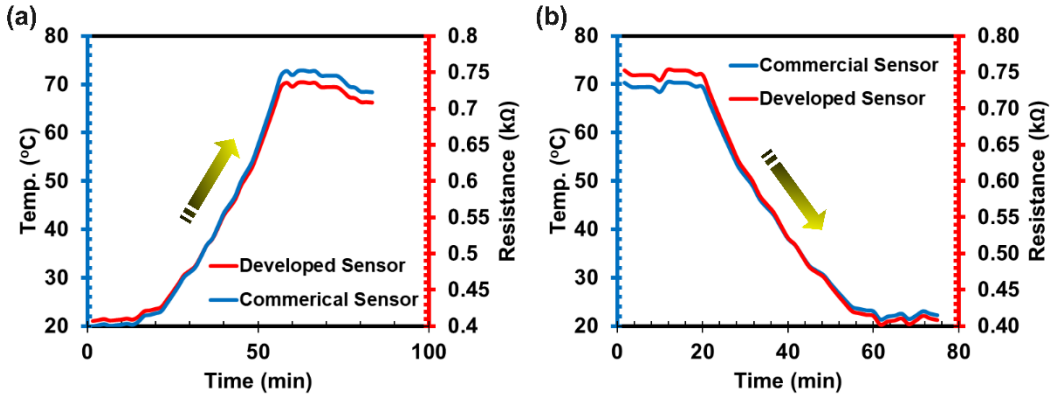


**Figure 4. Comparison between developed and commercial sensors at different temperatures from 20°C to 70°C under fixed relative humidity of 20%, (a) increasing, (b) decreasing.**

### *3.3 Temperature selectivity of best design*

Figure 5 presents the temperature selectivity of the developed 3D-printed thermoplastic nanocomposite sensor under two different relative humidity (RH) conditions of 20% and 90%, with temperature varying from 20 °C to 70 °C during both heating (red curve) and cooling (blue curve) cycles. At 20% RH, the sensor exhibits a hysteresis of 3.9%, indicating a noticeable difference between the heating and cooling paths due to thermal lag and internal friction within the polymer matrix. In contrast, at 90% RH, the hysteresis is reduced to 2.6%, suggesting that increased moisture may facilitate polymer chain mobility, thereby improving structural recovery and reducing thermal memory effects. Despite the differences in humidity, the sensor maintains consistent temperature sensitivity and demonstrates reliable performance, highlighting its robustness and suitability for real-time thermal monitoring in environments with fluctuating humidity levels.

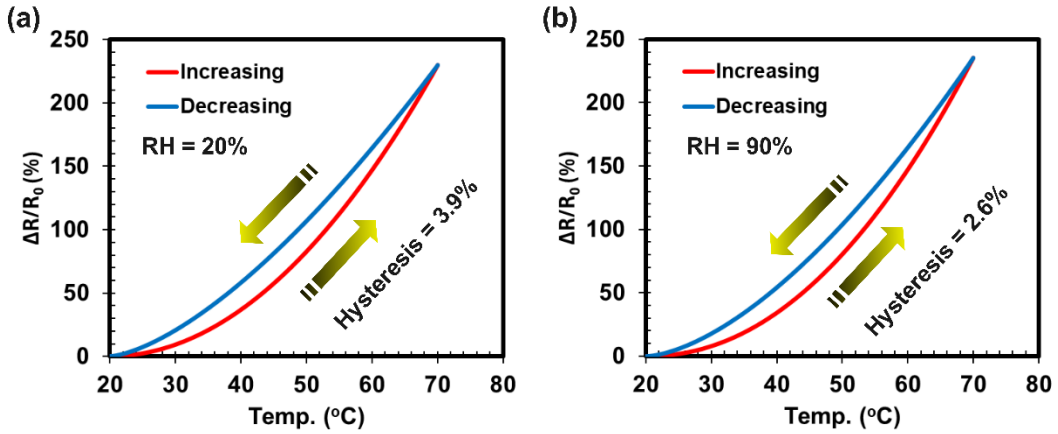


**Figure 5. Investigation of the temperature selectivity of the developed sensor under varying relative humidity levels ranging from 20% to 90%, with (a) heating and cooling behavior at 10% RH and (b) heating and cooling behavior at 90% RH.**

## 4. CONCLUSIONS

In this study, a novel thermoresistive temperature sensor was successfully designed, fabricated, and evaluated using FDM 3D printing technology with a conductive TPU nanocomposite. The optimum temperature sensor (coaxial cylindrical geometry and inter-cylinder spacing, of 0.1 mm gap) the sensor demonstrated exceptional sensitivity to temperature variations, with a TCR of 2.10 % $°C^{-1}$ in the 10–50 °C range and 7.20 % $°C^{-1}$ in the 50-70 °C range, values significantly higher than those reported in the literature for comparable thermo-sensitive materials. The performance comparison with a commercial temperature sensor confirmed the superior responsiveness, stability, and repeatability of the developed sensor. Furthermore, the sensor exhibited reliable temperature selectivity under varying humidity conditions, with reduced hysteresis observed at higher relative humidity levels, highlighting its robustness for deployment in diverse environmental conditions. The results validate the potential of conductive TPU nanocomposites and FDM 3D printing for developing cost-effective,

high-performance sensors tailored for embedding in concrete infrastructure. These sensors represent a promising solution for real-time thermal response monitoring in SHM systems, contributing to the proactive maintenance strategies and enhancing the safety and longevity of critical infrastructure. Future work may focus on integrating the developed sensor with wireless data acquisition systems and exploring its long-term performance under field conditions to further support its application in smart civil infrastructure.

## 5. ACKNOWLEDGMENT

The authors acknowledge the financial support of the SmartCrete Cooperative Research Centre, established and supported under the Australian Government's Cooperative Research Centres Program. We acknowledge Transport for New South Wales (TfNSW) for their significant contribution to this research. In particular, we express our sincere thanks to Dr. Hossein Asadi, Mr. Basil Ben, and Mr. Harish Srivastava for their expert advice, technical insights, and continuous support throughout the experimental design, concrete mix preparation, and performance evaluation phases. Their collaboration has been instrumental in aligning the research with practical applications in infrastructure monitoring.

## 6. REFERENCES

1. Ukpata, J. O., Ewa, D. E. et al., 2023, "Effects of elevated temperatures on the mechanical properties of laterized concrete," Scientific Reports, **13**(1), p. 18358, DOI: https://doi.org/10.1038/s41598-023-45591-5.

2. Memon, S. A., Shah, S. F. A. et al., 2019, "Durability of sustainable concrete subjected to elevated temperature–A review," Construction and Building Materials, **199**, pp. 435-455, DOI: https://doi.org/10.1016/j.conbuildmat.2018.12.040.

3. Li, L., Chen, B. et al., 2023, "Thermal behaviors of bridges — A literature review," Advances in Structural Engineering, **26**(6), pp. 985-1010, DOI: https://doi.org/10.1177/13694332231153976.

4. Presa Madrigal, L., Rodríguez Rama, J. A. et al., 2024, "Cost-Effective Temperature Sensor for Monitoring the Setting Time of Concrete," Applied Sciences, **14**(11), p. 4344, DOI: https://doi.org/10.3390/app14114344.

5. Roopa, A. K., Hunashyal, A. M. et al., 2022, "Development and Implementation of Cement-Based Nanocomposite Sensors for Structural Health Monitoring Applications: Laboratory Investigations and Way Forward," Sustainability, **14**(19), p. 12452, DOI: https://doi.org/10.3390/su141912452.

6. Zhao, D., Liu, X. et al., 2023, "3D Printed and Embedded Strain Sensors in Structural Composites for Loading Monitoring and Damage Diagnostics," Journal of Composites Science, **7**(10), p. 437, DOI: https://doi.org/10.3390/jcs7100437.

7. Leung, S. N., 2018, "Thermally conductive polymer composites and nanocomposites: Processing-structure-property relationships," Composites Part B: Engineering, **150**, pp. 78-92, DOI: https://doi.org/10.1016/j.compositesb.2018.05.056.

8. Kumar, S., Singh, H. et al., 2024, "A comprehensive review of FDM printing in sensor applications: Advancements and future perspectives," Journal of Manufacturing Processes, **113**, pp. 152-170, DOI: https://doi.org/10.1016/j.jmapro.2024.01.030.

9. Zhu, G., Wang, F. et al., 2021, "Highly flexible TPU/SWCNTs composite-based temperature sensors with linear negative temperature coefficient effect and photo-thermal effect," Composites Science and Technology, **217**, p. 109133, DOI: https://doi.org/10.1016/j.compscitech.2021.109133.

10. Zhu, G., Wang, F. et al., 2022, "Highly flexible TPU/SWCNTs composite-based temperature sensors with linear negative temperature coefficient effect and photo-thermal effect," Composites Science and Technology, **217**, p. 109133, DOI: https://doi.org/10.1016/j.compscitech.2021.109133.

11. Choi, Y., Kim, M. et al., 2024, "Negative temperature coefficient effect of TPU/SWCNT/PEDOT:PSS polymer matrices for wearable temperature sensors," Polymer Testing, **141**, p. 108652, DOI: https://doi.org/10.1016/j.polymertesting.2024.108652.

12. *Roads and Maritime Services, Register of Concrete Mixes* [Online]. Available: https://tfnswassets.transport.nsw.gov.au/file-share-rms/conform-conc-mix.pdf

13. Huang, J., Xu, Z. et al., 2020, "Stretchable and heat-resistant protein-based electronic skin for human thermoregulation," Advanced Functional Materials, **30**(13), p. 1910547, DOI: https://doi.org/10.1002/adfm.201910547.

14. Li, Y., Zheng, C. et al., 2020, "Smart glove integrated with tunable MWNTs/PDMS fibers made of a one-step extrusion method for finger dexterity, gesture, and temperature recognition," ACS Applied Materials & Interfaces, **12**(21), pp. 23764-23773, DOI: https://doi.org/10.1021/acsami.0c08114.

15. Lee, J., Kim, D. W. et al., 2020, "Intrinsically strain-insensitive, hyperelastic temperature-sensing fiber with compressed micro-wrinkles for integrated textronics," Advanced Materials Technologies, **5**(5), p. 2000073, DOI: https://doi.org/10.1002/admt.202000073.

16. Wang, C., Xia, K. et al., 2017, "An all-silk-derived dual-mode e-skin for simultaneous temperature–pressure detection," ACS applied materials & interfaces, **9**(45), pp. 39484-39492, DOI: https://doi.org/10.1021/acsami.7b13356.

17. Wu, R., Ma, L. et al., 2019, "Silk composite electronic textile sensor for high space precision 2D combo temperature–pressure sensing," Small, **15**(31), p. 1901558, DOI: https://doi.org/10.1002/smll.201901558.

18. Hong, S. Y., Lee, Y. H. et al., 2016, "Stretchable active matrix temperature sensor array of polyaniline nanofibers for electronic skin," Advanced materials, **28**(5), pp. 930-935, DOI: https://doi.org/10.1002/adma.201504659.

# Tesseract-Structured Piezoresistive Sensors for Embedded Monitoring of Cementitious Materials

Milad Razbin[1], Sillawat Sathorn[2], Sajad Abolpour Moshizi[1], Shuying Wu[1], Mohsen Asadnia[2], Vanissorn Vimonsatit[2]

[1]School of Aerospace, Mechanical and Mechatronic Engineering, The University of Sydney, Sydney, NSW, 2006, Australia
[1] School of Engineering, Faculty of Science and Engineering, Macquarie University, Sydney, NSW 2113, Australia.

*Corresponding authors:
sorn.vimonsatit@mq.edu.au

## Abstract

The development of scalable, cost-effective, and reliable sensing systems for structural health monitoring of cementitious materials remains a significant challenge, particularly due to limitations associated with complex fabrication processes, high material costs, and environmental sensitivity of existing technologies. In this study, a novel geometry-driven piezoresistive sensor based on a tesseract-inspired architecture is proposed and fabricated using conductive thermoplastic polyurethane via a single-step fused deposition modeling process. The designed three-dimensional structure enables controlled spacing evolution and deformation-induced contact between conductive domains, resulting in amplified electromechanical coupling. Prior to embedding, the sensor exhibits a high and tunable gauge factor ranging from 20% to 92%, attributed to the geometry-induced amplification of conductive pathways. After embedding within mortar, the effective gauge factor decreases to the range of 0.011% to 0.003% due to environmental interactions and matrix constraints yet remains sufficient for reliable strain monitoring. Mechanical testing confirms that embedding the sensor does not significantly alter the compressive behavior of the host material. The developed sensor demonstrates accurate strain tracking with strong agreement to a commercial strain gauge under identical loading conditions. Environmental studies reveal that humidity and temperature influence the piezoresistive response, while cyclic loading tests confirm stable, repeatable, and reversible performance. Compared to existing studies, the proposed sensor offers a simple, low-cost, and scalable alternative using commercially available materials and accessible manufacturing techniques. This work establishes a practical pathway toward geometry-engineered embedded sensing systems for real-time monitoring of cementitious infrastructure.

**Keywords:** Mortar, Conductive polymer, Fused deposition modelling, Real-time monitoring.

# 1. Introduction

Concrete remains the most widely used construction material worldwide due to its structural versatility, durability, and cost-effectiveness. However, its quasi-brittle nature and susceptibility to cracking, damage accumulation, and long-term degradation necessitate reliable structural health monitoring (SHM) systems to ensure safety and serviceability throughout its lifespan. Conventional SHM approaches, including externally bonded strain gauges, fiber optic sensors, piezoelectric transducers, and acoustic emission techniques, have been extensively employed for this purpose. Despite their effectiveness, these systems often suffer from complex installation procedures, susceptibility to debonding, limited durability in harsh alkaline environments, and sensitivity to environmental conditions, which restrict their long-term applicability in cementitious structures [1-3]. These challenges have driven increasing interest toward embedded sensing technologies that can provide stable, real-time monitoring while maintaining mechanical compatibility with the host material.

Among emerging sensing strategies, piezoresistive materials have attracted considerable attention due to their intrinsic ability to convert mechanical deformation into measurable electrical resistance changes. In cement-based systems, this functionality is typically achieved through the incorporation of conductive fillers such as carbon fibers, carbon nanotubes (CNTs), graphene nanoplatelets (GNPs), and carbon black, which form percolated conductive networks within the matrix [4-6]. Under applied loading, resistance variations arise from tunneling effects, contact resistance changes, and deformation of conductive pathways [7-10]. While such self-sensing cementitious composites have demonstrated promising capabilities, they often require high filler contents to achieve electrical percolation, which can adversely affect workability, mechanical performance, and cost. Furthermore, issues related to filler dispersion, scalability, and repeatability remain significant barriers to practical implementation in large-scale infrastructure.

An alternative approach involves embedding discrete sensing elements within cementitious materials, thereby localizing the sensing function while preserving the intrinsic properties of the host matrix. Embedded sensors have shown potential for improving durability and measurement reliability; however, many existing designs rely on complex fabrication techniques, expensive materials, or geometries that are not optimized for compressive stress transfer. Conventional planar or cylindrical sensor configurations are often associated with stress concentration, mechanical

mismatch, signal instability, and limited multidirectional sensitivity [11, 12]. In addition, several advanced sensing systems require sophisticated signal processing or data acquisition hardware, further limiting their adoption in practical civil engineering applications.

Recent advances in additive manufacturing (3D printing) have opened new opportunities for the development of architected sensing systems with tailored geometry and tunable electromechanical properties. Additive manufacturing enables precise control over internal lattice structures, conductive pathway distribution, and surface morphology, thereby enhancing strain transfer and interfacial interaction within cementitious matrices [13, 14]. Various architected designs, including lattice, porous, auxetic, and kirigami structures, have demonstrated improved sensitivity through geometric amplification of deformation. However, many of these systems rely on multi-step fabrication processes, hybrid printing techniques, or post-processing steps, which increase complexity and limit scalability. Moreover, relatively limited research has focused on developing simple, low-cost, and fully embedded piezoresistive sensors specifically optimized for compressive stress monitoring in cementitious materials, particularly using accessible manufacturing technologies.

Despite recent progress, a critical scientific gap remains in the development of geometry-driven sensing systems that simultaneously achieve high sensitivity, mechanical compatibility, fabrication simplicity, and scalability. Most existing studies emphasize either material modification (e.g., nanofiller incorporation) or complex structural designs requiring advanced manufacturing techniques, while the potential of simple, topology-driven architectures fabricated via widely accessible methods remains underexplored. In particular, the role of controlled spacing evolution and deformation-induced conductive pathway multiplication within three-dimensional architected geometries has not been systematically investigated for embedded sensing in cementitious systems.

To address this gap, the present study proposes a novel tesseract-inspired piezoresistive sensor fabricated from conductive thermoplastic polyurethane (TPU) using a single-step fused deposition modeling (FDM) process. The proposed architecture introduces a spacing-controlled three-dimensional geometry that enables deformation-induced contact between conductive regions, thereby amplifying the piezoresistive response through geometric effects rather than material complexity. The sensor is embedded within mortar specimens and experimentally evaluated under

compressive loading to assess its mechanical compatibility, sensing performance, and environmental stability. By combining accessible materials, low-cost fabrication, and geometry-driven design, this work establishes a practical and scalable pathway toward embedded SHM systems for real-time monitoring of cementitious infrastructure.

## 2. Theoretical conceptualization

Designing a piezoresistive sensor depends on both the material properties and the structural design of the sensor. Materials influence mechanical properties such as Young's modulus, elastic strain limit, and Poisson's ratio, as well as electrical properties including initial electrical resistance, gauge factor, and hysteresis. In this study, conductive TPU was selected due to its low Young's modulus, which minimizes interference with the deformation of cementitious materials (which possess a much higher Young's modulus than conductive TPU) [15]. Furthermore, among commonly used polymer matrices for conductive composites, TPU exhibits one of the highest Poisson's ratios (approximately 0.49), making it highly suitable for applications requiring significant lateral deformation [16]. In addition, recent studies have shown that conductive TPU exhibits very low initial electrical resistance and high gauge factors when used as a piezoresistive sensor [17], indicating strong potential for embedded sensing application in cementitious materials, particularly for deformation and shrinkage monitoring[18]. While the presence of coarse aggregate in concrete increases material heterogeneity, the underlying sensing behavior is not necessarily different from that in mortar, although greater variability in sensor response may occur[19]. In terms of structural design, the geometry of the sensor plays a significant role, and this work is inspired by tesseract geometry. A tesseract is a four-dimensional analogue of a cube, formed by extending a cube into a fourth spatial dimension perpendicular to the three familiar spatial dimensions. The objective of adopting this geometry is to create multiple conductive pathways for electron transport under mechanical deformation. Conductive TPU inherently enables electron transport through established conductive networks. By introducing a tesseract-based structural design, electron transmission can also be manipulated at the meso-scale through the formation of initial spacings before loading and mechanical contacts during loading. As illustrated in Figure 1a–b, four stages occur when spacing exists between two solid regions(Stage I). Upon applying compressive loading, the spacing decreases due to lateral expansion of the material (Stage II). With further loading, the expansion continues until the spacing is eliminated

(Stage III). If the applied load exceeds the elastic limit, the material enters the plastic deformation region while no spacing remains (Stage IV).

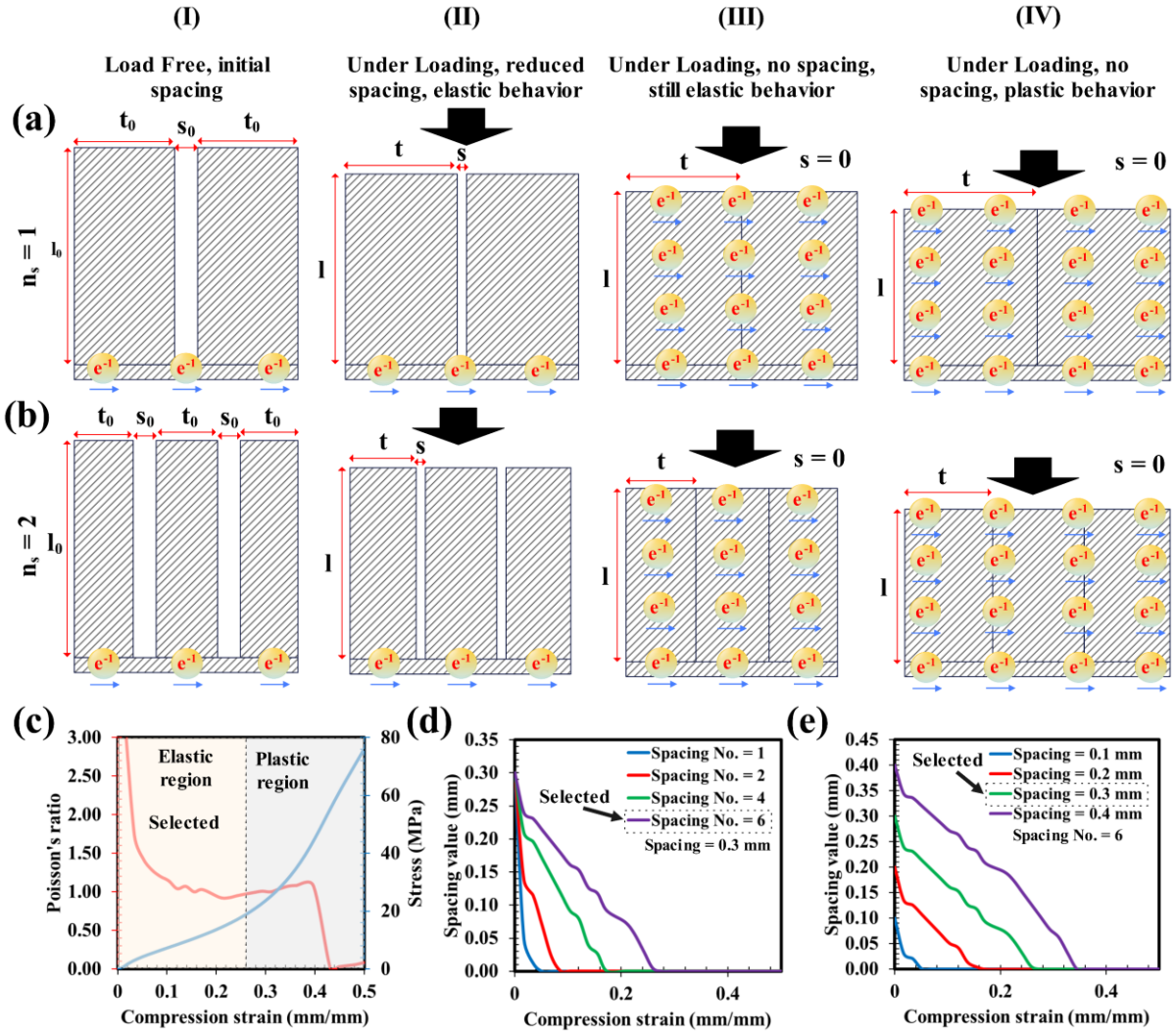


Figure 1. Schematic illustrations, compressive behavior, and electron transport mechanism of the tesseract piezoresistive sensor. (a, b) deformation mechanism under uniaxial compression for spacing numbers ($n_s$) of 1 and 2; (c) experimental evolution of Poisson's ratio and compressive stress as a function of compression strain for a fully solid cube prior to embedding in mortar; (d) theoretical investigation of the effect of spacing number ($n_s$ = 1, 2, 4, 6) on spacing evolution during compression at a fixed initial spacing of 0.3 mm; and (e) theoretical investigation of the influence of different initial spacings (0.1, 0.2, 0.3, and 0.4 mm) on spacing evolution for $n_s$ = 6.

It is important to note that even in the initial state, the conductive TPU already contains intrinsic solid conductive regions that enable electron transport through established conductive networks. However, when the spacing reduces to zero (Stage III), additional conductive pathways are created

due to direct physical contact between adjacent solid regions. This contact formation significantly increases the number of available electron transport paths at the meso-scale, thereby enhancing electrical connectivity and amplifying the piezoresistive response. In other words, the transition from separated domains to fully contacted regions result in a multiplication of electron pathways, which directly contributes to the improved sensitivity of the sensor. To mathematically describe this deformation behavior, Hooke's law was used to establish governing relationships. Considering strain applied in different directions, we can write:

$$\varepsilon_a = \frac{\Delta l}{l_o} \tag{1}$$

$$\varepsilon_t = \frac{\Delta t}{t_o} \tag{2}$$

According to the definition of Poisson's ratio, the relationship between axial and transverse strains is given by:

$$\varepsilon_t = -\nu\varepsilon_a \tag{3}$$

Now, if we consider only one spacing between two solid regions, as shown in Figure 1a, the spacing value after applying the load can be calculated as:

$$s_1 = s_{0_1} - \Delta t_1 \tag{4}$$

If the dimension of the cube is assumed to be A, it can be expressed as:

$$A_1 = 2t_{o_1} + s_{0_1} \tag{5}$$

By substituting Equations (2), (3) and (5) into Equation (4), we obtain:

$$s_1 = s_{0_1}(1 - \frac{1}{2}\nu\varepsilon_a) + \frac{A_1}{2}\nu\varepsilon_a \tag{6}$$

Equation (6) expresses the change in spacing between the solid regions when there is only one spacing, as a function of the initial spacing, Poisson's ratio, axial strain, and cube dimension. If

we extend the design to two spacings, as shown in Figure 1b, while keeping the initial spacing and cube dimension the same, we can write

$$s_{0_1} = s_{0_2} \;\; \& \;\; A_1 = A_2 \tag{7}$$

$$s_2 = s_{0_2} - \Delta t_2 \tag{8}$$

$$A_2 = 3t_{o_2} + 2s_{0_2} \tag{9}$$

$$s_2 = s_{0_1}(1 - \frac{2}{3}\nu\varepsilon_a) + \frac{A_1}{3}\nu\varepsilon_a \tag{10}$$

Similar to Equation (6), the spacing remains a function of the initial spacing, Poisson's ratio, axial strain, and cube dimension, but with different coefficients for each term. To derive a general expression that accounts for an arbitrary number of spacings within the elastic region, we can conclude that:

$$s_n = s_0(1 - \frac{n}{n+1}\nu\varepsilon_a) + \frac{A}{n+1}\nu\varepsilon_a \qquad \varepsilon_a \leq \varepsilon_e \tag{11}$$

Equation (11) expresses the final relationship between spacing evolution and the design parameters. Among these parameters, Poisson's ratio, one of the key criteria for selecting TPU, plays a vital role in determining the spacing value under loading conditions. The simplest approach is to assume a constant Poisson's ratio (approximately 0.49) based on linear elastic behavior. However, we also investigated Poisson's ratio of fully solid 3D-printed conductive TPU and found that it is not perfectly linear due to material characteristics [20, 21] and microstructural effects introduced during the 3D-printing process [22].

By correlating Poisson's ratio with stress values, the elastic region was identified to extend up to approximately 0.25 compressive strain, as shown in Figure 1c. Therefore, the designed sensor must utilize the advantages of the tesseract geometry before exceeding 0.25 compressive strain. Two key design parameters, the number of spacings and the initial spacing value, can be used to control the strain level at which the spacing becomes zero, ensuring that this transition occurs within the elastic region. Using Equation (11) with a cube dimension of 10 mm and an initial spacing of 0.3 mm, it was found that increasing the number of spacings requires a higher

compressive strain to reach zero spacing. A spacing number of 6 was selected because it ideally aligns with the elastic region of conductive TPU, as shown in Figure 1d. Furthermore, increasing the initial spacing also shifts the zero-spacing condition to higher compressive strains. For the same reason, matching the zero-spacing transition with the elastic region, an initial spacing of 0.3 mm was selected. Importantly, the model demonstrates that structural parameters, specifically spacing number ($n$) and initial spacing ($s_0$), control the strain level at which conductive path multiplication occurs. Increasing either parameter delays the zero-spacing condition to higher compressive strains. By selecting $n$ = 6 and $s_0$ = 0.3 mm for a 10 mm cube, the zero-spacing transition is intentionally aligned with the elastic region of conductive TPU (~0.25 strain), ensuring that conductive path enhancement occurs before plastic deformation. This guarantees reversible contact formation, stable cyclic performance, and maximized sensitivity, as shown in Figure 1e. Thus, the proposed model provides a mechanical–electrical framework linking tesseract-based geometry, spacing evolution, and strain-induced conductive path amplification for optimized cementitious piezoresistive sensing applications. On this basis, the developed analytical model not only predicts the mechanical evolution of spacing under compression but also explains the electromechanical response of the tesseract-inspired piezoresistive sensor. As described above, spacing decreases progressively with increasing axial strain, governed by Poisson-driven lateral expansion. When $s_n$ approaches zero within the elastic regime, adjacent conductive TPU regions come into physical contact, as schematically illustrated by the increased electron symbols in Figure 1. This contact formation dramatically increases the number of available meso-scale conductive pathways, supplementing intrinsic molecular-scale conduction with newly formed bulk contact networks. Consequently, the transition from separated domains to full contact corresponds to a sharp enhancement in electron transport density, directly amplifying the resistance variation and gauge response of the sensor.

## 3. Experimental section

### 3.1. Sensor material and fabrication methodology

A carbon black–filled conductive TPU filament (FILAFLEX, Shore hardness 92A, diameter 1.75 mm) with a volume resistivity below 800 Ω·m was supplied by Recreus Industries (Spain). Prior to printing, the filament was dried in an oven for 24 h at 60 °C to remove residual moisture

and minimize bubble formation or porosity during extrusion, which could adversely affect both mechanical integrity and electrical conductivity. The sensor geometry was designed in AutoCAD 2024 based on a tesseract-inspired architecture (Figure 2) with overall dimensions of 10×10×10 $mm^3$. The finalized CAD model was exported and sliced using FlashPrint 5 software to generate the corresponding G-code. Fabrication was carried out via fused deposition modeling (FDM, FlashForge Dreamer 3D) 3D printer. The printing parameters were set to a layer height of 0.200 mm, printing temperature of 205 °C, bed temperature of 70 205 °C, printing speed of 20 mm/s, 100% infill density, and 15% overlap to ensure full structural continuity and consistent conductive pathways.

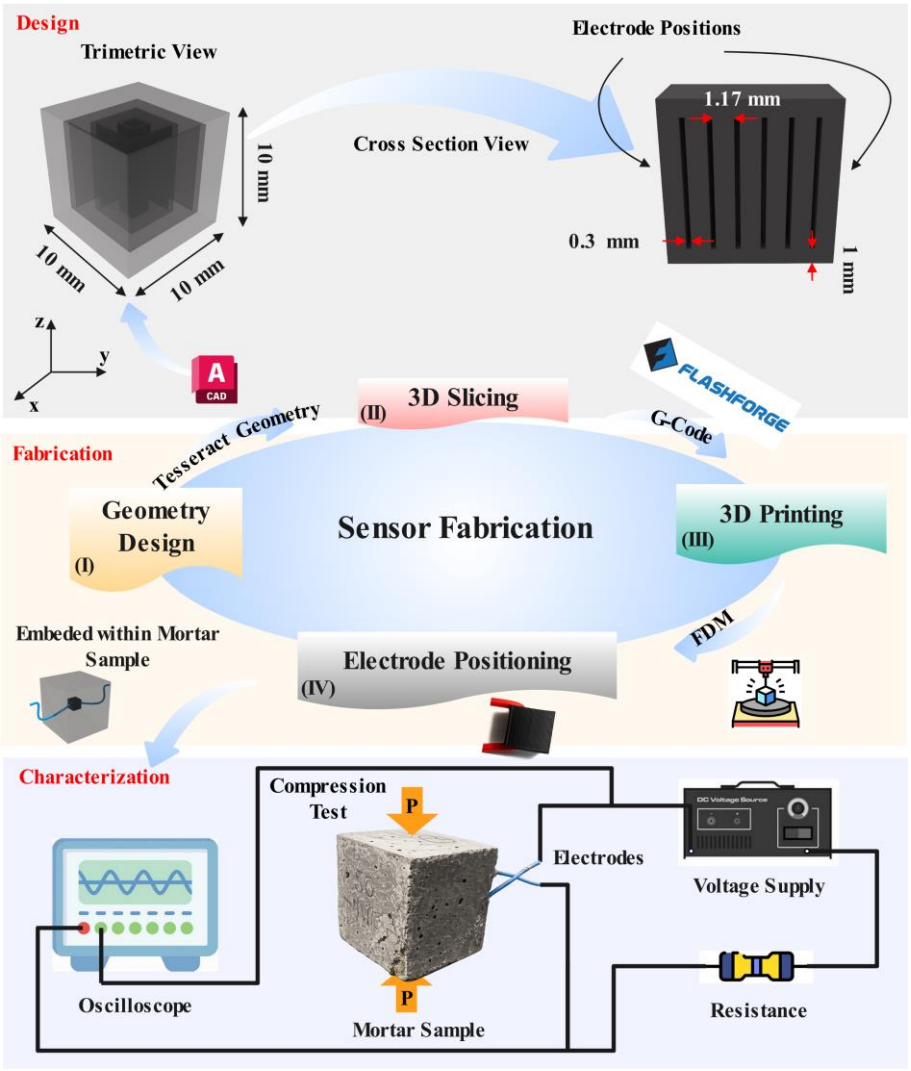


Figure 2. Design, fabrication, and characterization workflow of the 3D-printed tesseract piezoresistive sensor for compressive stress monitoring in cementitious materials.

## 3.2. Mortar composition and specimen preparation

In this study, a single-binder mortar system was adopted to ensure controlled material behavior and eliminate variability associated with blended cement systems. General Purpose (GP) Portland cement conforming to the requirements of Type GP cement under Australian Standard AS 3972 [23] was used as the sole binder. The total binder content was maintained at 450 kg/m³ to provide adequate matrix density and mechanical strength suitable for compressive stress monitoring. The water-to-cement (w/c) ratio was fixed at 0.40 to achieve a balance between workability and mechanical performance, while limiting excessive porosity that may influence stress transfer to the embedded sensor. A sand-to-cement ratio of 1.76 was selected to obtain appropriate consistency and ensure uniform stress distribution within the 50 mm cube specimens. Natural fine aggregate complying with relevant grading requirements was used. The detailed mixture of proportions and chemical composition of cement are summarized in Table 1.

Table 1. specification of mortar mix design.

| Mix properties | Unit | Value |
|---|---|---|
| Cement | ($kg/m^3$) | 450 |
| Water to binder ratio | - | 0.4 |
| Sand | ($kg/m^3$) | 792 |
| Mortar slump flow | (cm.) | 17.9 |
| Chemical Composition | | (%) |
| $SiO_2$ | | 5.85 |
| CaO | | 78.36 |
| $Fe_2O_3$ | | 5.24 |
| $K_2O$ | | 0.24 |
| MnO | | 0.37 |
| $Al_2O_3$ | | 3.91 |
| Others compound | | 6.03 |

Mixing and specimen preparation were conducted in accordance with Australian Standard AS 1012.2 [24], which specifies procedures for the preparation and curing of concrete and mortar test specimens. All materials were weighed prior to mixing to ensure batch consistency. Dry materials were first blended to achieve uniform distribution, followed by gradual addition of water. Mixing was performed using a laboratory Hobart mixer to ensure homogeneous dispersion of constituents and minimize localized segregation. Fresh mortar was taken to conduct a flowability with flow table test [25] before cast into pre-prepared 50×50×50 $mm^3$ steel molds. During casting, the 3D-printed tesseract-inspired conductive TPU sensors were positioned centrally within the mold to

ensure symmetric stress transfer during compressive loading. Care was taken to maintain consistent sensor alignment and embedment depth across all specimens. The mortar was placed in layers and lightly compacted to eliminate entrapped air without disturbing sensor positioning. Immediately after casting, specimens were covered with plastic sheets to minimize moisture loss and prevent premature surface drying. After 24 hours, specimens were demolded and transferred to a water-curing tank maintained at laboratory temperature for 28 days prior to mechanical and electromechanical testing.

### 3.3. Characterization of samples

The mechanical and electromechanical properties of the 3D-printed piezoresistive tesseract sensors were evaluated under compressive loading at a constant displacement rate of 1 mm/s with a gauge length of 10 mm. To calculate Poisson's ratio of the 3D printed fully solid piezoresistive sample, the lateral deformation was recorded using a high-speed camera and processed using an image processing technique, following our previous work [26]. To measure the electrical response from the lateral directions, two electrodes were attached to the sensor surface by locally melting the polymer, followed by the application of silver paste to ensure stable electrical contact between the conductive wires and the sensor. Signal acquisition was performed using an Analog Discovery 2 data acquisition system. A voltage divider configuration was employed with a fixed external resistor of 330 Ω and an input voltage of 9 V to monitor the voltage variation corresponding to resistance changes during compression, as shown in Figure 2. For cyclic loading of the sensor prior to embedding, a triangular waveform with a frequency of 1 Hz was applied.

Mortar specimens with and without embedded sensors were subjected to the same compressive loading rate of 1 mm/s, with a gauge length of 50 mm. A similar electrical measurement setup was used to record the sensor output under loading, ensuring consistency in electromechanical characterization. After embedding the sensors, the mortar samples were subjected to cyclic loading using a triangular waveform with a 0.5 s dwell time at a frequency of 0.2 Hz.

# 4. Results and discussion

## 4.1. piezoresistive response of 3D-printed tesseract sensors before embedding

As shown in Figure 3a, the relative resistance change ($\Delta R/R_0$) increases monotonically with increasing compressive strain for all spacing numbers ($n_s$), confirming the characteristic piezoresistive response governed by strain-induced structural deformation and modulation of conductive pathways. Notably, increasing the spacing number from a fully solid configuration ($n_s = 0$) to $n_s = 6$ results in a substantial enhancement in the resistance response magnitude, with $\Delta R/R_0$ reaching approximately −90% at high strain for $n_s = 6$, compared to less than −15% for the fully solid structure. This pronounced improvement is attributed to the increased structural compliance and deformability introduced by the tesseract architecture, which facilitates greater strain-induced geometric deformation and more significant rearrangement of conductive networks. The enlarged elastic-strain region (Figure 3b) further demonstrates that the strain sensitivity increases progressively with increasing spacing number, as evidenced by the steeper slopes of the $\Delta R/R_0$–strain curves within the low-strain regime (<0.25 mm/mm). This enhanced sensitivity arises from the increased number of deformable structural units and contact interfaces, which amplify deformation-induced variations in contact resistance and electron transport pathways. Correspondingly, the calculated gauge factor (Figure 3c) increases markedly from approximately 20 for the fully solid structure to approximately 87 for $n_s = 6$, representing more than a four-fold improvement in sensitivity. This enhancement highlights the effectiveness of tesseract architecture in amplifying electromechanical coupling through geometric and structural optimization. Mechanistically, this behavior can be attributed to three synergistic effects: (i) increased deformation-induced variation in contact resistance due to enhanced structural flexibility, (ii) geometric amplification of localized strain within conductive regions enabled by the architected tesseract geometry, and (iii) reduced effective stiffness associated with increased spacing, which allows greater deformation under identical loading conditions. Similar trends have been reported in architected piezoresistive sensors, where lattice-based and porous geometries improve sensitivity by promoting efficient strain transfer and conductive network modulation [27, 28].

Figure 3d and 3e present the electromechanical response of the tesseract-structured sensor for different initial spacing values ranging from 0 to 0.4 mm, revealing a clear dependence of

resistance variation on structural spacing. Similar to the effect observed for spacing number, increasing the initial spacing value significantly enhances the magnitude of the relative resistance change ($\Delta R/R_0$) under compressive loading. Specifically, structures with larger spacing values exhibit greater $\Delta R/R_0$ magnitudes and steeper slopes in the elastic region, indicating substantially improved strain sensitivity. This trend is quantitatively confirmed by the gauge factor analysis shown in Figure 3f, where the gauge factor increases from approximately 20 for the fully solid structure to approximately 92 for the largest spacing value (0.4 mm), representing more than a 4.5-fold enhancement in sensitivity. Statistical analysis further confirms the significant improvement in sensitivity at higher spacing values, emphasizing the critical role of structural spacing as a key design parameter for tuning electromechanical performance. This enhancement can be primarily attributed to increased structural compliance and deformation amplification associated with larger spacing, which reduces geometric constraints and allows greater strain-induced modulation of conductive pathways. As spacing increases, the conductive network experiences more pronounced deformation, resulting in larger variations in contact resistance between adjacent conductive domains. Furthermore, tesseract architecture enables efficient strain transfer and geometric amplification, ensuring that macroscopic deformation is effectively translated into localized conductive pathway modulation without compromising structural stability. These findings are consistent with previously reported architected piezoresistive systems, where increased structural spacing and porosity enhance strain sensitivity by facilitating deformation-induced conductive network reconfiguration and resistance variation [29, 30].

The long-term cyclic stability of the tesseract-structured sensor was evaluated over 1000 loading–unloading cycles at a frequency of 1 Hz and a compressive strain of 0.22, as shown in Figure 3g. The $\Delta R/R_0$ response remains highly consistent throughout the entire test, exhibiting negligible signal drift, fluctuation, or degradation, which confirms the excellent durability and stability of the sensor under repeated mechanical loading. This stable electromechanical response indicates that the architected structure effectively maintains its structural integrity and conductive network continuity, even under prolonged cyclic deformation. Such high cyclic stability is essential for reliable operation in practical applications, including structural health monitoring, embedded sensing in cementitious or composite materials, and other environments subjected to repeated mechanical loading. The enlarged cyclic response presented in Figure 3h further

demonstrates the excellent repeatability and reversibility of the sensor, as evidenced by the nearly identical loading and unloading curves over multiple cycles with minimal signal deviation.

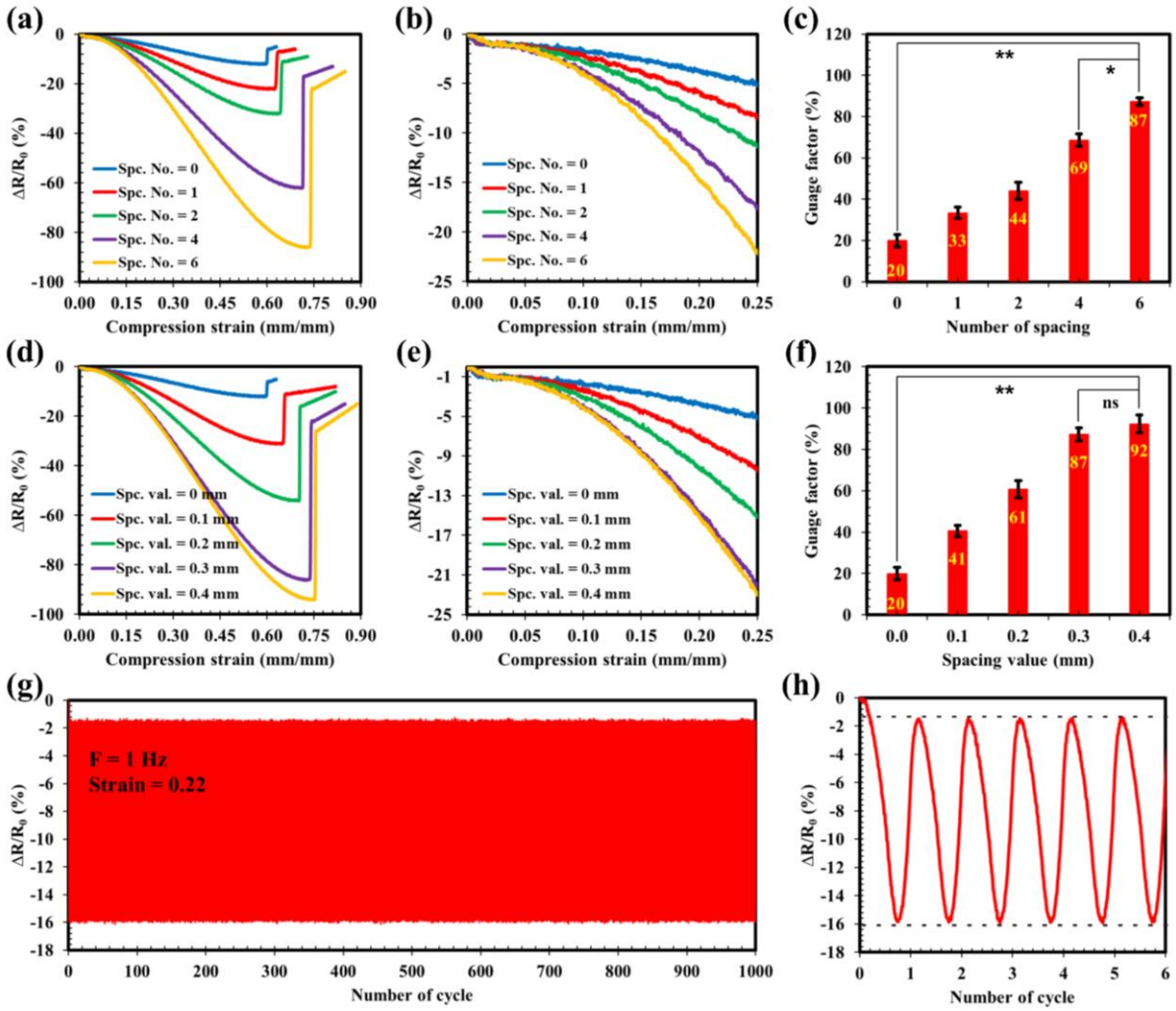


Figure 3. Electromechanical performance of the tesseract-structured piezoresistive sensor before embedding; (a) relative resistance change ($\Delta R/R_0$) versus compression strain for different spacing numbers (fully solid, $n_s$ = 1, 2, 4, and 6), (b) enlarged elastic-strain region highlighting sensitivity enhancement with increasing spacing number, (c) corresponding gauge factor comparison as a function of spacing number, indicating significantly improved sensitivity at higher $n_s$, (d) $\Delta R/R_0$ versus compression strain for different initial spacing values (0.1–0.4 mm), (e) enlarged elastic-strain response for different spacing values, demonstrating increased strain sensitivity with larger spacing, (f) calculated gauge factors as a function of spacing value, with statistical significance indicated, (g) long-term cyclic stability test at 1 Hz and 0.22 strain for 1000 cycles, showing stable and repeatable signal response, (h) enlarged view of representative cyclic loading–unloading curves over six cycles, confirming excellent repeatability and minimal hysteresis.

The negligible hysteresis observed in the $\Delta R/R_0$ response suggests low energy dissipation and efficient structural recovery, indicating that the deformation-induced changes in conductive

pathways are highly reversible. This superior cyclic performance can be attributed to the mechanically robust tesseract architecture, which enables uniform stress distribution and prevents localized stress concentration or permanent structural damage, as well as the stability of the conductive network, which undergoes reversible deformation without irreversible conductive pathway disruption. Furthermore, the architected geometry promotes efficient strain transfer and controlled deformation, ensuring consistent modulation of contact resistance during cyclic loading. These results are consistent with previously reported architected piezoresistive sensors, where lattice and porous structures exhibit excellent durability and repeatability due to their ability to accommodate mechanical deformation through distributed structural compliance and reversible conductive network reconfiguration [31, 32].

A comparative evaluation of recent piezoresistive sensing systems (Table 2) highlights the dominant strategies used to enhance sensitivity, including microstructural engineering, material optimization, electrode design, and architectural structuring. Microstructured elastomeric sensors such as PDMS/MWCNT composites [29] achieve moderate sensitivity (10–50) through micro-porous or micro-contact structures fabricated via mold casting. While effective, such approaches rely on micromolding processes that introduce fabrication complexity and limit scalability. Material-driven approaches, such as acrylate/CNT nanocomposites fabricated via DLP 3D printing [33], exhibit relatively low sensitivity (2.40–4.78), as their performance is governed primarily by conductive network evolution within a bulk matrix without structural amplification. Similarly, HDPE/MWCNT auxetic structures [34] utilize geometric effects to enhance sensing performance (7.6); however, their sensitivity remains limited due to the relatively rigid polymer matrix and constrained deformation capability. More advanced strategies incorporate hybrid fabrication and multi-functional design. For instance, TPU/CB sensors integrated with silver interdigitated electrodes (IDE) [35] achieve improved sensitivity (23.8) by enhancing electrical signal collection through electrode engineering. Likewise, conductive polymer reinforcement grids composed of PLA/TPU/CF [36] are designed for infrastructure applications, offering multifunctionality such as self-sensing and self-heating, but exhibit relatively low sensitivity (5–10) due to reliance on bulk conductive pathways. Architected lattice-based sensors, such as TPU/MWCNT systems fabricated via DIW and FDM hybrid printing [27], demonstrate significantly higher sensitivity (40–80) through periodic lattice structures that amplify strain via controlled deformation. In contrast to these approaches, the present work introduces a geometry-driven sensing strategy based on

hierarchical tesseract architecture fabricated using a single-step FDM process. The proposed TPU/CB sensor achieves a high and tunable sensitivity (20–92), comparable to or exceeding that of advanced architected systems [27], while eliminating the need for hybrid fabrication, microfabrication, or electrode engineering as required in other studies [29, 35]. The enhanced performance originates from controlled spacing evolution and deformation-induced multiplication of conductive pathways, which significantly amplifies the piezoresistive response within the elastic regime. Importantly, this study demonstrates a substantial advantage in terms of fabrication simplicity, cost, and accessibility. Unlike DLP-based systems [33], DIW-assisted hybrid processes [27, 35], or micromolding techniques [29], the proposed sensor is fabricated using a commercially available conductive TPU filament and a low-cost desktop FDM 3D printer, without requiring specialized equipment or multi-step processing. This significantly reduces manufacturing costs, improves scalability, and facilitates practical implementation, particularly.

Table 2. Comparison of piezoresistive performance and fabrication strategies of architected polymer nanocomposite sensors.

| Materials | Sensitivity | Fabrication method | Key Feature / Structure | Reference |
|---|---|---|---|---|
| PDMS/MWCNTs | 10–50 | Mold casting | Micro-porous structure | [29] |
| Acrylate/CNT | 2.40–4.78 | DLP 3D-printing | Bulk nanocomposite | [33] |
| HDPE/MWCNT | 7.6 | FFF 3D-printing | Auxetic geometry | [34] |
| TPU/CB/Ag | 23.8 | FFF + DIW hybrid printing | Elastomer nanocomposite + electrode engineering | [35] |
| PLA/TPU/CF | 5–10 | FDM 3D printing | Grid-shaped self-sensing infrastructure material | [36] |
| TPU/MWCNTs | 40–80 | DIW + FDM hybrid printing | Periodic lattice | [27] |
| TPU/CB | 20–92 | FDM 3D-printing | Hierarchical tesseract geometry | This Work |

## 4.2. piezoresistive response of 3D-printed tesseract sensors after embedding

As shown in Figure 4a, the stress–strain responses of mortar specimens with and without the embedded sensor follow similar overall trends, indicating that incorporation of the sensor does not cause a detrimental change in the compressive behavior of the host matrix. Although slight differences in stiffness and peak response are observed, the embedded specimen maintains a comparable load-bearing profile, confirming that the soft conductive TPU sensor can be integrated within mortar without severely compromising the mechanical integrity of the composite system.

This behavior is attributed to the relatively low modulus and compliant nature of the sensor, which minimizes mechanical incompatibility and stress concentration inside the cementitious matrix.

Figure 4b compares the strain response measured by the developed embedded sensor with that obtained from a commercial strain gauge under identical loading conditions at 25 °C and 65% RH. The two signals show a similar trend during the loading stage, demonstrating that the embedded sensor is capable of accurately following the strain evolution of the mortar specimen. The strong agreement in the loading region confirms the feasibility of the sensor for real-time embedded compressive strain monitoring in cementitious materials.

The effect of relative humidity on the piezoresistive response is presented in Figure 4c. For all humidity levels, the magnitude of $\Delta R/R_0$ increases with increasing strain, confirming stable strain-dependent electromechanical transduction after embedding. However, the response is strongly affected by moisture level. The largest resistance variation is observed at low humidity (10% RH), followed by 65% RH, while the smallest response is obtained at saturated conditions (100% RH). This trend indicates that increased humidity suppresses sensor sensitivity. Such behavior can be attributed to the presence of absorbed moisture in the surrounding mortar and at the sensor–matrix interface, which may alter local charge transport, partially screen resistance changes, and reduce the effective modulation of conductive pathways under compression. These observations are quantitatively supported by Figure 4d, where the calculated gauge factor decreases from 0.011 at 10% RH to 0.007 at 65% RH and further to about 0.003 at 100% RH, confirming that dry conditions favor stronger piezoresistive sensitivity. Similar environmental dependence is observed for temperature, as shown in Figure 4e. Under constant RH of 65%, the embedded sensor exhibits the greatest $\Delta R/R_0$ response at 10 °C, followed by 25 °C, while the lowest response occurs at 45 °C. The reduction in resistance change with increasing temperature suggests that elevated temperature reduces the sensitivity of the embedded conductive TPU structure. This may be explained by thermal softening of the polymer matrix and temperature-induced changes in conductive network stability, which reduce the extent of resistance modulation under a given mechanical strain. Figure 4f confirms this effect quantitatively, with the gauge factor decreasing from 0.011 at 10 °C to 0.007 at 25 °C and approximately 0.003 at 45 °C. These results indicate that both humidity and temperature influence the sensor response and should be considered in practical calibration for field deployment.

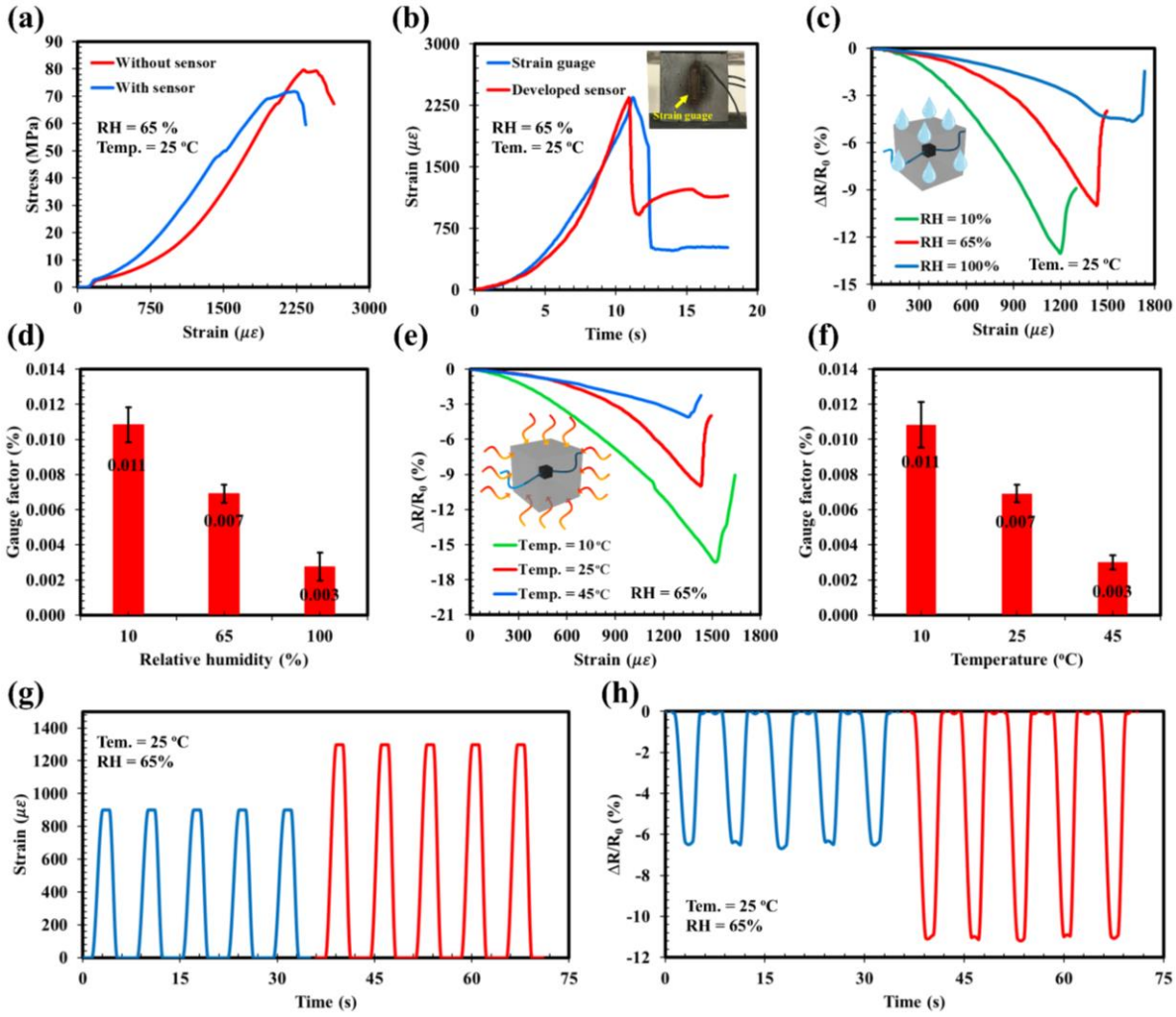


Figure 4. Mechanical performance of mortar and electromechanical performance of the tesseract-structured piezoresistive sensor after embedding; (a) stress–strain curves of mortar with and without the embedded sensor at 25 °C and 65% relative humidity (RH), (b) comparison of strain responses measured by a commercial strain gauge and the developed sensor under identical loading conditions (RH = 65%, 25 °C), (c) $\Delta R/R_0$ as a function of strain under different relative humidity levels (10%, 65%, and 100%) at 25 °C, (d) corresponding gauge factor as a function of relative humidity, (e) $\Delta R/R_0$ versus strain at different temperatures (10 °C, 25 °C, and 45 °C) under constant RH (65%), (f) calculated gauge factor as a function of temperature, (g) cyclic strain loading profiles applied to the system at 25 °C and 65% RH, (h) corresponding cyclic $\Delta R/R_0$ responses.

The cyclic performance of the embedded system is shown in Figure 4g and 4h. The imposed cyclic strain profiles at 25 °C and 65% RH are well defined and repeatable, with two distinct loading amplitudes applied sequentially. The corresponding $\Delta R/R_0$ responses closely follow the strain input, exhibiting stable, periodic, and reversible signals across repeated cycles. Lower-

amplitude cycles produce smaller resistance changes, whereas higher-amplitude cycles generate proportionally larger signal magnitudes, confirming the sensor's ability to distinguish different strain levels after embedding. The absence of pronounced signal drift or irregular fluctuation during repeated cycling demonstrates that the tesseract-structured sensor retains stable electromechanical functionality within the mortar environment. This cyclic reliability is consistent with the reversible spacing-controlled conductive pathway modulation proposed in the sensing mechanism and further supports the suitability of the developed sensor for long-term structural health monitoring applications in cementitious systems.

Despite the promising performance demonstrated in this study, several limitations should be acknowledged. The sensing response exhibits noticeable dependence on environmental conditions, particularly humidity and temperature, which can reduce sensitivity and introduce variability in practical applications. It is important to note that the current design and testing conditions are aligned with typical Australian environments, particularly Sydney, where extreme low-temperature conditions and freeze–thaw cycles are generally absent. As such, the sensor has not been evaluated under severe thermal cycling conditions commonly encountered in colder climates. Additionally, the current work is limited to laboratory-scale mortar specimens under controlled loading, and long-term durability under real field conditions (e.g., chemical exposure, sustained loading, and environmental aging) remains to be investigated. Future research should therefore focus on extending the applicability of the proposed sensor to broader environmental conditions through material and structural tailoring, such as modifying the polymer matrix or conductive network to maintain performance at lower temperatures. The development of compensation strategies for environmental effects, including calibration models or multi-parameter sensing, will also be essential. Furthermore, optimization of the tesseract geometry and integration with wireless or self-powered data acquisition systems could enhance scalability and enable robust, real-time structural health monitoring across diverse climatic conditions.

## 5. Conclusion

In this study, a novel tesseract-inspired piezoresistive sensor based on conductive TPU was successfully developed and embedded within mortar for real-time compressive stress monitoring. The proposed sensor leverages a geometry-driven mechanism, where controlled spacing evolution

and deformation-induced contact between conductive domains lead to significant amplification of the piezoresistive response. Prior to embedding, the sensor exhibited a high and tunable sensitivity (gauge factor up to 92), which was maintained after integration into the mortar matrix, demonstrating effective electromechanical coupling and reliable strain tracking comparable to a commercial strain gauge. Importantly, the embedded system preserved the mechanical integrity of the host material, confirming its compatibility for structural applications. Compared with existing approaches that rely on complex material systems, hybrid fabrication, or electrode engineering, the present work offers a simple, cost-effective, and scalable solution, achieved using commercially available conductive TPU filament and a single-step FDM 3D-printing process. This significantly reduces fabrication complexity and enhances accessibility for practical deployment. While the sensor response is influenced by environmental factors such as humidity and temperature, the system was specifically designed for typical Australian conditions, particularly Sydney, where extreme freeze–thaw cycles are not prevalent. Nevertheless, the proposed architecture provides a flexible platform that can be tailored for broader climatic conditions through material and structural optimization.

## Author Contributions

**Milad Razbin:** Conceptualization, Methodology, Soft and Hard Analysis, Visualization, Writing Original Draft, and Review and Editing Draft. **Sillawat Sathorn:** Methodology, Writing Original Draft. **Sajad Abolpour Moshizi:** Review and Editing Draft, Funding Acquisition, and Supervision. **Li Chang:** Review and Editing Draft, Funding Acquisition, and Supervision. **Shuying Wu:** Review and Editing Draft, Funding Acquisition, and Supervision. **Mohsen Asadnia:** Review and Editing Draft, and Supervision. **Vanissorn Vimonsatit:** Review and Editing Draft, Funding Acquisition, and Supervision.

## Declaration of conflicting interests

The authors declared no potential conflicts of interest concerning the research, authorship, and/or publication of this article.

## Data availability statement

The data that support the findings of this study are available on request from the corresponding authors.

## Competing interests

The authors declare no competing interests.

## References


[1] J. Ou and H. Li, "Structural health monitoring in mainland China: review and future trends," *Structural health monitoring,* vol. 9, no. 3, pp. 219-231, 2010.

[2] D. Inaudi and B. Glisic, "Long-range pipeline monitoring by distributed fiber optic sensing," 2010.

[3] G. Park, H. Sohn, C. R. Farrar, and D. J. Inman, "Overview of piezoelectric impedance-based health monitoring and path forward," *Shock and vibration digest,* vol. 35, no. 6, pp. 451-464, 2003.

[4] L. Wang and F. Aslani, "A review on material design, performance, and practical application of electrically conductive cementitious composites," *Construction and Building Materials,* vol. 229, p. 116892, 2019.

[5] S. Wen and D. Chung, "Strain-sensing characteristics of carbon fiber-reinforced cement," *ACI materials journal,* vol. 102, no. 4, p. 244, 2005.

[6] M. S. Konsta-Gdoutos, Z. S. Metaxa, and S. P. Shah, "Highly dispersed carbon nanotube reinforced cement based materials," *Cement and concrete research,* vol. 40, no. 7, pp. 1052-1059, 2010.

[7] K. C. Ackermann, *Self-sensing concrete for structural health monitoring of smart infrastructures*. University of Rhode Island, 2018.

[8] B. Han, X. Yu, and J. Ou, *Self-sensing concrete in smart structures*. Butterworth-Heinemann, 2014.

[9] F. Ubertini, A. L. Materazzi, A. D'Alessandro, and S. Laflamme, "Natural frequencies identification of a reinforced concrete beam using carbon nanotube cement-based sensors," *Engineering structures,* vol. 60, pp. 265-275, 2014.

[10] B. Han, S. Ding, and X. Yu, "Intrinsic self-sensing concrete and structures: A review," *Measurement,* vol. 59, pp. 110-128, 2015.

[11] P. M. Ferreira, M. A. Machado, M. S. Carvalho, and C. Vidal, "Embedded sensors for structural health monitoring: methodologies and applications review," *Sensors,* vol. 22, no. 21, p. 8320, 2022.

[12] A. Barrias, J. R. Casas, and S. Villalba, "Embedded distributed optical fiber sensors in reinforced concrete structures—A case study," *Sensors,* vol. 18, no. 4, p. 980, 2018.

[13] S. J. Leigh, R. J. Bradley, C. P. Purssell, D. R. Billson, and D. A. Hutchins, "A simple, low-cost conductive composite material for 3D printing of electronic sensors," *PloS one,* vol. 7, no. 11, p. e49365, 2012.

[14] M. Razbin, S. Sathorn, S. Wu, M. Asadnia, and V. Vimonsatit, "3-D-Printed Piezoresistive Sensor for Real-Time Shrinkage Monitoring of Cementitious Materials," *IEEE Sensors Journal,* vol. 26, no. 4, pp. 5358-5368, 2026, doi: 10.1109/JSEN.2025.3648830.

[15] M. Razbin *et al.*, "Piezoresistive polymer nanocomposite sensors for structural health monitoring of concrete beams," *Smart Materials and Structures,* vol. 35, no. 1, p. 015006, 2026.

[16] A. Bezazi and F. Scarpa, "Mechanical behaviour of conventional and negative Poisson's ratio thermoplastic polyurethane foams under compressive cyclic loading," *International Journal of fatigue,* vol. 29, no. 5, pp. 922-930, 2007.

[17] M. Razbin *et al.*, "Application of soft computing techniques in the optimization of 3D-printed piezoresistive sensors," *Sensors and Actuators A: Physical,* vol. 385, p. 116277, 2025.

[18] S. Sathorn, M. Razbin, V. Vanissorn, M. Asadnia, and S. Wu, "Monitoring of Shrinkage in Mortar and Concrete Using Conductive Thermoplastic Polyurethane," in *Proceedings of the 18th East Asia-Pacific Conference on Structural Engineering and Construction-Volume1*, Singapore, S. Tangtermsirikul, P. Warnitchai, K. Panuwatwanich, and G. Tanapornraweekit, Eds., 2025// 2025: Springer Nature Singapore, pp. 88-94.

[19] H. Zhang, S. Hou, and J. Ou, "SA-based concrete seismic stress monitoring: The effect of maximum aggregate size," *Journal of Building Engineering,* vol. 88, p. 109232, 2024/07/01/ 2024, doi: https://doi.org/10.1016/j.jobe.2024.109232.

[20] M. Razbin, M. Jamshidi Avanaki, A. A. A. Jeddi, and H. Dabiryan, "A systematic study on the predictability of different methods to predict the maximum Poisson's ratio of helical auxetic yarn," *The Journal of the Textile Institute,* vol. 113, no. 1, pp. 90-100, 2022.

[21] M. Razbin, M. Jamshidi Avanaki, A. A. Asghariyan Jeddi, and H. Dabiryan, "Double-core helical auxetic yarn: a Novel structure, geometrical modeling and experimental verification," *The Journal of the Textile Institute,* vol. 113, no. 7, pp. 1256-1269, 2022.

[22] S. Jaganathan, R. Kandasamy, R. Venkatachalam, M. Gunalan, and R. Dhairiyasamy, "Advances in optimizing mechanical performance of 3D-printed polymer composites: A microstructural and processing enhancements review," *Advances in Polymer Technology,* vol. 2024, no. 1, p. 3168252, 2024.

[23] *AS3972-2010 General purpose and blended cement*, StandardAustralia, 2010.

[24] *AS 1012.2:2014 Methods of testing concrete Method 2: Preparing concrete mixes in the laboratory*, StandardsAustralia, 2014. [Online]. Available: https://www.intertekinform.com/en-au/standards/as-1012-2-2014-111737_saig_as_as_233715

[25] *ASTM C1437-20: Standard Test Method for Flow of Hydraulic Cement Mortar*, A. International, West Conshohocken, PA, USA, 2020. [Online]. Available: https://www.astm.org/c1437-20

[26] M. Razbin, A. A. A. Jeddi, D. Semnani, and M. Ramzanpoor, "A generalized method of measuring the Poisson's ratio of warp knitted fabrics under uniaxial loading based on image processing technique," *The Journal of The Textile Institute,* vol. 113, no. 1, pp. 70-79, 2022.

[27] Y. Li, S. Luo, M. C. Yang, R. Liang, and C. Zeng, "Poisson ratio and piezoresistive sensing: a new route to high-performance 3D flexible and stretchable sensors of multimodal sensing capability," *Advanced Functional Materials,* vol. 26, no. 17, pp. 2900-2908, 2016.

[28] W. Li *et al.*, "Synergy of porous structure and microstructure in piezoresistive material for high-performance and flexible pressure sensors," *ACS applied materials & interfaces,* vol. 13, no. 16, pp. 19211-19220, 2021.

[29] J. Park *et al.*, "Giant tunneling piezoresistance of composite elastomers with interlocked microdome arrays for ultrasensitive and multimodal electronic skins," *ACS nano,* vol. 8, no. 5, pp. 4689-4697, 2014.

[30] T. Zhao, T. Li, L. Chen, L. Yuan, X. Li, and J. Zhang, "Highly sensitive flexible piezoresistive pressure sensor developed using biomimetically textured porous materials," *ACS applied materials & interfaces,* vol. 11, no. 32, pp. 29466-29473, 2019.

[31] T. Yamada *et al.*, "A stretchable carbon nanotube strain sensor for human-motion detection," *Nature nanotechnology,* vol. 6, no. 5, pp. 296-301, 2011.

[32] M. Amjadi, K. U. Kyung, I. Park, and M. Sitti, "Stretchable, skin-mountable, and wearable strain sensors and their potential applications: a review," *Advanced Functional Materials,* vol. 26, no. 11, pp. 1678-1698, 2016.

[33] O. W. Saadi, A. Schiffer, and S. Kumar, "Piezoresistive behavior of DLP 3D printed CNT/polymer nanocomposites under monotonic and cyclic loading," *The International Journal of Advanced Manufacturing Technology,* vol. 126, no. 5, pp. 1965-1978, 2023.

[34] S. AlMahri, J. Schneider, A. Schiffer, and S. Kumar, "Piezoresistive sensing performance of multifunctional MWCNT/HDPE auxetic structures enabled by additive manufacturing," *Polymer Testing,* vol. 114, p. 107687, 2022.

[35] C. Sánchez, D. Rodríguez, S. Otero, and C. A. Monje, "Enhancing sensing performance of 3D-printed TPU/CB piezoresistive strain sensors through integration of silver ink IDE," *Sensors and Actuators A: Physical,* vol. 393, p. 116757, 2025.

[36] M. Abedi, K. Al-Jabri, B. Han, R. Fangueiro, P. B. Lourenço, and A. G. Correia, "Advancing infrastructure resilience: A polymeric composite reinforcement grid with self-sensing and self-heating capabilities," *Construction and Building Materials,* vol. 435, p. 136730, 2024.